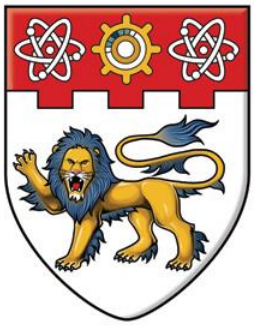

NANYANG TECHNOLOGICAL UNIVERSITY

DEVELOPMENT OF A LUBRICANT-FREE REVOLVING VANE COMPRESSOR

AW KUAN THAI

SCHOOL OF MECHANICAL AND AEROSPACE ENGINEERING

2017

DEVELOPMENT OF A LUBRICANT-FREE REVOLVING VANE COMPRESSOR

AW KUAN THAI

School of Mechanical and Aerospace Engineering

2017

A thesis submitted to the Nanyang Technological University
in partial fulfilment of the requirements for the degree of
Doctor of Philosophy

Acknowledgements

First of all, the author would like to give his greatest gratitude to his thesis supervisor, Prof Ooi Kim Tiow for his guidance and assistance throughout the thesis project. Apart from academic guidance and inspiration, Prof Ooi also mentored the author on valuable life lessons and the author has picked up numerous insights and perspectives on everyday life.

Next, the author would like to thank NTU for giving him the opportunity to pursue his PhD with a scholarship. Many other opportunities were also presented to the author by the School of Mechanical and Aerospace Engineering, namely nominations to attend an international transferable skills workshop, a three-month exchange programme to Tokyo Institute of Technology and the chance to attend a private dialogue session with Nobel Laureates Professor Ada Yonath (Chemistry, 2009) and Sir Harold Walter Kroto (Chemistry, 1996). The author has gained a lot of international exposure and experience which would have been impossible if not for NTU.

Thirdly, the author would like to appreciate and thank his seniors and fellow colleagues, Dr Tan Kok Ming, Dr Alison Subiantoro, Dr Kong Kian Shing and Yap Ken Shaun for their help and guidance. Dr Tan has helped tremendously in the project with his groundbreaking developmental work on the revolving vane compressor on which the thesis is built on. Dr Subiantoro's work on the revolving vane expander has also helped the author to broaden his insights on the revolving vane mechanism as well. Dr Kong shared his expertise on measurement instrumentation with the author and this knowledge has aided the author well when his turn came to design and set up his experiment for the compressor prototype. Furthermore, as the author had no research funds for the thesis project, Shaun had kindly provided part of his own research funds to allow the author to build the compressor prototype; without the graciousness of Shaun, this project would not have been possible.

Next up, the author would like to thank the technical staff, Roger Lee, Lawrence Ang and Edward Yeo from Energy Systems Laboratory, Yuan Kee Hock from Thermal and Fluids Laboratory, Eric Yap and Lai Tay Boon from Fluid Mechanics Laboratory, Steven Lim, Chia Yak Khoong and William Foo from Heat Transfer Laboratory, Lee Siew Chuan and Elson Ng from Manufacturing Process Laboratory. Their kind assistance in aiding the author for the setup of the experiment testbed and during the experiment runs was very much appreciated and has

saved the author quite some hassle. The author has also picked up some technical knowledge and skills from the technical staff which have serve the author well.

In addition, the author would also like to thank his fellow PhD batch-mates, William Toh, Tan Chun Kiat, Ken Tay, Chew Kok Hon, Koh Jian Hao, Martin Koh for their friendship and daily lunch banters. The camaraderie and companionship have definitely made the author's PhD journey less mundane and more interesting.

Last but not least, the author would like to thank the support and encouragement from his family. Their understanding and concern have helped to pick up the author during difficult times and spurred him to keep going.

Contents

List of Figures

List of Tables

Nomenclature

A	area; normalisation constant [m^2 ; –]
a	polynomial coefficient [–]
B	spatial periodicity between asperities [m]
b	distance, asperity width [m]
C	coefficient; [–]
c_p	specific heat [J kg^{-1} K^{-1}]
D	hydraulic diameter; diameter [m]
E	Young's modulus [Pa]
F	force; view factor [N ; –]
f	holonomic constraint function; force per unit area [– ; N m^{-2}]
G	time response [m]
g	gravitational constant [kg m s^{-2}]
H	thermal conductance coefficient; asperity height [W K^{-1} ; m]
h	specific enthalpy; heat transfer coefficient [J kg^{-1} ; W m^{-2} K^{-1}]
I	moment of inertia [kg m^2]
j	time or angle step number [–]
k	thermal conductivity [W m^{-1} K^{-1}]
k-ε	k-epsilon turbulence flow model
L	Lagrangian of system [J]
l	length [m]
M	Mach number; moment [– ; N·m]
m	mass [kg]
N	normal reaction force [N]
n	safety factor; total number of time or angle steps; numeric count [–]
O	origin; centre of rotation [–]
P	power, [W]
p	pressure [Pa]
Q	heat [J]
R	specific gas constant; Rayleigh's quotient; thermal contact resistance [J kg^{-1} K^{-1} ; Hz^2 ; m^2 K W^{-1}]

r	radius; radial distance [m]
T	temperature; torque [K ; N·m]
t	time; thickness [s ; m]
U	mode shape [–]
u	specific internal energy [J kg^{-1}]
V	volume [m^3]
v	velocity [m s^{-1}]
W	work [J]
w	width [m]
x	x-coordinate [m]
y	y-coordinate [m]
z	z-coordinate [m]

Greek Symbols

α	angular acceleration; thermal diffusivity [rad s^{-2} ; m^2 s^{-1}]
β	eigenvalue; thermal expansion coefficient [– ; K^{-1}]
γ	angle of vane from cylinder/rotor centre [rad]
δ	clearance; Kronecker delta [m ; –]
ε	eccentricity; surface emissivity [m ; –]
ζ	damping
η	volumetric efficiency [–]
θ	rotation angle [rad]
ι	vane thickness [m]
κ	ratio of specific heats [c_p/c_v]
λ	friction factor; Lagrange multiplier [–]
μ	dynamic viscosity; coefficient of friction [Pa s ; –]
ξ	heat generation coefficient [–]
ρ	density [kg m^{-3}]
σ	stress ; Stefan-Boltzmann constant [Pa ; W m^{-2} K^{-4}]
τ	shear force [N]
ϕ	displacement angle of bushing [rad]
φ	angle [rad]

χ	frequency; natural frequency [Hz]
ψ	number of stator poles [–]
Ω	vibration frequency [Hz]
ω	angular speed [rad s^{-1}]

Subscripts (Only abbreviated subscripts are covered)

avg	average
b	bush
bc	bush to cylinder centre
bf	bearing; bearing flange
br	bush to rotor centre
c	cylinder
ch	characteristic
$cham$	chamber
cr	cylinder edge to rotor centre
com	compression
$cond$	conduction
$conv$	convection
$crit$	critical
cv	control volume
d	discharge
$damp$	damping
e	exit
ef	effective; equivalent
enf	endface
f	friction
ft	fillet
g	gas; fluid
gen	generated
geo	geometric
h	housing shell
i	vibration mode; numerical index; inlet; inner

$isen$	isentropic
j	generalised coordinate; vibration mode
jbr	journal bearing
k	holonomic constraint
l	length
m	motor
n	non-conservative
o	outlet; outer
orf	orifice
ort	orientation
P	perpendicular
p	pressure
pt	port
r	rotor
rad	radial; radius
rc	rotor edge to cylinder centre
$radn$	radiation
s	suction chamber
sl	sliding
suc	suction line
$supp$	support
$surr$	surroundings
swl	swivel
$sync$	synchronous speed
t	throat; turbulent
v	vane
vc	vane tip to cylinder centre
vl	valve
vr	vane tip to rotor centre
vs	vane slot chamber
w	wall
x	x-direction

y	y-direction
z	z-direction

Abstract

This thesis presents the development of the revolving vane (RV) compressor into a lubricant-free variant. The concept of such a compressor is attractive as it would be unconstrained by orientation and be applicable for portable small-scale cooling and heating applications. However, there are challenges of high friction losses, material wear and also significant internal leakage due to the absence of lubricants. With inherently low friction losses, the RV mechanism is a mechanically efficient, positive-displacement rotary compressor design which has the potential for development into a lubricant-free variant.

This project starts with the design of a lubricant-free RV compressor. In order to reduce the number of moving components in the compressor, a new vane and vane slot design is proposed. The suitability of self-lubricating materials polytetrafluoroethylene (PTFE) and polyetheretherketone (PEEK) were reviewed and tested for use in the fabrication of RV prototype components that would be subjected to dry rubbing. These components include the bearing liners, rotor, rotor shaft and vane. Between PTFE and PEEK, the latter was chosen for its excellent wear properties and low coefficients of friction at high loading forces and speeds.

Next, theoretical models for the RV compressor prototype were formulated, namely the geometric, thermodynamics, dynamics and thermal models.

With the introduction of the new vane and vane slot design, new geometric relations were formulated. These relations form the basis for describing the rate of volume changes in the working chambers for the thermodynamics model and were also used to determine the kinematics and dynamics of the compressor assembly.

For the thermodynamics model, heat transfer between the working fluid and chamber walls was also considered for a more comprehensive analysis. Three-dimensional computational fluid dynamics simulations for internal leakage were carried out and used in conjunction with the Fanno flow model to develop a method for quantifying the internal leakage.

The dynamics model utilises Lagrangian mechanics to formulate a comprehensive equation of motion for the entire RV cylinder-rotor assembly and this equation can be applied to other RV design variants. This enabled the rotational vibration characteristics of the RV

mechanism to be studied, which had not been done since the RV was first developed. Individual expressions for each of the friction loss in the compressor were also formulated. Equations for describing the dynamics of reed valves with non-uniform cross-sections were also derived. The analysis showed that there were significant friction losses due to the weight of the components – it constituted 38% of the total friction loss for a suction and discharge pressure of 1 and 2 bar (abs), respectively; and is 18% for a suction and discharge pressure of 1 and 5 bar (abs), respectively.

The thermal model was used to simulate heat transfer between the compressor components during operation to predict the steady-state component temperatures of the RV prototype compressor. Assuming no internal leakage, at an operating condition of 2000 rev min^{-1} with a pressure difference of 4 bar between suction and discharge, the average steady-state operating temperatures of the housing shell, cylinder and rotor are found to be 110.1°C, 107.2°C and 43.4°C, respectively.

Instrumentation and measurement of the prototype were also carried out. Due to poor machining accuracy, the lower cylinder bearing liner was slightly warped and large endface clearance gaps of 0.13 – 0.18 mm were present in the prototype. The resulting prototype was unable to attain compression ratios beyond 1.6 at running speeds of 1000 rev min^{-1} with low volumetric efficiencies between 17% and 45%. Measured mass flow rates were used to validate the thermodynamics and internal leakage model, with prediction errors at ±15%. Additional analysis showed that the output mass flow rate can be increased by 120% – 460% if the clearance gaps were at their intended values of 10 μm.

Lastly, the dynamics model for the RV mechanism was validated with measurements from a previous work carried out on an RV air expander. The predicted variations in fluctuations in output torque due to rotational vibration were found to be in good agreement. The measured output torque showed that the vibration of the RV mechanism was bimodal due to the presence of the clearance gap between the vane and vane slot. This effect became less pronounced at higher operating speeds.

With the above-mentioned work that was done, this research project has laid out the groundwork for future development of the lubricant-free RV compressor.

1 Introduction

1.1 Background

Cooling and heating applications are necessities in any part of the world where people inhabit; refrigeration is imperative for food storage and preservation whereas heaters are necessary for survival in cold temperate regions and air-conditioning provides comfort in the tropical climate. Vapour compression systems are extremely popular due to their high coefficient of performance (COP) values and hence, are ubiquitously used for such cooling and heating applications. At its core is the compressor; it is the key component that drives the entire system. Positive displacement compressors are mostly used in such systems especially for applications in medium and small cooling capacities.

Current positive displacement compressor designs require the extensive use of lubricants to ensure reliable operation and improved efficiency. The lubricants serve to lubricate, to seal and to cool.

Furthermore, the use of liquid lubricants also restricts the orientation of the compressor, as it has to be fixed in a way to ensure that the oil sump is always at the lowest position to allow the lubricant to flow back to it by gravity. This is to maintain a functional lubrication system for reliable operation. This necessitates a fixed orientation and thus limits the applications of conventional compressors since the orientation of the compressor is fixed.

Commercially available lubricant-free compressor designs include the axial centrifugal compressors and screw compressors, operating at speeds between 20,000 and 80,000 rev min^{-1} [1, 2]. In addition, these systems often require multi-stage compression in order to achieve pressure ratios comparable to those of conventional positive-displacement compressors. Such compressors are therefore power-intensive, noisy and bulky.

On the other hand, successful development of a lubricant-free positive displacement compressor would allow operation under any orientation and open up the use of vapour compression systems to venues where the orientation may not be fixed, such as those in small-scale portable cooling and heating applications.

Current small-scale portable cooling/heating systems mostly utilise thermoelectric systems with coefficients of performance ranging from 0.3 to 0.6 [3–5] which are inefficient and typically possess low capacities. Examples include the cooling or heating of beverages in mini-fridges for personal consumption.

Transparency Market Research [6] reported that the market for thermoelectric cooling/heating modules was US$364.1 million in 2014 and a projection of US$829.5 million by the end of 2023. The development of a lubricant-free compressor would allow vapour compression systems to supplant such thermoelectric systems and extend the practicability of the applications with higher efficiencies. Apart from replacing thermoelectric systems, new potential applications include highly efficient cooling systems for portable computing applications or even used in personal protection equipment to protect the wearer under harsh environmental conditions.

There are many designs pertaining to positive-displacement compressors, ranging from the age-old reciprocating compressors [7, 8] to well-established rotary compressors such as the rolling piston compressor [9, 10], rotary vane compressor [11], screw compressor [12, 13] and scroll compressor [14]. The above-mentioned compressors are rather mature in terms of design development and hence, only incremental advancements are achieved with further research [15, 16].

Hence, a new energy efficient compressor mechanism has been designed by Teh and Ooi [17–19], known as the revolving vane (RV) compressor.

The initial design iteration of the RV compressor has proved that its mechanism is more efficient than other compressor designs [17]. Design refinements have also been conducted by Tan and Ooi in terms of the fixed vane design [20] and journal bearings [21] to further improve the compressor efficiency.

The main reason for the better mechanical efficiency of the RV compressor would be due to the low relative velocities between its rubbing parts [17] and to this end, the RV mechanism has been identified as the design which has the greatest potential for designing a compressor that requires no liquid lubrication.

1.2 Objectives and Scope

The main objective of this project is to develop a revolving vane compressor that requires no liquid lubricant. This includes the mathematical model, design, fabrication and testing of a working prototype. To achieve this, the scope of work is as follows:

1. Development of a comprehensive mathematical model for a lubricant free RV compressor with the following considerations:
    a. Heat transfer model in working chamber
    b. Internal leakage between working chambers
    c. Vibration modelling
    d. Component temperature modelling
2. Design, fabrication and instrumentation of a lubricant free RV compressor prototype
3. Measurement and evaluation of RV compressor prototype
4. Verification of thermodynamics and dynamics model with measured data

1.3 Thesis Organisation

This thesis consists of 10 chapters and appendices. Chapter 1 opens with the background information, motivation, scope and objective for the project. This is followed by Chapter 2 with relevant literature review of current revolving vane technology, oil free compressors, vibration of different compressor designs, dry sliding friction and self-lubricating materials.

Chapter 3 discusses the design challenges of a lubricant free compressor and then proceeds with the elaboration on the design features of the RV compressor prototype – new vane design, selection and use of self-lubricating materials for various components such as bearing liners.

The theoretical models are presented in Chapters 4 to 7. Chapter 4 first presents the geometric model with the working volumes and their rate of change which are required for use in thermodynamics modelling of the working chamber processes. These geometric relations are also used for component kinematics in dynamics modelling.

This is followed by Chapter 5 which covers the full thermodynamics model of the RV compressor with heat transfer in the working chambers and internal leakage between the chambers. As internal leakage is expected to be severe in the prototype due to the lack of lubricants to fill the clearance gaps, computational fluid dynamics simulations of the internal leakage paths are presented and the data applied to the thermodynamics model.

Chapter 6 goes on to evaluate the dynamics of the compressor. Lagrangian mechanics is used to formulate a comprehensive equation of motion for the moving assembly that allows evaluation of the vibrational characteristics of the compressor as well. Each source of friction in the compressor is formulated and presented individually in Chapter 6 as well.

Last but not least, as heat generated in the compressor rubbing components due to dry friction would be significant, Chapter 7 presents a thermal model for prediction of the steady-state operating temperatures of the components to ensure that these temperatures are safe for the compressor to operate reliably.

Following the presentation of the theoretical models, Chapter 8 will first proceed to validate the thermodynamics and leakage model of the RV compressor prototype. Details of the experimental investigation are first presented before comparing the predicted mass flow values from the model against that of the measured values.

Chapter 9 will then validate the dynamics model albeit using an RV air expander. At the same time, this can evaluate the robustness of the proposed Lagrangian mechanics model in Chapter 6 as proof that it can be adapted for most RV mechanisms. The chapter will first give a preamble on air expanders before comparing the predicted output torque from the model against that of measurements from the experimental investigation of an RV air expander.

Finally, with the validation of both the thermodynamics and dynamics model, Chapter 10 would conclude the thesis along with recommendations for future works.

2 Literature Review

This chapter will discuss literature relevant to the revolving vane (RV) compressor, current state of the art on the development of oil-free positive-displacement compressors and aspects pertaining to the challenges of lubricant-free compressors such as mechanical losses and material selection. As the design of the RV compressor was derived from the rolling piston compressor, a preamble to the rolling piston compressor will first be presented, followed by the design and development of the RV compressor. Subsequently, current development on lubricant-free compressors will be discussed, followed by the vibration studies of various compressors. Last but not least, there is a review on dry sliding friction and material selection which are crucial aspects in designing a lubricant-free compressor.

2.1 Rolling Piston Compressor Preamble

The rolling piston compressor was developed in the 1980s and is now a very mature and popular compressor design. The operating principles, design and engineering aspects of the compressor such as leakage analysis [22, 23], thermodynamics [24], tribological [25, 26] and vibration [27] are well understood. Its usage is ubiquitous in air-conditioning applications today. The compressor has high volumetric efficiency, and due to the simplicity of its design, it can be very compact as well. However, it is not without its shortcomings such as high vane contact friction which causes wear and tear at the interface [28–30]. A schematic of the rolling piston compressor is provided by Yanagisawa et al. [10] in Figure 2.1.

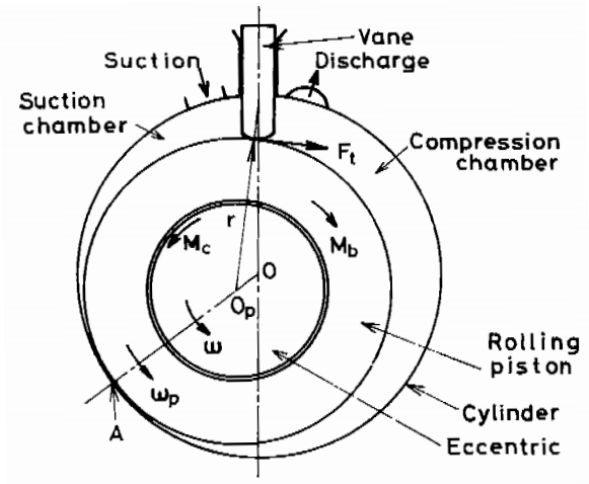

Figure 2.1: Rolling Piston Compressor [10]

The rolling piston mechanism, as its name suggests, consists of a piston mounted onto the eccentric of a driving shaft in a cylinder. The vane is an integral component since it forms the partition separating the suction chamber from the compressor chamber. The action of the piston scrolling around the inner cylinder would cause the suction and subsequently, the compression of the fluid every two revolutions.

The vane is actually attached to a spring that provides a downward force onto the rotor to reduce leakage across the chambers. However, this vane spring force is a source of contention in the rolling piston design as there are various studies on this design aspect. Notable examples include a study done by Ooi et al. [28] on the magnitude of the spring force and compressor performance, another by Liu and Kosco [29] studying the effect of using a tilted vane as opposed to the conventional vertically straight vane and even one by Sung [30] to study the different coatings that can reduce material wear induced by this large contact force. The general consensus from the literature was that the vane spring force is indeed a critical component and the resultant contact force generates a huge loss in terms of mechanical efficiency. This phenomenon was demonstrated by Liu and Kosco [29] to be inevitable in their study, in which a tilted vane only mitigates the material wear but not the friction loss.

In general, the rolling piston compressor boasts high levels of volumetric efficiencies coupled with a compact and simple design. However, it is also not without any flaws as well, evident from its vane design which causes high friction losses and material wear. With these undesirable characteristics in mind, the RV compressor design was conceived in a bid to remove these traits. The next Section 2.2 will detail the development of the RV compressor.

2.2 Revolving Vane Compressor Development

2.2.1 Revolving Vane Compressor Working Principle

The RV compressor design was first presented by Teh and Ooi [17–19] as a more mechanically efficient compressor alternative to the rolling piston compressor. A schematic of the very first RV compressor design is shown in Figure 2.2.

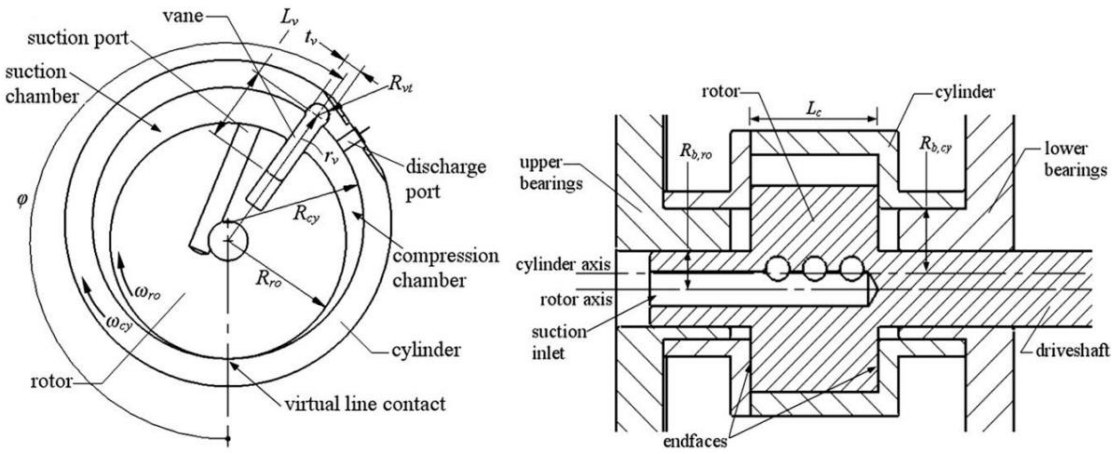

Figure 2.2: Original Revolving Vane Compressor Design [17]

The RV compressor design appears to be similar to that of the rolling piston with the eccentric arrangement of the rotor and cylinder but the operating principles of both compressors are actually very much different. In the case of the RV mechanism, the roller and eccentric shaft of the rolling piston are merged into a single rotor and shaft component with a vane port and suction port cut into it. This reduces the friction loss between the roller and eccentric component. In addition, in order to circumvent the high contact force caused by the vane spring on the roller, the vane in the RV has been replaced with that of a swiveling one that is affixed to the cylinder and slides within the rotor slot during compressor operation. Hence, the rotor and cylinder now rotate about their own axis during operation which largely differs from the rolling piston in which only the roller orbits the inside of the stationary cylinder. For this RV design variant, it was found that there is a 19.7% reduction in frictional losses over the rolling piston design [17]. A diagram illustrating the working principle of the RV compressor is presented by Teh and Ooi [17] in Figure 2.3.

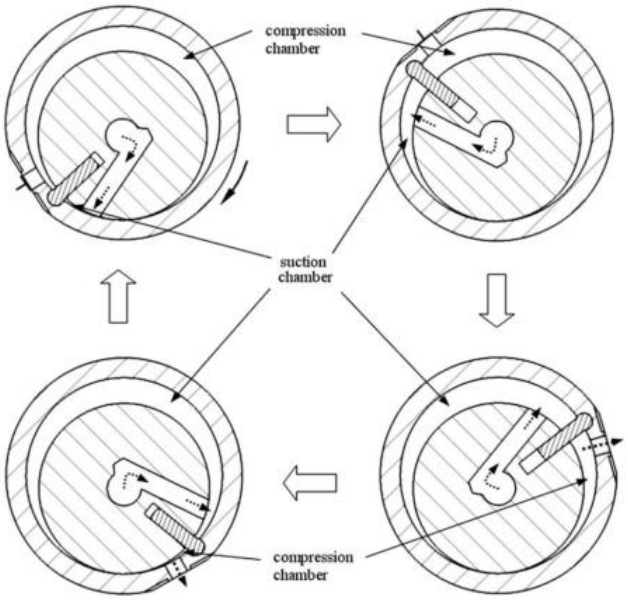

Figure 2.3: Revolving Vane Working Principle [17]

In the original design, the motor powers the rotor component similar to that of the rolling piston. With the vane connecting the rotor and cylinder, the cylinder turns as well. This rotational motion causes the volumes in the suction and compression chamber to increase and decrease respectively. This draws in the working fluid into the suction chamber and at the same time, the decreasing volume in the compression chamber would compress the fluid. The complete cycle requires two revolutions of the RV; the first to draw the fluid into the suction chamber and the second revolution to compress the fluid.

2.2.2 Fixed Vane Design

In the original RV design with the swivelling vane, the compressor was driven by the rotor and as noted by Teh and Ooi [17], this is a source of lowered mechanical efficiency since the heavier cylinder would require a higher driving torque and increases the vane side friction loss as well. To this end, Tan and Ooi [20] proposed a rigid fixed vane design for the RV mechanism and studied the benefits of a cylinder-driven compressor instead of the original rotor-driven compressor.

The fixed vane design proved to be much better than the original; the vane tip friction component is eliminated, the vane is no longer subjected to a gas differential pressure force and due to the pure rotation of the fixed vane, there is no longer any Coriolis force [20] acting on the vane which also results in a lower vane side friction loss.

The required inertial torques for the cylinder-driven variant versus the rotor-driven design is presented by Tan and Ooi [20] in Figure 2.4. The original swivel vane design has been included for comparison.

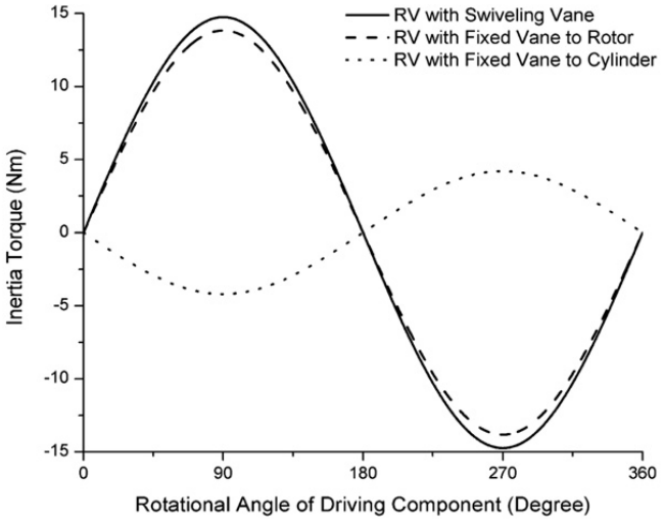

Figure 2.4: Revolving Vane Inertial Torque Comparison [20]

The fixed vane variant is clearly advantageous compared to that of the swivelling vane. In fact, the best design variant was found to be that of the fixed vane cylinder-drive compressor in which the inertia torque was found to be much lower than that of the rotor-drive. This is simply due to the fact the heavier cylinder is being used to turn the lighter rotor component, resulting in a lesser torque requirement. The overall improvement in mechanical efficiency was noted to be at 2.8% [20]. This is an important design feature that would help to improve the mechanical efficiencies of future RV compressors.

2.2.3 Revolving Vane Journal Bearing Design

As noted by Tan and Ooi [20], a cylinder driven compressor would be more mechanically efficient. However, this would require a redesign of the journal bearing system to support the rotational motion of the cylinder and rotor components.

Tan and Ooi [21] then proceeded to work on the journal bearing design and calculated the minimum oil film thickness and pressure variation in the bearings during compressor operation. It was found that the minimum oil film thickness increases as the length or radius of the bearings increase but the trade-off would be that the friction loss would also increase due

to the larger surface area. However, the increase in friction loss due to the increase in bearing radius is much more severe compared to the increase in bearing length.

Tan and Ooi [21] also investigated the different configurations of bearing support for the rotor and cylinder. It was concluded that having a cantilever support [21] for both components yielded poorer performance compared to when the cylinder supports are at both ends and cantilever support for the rotor. This is due to the higher loads that a single bearing will have to take in a cantilever configuration which also leads to higher friction losses. Figure 2.5 shows the best configuration for the journal bearing redesign in which the cylinder is supported at both ends while the rotor has a cantilever support.

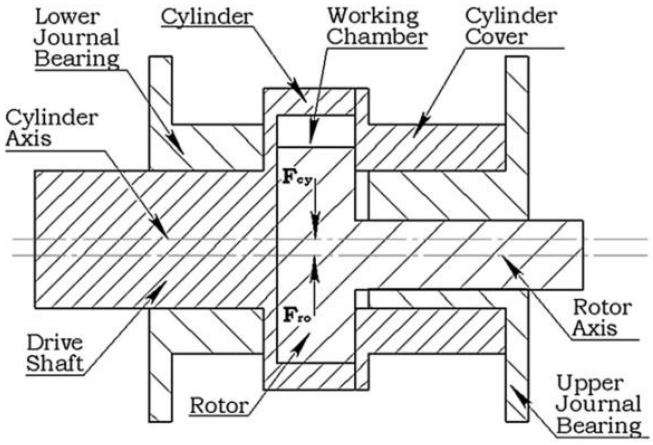

Figure 2.5: Improved Revolving Vane Journal Bearing Design [21]

2.2.4 Heat Transfer in Working Chambers

In addition to implementing design improvements to the RV mechanism, Tan and Ooi also investigated the effect of heat transfer in the working chamber [16]. In their initial mathematical modelling of the compressor with no heat transfer mechanism, it was found that the model always under predict the fluid pressure variation in the chamber. To this end, they attributed the discrepancy to the absence of a heat transfer model within the working chamber.

Tan and Ooi [16] proceeded to explore different convective heat transfer correlations in their RV model, namely those by Adair et al. [31], Benson et al. [32], Liu and Zhou [33]. As these correlations were intended for use in reciprocating compressors, Tan and Ooi had to adapt the heat transfer parameters of the RV mechanism for use in these correlations. The flow prediction of the fluid in the working chamber by Tan and Ooi [16] is depicted in Figure 2.6.

With this flow prediction, they then proceeded to define the hydraulic diameter, average flow velocity for calculating the Reynolds number and subsequently the heat transfer coefficient.

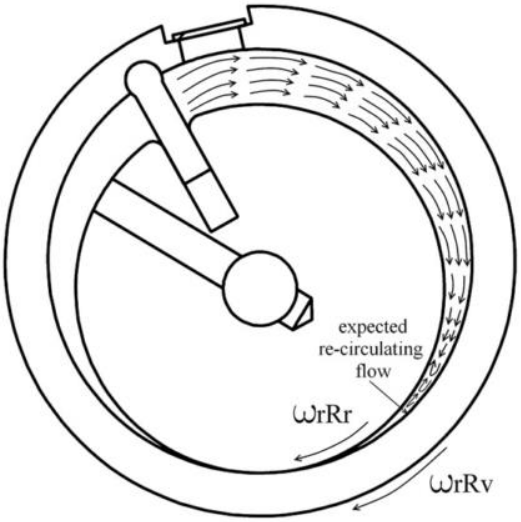

Figure 2.6: Predicted Fluid Flow in Revolving Vane Working Chamber [16]

Amongst the three different heat transfer correlations tested, it was concluded that the correlation by Liu and Zhou [16] is most suitable for modelling the heat transfer effect in the RV compressor as it offers the most accurate prediction for the experimental results. This correlation would be useful for modelling the heat transfer effects in the working chamber for the lubricant-free RV compressor. To this end, the current state of the art on RV compressors has been presented. The next Section 2.3 would delve into the work and progress of oil-free compressor development for other compressor designs.

2.3 Oil Free Compressors

There are other works carried out which are similar to the aim of this thesis. The works reviewed in this section include scroll compressors [34–36] and reciprocating compressors [37].

2.3.1 Scroll Compressor

Ni and Cai [35] studied the loads imposed on the moving interfaces during compressor operation and subsequently proposed a “floating-scroll” design that reduces the friction and hence the wear of the components by balancing the forces and moments affecting these components during compressor operation.

On the other hand, Zhao et al. [34] proposed an oil-free scroll compressor that uses water as the lubricant to avoid contamination of the fuel cell system that the air compressor was deployed in. It was concluded that the compressor performance was still up to par and that the water was useful for lubrication and heat dissipation. However, it was also noted that a Teflon coating should be applied to the friction surfaces to reduce the impact of the loads during starting operation.

In addition, Li et al. [36] also designed and built a dry scroll vacuum pump in order to model its performance characteristics more accurately with heat transfer and leakage effects. In their investigation, it was noted that increasing the pump speed increases the suction pressure in general, but this trend would taper off at high speeds.

2.3.2 Reciprocating Compressor

For the case of the reciprocating compressor, Grzyll and Cole [37] implemented self-lubricating polyimide coating to the compressor as an alternative to oil lubrication. In addition, they also utilised sealed bearings that were permanently lubricated for supporting the crankshaft and rod. Certain aspects of the compressor were changed and machined to accommodate these modifications. Initial testing results revealed that there was more leakage in the compressor due to the increase in the component clearances brought by the modifications and further material wear during compressor operation. It was also noted that the temperature of the discharged fluid was higher due to the increase in friction and subsequent heat generation.

2.4 Compressor Vibrations

Vibration is an often undesirable aspect of mechanical devices as energy is consumed and noise is generated as well. Furthermore, they can cause fatigue stress in the components

which may result in premature failure. Compressors are no exception to this and their vibrations are further aggravated due to the high speeds at which they operate. Due to the eccentricity of the crank and shaft in reciprocating compressors during operation, rotary compressors such as the scroll [34, 36] and rolling piston [38] have better vibration characteristics. Nevertheless, there is a need to characterise the vibration profiles of the compressors so as to implement design changes to further reduce vibration.

2.4.1 Reciprocating Compressor Vibration

The reciprocating compressor is one of the earliest compressor designs and there are various publications in the literature [7, 39–45] pertaining to its vibration analysis.

Hiller and Glickman [7] show a working schematic of a typical reciprocating compressor in Figure 2.7. The abbreviations TDC and BDC represents ‘top dead centre’ and ‘bottom dead centre’ respectively, which indicates the extent of the piston movement during operation.

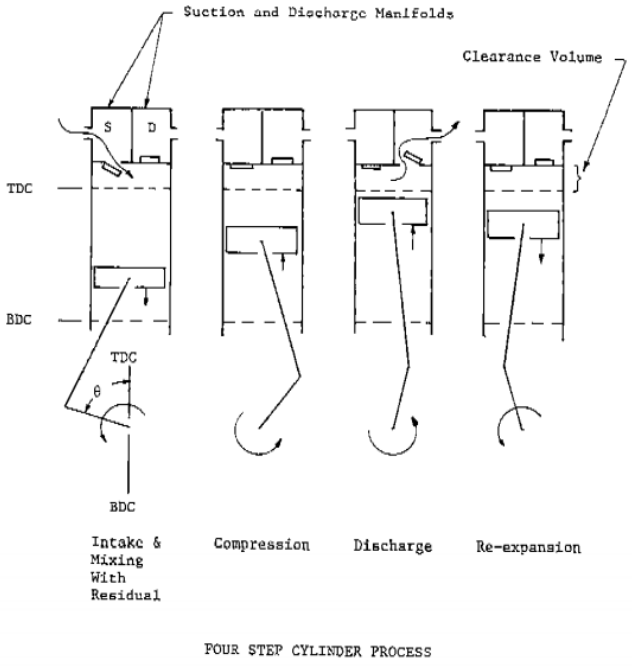

Figure 2.7: Reciprocating Compressor Schematic [7]

The reciprocating compressor is a four step process as shown in Figure 2.7. To mitigate excessive vibration, numerous springs and counterweights can be employed to reduce the transmission of vibrations from the moving components to the outer compressor shell [45, 46].

Furthermore, a multi-balancing approach has also been shown to reduce the vibration of the reciprocating compressor [39].

2.4.2 Rolling Piston Compressor Vibration

For the rolling piston compressor, the outer compressor shell may be subjected to more severe vibrations due to the orbiting motion of the eccentric roller on the inner surface [46].

To this end, Yanagisawa et al. [27] set out to analyse the vibration characteristics of the rolling piston compressor. In their analysis, they divided the compressor into two main components, namely the rotor shaft and eccentric as the moving component and the cylinder shell as the stationary component, and studied their respective vibrations during steady state operation, starting and stopping operation.

It was eventually concluded that the vibrations of the two components were approximately 180^{o} out of phase from each other, with the rotating components adopting a sine profile whereas the stationary cylinder shell displaying a cosine profile [27] during steady-state operation. In addition, it was found that the moment of inertia of the compressor tends to reduce the vibration amplitudes during steady state operation but had little influence on the starting and stopping operation of the compressor. On the other hand, the spring constant for the vane contact had little influence on the vibration amplitude during steady state operation but would greatly affect the vibration during starting and stopping operation instead.

2.4.3 Scroll Compressor Vibration

The second type of rotary compressor included in this review is the scroll compressor. Padmanabhan [47] studied the rigid body vibration of the entire scroll compressor body and also the effect of utilising counterweights to reduce overall vibrations of the compressor. It is noted that the angular alignment of these counterweights would produce a greater effect on the vibration of the scroll compressor than mass effects of the weights.

Bukac [48] went on to study the internal vibrations of the scroll compressor mechanism. He utilised a series of springs and masses to model the mating vanes in the scroll compressor in which the centripetal force was used as the excitation force in the model. He concluded that there is amplitude modulation due to the modal coupling of the spring masses in orthogonal

directions and also found out that there are multiple resonance peaks in the frequency response of the scroll compressor vibration.

2.5 Dry Sliding Friction

Due to absence of lubricant, an oil-free compressor would undergo dry sliding friction between the moving parts such as the shaft bearings and vane contact. The modelling of the magnitude of the friction force is simply the product of the normal force at the interface and the coefficient of friction; independent of the contact area. Dry friction creates heat buildup in the components which in most cases are undesirable due to thermal fatigue due to operation cycles or even premature failure when the temperature gets critical. However, friction heating might also be useful in cases when employed for friction stir welding [49–52]. It would therefore be of interest to understand the mechanism of dry friction so as to model the heat dissipation and heat transfer effects for better prediction of compressor performance.

2.5.1 Aspects of Dry Sliding Friction

The resistance force experienced during dry sliding friction can be attributed to the adhesive bonds between the atoms at the rubbing surfaces and force required for the deformation of the asperities at the rubbing interface as they plough into each other [53]. However, it was found that only a small part of the work expended during dry sliding is associated with the plastic deformation of the material; majority of the frictional work is in fact dissipated as heat at the interface [54]. Figure 2.8 shows the transformation of frictional energy into other forms. The ratio of the energy dissipated as heat increases with the strain in the material or with increasing temperatures [55]. Therefore, dry sliding friction is essentially a thermomechanical phenomenon – with both mechanical aspects and thermal aspects.

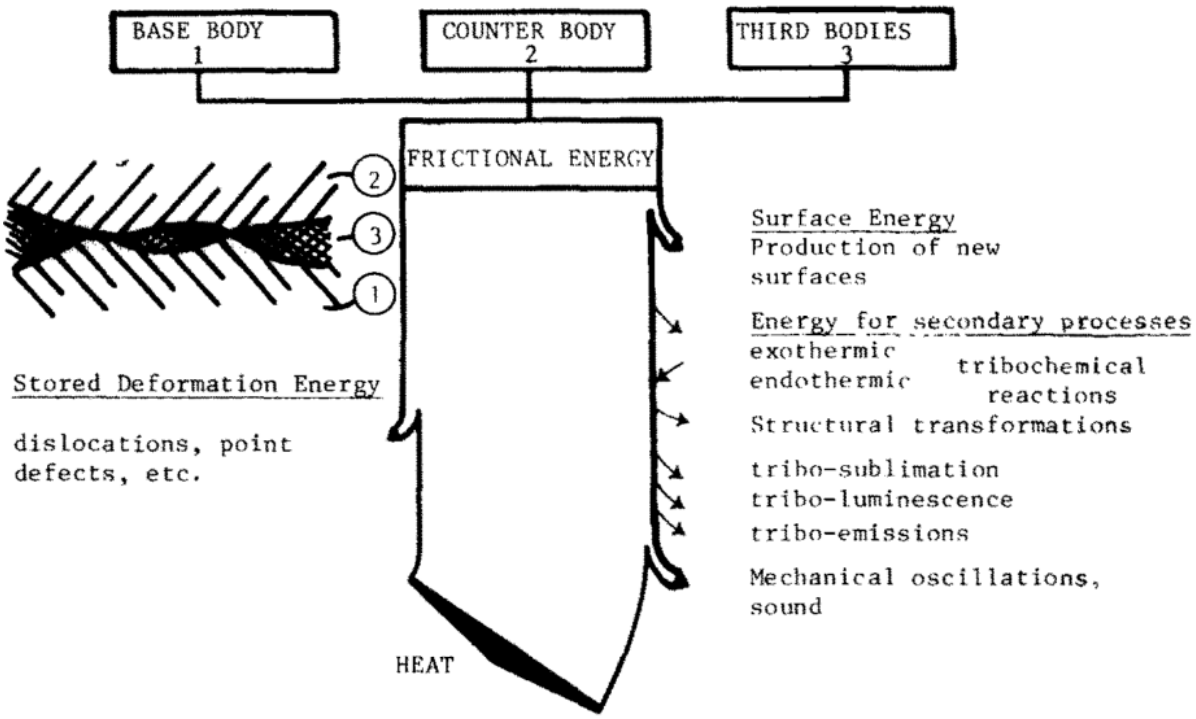

Figure 2.8: Transformation of Frictional Energy [54]

For the mechanical aspects, factors that affect the strength of the friction force at the sliding interface depends on the type of interfacial bonds between the surfaces, material strength which affects the deformation energy and the area of actual contact due to surface asperities [53]. Furthermore, the asperities would deform due to increasing contact forces, thus increasing the actual contact area and consequentially, the friction force as well. In addition, due to the effect of strong interfacial bonds between similar materials, dry sliding friction between metals results in large frictional forces with severe wear. This can be mitigated through the application of surface films which would weaken the interfacial bonds [53].

Furthermore, during dry sliding, high temperatures at the contacting asperities can occur, albeit for only a very short duration [56]. Known as flash temperatures, these occurrences cause multiple hot spots on the contact surfaces which in turn causes asperities to deform and change the contact pressure distribution at the interface – the resulting uneven pressure causes further heating and thermal expansion at the contact spots [55]. This process is known as thermoelastic instability which occurs above a critical velocity during the wear-in phase of dry friction sliding and would stabilise with wear as the area and number of contact spots increase due to thermal expansion to reach a steady state eventually [55].

The combination of both thermal loading due to frictional heating and mechanical loading due to compressive stress at the interface would cause thermomechanical stress in the rubbing components. Furthermore, there is also tensile stress beneath the surface on the trailing edge of the contacting solid which when coupled with the compressive stress at the contact, resulting in plastic flow of the material [55].

Such temperature changes may damage the material due to structural changes, oxidation or melting [57]; this would change the friction and wear behaviour of the components and result in premature failure. Abdel-Aal [58] investigated the efficiency of heat dissipation in materials for mitigating such effects and found that materials with high heat dissipation can prevent excessive build-ups in temperature and that there occurs a definite temperature in which the rate of heat dissipation is at its maximum and that this property is inherent to different combinations of sliding material pairs. It is therefore of great interest to model and predict the temperature changes due to frictional heating in dry friction sliding.

2.5.2 Modelling of Frictional Heating

Kennedy [55, 57] wrote that the basic method of modelling the frictional heat would be that of a heat source method. From this, more complex variations have been developed [55] such as thermal network analogies with considerations for incorporation of flash temperatures, considerations for the variation of thermal conductivity of the materials with temperature [56], inclusion of a stochastic distribution for asperities [59], heat partitioning methods whereby the heat generated is split between the two sliding solids [60, 61], integral transform methods [62], third-body techniques [63] in which a third body is included between the sliding contacts, and last but not least, finite element methods [64–66]. It is also noted that analytical solutions are available, albeit applicable only to semi-infinite solids [67].

Amongst the different methods, the most commonly used methods are those that employ heat partitioning. Much of the literature is focused on determining the ratio of the partition. Such methods are first developed from the microscopic model [68] in which sliding contact resistance and heat generation coefficient are first determined, before they are extended to the macroscopic scale of the sliding interface [66]. In addition, there are also other methods that go one step further to include the calculation of the thermal constriction resistance [64, 65, 67,

69, 70] in which the heat is only conducted through the contacting asperities with no convection/radiation through the interstitial gaps.

Such heat partition methods are commonly used in conjunction with finite element methods but due to the convective-diffusion term in the differential equations, the stability of the solution depends on the Peclet number, and numerical stability is only be achieved at low sliding velocities [55, 57]. However, correlation methods have been developed for calculating the constriction resistance [70] and predicting temperature changes that are applicable for a wide range of Peclet numbers [71] of which the latter can actually be used for coated sliding solids as well.

2.6 Self-Lubricating Materials

For an oil-free compressor, special materials or coatings may have to be employed to reduce the friction and wear between the components. This section will review such materials that have good tribological properties.

2.6.1 Diamond-Like Carbon (DLC)

Diamond-like carbon (DLC) is a self-lubricating material with low coefficients of friction which further decrease with increasing load and sliding speeds, superb wear resistance and a wide range of operating temperatures [72–78]. By careful selection and optimization of a sliding surface for DLC, coefficients of friction lower than 0.1 and wear rates of less than 10^{-7} mm^3 N^{-1} m^{-1} can be achieved [73].

Furthermore, Liu et al. [75] discovered that when pairing the material with titanium or steel, the coefficient of friction can go as low as 0.05 – 0.07 after the wearing-in phase. They discovered that the material at the surface has been transformed into graphite in which the continuous transfer and exchange of the graphite layers between the two sliding bodies account for the low coefficients of friction and wear rate.

DLC has good mechanical properties; it is highly wear resistant and maintains this property even under cryogenic conditions [72] when most materials would have undergone brittle failure. Due to its high mechanical strength, a DLC coating is able protect the components from operational wear [74] while maintaining low coefficients of friction.

In addition, DLC works best under inert conditions since the carbon content in the material may be absorbed into steel bodies at high temperatures [73]. However, when the DLC is combined with tungsten as a composite, it becomes operable at high temperatures up to 500°C with low coefficients of friction less than 0.1 [77].

Despite its excellent properties, the applications of DLC as a dry lubricant are still rather limited due to high residual stresses and poor adhesion of DLC [78] to other surfaces, especially with aluminum and magnesium alloys [77], resulting in coatings with limited thickness. Recommended coating techniques include microwave plasma chemical vapour deposition for diamond films [76] and cathodic arc plasma methods be used for composite DLCs such as those containing titanium carbide [78] and tungsten [77].

2.6.2 Molybdenum Disulfide (MoS_2)

The usage of molybdenum disulfide (MoS_2) for its tribological properties goes back a few centuries [79] with an appearance that is very similar to graphite. It possesses low coefficients of friction with good adhesion to metallic surfaces [79–84]. It adheres easily through the burnishing of MoS_2 against metallic surfaces [79, 80], epoxy bonding [82], sputter coating [83] or by sulphurizing a molybdenum surface [81].

Like graphite, MoS_2 also has a layered lattice structure in which the layers slide over each other to achieve low coefficients of friction; albeit with anisotropic sliding properties due to the polarisation of the molybdenum atoms [79, 80]. Figure 2.9 shows the polarised, layered structure of MoS_2.

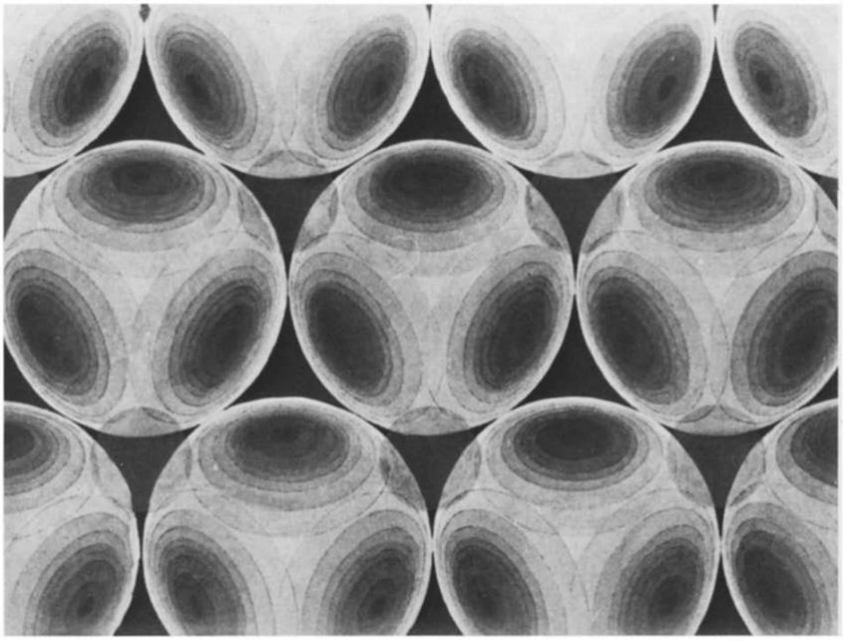

Figure 2.9: Layered Structure of MoS_2 [80]

MoS_2 has excellent tribological properties; coefficients of friction were found to decrease with increasing loads and sliding speeds [79, 80], and performs well under fretting conditions with reduced wear rates [82, 84]. The formation of a lubricating MoS_2 transfer film onto the counter-body after the wear-in phase helps to reduce wear at the contacting surface [80].

Winer [79] states that material undergoes oxidation at a temperature of only 85°C, but the oxide layer formed would protect the material underneath from further oxidation and its lubricating properties remain effective as long as it is not completely oxidized. He then goes on to explain that because of the oxide layer protection, the oxidation rate of MoS_2 remains stable until 560°C whereby the rate would start to increase beyond that temperature. In addition, is also suitable for cryogenic conditions and that the coefficient of friction remains low (0.05) at temperatures as low as 240 K after which it will increase linearly upon further decrease of temperature to reach a value of 0.125 at 4 K [83].

However, MoS_2 is susceptible to humidity in which the absorption of moisture would reduce the performance of the lubricant; frictional heating would reverse this effect since the moisture would evaporate from the film [79].

2.6.3 Polytetrafluoroethylene (PTFE)

Polytetrafluoroethylene (PTFE) is a self-lubricating polymer with low coefficients of friction when paired with metals [85–92]. The long and smooth nature of the PTFE polymer chains allows them to slide over each other easily [87] and the transfer of material between the sliding bodies help to fill up the interstitials between asperities and reduce the friction [92].

PTFE has low coefficients of friction, which decreases with increasing loads but with increasing speeds, the coefficient of friction would increase accordingly up to a maximum before decreasing again [87]. Furthermore, the coefficients of friction for PTFE are very dependent on temperature in which it increases with temperature [87] and with little resistance to heat [90].

In its pure form, PTFE experiences severe wear rate due to the poor adhesion of the material to the counter-body resulting in continuous wear of PTFE [85], which is further aggravated by the increasing roughness of the counter-body [91]. To mitigate this, the wear resistance of PTFE can be improved by introducing filler materials into the polymer but care has to be taken such that the filler materials do not act as abrasives for the counter-body [86].

There is much research interest in evaluating the effect that different filler materials have on PTFE, such as those with good thermal conductivity to increase the thermal resistance of PTFE [90]. Other types of filler materials include aluminium oxides [89], zinc oxides which can further improve its tribological properties by lowering the coefficient of friction even further but discourages the usage of liquid lubricants [88], and even MoS_2 which was postulated to catalyse the morphology of PTFE to have better wear resistance [91].

2.6.4 Polyetheretherketone (PEEK)

Polyetheretherketone (PEEK) is another self-lubricating material which has good thermal stability with a high melting point, high strength and toughness on top of its appealing friction properties and wear resistance [93–98]. In addition, its tensile and toughness strength which can be further enhanced by the addition of filler materials such as fibres. It is also lightweight and can be relatively inexpensive. In view of these attractive properties, extensive research has been carried out evaluating the properties of PEEK and its different variations of filler materials and orientations [94, 96, 99].

In one of the earlier research papers on the properties of PEEK in 1987, Voss and Friedrich [93] noted the advantages of the material and carried out a study on its wear properties for with and without filler materials. It was found that the addition of filler material would improve the wear resistance of the polymer and that carbon fibre fillers prove to be stronger than silicon dioxide (SiO_2) fillers. Since then, extensive research has gone into the PEEK polymer as a tribological material.

Recently, Zhang et al. [99] investigated the effects of having nano-SiO_2 particles in carbon fibre reinforced PEEK and found that the nano particles actually help to further reduce the friction coefficient by acting as mini rollers at the interface albeit at the cost of material wear. However, it was further discovered that under high pressures, the wear resistance improves due to the crushing of these nano-particles into even smaller particles that help reduce the wear of the material.

Zhang et al. [96] also further investigated the effect of fibre orientation on the wear rate and lubricating properties of PEEK and found that fibres orientated anti-parallel to the sliding direction produced the best effect for lower friction coefficients and wear rate under high pressures.

To this end, PEEK composites do show promise as a suitable dry lubricant but such characteristics may be circumstantial as discovered by Greco et al. [97] and Koike et al. [98]. Both studies point to a certain operating point for PEEK whereby it would have optimum lubricating characteristics. Greco et al. discovered that the trait of decreasing friction coefficient with increasing load is due to thermal effects in which the polymer softens, resulting in lower shear stresses at the surface [97]. In addition, due to the softening, there is a transfer of polymer material at the interface but this phenomenon can be mitigated with fibre reinforcement. These effects are verified by Koike et al. [98] in their investigation of PEEK polymer bearing wear in radial loads in which the bearings tend to fail due to the adhesion of the softened polymer material on both surfaces at low speeds or the oxidation and subsequent material breakdown of the polymer at high speeds. As such, this points to an optimum mid-point in which the bearings function that prevents the softened film from building up while at the same time, avoiding high temperatures that can cause oxidation in the material [98].

2.6.5 Concluding Remarks

This literature review chapter has covered the following points in general:

- The key advantage of the RV mechanism over that of the ubiquitous rolling piston mechanisms is that mechanically, the RV is more efficient than that of the rolling piston due to a simpler geometry, less rubbing interfaces, and lower relative velocities between the rotor and cylinder.
- This positions the RV mechanism as a suitable design for further development into that of a lubricant-free compressor.
- The aspects and modelling of dry sliding friction are also covered as it is relevant to that of lubricant-free systems.
- A selection of low-friction materials that can be potentially used to mitigate large friction losses has also been reviewed.

3 Lubricant-free Revolving Vane Compressor Design

Following the development and design variants of the revolving vane mechanism in Chapter 2, this chapter will first delve into the design challenges of a lubricant-free compressor. The vane and bush design of the RV mechanism is reviewed before the new triangle-tip vane design is proposed and discussed. In addition, rubbing components which will be made from self-lubricating materials are identified and such materials are then tested to select the best one for use in the RV prototype. Lastly, the design of prototype is discussed.

3.1 Lubricant-free Compressor Design Challenges

An important parameter for defining the performance of an RV compressor would be the eccentricity of the assembly which is the offset distance between the cylinder and rotor centres. The eccentricity greatly affects the working volume and mechanical efficiencies in which there is a trade-off between the two; a greater eccentricity increases the working volume of the compressor but reduces the mechanical efficiency and vice versa, a smaller eccentricity would improve the mechanical efficiency at the cost of a smaller working volume.

A lubricant-free compressor must be able to function in the absence of oil lubrication. The rubbing components will then undergo dry friction, leading to material wear and excess heat generated in the compressor. As a consequence, the compressor would suffer from higher mechanical losses due to the increase in friction and higher volumetric losses due to leakage from material wear and excessive heat in the working chambers.

Therefore, it would be advantageous to reduce the number of rubbing components so as to mitigate excessive friction losses and material wear. Secondly, the use of low friction, high wear resistance materials in the prototype would further alleviate these problems as well.

For the purposes of measurement, the compressor prototype will be designed with a large working volume; in the event of severe leakage, the mass flow rate out of the compressor can still be effectively measured. Hence, the prototype shall have a working volume of 50 cm^3. Furthermore, as the leakage flow area at the radial clearance increases with chamber length, the compressor prototype shall also have a shorter chamber length so as to mitigate such leakage losses. The end design will have a cylinder with a short length so as to reduce the

chamber length but with a large diameter to accommodate the large working volume in the chambers. The preliminary design dimensions of the prototype are presented in Table 3.1 with a working volume of 50 cm^3.

Table 3.1: Preliminary Design Dimensions

Dimension	Value
Working Volume, cm^3	50.0
Cylinder Radius, mm	50.0
Rotor Radius, mm	42.5
Chamber Length, mm	23.0
Vane Length, mm	18.0

The rest of this chapter would go on to propose a new vane design which reduces the number of rubbing components by two, design features in the prototype to implement low friction rubbing materials into the components and to select a suitable self-lubricating material for use in such components.

3.2 Vane Design

3.2.1 Vane and Bush Component

In the design variant for the fixed vane RV compressor, a bush component is added to accommodate the movement of the vane within the rotor slot. Figure 3.1 shows a cross-section of the fixed vane RV compressor with the bush component.

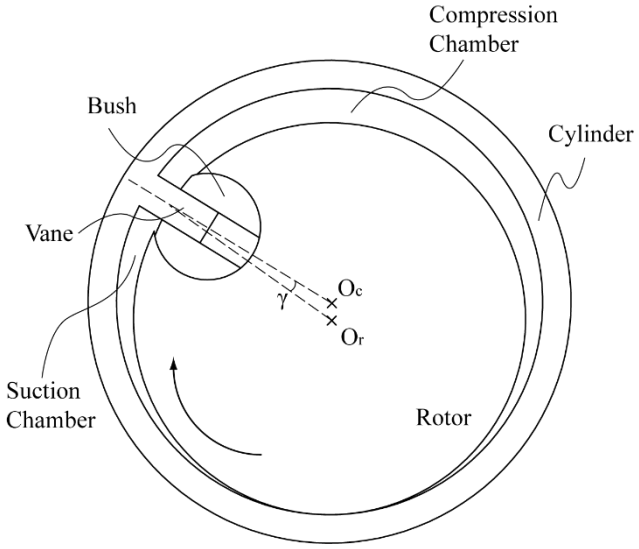

Figure 3.1: Revolving Vane Compressor with Bush Component

The bush component is a simple and effective design that is able to accommodate the vane movement in the rotor slot while preventing leakage between the chambers. However, it is not without its disadvantages. The bush component presents an additional source of frictional loss and material wear while rotating in its slot and in addition, it imposes an additional constraint regarding the length of the vane; the length of vane in the slot must always extend past the centre of the bush at all times so as to hold the bush component in place – failure to do so would cause the bush to dislodge from its slot and jam the mechanism. Hence, it would best to redesign the vane slot such that no bush component is required.

3.2.2 Triangle-Tip Vane Design

Adahan [100] proposed a bulbous rounded end for the vane with a straight vane slot for a single-vane rotary pump patent. Application of this vane design to the RV mechanism is shown in Figure 3.2. The illustrated vane design allows proper operation of the compressor while eliminating the bush component. However, this introduces volumetric losses into the compressor due to the presence of dead volume highlighted in Figure 3.2. The amount of dead volume as a consequence of this design is shown in Figure 3.3 as a percentage of the total working volume. It is noted that at maximum, the amount of dead volume is approximately 2% of the total working volume.

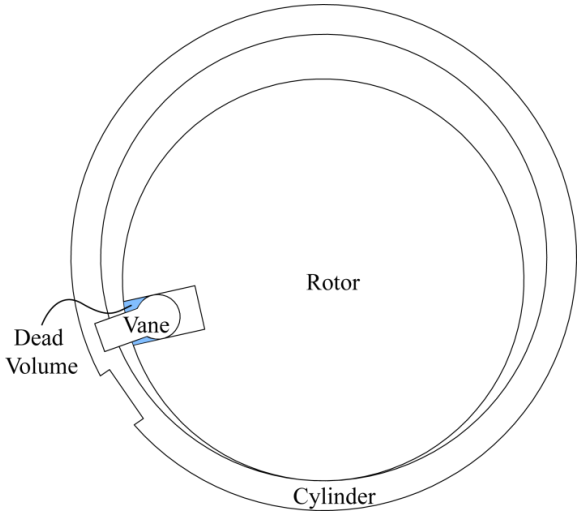

Figure 3.2: Bulbous Vane Design

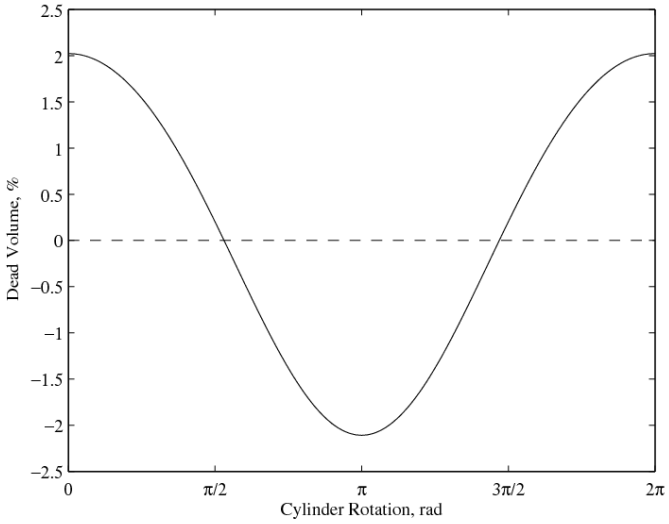

Figure 3.3: Dead Volume Characteristics

Further improvements are made to the bulbous vane to mitigate the amount of dead volume in the design – a fillet is added to the sides of the vane to reduce the dead volume. In addition, as the angle of the vane swivel is fixed during compressor operation, the entire rounded edge of the bulbous end will not be fully utilised and can be removed as well. This reduces the required depth of the vane slot which in turn reduces the potential amount of fluid that leaks into the space as dead volume. Figure 3.4 shows the design process in which the bulbous vane is modified into a triangle-tip vane with the addition of fillets and partial removal of the bulbous end.

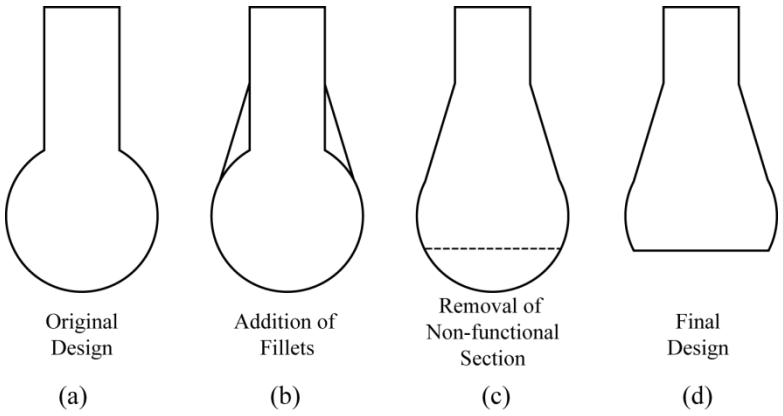

Figure 3.4: Triangle-tip Vane

In order to minimise the dead volume in the working chambers, the vane tip radius has to be kept to a minimum and the fillet height has to be maximised. The technical dimensions of the triangle-tip vane are depicted in Figure 3.5 and construction lines have been added for clarity. The comparison between the dead volume in the compressor for the normal bulb vane and new vane design is presented in Figure 3.6.

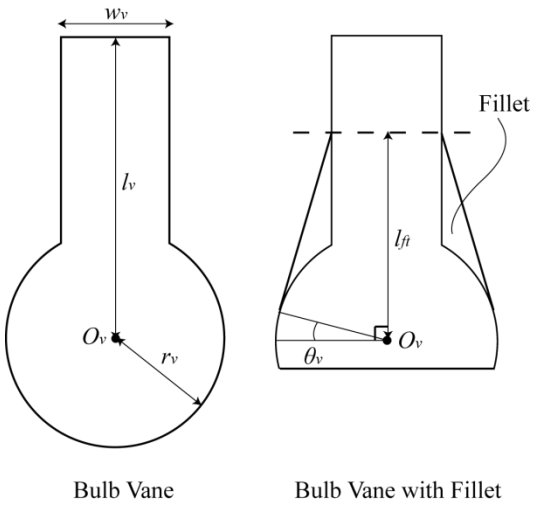

Figure 3.5: Vane Technical Dimensions

With the new vane design, the RV mechanism now requires one less component and improved surface finishing is only needed for the rounded edges compared to the configuration with the bush component which required all the edges for all the components to be polished. In addition, the fillet also reduces the amount of dead volume in the compressor (as a ratio of total working volume) as shown in Figure 3.6. The fillet reduces the dead volume in the compressor by an average of approximately 20%.

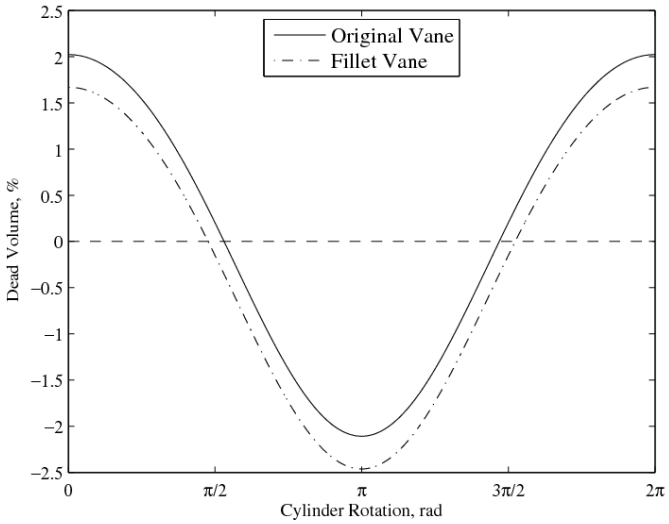

Figure 3.6: Comparison of Dead Volume Variation

Furthermore, the new vane and slot design has changed the geometric relationship between the cylinder and rotor. With the bush component, the centerline of the vane coincides at the edge of the rotor with the angle of swivel depicted by γ as shown in Figure 3.1 but for the new design, the tip of the vane now coincides with the slot centreline with the swivel angle represented by θ_v in Figure 3.5. The next section will go into the optimisation of these dimensions in order to minimise the amount of dead volume.

3.2.3 Vane Design Dimensions

First of all, the length of the vane has to be determined, which in turn dictates the depth of the slot. As the vane is required to be in contact at all times with the vane slot wall, the length of the vane has to be at least double the eccentricity of the cylinder and rotor and the slot length has to be even longer than the vane as it has to be able to accommodate the entire vane itself. These length restrictions are shown in Equations (3.1) and (3.2) respectively.

$$l_v > 2\varepsilon \tag{3.1}$$

$$l_{vs} > l_v \tag{3.2}$$

The next step would be to determine the thickness of the vane required. The vane must be robust enough to withstand the pressure differential between the chambers and drive the rotor component without yielding. For calculation of the bending moment stresses that the vane

would experience during operation, it can be safe to assume that the vane has a uniform rectangular cross-section area since the actual vane design would have a much thicker cross-section due to the addition of fillets. Figure 3.7 shows the cross-section and free body diagram of the vane subject to gas pressure forces between the chamber and the reaction force from the rotor. It is assumed that these forces are at their maximum; the reaction force is acting at the tip of the vane with the maximum magnitude in which the moment arm for the rotor is its shortest at maximum acceleration and the pressure differential across the vane is at its maximum. Based on the diagram, the bending moment exerted on the vane can be summarised as shown in Equation (3.3).

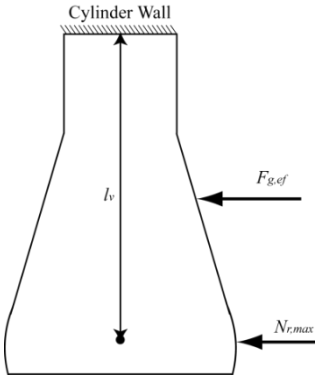

Figure 3.7: Vane Free Body Diagram

$$M_v = N_{r,max} l_v + F_{g,ef} \frac{l_v}{2} \tag{3.3}$$

where

$$N_{r,max} = \frac{I_r \alpha_{r,max}}{r_r - l_v} \tag{3.4}$$

$$F_{g,ef} = (p_{dis} - p_{suc}) l_c l_v \tag{3.5}$$

As the vane undergoes pure bending, the bending moment stress can then be calculated as shown in Equation (3.6) [101]. For practical application, the yield strength of the material σ_{yield} has to be higher than the calculated stress for the vane. From this criterion, the minimum vane thickness can then be calculated as shown in Equation (3.7) with the desired safety factor. In addition, the calculation assumes that the vane is of a uniform rectangular shape – with the additional fillet at the sides, the actual vane would actually be able to withstand higher bending moment stresses.

$$\sigma_v = \frac{M_v w_v}{2I_v} < \sigma_{yield} \tag{3.6}$$

$$w_v > \sqrt{\frac{6nM_v}{l_c \sigma_{yield}}} \tag{3.7}$$

where

$$I_v = \frac{1}{12}(l_c w_v^3) \tag{3.8}$$

Based on the preliminary design dimensions in Table 3.1, the calculation for the minimum vane width is presented in Table 3.2 along with its assumed parameters.

Table 3.2: Vane Width Design

Parameter	**Value**
Pressure Difference ($p_{dis} - p_{suc}$)	20 bar
Material; Yield Strength (σ_{yield})	AISI 4140 Steel; 417.1 MPa [102]
Safety Factor (n)	3
Calculated Vane Width (w_v)	4.92 ≈ 5.00 mm

With the basic dimensions of the vane established, the dimensions of the vane slot can now be determined. The construction lines for the vane slot are drawn as shown in Figure 3.8 in which some of the dimensions have been exaggerated for clarity.

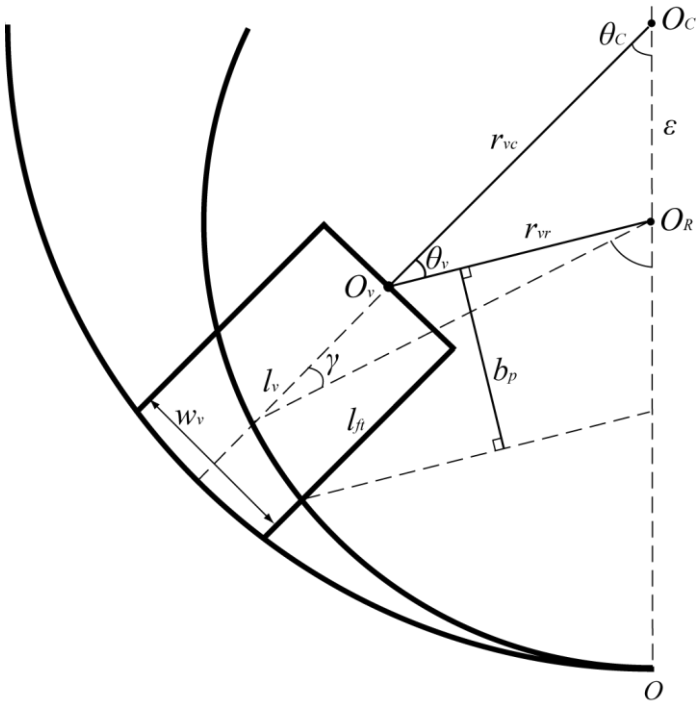

Figure 3.8: Vane Slot Construction Lines

To this end, the geometric relations for the vane with respect to the rotor can be derived as shown in Equations (3.9)–(3.13).

$$r_{vr} = \sqrt{r_{vc}^2 + \varepsilon^2 - 2\varepsilon r_{vc} \cos\theta_c} \tag{3.9}$$

$$\sin\theta_v = \frac{\varepsilon}{r_{vr}} \sin\theta_c \tag{3.10}$$

$$r_r \sin\gamma = \varepsilon \sin\theta_v - \frac{w_v}{2} \tag{3.11}$$

$$b_P = r_r \sin(\theta_v - \gamma) \tag{3.12}$$

$$l_{ft} = l_v + \varepsilon \cos\theta_c + r_r \cos\gamma - r_c \tag{3.13}$$

The derivative of Equation (3.10) is presented in Equation (3.14). At the maximum swivel angle θ_v, the perpendicular distance b_P of the vane edge at the rotor circumference to the slot centreline would dictate the vane slot width and also the maximum allowable fillet height l_{ft}. Hence, Equation (3.14) is equated to zero and solved for the cylinder rotation angle at which maximum swivel occurs as shown in Equation (3.17). To this end, the vane swivel angle, minimum slot width and maximum fillet height can be calculated by substitution of the

cylinder rotation angle value from Equation (3.17) into Equations (3.10), (3.12) and (3.13) respectively.

$$\frac{d\theta_v}{d\theta_c} = \frac{1}{r_{vr}\cos\theta_v}\left(\varepsilon\cos\theta_c - \frac{dr_{vr}}{d\theta_c}\sin\theta_v\right) \tag{3.14}$$

where

$$\cos\theta_v = \frac{r_{vc}^2 + r_{vr}^2 - \varepsilon^2}{2r_{vc}r_{vr}} \tag{3.15}$$

$$\frac{dr_{vr}}{d\theta_c} = \frac{\varepsilon r_{vc}}{r_{vr}}\sin\theta_c \tag{3.16}$$

when $$\frac{d\theta_v}{d\theta_c} = 0, \qquad \theta_c = \cos^{-1}\frac{\varepsilon}{r_{vc}} \tag{3.17}$$

Based on the designed vane width of 5.00 mm and the respective radii of the cylinder and rotor at 50.0 mm and 42.5 mm, the calculated vane swivel angle, minimum slot width and fillet height are calculated and presented in Table 3.3 along with the final design dimensions.

Table 3.3: Vane Design Dimensions

Dimension	Calculated Value	Design Value
Vane Swivel Angle, °	13.5	15.0
Vane Tip Radius, mm	5.6	6.0
Fillet Height, mm	14.7	14.0

With the critical vane dimensions accounted for, Section 3.3 will first go on to identify the key components that undergo dry friction rubbing in the compressor before proposing a suitable replacement self-lubricating material for these components. Section 3.4 shall then proceed to discuss the bearing design features of the oil-free RV compressor.

3.3 Material Selection for Dry Friction Rubbing in Prototype

In the absence of oil, it is important to ensure that dissimilar materials form rubbing pairs at the friction interface so as to reduce material wear and avoid excessive friction heating which may lead to failure in the components due to bonds forming between the similar materials under heat and pressure [103]. This section will look into the selection of the material for the rubbing

interfaces in the compressor. The material has to be strong enough to withstand the dynamic forces during operation especially at the bearings with a low coefficient of friction to reduce heat buildup at the interface. This section will first discuss the components affected followed by the selection of the self-lubricating material that would be used in the prototype.

3.3.1 Identification of Components that Undergo Dry Friction

Figure 3.9 shows a cross-section of a conventional RV compressor in which each individual component has its own colour. Apart from the grey shell housing and green shell housing cover, all the other components would be moving and turning during operation. As the majority of the prototype would be made from steel, components subjected to dry friction rubbing at the moving interfaces are to be made of a self-lubricating material so as to prevent metal-on-metal rubbing which will lead to eventual failure of the prototype. These components are hence identified as follows:

- Rotor (including shaft)
- Vane
- Cylinder bearings

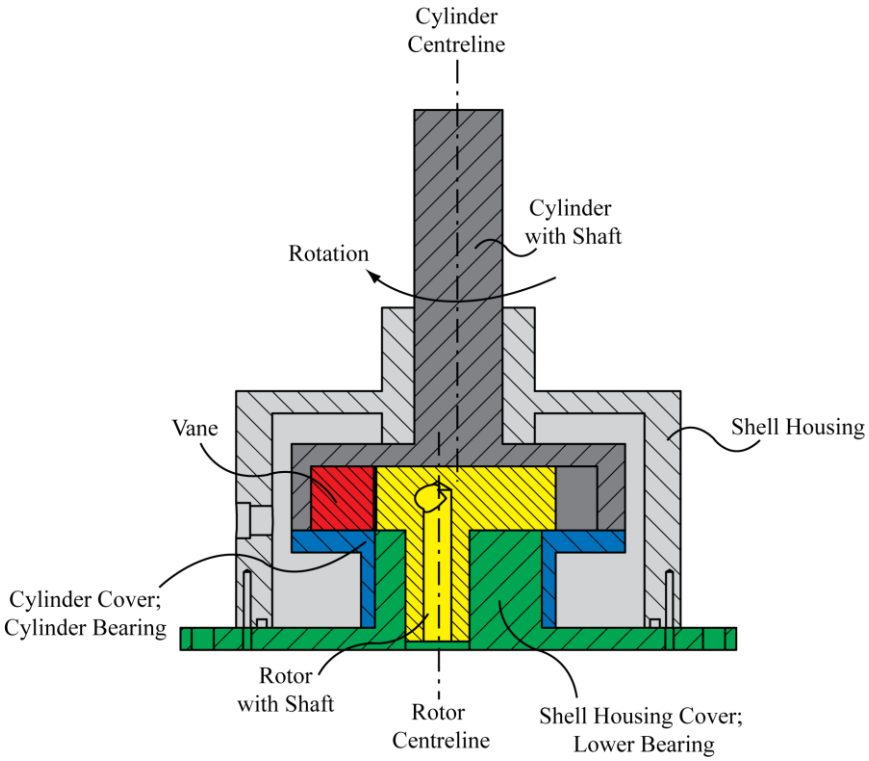

Figure 3.9: Cross-section of Conventional RV Compressor

These components would have to be made from a self-lubricating material to form a rubbing pair with a steel counterpart. For the cylinder bearings, a bearing liner made from the self-lubricating material shall be employed between the steel shafts and bearings. The next Section 3.3.2 shall proceed with the description of an experiment for evaluation of different self-lubricating materials.

3.3.2 Experimental Evaluation of Self Lubricating Materials

a) Test Rig Set Up

A test rig was set up to simulate the rubbing of a metal shaft with various materials so as to evaluate the coefficient of friction and wear rate of the different materials. The experiment setup would emulate the friction interface of the rubbing pairs in the compressor during operation. A torque transducer Torquemaster TM107 was used to measure the counter torque due to friction for calculation of the friction coefficient. Specifications for the torque transducer can be found in Appendix A-8. The test piece was held against a 100 mm metal shaft of 8 mm diameter using a pivoted cantilever beam in which the load can be adjusted by moving a weight along the cantilever. For the shaft material, two types of metals are tested; steel and aluminium. The induction motor has a frequency controller to regulate and control its output speed. A schematic of the experiment is shown in Figure 3.10(a) and the loading of the shaft via the cantilever is shown in Figure 3.10(b).

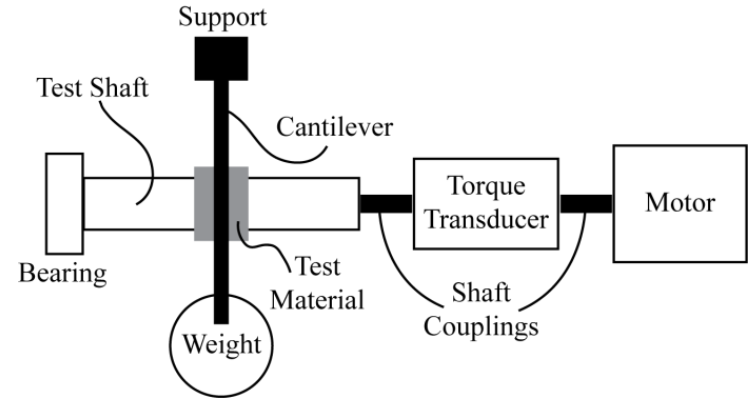

(a) Plan View

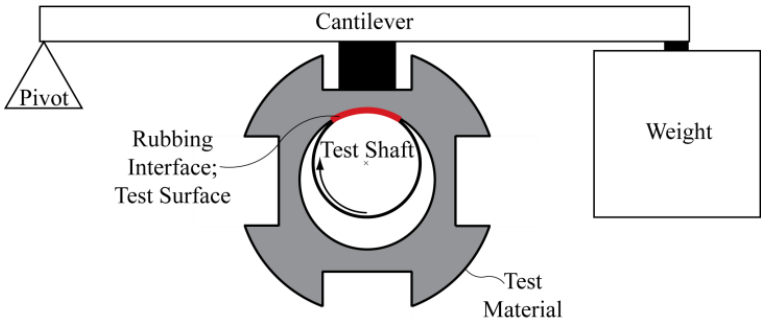

(b) Axial View

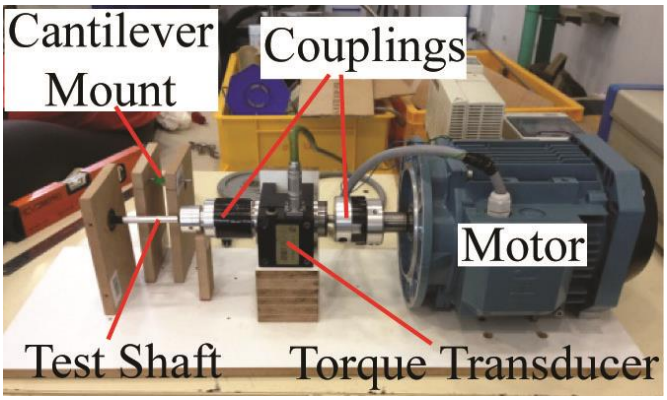

(c) Overview without Cantilever

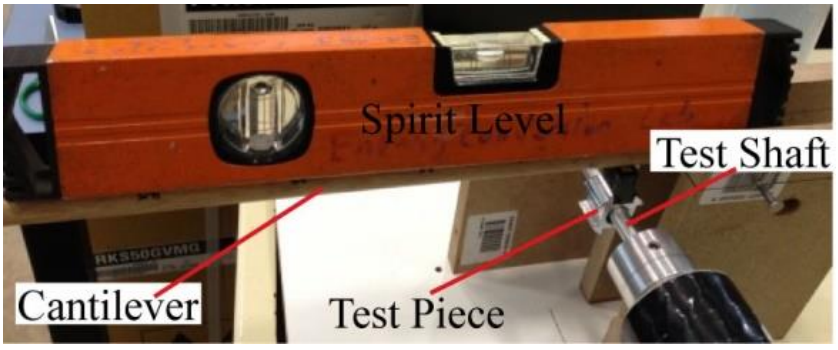

(d) Cantilever with Spirit Level

Figure 3.10: Material Evaluation Experiment Set Up

The test pieces are made from polytetrafluoroethylene (PTFE), bearing grade polyether-etherketone (PEEK) and chrome steel with an internal diameter of 10 mm and a depth of 15 mm. The hole size is larger than that of the shaft so that the same piece can be used for multiple runs (up to four) involving different conditions, each on a different surface. These test pieces are shown in Figure 3.11. Note that there are four grooves on each test piece for mounting the test piece onto the cantilever.

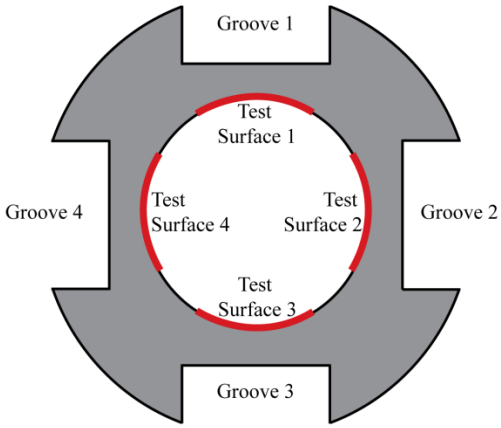

(a) Test Piece Schematic

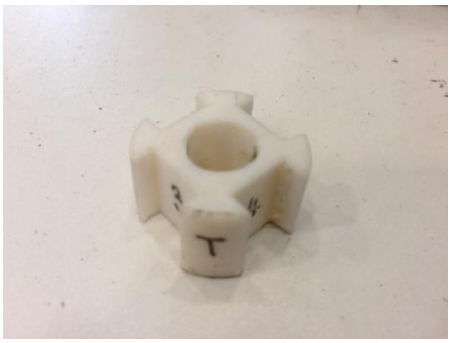

(b) PTFE

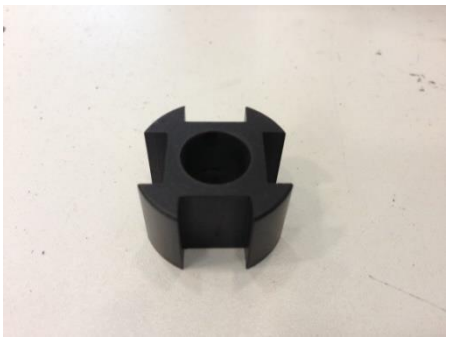

(c) PEEK

(d) Chrome Steel

Figure 3.11: Test Material Pieces

For the testing and evaluation for each of the materials, the various operating conditions for the experiment are presented in Table 3.4. The sliding speeds of the test pieces against the shafts that correspond to the rotation speeds of 250 rev min^{-1} and 500 rev min^{-1} would be at 0.105 m s^{-1} and 0.209 m s^{-1}, respectively. Each run lasted for two hours to ensure that the material had sufficient time to run-in and obtain the steady state coefficient of friction.

Table 3.4: Experiment Runs

Run	Shaft Material		Bearing Material		Speed, rev min^{-1}		Load, N	
	Steel	Aluminium	PTFE	PEEK	250	500	20	25
1	x		x		x		x	
2	x		x		x			x
3	x		x			x	x	
4	x		x			x		x
5	x			x	x		x	
6	x			x	x			x
7	x			x		x	x	
8	x			x		x		x
9		x	x		x		x	
10		x	x		x			x
11		x	x			x	x	
12		x	x			x		x
13		x		x	x		x	
14		x		x	x			x
15		x		x		x	x	
16		x		x		x		x

b) Procedure

The test shaft was simply supported on both ends by a ball bearing and coupling to the torque transducer. For evaluating the different material test pieces against the shaft, the experimental procedures for the test are listed below:

1. Before any experiment run with the test piece, it was weighed to ascertain the original mass.
2. The shaft would have to be detached from the coupling each time the test piece or test shaft is to be changed. A 3 mm diameter hex key was used to loosen and detach the shaft coupling followed by threading the test material through the shaft. The shaft was then reconnected back to the coupling and the cantilever beam is then mounted onto the test piece.

3. A 1 kg mass was hung onto the cantilever to simulate the effect of bearing load onto the shaft. The position of the mass was adjusted to achieve the desired load.
4. A spirit level was then used to ensure that the cantilever beam was levelled. This is important for accurate calculation of the load.
5. The desired speed for the motor was set on the frequency controller and then the motor is switched on to record the torque caused by the friction at the rubbing interface.
6. The motor is kept on for a period of two hours for the material to run-in and achieve a steady state reading for the friction torque. This concluded a set of reading for one experiment run.
7. The test piece was then removed using step 2 and weighed to determine the final mass after the experiment. The change in mass would indicate the wear of the material.
8. Steps 1 – 7 were repeated for each condition of the experiment runs listed in Table 3.4.

3.3.3 Chrome Steel Test Piece

A chrome steel test piece was first used to observe the detrimental effects of metal-on-metal rubbing. In the absence of lubricant, severe wear marks were observed on both the interior of the bearing and the shaft as shown in Figure 3.12 and highlighted by the red circles. The coefficient of friction was recorded to be 0.52 for steel and 0.44 for aluminium at a rotation speed of 250 rev min^{-1} with a load of 20 N. This result highlights the importance of ensuring that only dissimilar materials should form rubbing pairs and that metal-to-metal rubbing should always be avoided.

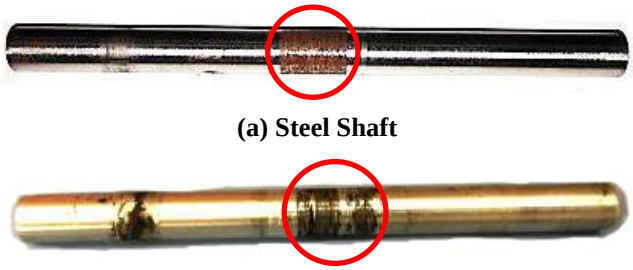

(a) Steel Shaft

(b) Aluminium Shaft

Figure 3.12: Wear of Metal Shafts with Chrome Steel Test Piece

3.3.4 Polytetrafluoroethylene (PTFE) Test Piece

The results for the runs with PTFE test piece are shown in Figure 3.13. The coefficient of friction ranges between 0.35 and 0.51 for the steel shaft and 0.23 and 0.50 for the aluminium shaft. The values for the coefficient of friction in this investigation are inconsistent and much higher than that found in literature. The typical coefficients of friction for PTFE sliding on steel were reported to be between 0.200 and 0.127 for loads between 20 – 30 N and sliding speeds between 0.32 – 1.28 m s^{-1} [104]. This may be attributed to the high wear rate of the material and thermal decomposition of PTFE at the rubbing interface as seen in Figure 3.14.

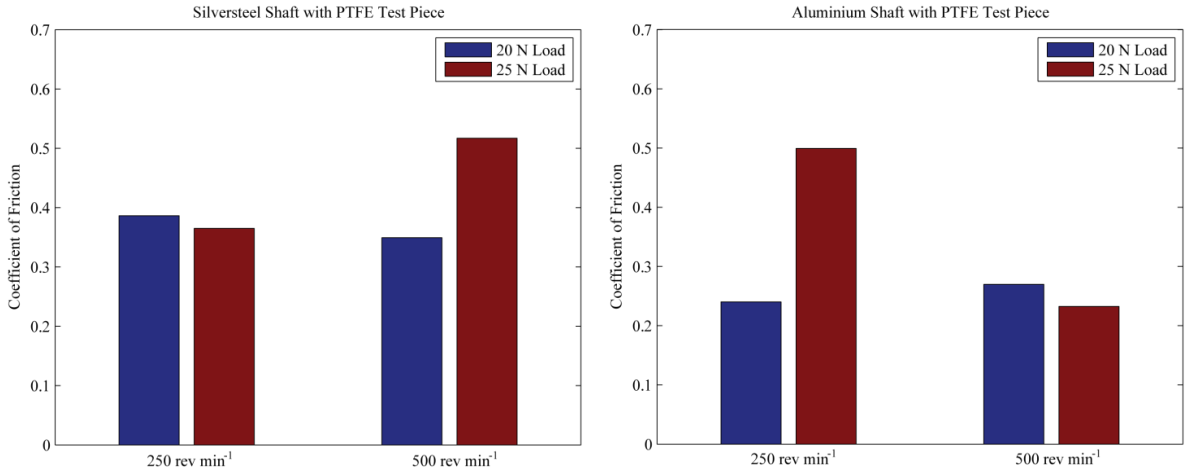

(a): PTFE Test Piece Rubbing with Silversteel Shaft

(b): PTFE Test Piece Rubbing with Aluminium Shaft

Figure 3.13: PTFE Test Piece Performance

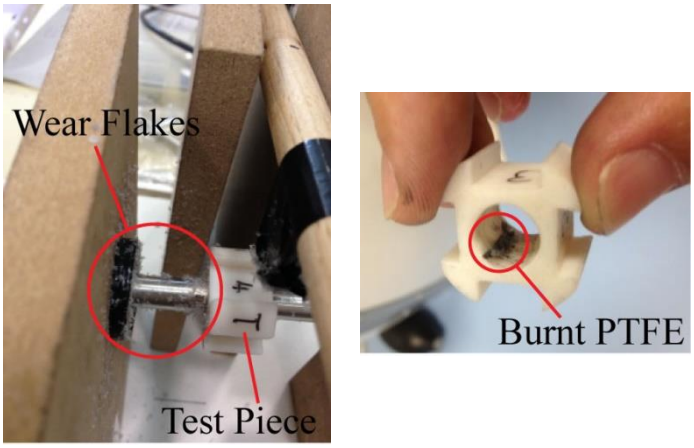

Figure 3.14: PTFE Wear Flakes and Thermal Decomposition of PTFE on Rubbing Surface

3.3.5 Polyetheretherketone (PEEK) Test Piece

The results for the runs with PEEK test piece are shown in Figure 3.15. It is observed that the coefficient of friction for PEEK decreases with increasing load and increasing rotation speed when paired with steel, which is consistent with the literature. On the other hand, the coefficient of friction remains largely unchanged when paired with aluminium regardless of load or rotation speed. In addition, it was found that the wear rate of PEEK is very low; weighing of samples before and after the test runs yielded no measureable change in mass.

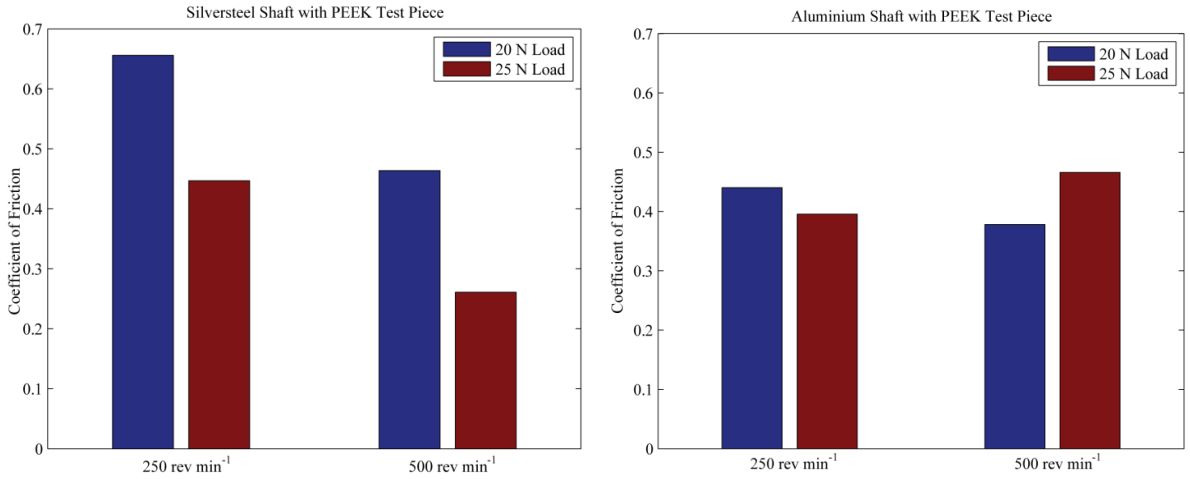

(a): PEEK Test Piece Rubbing with Steel Shaft

(b): PEEK Test Piece Rubbing with Aluminium Shaft

Figure 3.15: PEEK Test Piece Performance

3.3.6 Comparison and Selection of Materials for Prototype Fabrication

From the experiment, bearing grade PEEK exhibits better performance at high rotation speeds and load conditions with lower coefficient of friction compared to that of PTFE. In addition, the severe wear characteristic of PTFE as seen in Figure 3.14 shows that it is unsuitable for such application. In conclusion, PEEK shall be chosen as the material of choice for the fabrication of the components that undergo dry friction.

3.4 Prototype Design

With the proposal of the new vane design and selection of PEEK as the self-lubricating material for the compressor prototype, this section will now go into the design of the prototype. The exposed cylinder-rotor assembly can be found in Figure 3.16 to show the implementation of the proposed vane design. The thermodynamics of the chambers shall be discussed in detail in Chapter 5.

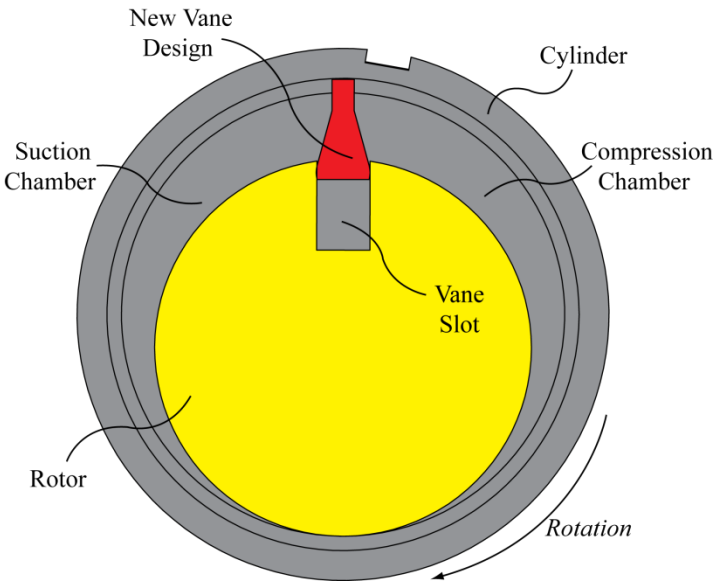

Figure 3.16: New Vane Design in Cylinder-Rotor Assembly

Due to the unique characteristic of the eccentric rotor rotation in a rotating cylinder, the bearing layout for the revolving vane mechanism would be similar to that as proposed by Teh and Ooi [21] in which the cylinder is supported on both ends with the rotor supported on one end as shown by the cross-section layout in Figure 3.9. There is a cylinder cover that acts as the second bearing support for the cylinder. However, with the additional cylinder cover,

alignment issues may result in the prototype during assembly in which the top cylinder shaft and cover may not be properly aligned with the bearings in the housing shell. Hence, to mitigate the complexity of aligning an additional component during prototype assembly, the housing shell cover that serves as the cylinder bearing shall be enlarged to serve as a cover for the cylinder as well. This is illustrated in Figure 3.17.

In addition, metal-to-metal contact at the bearings during operation for a lubricant-free compressor will result in failure and as a result, PEEK has been chosen as a rubbing surface for the metal shaft/bearing at these interfaces. The implementation of PEEK as the interface material shall be achieved through the use of a bearing liner with a flange at the bearings so that the metal shafts and bearing surfaces can rub against the PEEK liner instead of each other. In addition, the flange helps to hold the liner in place and furthermore, helps to prevent leakage of fluid through the bearings by adding additional path constriction where the bearing meets the flange as shown in Figure 3.17.

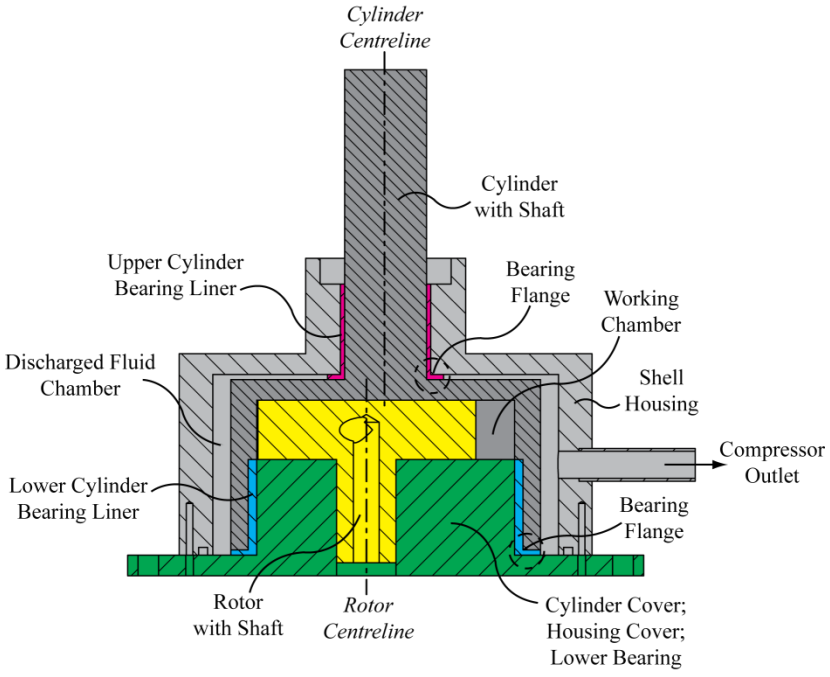

Figure 3.17: Prototype Cross-section

The bearing liners are not adhered to any surface and thus free to rotate about either the inner shaft or outer bearing. During compressor operation, the liners would follow the path of least resistance and rotate accordingly; rubbing against whichever surface that has the lowest friction.

3.5 Concluding Remarks

The operating challenges of lubricant-free RV compressor have been discussed and the design of the RV compressor prototype has been proposed in this chapter. A brief summary of the chapter is as follows:

- For the purpose of measurement data during testing of the prototype, it will be designed to have a large working volume of 50 cm^3.
- In order to reduce the number of rubbing components in the compressor, a new vane design is proposed to cut down the number of components by two, namely the split bush.
- The addition of fillets for the new vane design would help to reduce the amount of dead volume in the vane slot chamber by approximately 20%.
- Rubbing components in the prototype for the vane, rotor and bearings would be made from a self-lubricating material to reduce material wear.
- Design dimensions of the prototype are presented in Table 3.5.
- A separate experiment has been set up to determine a suitable self-lubricating material for use in the prototype as metal-to-metal rubbing without lubricant will have disastrous consequences.
- Between PEEK and PTFE, PEEK was found to be more suitable for rubbing with steel surfaces as it has high wear-resistance and the coefficient of friction decreases with increasing load and rubbing speeds. It is thus selected for use in the prototype.
- Bearing liners made of PEEK will be introduced into the bearings to prevent metal-to-metal contact between the shafts and journal bearings.

Table 3.5: Prototype Design Dimensions

Dimension	Value
Working Volume, cm^3	50.0
Cylinder Radius, mm	50.0
Rotor Radius, mm	42.5
Chamber Length, mm	23.0
Vane Length, mm	18.0
Vane Swivel Angle, °	15.0
Slot Width, mm	6.0
Fillet Height, mm	14.0

4 Geometric Model

After discussing the prototype design, the next step would be to go into modelling the performance of the RV compressor. This chapter will start by delving into the geometric model of the prototype that will be required for use in the thermodynamics and dynamics modelling. Perfect dimensions are assumed for deriving the geometric relations. Note that there would be some deviations in the actual compressor due to manufacturing tolerances in the actual prototype.

4.1 Vane Geometric Relations for Compressor Modelling

With the new vane design presented in Chapter 3, the locus of the vane movement has changed since the tip of the vane is now constrained and its centre now slides along the centreline of the slot.

The vane geometric relations form the basis for computing the working chamber volume variations and vane kinematics. These are required in the thermodynamics model and heat transfer relations that will be presented in Chapter 5. In addition, these relations will also be used for modelling the dynamics of the compressor components in Chapter 6. These new geometric dimensions are presented in Figure 4.1 with exaggerated dimensions for clarity. Note that some of the relations have been presented in Chapter 3 and are repeated here for comprehensiveness.

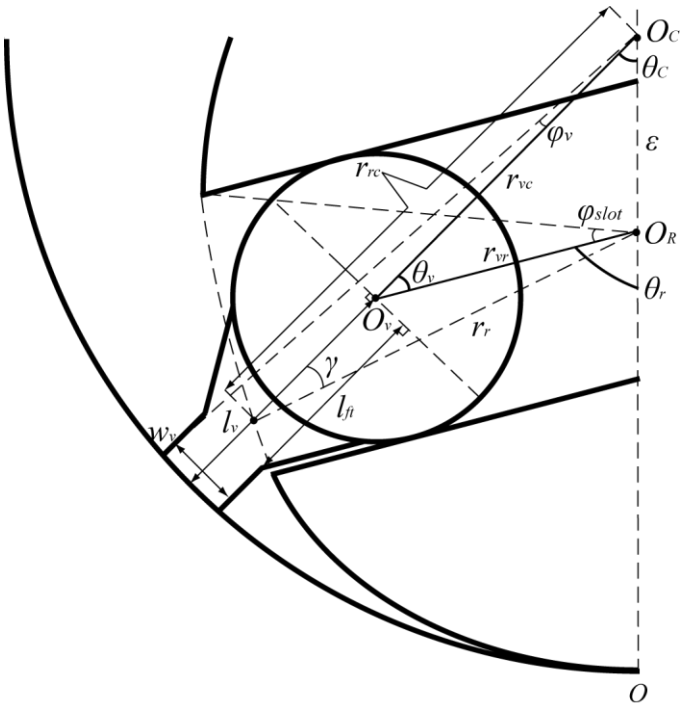

Figure 4.1: Cylinder-Rotor Geometry

Based on the new vane design, the expressions for the geometric relations in Figure 4.1 are presented in Equations (4.1)–(4.5). The first order derivatives and second order derivatives of these relations with respect to the cylinder rotation angle can be found in Equations (4.6)–(4.10) and are used for the kinematics and dynamics modelling in Chapter 6.

$$r_{vr} = \sqrt{\varepsilon^2 + r_{vc}^2 - 2\varepsilon r_{vc}\cos\theta_c} \tag{4.1}$$

$$r_r^2 = r_{rc}^2 + \varepsilon^2 - 2r_{rc}\varepsilon\cos\theta_c$$

$$r_{rc} = \varepsilon\cos\theta_c + \sqrt{r_r^2 - (\varepsilon\sin\theta_c)^2} \tag{4.2}$$

$$\sin\theta_v = \frac{\varepsilon}{r_{vr}}\sin\theta_c \tag{4.3}$$

$$\cos\theta_v = \frac{r_{vc}^2 + r_{vr}^2 - \varepsilon^2}{2r_{vc}r_{vr}} \tag{4.4}$$

$$\theta_r = \theta_c + \theta_v \tag{4.5}$$

First order derivatives:

$$\frac{dr_{vr}}{d\theta_c} = \frac{\varepsilon r_{vc}}{r_{vr}}\sin\theta_c \tag{4.6}$$

$$\frac{d\theta_v}{d\theta_c} = \frac{1}{r_{vr}\cos\theta_v}\left(\varepsilon\cos\theta_c - \frac{dr_{vr}}{d\theta_c}\sin\theta_v\right) \tag{4.7}$$

$$\frac{d\theta_r}{d\theta_c} = 1 + \frac{d\theta_v}{d\theta_c} \tag{4.8}$$

Second order derivatives:

$$\frac{d^2r_{vr}}{d\theta_c^2} = \frac{1}{r_{vr}}\left[\varepsilon r_{vc}\cos\theta_c - \left(\frac{dr_{vr}}{d\theta_c}\right)^2\right] \tag{4.9}$$

$$\begin{aligned}\frac{d^2\theta_r}{d\theta_c^2} = \frac{d^2\theta_v}{d\theta_c^2} = \frac{\sin\theta_v}{\cos\theta_v}\left(\frac{d\theta_v}{d\theta_c}\right)^2 - \frac{2}{r_{vr}}\frac{dr_{vr}}{d\theta_c}\frac{d\theta_v}{d\theta_c} - \frac{\varepsilon\sin\theta_c}{r_{vr}\cos\theta_v} \\ - \frac{\sin\theta_v}{r_{vr}\cos\theta_v}\frac{d^2r_{vr}}{d\theta_c^2}\end{aligned} \tag{4.10}$$

where

$$r_{vc} = r_c - l_v \tag{4.11}$$

4.2 Working Chamber Volumes

With the vane geometric relations determined, this section will then go into the details of the actual working chamber volume in the RV prototype. As the RV prototype is a positive displacement compressor, the working chamber volume and volume variation are important for the thermodynamics modelling of the working fluid such as determining the rate of volume change and fluid density during operation.

Due to the design of the vane, it is important to account for the volume of the vane and dead volume produced in the slot during operation. This would be useful for future design work when miniaturisation of the RV mechanism would cause the thickness of the vane to be significant when compared to the radius of the rotor and cylinder. It is first assumed that the vane is infinitesimally thin [15] and the resulting working chamber volume and dead volume from the vane slot is computed before subtracting the volume of the vane for the exact working volume. Figure 4.2 shows an enlarged section of the vane tip and slot with the geometric features highlighted for the breakdown in volume calculation.

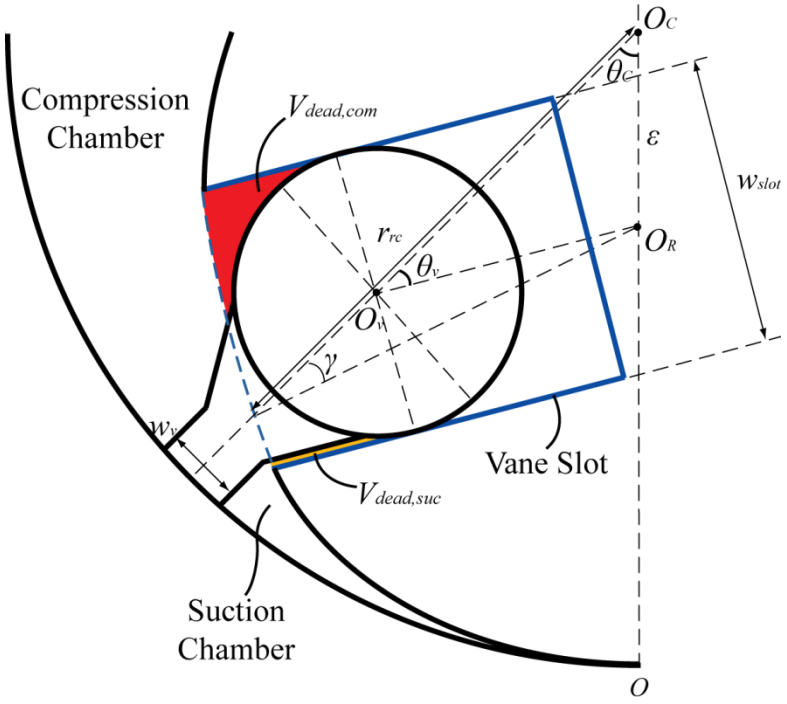

Figure 4.2: Vane Tip and Vane Slot Geometry

4.2.1 Working Chamber with Infinitesimally Thin Vane

From Figure 4.1, the volumes of the working chambers with negligible vane volume are expressed as shown in Equations (4.12) and (4.13) while the variations of the working chambers with respect to the cylinder rotation angle are expressed in Equations (4.14) and (4.15).

$$\begin{aligned} V_{thin,suc} &= \frac{l_c}{2}\int_0^{\theta_c}(r_c^2 - r_{rc}^2)\,d\theta_c \\ &= \frac{l_c}{2}\left[(r_c^2 - r_r^2)\theta_c - \frac{1}{2}\varepsilon^2 \sin 2\theta_c - r_r^2\gamma - \varepsilon \sin\theta_c \sqrt{r_r^2 - \varepsilon^2 \sin^2\theta_c}\right] \end{aligned} \tag{4.12}$$

$$\begin{aligned} V_{thin,com} &= \frac{l_c}{2}\int_{\theta_c}^{2\pi}(r_c^2 - r_{rc}^2)\,d\theta_c \\ &= \pi l_c(r_c^2 - r_r^2) - V_{thin,suc} \end{aligned} \tag{4.13}$$

Derivatives:

$$\frac{dV_{thin,suc}}{d\theta_c} = \frac{l_c}{2}(r_c^2 - r_{rc}^2) \tag{4.14}$$

$$\frac{dV_{thin,com}}{d\theta_c} = -\frac{l_c}{2}(r_c^2 - r_{rc}^2) \tag{4.15}$$

4.2.2 Vane Slot Volumes

The total dead volume in the vane slot can be expressed as Equation (4.16). Due to the swivel of the vane in the slot, the amounts of dead volume in the suction and compression chambers are not the same and can be calculated from Equations (4.18) and (4.19), respectively.

$$V_{dead} = l_c \left[r_r^2 \varphi_{slot} + \frac{w_{slot}}{2} (r_r \cos \varphi_{slot} - 2r_{vr}) \right] \tag{4.16}$$

$$V_{swl} = \frac{l_c}{2} (r_r^2 \varphi_{vr} - r_r r_{vr} \sin \varphi_{vr}) \tag{4.17}$$

$$V_{dead,suc} = \frac{1}{2} V_{slot} - V_{swl} \tag{4.18}$$

$$V_{dead,com} = \frac{1}{2} V_{slot} + V_{swl} \tag{4.19}$$

where

$$\varphi_{slot} = \sin^{-1} \frac{w_{slot}}{2r_r} \tag{4.20}$$

$$\varphi_{vr} = \theta_v - \gamma \tag{4.21}$$

On the other hand, the volume left in the vane slot can be expressed as Equation (4.22). Note that it is unaffected by the angle of the vane swivel.

$$V_{slot} = l_c w_{slot} (l_{slot} + r_{vr} - r_r) \tag{4.22}$$

The derivatives of the dead volume and vane slot volume with respect to the cylinder rotation angle can then be expressed as Equations (4.23)–(4.25). These rate of volume change expressions are important since they affect the thermodynamic processes in the working chamber.

$$\frac{dV_{dead,suc}}{d\theta_c} = -l_c w_{slot} \frac{dr_{vr}}{d\theta_c} - \frac{l_c r_r}{2} \left(r_r \frac{d\varphi_v}{d\theta_c} - r_{vr} \cos \varphi_v \frac{d\varphi_v}{d\theta_c} - r_r \sin \varphi_v \frac{dr_{vr}}{d\theta_c} \right) \tag{4.23}$$

$$\frac{dV_{dead,com}}{d\theta_c} = -l_c w_{slot} \frac{dr_{vr}}{d\theta_c} + \frac{l_c r_r}{2} \left(r_r \frac{d\varphi_v}{d\theta_c} - r_{vr} \cos \varphi_v \frac{d\varphi_v}{d\theta_c} - r_r \sin \varphi_v \frac{dr_{vr}}{d\theta_c} \right) \tag{4.24}$$

$$\frac{dV_{slot}}{d\theta_c} = l_c w_{slot} \frac{dr_{vr}}{d\theta_c} \tag{4.25}$$

where

$$\frac{d\varphi_v}{d\theta_c} = \frac{d\theta_v}{d\theta_c} - \frac{d\gamma}{d\theta_c} \tag{4.26}$$

4.2.3 Vane Volume

The volume of the vane can be computed by breaking down the vane into simpler geometric shapes and then adding up each of the components A_{v1}, A_{v2}, A_{v3} and A_{v4} which would give the volume for half of the vane by symmetry as shown in Figure 4.3.

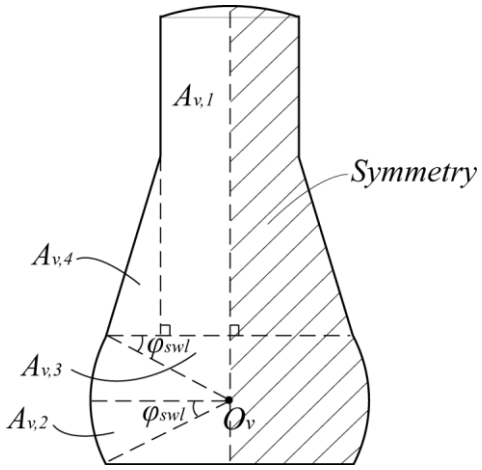

Figure 4.3: Vane Volume Calculation

Equations (4.27)–(4.30) show the area breakdown for each of the shape shown in Figure 4.3 and the volume of the vane can be calculated using Equation (4.31).

$$A_{v,1} = \frac{1}{2}\left(r_c^2\varphi_v - \frac{1}{2}r_c w_v \cos\varphi_v\right) + \frac{w_v}{2}\left(l_v - r_c + r_c\cos\varphi_v - \frac{w_{slot}}{2}\sin\varphi_{swl}\right) \tag{4.27}$$

$$A_{v,2} = \frac{1}{8}w_{slot}^2\varphi_{swl} \tag{4.28}$$

$$A_{v,3} = \frac{1}{8}w_{slot}^2\sin\varphi_{swl}\cos\varphi_{swl} \tag{4.29}$$

$$A_{v,4} = \frac{1}{2}\left(\frac{w_{slot}}{2}\cos\varphi_{swl} - \frac{w_v}{2}\right)\left(l_{ft} - \frac{w_{slot}}{2}\sin\varphi_{swl}\right) \tag{4.30}$$

$$V_{v,total} = 2l_c\left(A_{v,1} + 2A_{v,2} + 2A_{v,3} + A_{v,4}\right) \tag{4.31}$$

where

$$\varphi_v = \sin^{-1}\frac{w_v}{2r_c} \tag{4.32}$$

Similar to the calculation of dead volume in the vane slot, the exact vane volume in each chamber is calculated by taking into account the angle of swivel for the vane. The obstructions in the working volumes for each chamber due to the vane are summarised in Equations (4.33)–(4.35).

$$V_{v,suc} = l_c\left(A_{v,1} + A_{v,2} + A_{v,3} + A_{v,4} - \frac{1}{8}w_{slot}^2\theta_v\right) \tag{4.33}$$

$$V_{v,com} = l_c\left(A_{v,1} + A_{v,2} + A_{v,3} + A_{v,4} + \frac{1}{8}w_{slot}^2\theta_v\right) \tag{4.34}$$

$$V_{v,slot} = 2l_c\left(A_{v,2} + A_{v,3}\right) \tag{4.35}$$

As the vane volume is constant, the derivative of the vane volume with respect to the cylinder rotation angle is only affected by the swivel of the vane. This is shown in Equations (4.36) and (4.37) for the suction and compression chambers, respectively. Note that the variation of volume for the vane slot chamber is unaffected by the vane volume.

$$\frac{dV_{v,suc}}{d\theta_c} = -\frac{l_c}{8}w_{slot}^2\frac{d\theta_v}{d\theta_c} \tag{4.36}$$

$$\frac{dV_{v,com}}{d\theta_c} = \frac{l_c}{8}w_{slot}^2\frac{d\theta_v}{d\theta_c} \tag{4.37}$$

4.2.4 Actual Working Chamber Volumes

With each aspect of the vane and vane slot feature accounted for in Equations (4.12) – (4.37), the actual suction, compression and vane slot chamber volumes can be tabulated as shown in Equations (4.38)–(4.40) respectively.

$$V_{suc} = V_{thin,suc} + V_{dead,suc} - V_{v,suc} \tag{4.38}$$

$$V_{com} = V_{thin,com} + V_{dead,com} - V_{v,com} \tag{4.39}$$

$$V_{vs} = V_{slot} - V_{v,slot} \tag{4.40}$$

The variations of working volumes in the RV compressor prototype are presented in Figure 4.4. The volume of the vane slot chamber was noted to be significant – at maximum variation, the volume of the vane slot chamber occupies 8.3% of the total working volume.

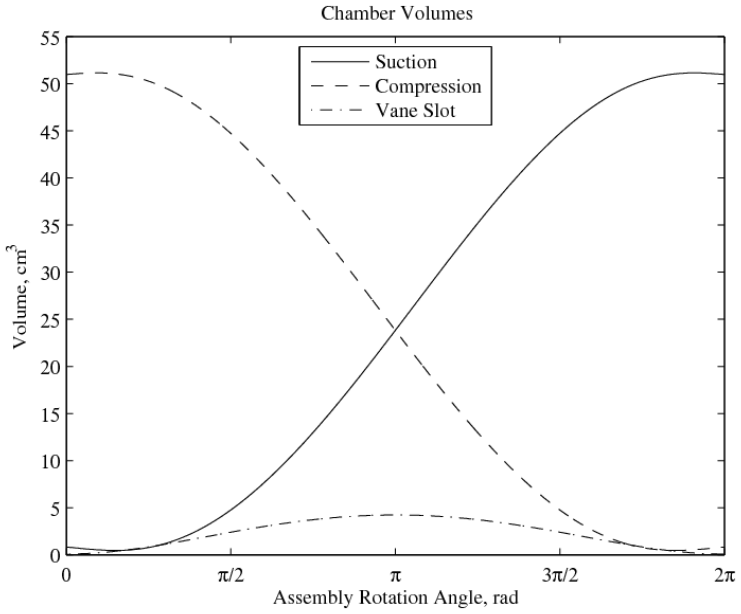

Figure 4.4: Variation of Chamber Volumes

In a similar fashion, the derivatives for the working chambers with respect to the cylinder rotation angle are shown in Equations (4.41) and (4.42), the derivative for the vane slot chamber has already been presented in Equation (4.25). These relations are used in thermodynamics modelling in Chapter 5 to evaluate the rate of density change of the fluid in the working chambers.

$$\frac{dV_{suc}}{d\theta_c} = \frac{dV_{thin,suc}}{d\theta_c} + \frac{dV_{dead,suc}}{d\theta_c} - \frac{dV_{v,suc}}{d\theta_c} \tag{4.41}$$

$$\frac{dV_{com}}{d\theta_c} = \frac{dV_{thin,com}}{d\theta_c} + \frac{dV_{dead,com}}{d\theta_c} - \frac{dV_{v,com}}{d\theta_c} \tag{4.42}$$

4.3 Concluding Remarks

With the new change in the vane design for the RV mechanism, new geometric relations have to be developed in order to obtain the volume variations of the working chambers and rate of volume change which are required for thermodynamics modelling of the fluid in the working

chamber, namely density calculations and density rate of change variations. In addition, these geometric relations are also important for describing the kinematics of the components required for dynamics modelling of the compressor.

In this section, detailed working chamber volume calculations were discussed for accurate modelling purposes. The following factors have been considered for the working chamber volume and derivative relations:

- infinitesimal thin vane for volume calculation during generic working processes
- finite vane slot volume for dead volume calculation
- finite vane volume for working chamber volume adjustment for small working chambers since vane volume can become significant in such cases
- vane slot chamber volume variations as the volume of the vane slot chamber can be significant at 8.3% of total working volume at maximum variation

5 Thermodynamics Model

Following the geometric model of the revolving vane compressor presented in Chapter 4, the working fluid processes of the compressor will now be presented. In this chapter, the thermodynamics model describing the suction, compression and discharge processes would be formulated and discussed. This includes the heat transfer model, and the various mass flow rate models for suction, discharge and internal leakages.

5.1 Thermodynamics Model

The various chambers of the RV compressor are shown in Figure 5.1. The compressor has two working chambers; the suction and compression chambers. These chambers are bounded by the inner wall of the cylinder, outer wall of the rotor, the sides of the vane and the radial contact between the cylinder inner wall and rotor.

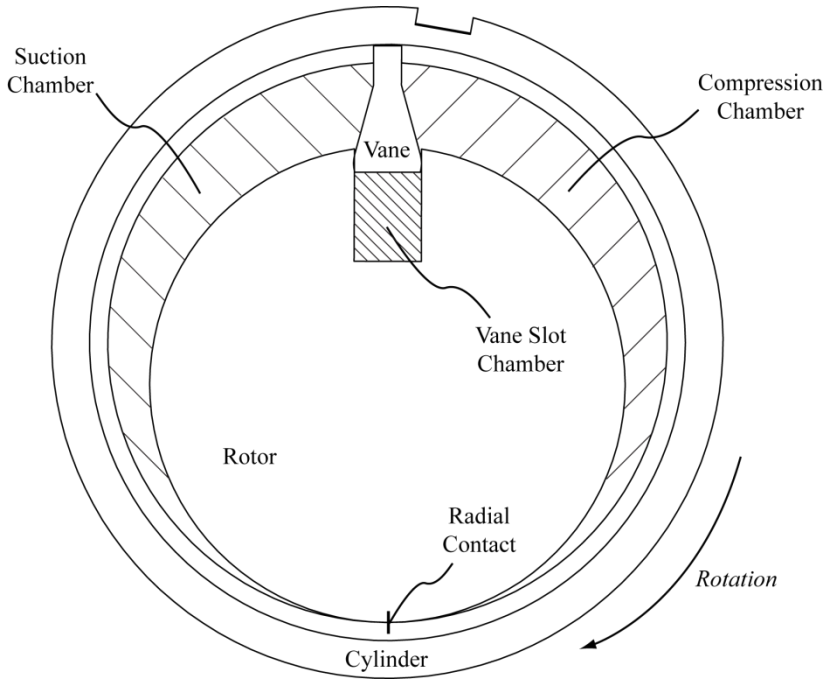

Figure 5.1: Revolving Vane Compressor Chambers

During operation, the suction chamber would transit to become a compression chamber and vice versa when the vane passes through the radial contact. In reality, there are actually three chambers, the third being the vane slot chamber. Due to manufacturing tolerances, the vane tip would not be in contact with both sides of the vane wall at the same time and thus, the working fluid would leak into the vane slot, creating the third chamber.

During operation, the volumes of the chambers would vary; the suction chamber would expand in volume and the compression chamber would decrease in volume while the vane slot chamber varies as the vane moves in and out. The thermodynamic properties of the fluid in the chamber will vary as the volumes change and can be modelled with the first law of thermodynamics [105] by setting up a control volume for each of the chambers. This is shown in Equation (5.1) which can be applied to each chamber. In addition, the conservation of mass in Equation (5.2) holds true for each chamber as well. The control volume diagram is shown in Figure 5.2 and note that the subscripts *i* and *o* denote all possible inlet and outlet flows for the control volume including leakages.

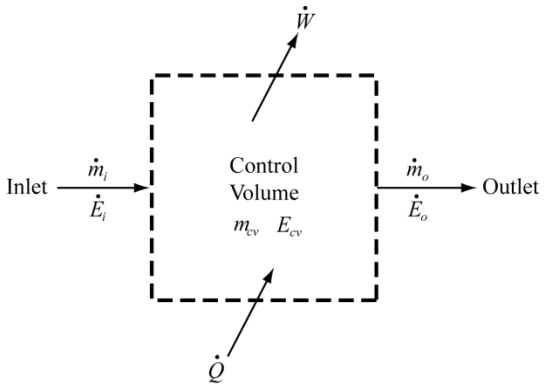

Figure 5.2: Generic Control Volume

$$\frac{d}{dt}\left[m_{cv}\left(u_{cv}+\frac{v_{cv}^2}{2}+gz_{cv}\right)\right]$$
$$=\dot{Q}-\dot{W}+\sum_i\left(h_i+\frac{v_i^2}{2}+gz_i\right)\dot{m}_i-\sum_o\left(h_o+\frac{v_o^2}{2}+gz_o\right)\dot{m}_o \quad (5.1)$$

$$\frac{dm_{cv}}{dt}=\sum_i\dot{m}_i-\sum_o\dot{m}_o \quad (5.2)$$

As the changes in the heights of the control volume and its inlets and outlets are small; the potential energy terms can be neglected. Similarly, the kinetic energy terms can be considered to be negligible as well since the values are small compared to the enthalpy; even with a speed of 50 m s^{-1} at room temperature, the kinetic energy of air is still less than 1% of its enthalpy. To this end, the kinetic and potential energy terms in Equation (5.1) are also ignored and the new equation is rewritten as Equation (5.3).

$$\frac{d}{dt}(m_{cv}u_{cv}) = \dot{Q} - \dot{W} + \sum_i \dot{m}_i h_i - \sum_o \dot{m}_o h_o \tag{5.3}$$

The expression for specific enthalpy is given in Equation (5.4) and its time derivative is shown in Equation (5.5). Additionally, according to the state postulate [105], the specific enthalpy can also be expressed as either a function of pressure and density in Equation (5.6) or as a function of temperature and density in Equation (5.7).

$$h_{cv} = u_{cv} + \frac{p_{cv}}{\rho_{cv}} \tag{5.4}$$

$$\frac{dh_{cv}}{dt} = \frac{du_{cv}}{dt} + \frac{1}{\rho_{cv}}\frac{dp_{cv}}{dt} - \frac{p_{cv}}{\rho_{cv}^2}\frac{d\rho_{cv}}{dt} \tag{5.5}$$

$$\text{for } h_{cv}(p_{cv}, \rho_{cv}),\ \frac{dh_{cv}}{dt} = \left.\frac{\partial h_{cv}}{\partial p_{cv}}\right|_{\rho} \frac{dp_{cv}}{dt} + \left.\frac{\partial h_{cv}}{\partial \rho_{cv}}\right|_{p} \frac{d\rho_{cv}}{dt} \tag{5.6}$$

$$\text{for } h_{cv}(T_{cv}, \rho_{cv}),\ \frac{dh_{cv}}{dt} = \left.\frac{\partial h_{cv}}{\partial T_{cv}}\right|_{\rho} \frac{dT_{cv}}{dt} + \left.\frac{\partial h_{cv}}{\partial \rho_{cv}}\right|_{T} \frac{d\rho_{cv}}{dt} \tag{5.7}$$

Substituting Equation (5.6) into Equation (5.5) would yield the expression for the time derivative of internal energy as shown in Equation (5.8).

$$\frac{du_{cv}}{dt} = \left(\left.\frac{\partial h_{cv}}{\partial p_{cv}}\right|_{\rho} - \frac{1}{\rho_{cv}}\right)\frac{dp_{cv}}{dt} + \left(\left.\frac{\partial h_{cv}}{\partial \rho_{cv}}\right|_{p} + \frac{p_{cv}}{\rho_{cv}^2}\right)\frac{d\rho_{cv}}{dt} \tag{5.8}$$

Furthermore, the work done on a control volume and the time derivative of density are shown in Equations (5.9) and (5.10) respectively.

$$\dot{W} = p_{cv}\frac{dV_{cv}}{dt} \tag{5.9}$$

$$\frac{d\rho_{cv}}{dt} = \frac{1}{V_{cv}}\frac{dm_{cv}}{dt} - \frac{m_{cv}}{V_{cv}^2}\frac{dV_{cv}}{dt} \tag{5.10}$$

Upon manipulation of Equation (5.3) based on the relations given in Equations (5.4) – (5.10), the time derivatives of the pressure and temperature in terms of volume, mass and density are shown in Equations (5.11) and (5.12), respectively.

$$\frac{dp_{cv}}{dt} = \frac{\begin{bmatrix} \dot{Q} + \sum \dot{m}_i h_i - \sum \dot{m}_o h_o \\ -\left(h_{cv} + \rho_{cv} \left.\frac{\partial h_{cv}}{\partial \rho_{cv}}\right|_p\right) \frac{dm_{cv}}{dt} + \rho_{cv}^2 \left.\frac{\partial h_{cv}}{\partial \rho_{cv}}\right|_p \frac{dV_{cv}}{dt} \end{bmatrix}}{\left(m_{cv} \left.\frac{\partial h_{cv}}{\partial p_{cv}}\right|_\rho - V_{cv}\right)} \tag{5.11}$$

$$\frac{dT_{cv}}{dt} = \frac{\begin{bmatrix} \dot{Q} + \sum \dot{m}_i h_i - \sum \dot{m}_o h_o \\ -\left(h_{cv} + \rho_{cv} \left.\frac{\partial h_{cv}}{\partial \rho_{cv}}\right|_T\right) \frac{dm_{cv}}{dt} + \rho_{cv}^2 \left.\frac{\partial h_{cv}}{\partial \rho_{cv}}\right|_T \frac{dV_{cv}}{dt} + V_{cv} \frac{dp_{cv}}{dt} \end{bmatrix}}{m_{cv} \left.\frac{\partial h_{cv}}{\partial T_{cv}}\right|_\rho} \tag{5.12}$$

By applying the appropriate mass flow, volume-time derivative and heat transfer terms for each of the control volumes, Equations (5.2), (5.5), (5.8), (5.10), (5.11) and (5.12) can be solved to obtain the respective mass, enthalpy, internal energy, density, pressure and temperature with six unknown variables for each of the suction, compression and vane slot chambers.

Alternatively, with two independent, intensive properties and the use of real gas equations, the calculation of the other working thermodynamic properties can be greatly simplified according to the state postulate [105]. This can be achieved by solving only Equations (5.2) and (5.11) to obtain the mass and pressure properties of the chambers. Furthermore, based on the known volume variation of the chambers from the geometric model in Chapter 4, the fluid densities can then be calculated. Thereafter, with the help of real gas equation programme such as REFPROP [106], the desired thermodynamic properties such as temperature, internal energy, enthalpy can then be computed with just the density and pressure inputs.

Equations (5.2) and (5.11) are initial value, first-order ordinary differential equations which are solved using the 4th order Runge Kutta method in MATLAB which supports REFPROP for calculating the thermodynamic properties of the working fluid. Details on the full simulation procedure for the compressor prototype that encompasses the other models covered in Chapters 4, 6 and 7 can be found in Appendix A-1.

5.2 Heat Transfer Model

5.2.1 Heat Transfer Correlation

As the RV mechanism is a relatively new design and hence, the internal flow aspect of the fluid in the working chambers for heat transfer is not fully understood. Pioneering work by Tan and Ooi [16] on the heat transfer model for the RV compressor has helped to gain valuable insight on the heat transfer model for the RV mechanism. Heat transfer between the working fluid and the walls of the compressor chamber must be taken into consideration for more accurate modelling of the fluid working processes.

The heat transfer model can be approximated according to Newton's law of cooling in Equation (5.13) in which the heat transfer coefficient *h* is calculated from the Nusselt number correlation by Liu and Zhou [33] in Equation (5.14). As the correlation was originally developed for use with the reciprocating compressor, Tan and Ooi [16] adapted new expressions for the characteristic velocity and hydraulic diameter for the Reynolds and Nusselt numbers with respect to the geometry of the RV compressor.

The adapted correlation proved to be very useful in modelling heat transfer in the RV compressor working chambers as it greatly improved the accuracy of chamber pressure prediction [16].

The temperature of the surface walls for each of the chamber will be approximated from the thermal model presented in Chapter 7. It is assumed that the temperatures of the components remain constant for the heat transfer since the thermal mass of the components $\Sigma(mc_p)_{solid}$ are much greater than that of the working fluid $(mc_p)_{fluid}$.

$$\dot{Q} = h\sum_{w} A_w(T_w - T_{cv}) \tag{5.13}$$

$$\mathrm{Nu} = 0.75\mathrm{Re}^{0.8}\mathrm{Pr}^{0.6} = \frac{hD_{cv}}{k_{cv}} \tag{5.14}$$

where

$$\mathrm{Re} = \frac{\rho_{cv} v_{cv} D_{cv}}{\mu_{cv}} \tag{5.15}$$

$$\mathrm{Pr} = \frac{c_{p_{cv}} \mu_{cv}}{k_{cv}} \tag{5.16}$$

When applying the heat transfer correlation by Liu and Zhou [33] to the revolving vane compressor, Tan and Ooi [16] defined the characteristic velocity of the fluid flow as the velocity of the vane rotation since the vane pushes the fluid in the direction of the rotation of the cylinder-rotor assembly. The corresponding hydraulic diameter would be the length of vane that is exposed and pushing the working fluid.

The RV compressor used by Tan and Ooi [16] for their investigation was driven by the rotor component but for the current prototype, the cylinder is the driving component. These expressions for the characteristic velocity v_{cv} and hydraulic diameters D_{cv} of the fluid for the suction and compression chambers are then adapted accordingly. The new expressions for the characteristic velocity and the hydraulic diameter for the suction and compression chambers are shown in Equations (5.17) and (5.18), respectively.

$$v_{cv} = \frac{1}{r_c - r_{rc}} \int_{r_{rc}}^{r_c} \dot{\theta}_c r \, dr = \frac{\dot{\theta}_c}{2} (r_c + r_{rc}) \tag{5.17}$$

$$D_{cv} = \frac{2 l_c (r_c - r_{rc})}{r_c - r_{rc} + l_c} \tag{5.18}$$

On the other hand for the vane slot chamber, since the vane movement in the vane slot chamber resembles that of a reciprocating compressor as shown in Figure 5.3, the characteristic velocity and hydraulic diameter are approximated to that of the reciprocating compressor given in various heat transfer correlations in the literature [31, 107–109]; the characteristic velocity for the vane slot chamber would be the speed of the vane akin to piston speed and the hydraulic diameter would be the vane slot width. The respective expressions are shown in Equations (5.19) and (5.20).

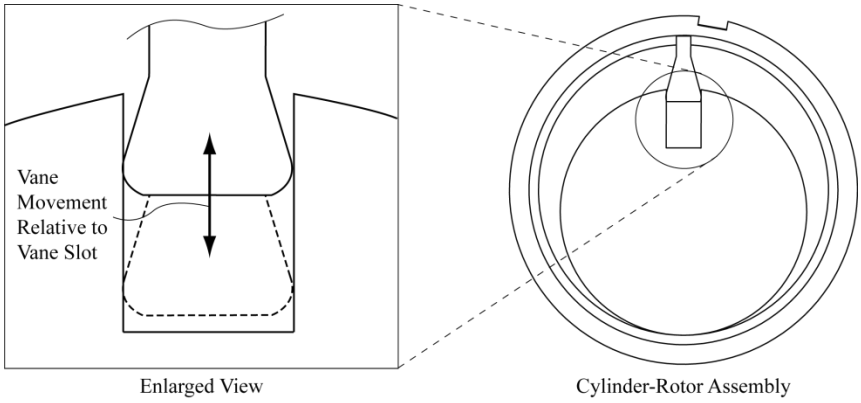

Figure 5.3: Vane Movement Relative to Vane Slot

$$v_{vane,cv} = \frac{dr_{vr}}{dt} \tag{5.19}$$

$$D_{vane,cv} = 2r_{v,tip} \tag{5.20}$$

5.2.2 Heat Transfer Surface Areas

With the heat transfer correlations presented in Section 5.2.1, this section will proceed with the computation of the surface areas in the working chambers for heat transfer.

As the cylinder and rotor are made of dissimilar materials, the temperature gradients at the respective surfaces will differ and thus, the area of the chamber walls would be computed separately for both the cylinder and rotor. The RV working chambers are presented in Figure 5.4 with the respective chamber walls highlighted and the surface areas computed in Equations (5.21)–(5.26) and the expressions for the endface areas are presented in Equations (5.27) and (5.28).

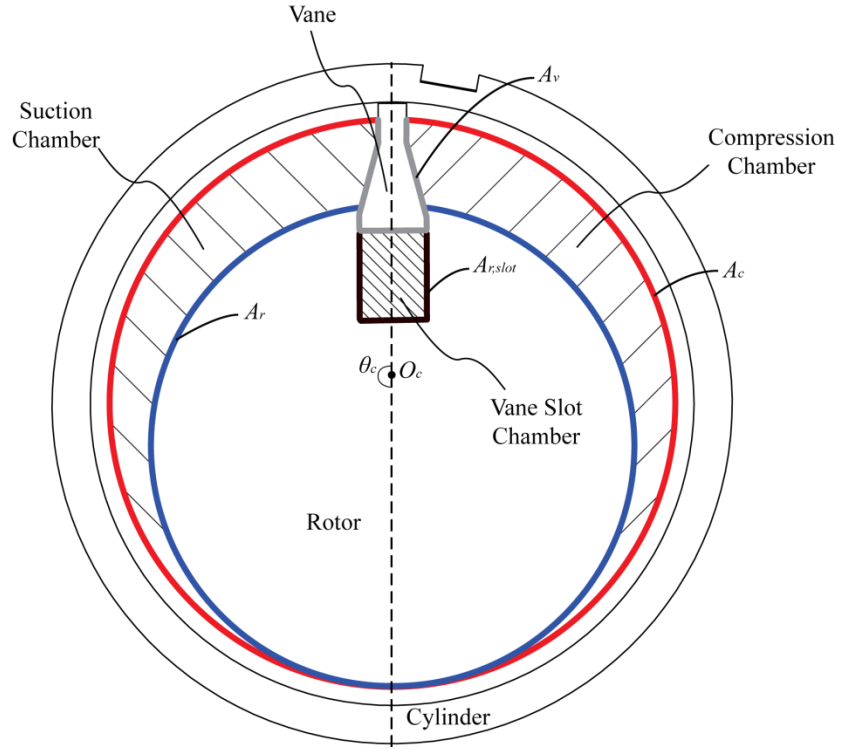

Figure 5.4: Working Chamber Surface Areas

$$A_{c,suc} = l_c r_c(\theta_c - \varphi_v) \tag{5.21}$$

$$A_{c,com} = l_c r_c(2\pi - \theta_c + \varphi_v) \tag{5.22}$$

$$A_v = l_c\left(\frac{w_{slot}}{2}\varphi_{swl} + \sqrt{\left(\frac{w_{slot}}{2}\cos\varphi_{swl} - \frac{w_v}{2}\right)^2 + \left(l_{ft} - \frac{w_{slot}}{2}\sin\varphi_{swl}\right)^2} + l_v - l_{ft} - r_c + r_c\cos\varphi_v\right) \tag{5.23}$$

$$A_{r,suc} = l_c r_r(\theta_r - \varphi_{slot}) \tag{5.24}$$

$$A_{r,com} = l_c r_r(2\pi - \theta_r + \varphi_{slot}) \tag{5.25}$$

$$A_{r,slot} = l_c(l_{slot} - r_r - r_{vr}) \tag{5.26}$$

$$A_{ef,suc} = \frac{V_{suc}}{l_c} \tag{5.27}$$

$$A_{ef,com} = \frac{V_{com}}{l_c} \tag{5.28}$$

To this end, the total surface area for both the cylinder and rotor can be summed up as shown in Equations (5.29) – (5.32). Note that due to the effect of the vane swivel, corrections have been made to the expressions for the cylinder wall and that the endface area A_{ef} values make up part of the expression as well.

$$A_{w,c,suc} = A_{c,suc} + A_v - \frac{l_c w_{slot} \theta_v}{2} + 2A_{ef,suc} \tag{5.29}$$

$$A_{w,c,com} = A_{c,com} + A_v + \frac{l_c w_{slot} \theta_v}{2} + 2A_{ef,com} \tag{5.30}$$

$$A_{w,r,suc} = A_{r,suc} + A_{r,slot} \tag{5.31}$$

$$A_{w,r,com} = A_{r,com} + A_{r,slot} \tag{5.32}$$

5.3 Suction and Discharge Flow Models

The mass flow rates through the suction and discharge ports can be modelled as a flow through an orifice [110] as shown in Figure 5.5. Assuming that the upstream fluid is stagnant and steady isentropic flow with negligible change in potential energy, and no addition of heat and work through the orifice, the energy equation describing the flow can be reduced to that shown in Equation (5.33). The mass flow rate can then be estimated as shown in Equation (5.34).

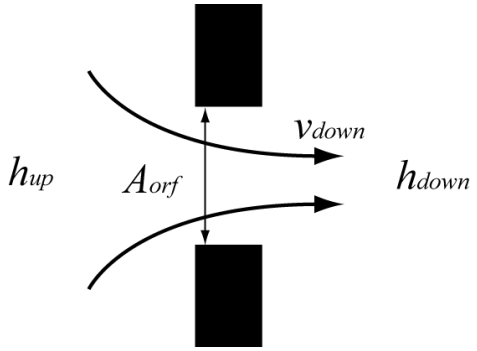

Figure 5.5: Orifice Flow Model

$$v_{down} = \sqrt{2\left(h_{up} - h_{down,isen}\right)} \tag{5.33}$$

$$\frac{dm_{orf}}{dt} = \rho_{up} A_{orf} v_{down} \tag{5.34}$$

Due to the assumption that the flow is isentropic, the mass flow rate is only applicable for an ideal case. To this end, a discharge coefficient C_d should be introduced into Equation (5.34) to account for the real phenomena with reduced flow due to the presence of vena contracta and viscous dissipation as shown in Equation (5.35). For simplicity, a constant discharge coefficient is assumed for different operating conditions.

$$\frac{dm_{pt}}{dt} = C_d \rho_{up} A_{orf} v_{down} \tag{5.35}$$

For the case of the compressor prototype, the ports are that of a sharp-edged orifice flow. The flow coefficients are in the range of 0.58 – 0.65 provided by Munson et al. [111] and the value depends on the ratio of the orifice diameter to the pipe diameter. It decreases with smaller diameter ratios and with higher Reynolds numbers.

However, the actual suction/discharge port flow in the compressor prototype is not the same as pipe flow. Hence, an exact diameter ratio cannot be computed for determining the orifice flow coefficient. Instead, it shall be determined from measurements during testing of the prototype. A discharge coefficient shall be selected from the range 0.58 – 0.65 such that the theoretical predictions with the specific chosen value would fit all aspects of the operating conditions tested.

The orifice area for the suction port is not constant due to the location of the suction port at a distance from the vane centerline and varies during its transition through the radial contact between the rotor and cylinder. Figure 5.6 shows an illustration of the suction port transition. Similarly, the orifice area for the discharge port is not constant and is dependent on the deflection angle of the discharge reed valve which can be calculated from the valve dynamics model.

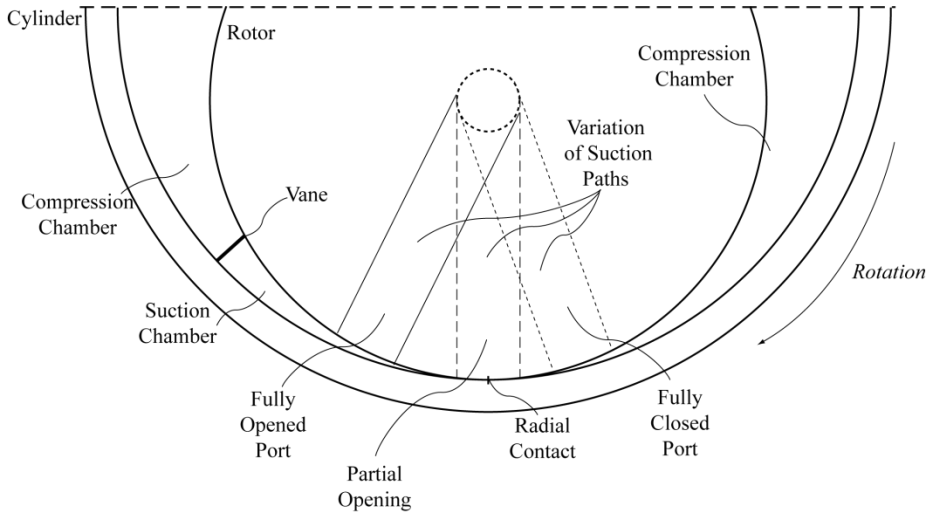

Figure 5.6: Suction Port Transition

5.4 Flow Orifice Areas

5.4.1 Suction

At the start of the suction cycle, the suction port is still on the other side of the radial contact and thus it is considered covered. As the rotor turns and the suction port passes through the radial contact, there is partial opening of the port which transitions into a full opening once the port passes through the radial contact completely.

Figure 5.7 depicts the suction port geometry with respect to the radial contact line. Based on the geometry, the partial opening of the suction port with respect to the cylinder rotation angle can be written as shown in Equation (5.37). The variation of orifice area for the suction chamber with respected to the rotor rotation angle for the compressor prototype can then be plotted as shown in Figure 5.8.

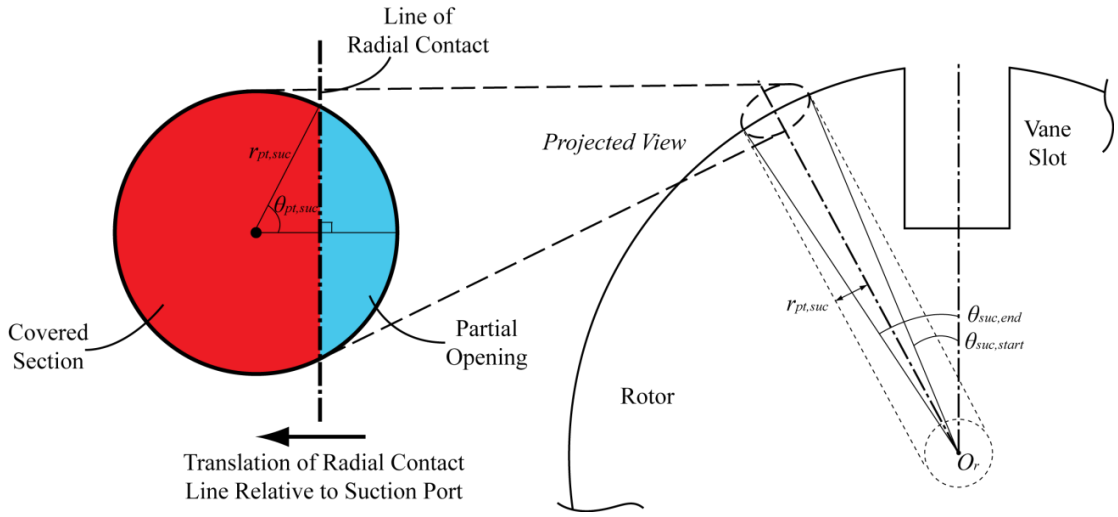

Figure 5.7: Suction Port Geometry

$$A_{orf,suc} = 0, \qquad 0 \le \theta_r < \theta_{suc,start} \tag{5.36}$$

$$A_{orf,suc} = r_{pt,suc}^2 \left[\theta_{pt,suc} - \frac{1}{2}\sin(2\theta_{pt,suc})\right], \qquad \theta_{suc,start} \le \theta_r < \theta_{suc,end} \tag{5.37}$$

$$A_{orf,suc} = \pi r_{pt,suc}^2, \qquad \theta_r \ge \theta_{suc,end} \tag{5.38}$$

where

$$\theta_{pt,suc} = \cos^{-1}\left(\frac{r_r \sin\theta_r}{r_{pt,suc}}\right) \tag{5.39}$$

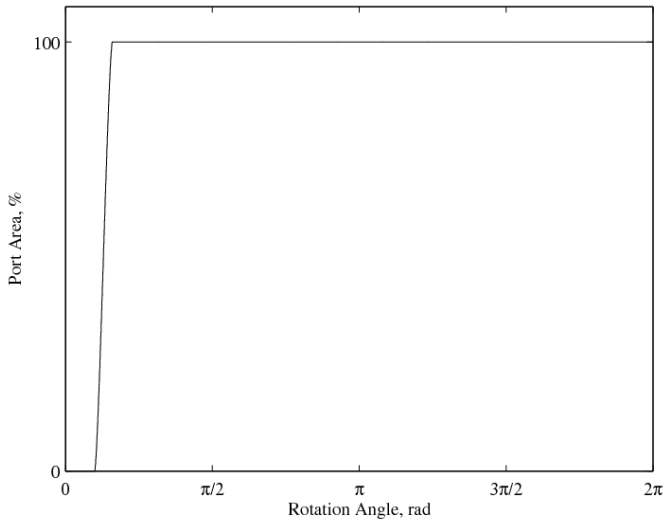

Figure 5.8: Suction Orifice Area

5.4.2 Discharge

The effective cross-section area of discharge port is also affected by the radial contact line similar to that of the suction port. Other than determining the flow area, the effective cross-section area of the discharge port that is exposed to the fluid in the working chamber is an important parameter for determining the valve dynamics since it affects the pressure force on the valve plate. Chapter 6 will go into detail the valve dynamics model for determining the valve deflection height. For this section, only the effective exposed area for the discharge port and orifice area based on the valve deflection would be covered.

Figure 5.9 shows the discharge port geometry with respect to the radial contact line. The expressions for the effective exposed area for the discharge port are presented in Equations (5.40)–(5.42) and the variation of the effective exposed discharge port area with respect to the cylinder rotation angle is plotted in Figure 5.10.

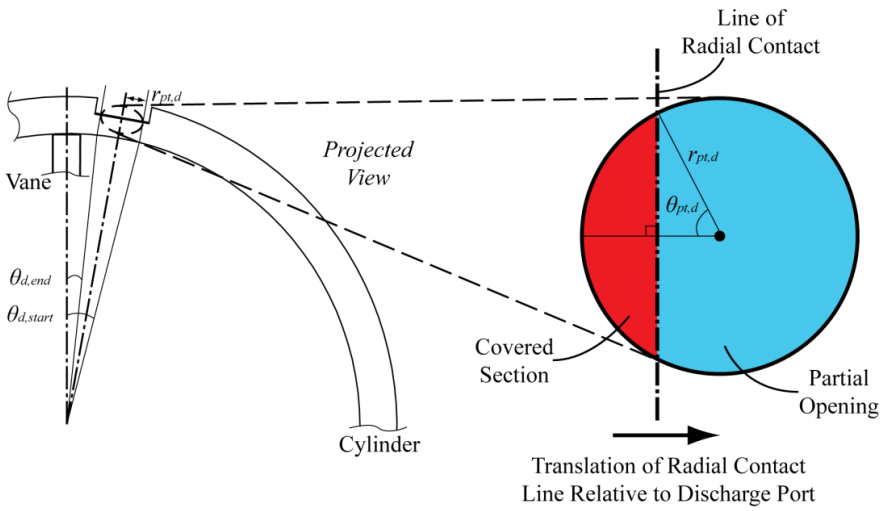

Figure 5.9: Discharge Port Geometry

$$A_{ef,d} = \pi r_{pt,d}^2, \qquad 0 \le \theta_c < \theta_{d,start} \tag{5.40}$$

$$A_{ef,d} = r_{pt,d}^2 \left[\theta_{pt,d} + \frac{1}{2}\sin(2\theta_{pt,d})\right], \qquad \theta_{d,start} \le \theta_c < \theta_{d,end} \tag{5.41}$$

$$A_{ef,d} = 0, \qquad \theta_c \ge \theta_{d,end} \tag{5.42}$$

where

$$\theta_{pt,d} = \cos^{-1}\left(\frac{r_c \sin\theta_c}{r_{pt,d}}\right) \tag{5.43}$$

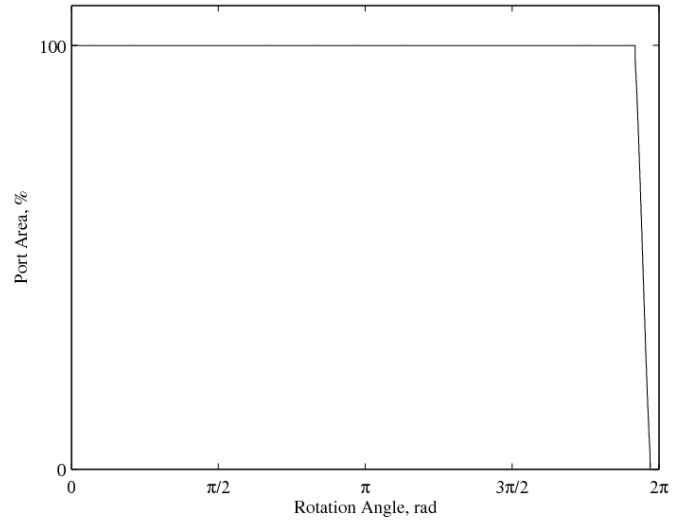

Figure 5.10: Discharge Port Area

When the valve is deflected due to fluid pressure in the working chamber, an opening is created. At this point in time, there are two possible flow areas occurring simultaneously; the first of which is the discharge port area as shown in Figure 5.9 and the second would be the circumferential space between the deflected valve and port depicted in Figure 5.11. Assuming negligible curvature of the valve at the discharge port, an approximation for the flow area around the valve is shown in Equation (5.44).

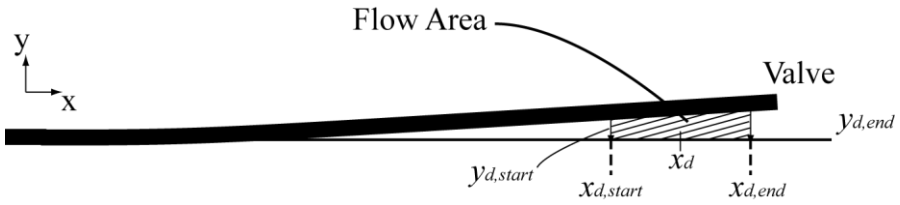

Figure 5.11: Flow Area around Deflected Valve

$$A_{flow,valve} = \pi r_{pt,d}\left(y_{d,start} + y_{d,end}\right) \tag{5.44}$$

The effective flow area around the valve is then compared to the effective discharge port area and the orifice flow area for the discharge flow model would be the smaller of the two values as shown in Equation (5.45).

$$A_{orf,d} = \min\left(A_{flow,valve}\,, A_{eff,d}\right) \tag{5.45}$$

5.5 Leakage Flow Models

Based on the prototype design, four internal leakage channels have been identified and are illustrated in Figure 5.12. These leakage channels are listed as follows:

1. Radial clearance leakage at the radial contact between the rotor and the cylinder
2. Leakage around the vane tip
3. Vane endface leakage (both endfaces)
4. Rotor endface leakage (both endfaces)

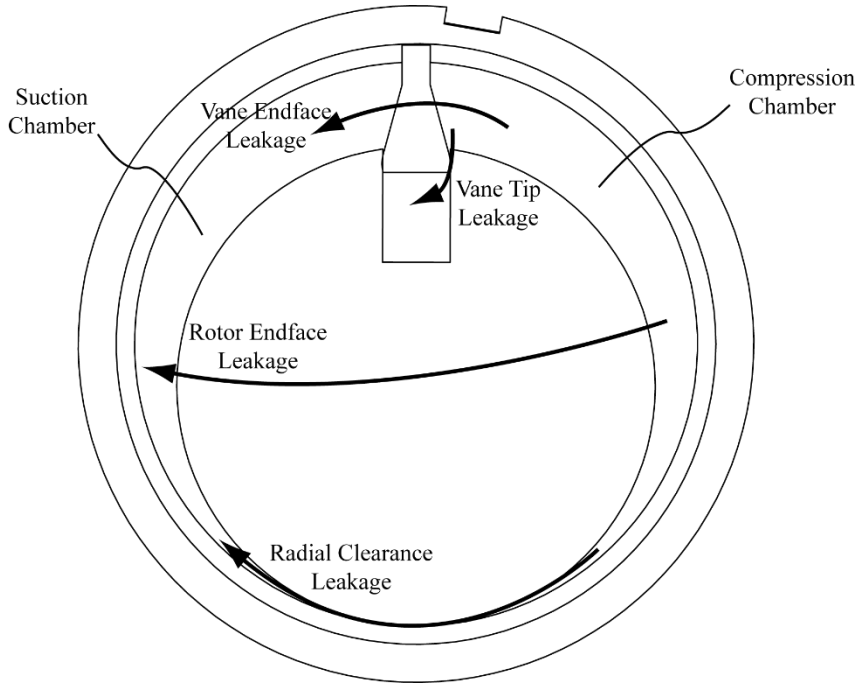

Figure 5.12: RV Compressor Leakage Channels

5.5.1 Radial Clearance Leakage

Since the revolving vane mechanism shares a similar rotor and cylinder configuration to that of the rolling piston, the leakage through the radial clearance gap is modelled using the same method as that of a rolling piston proposed by Yanagisawa and Shimizu [112]. Figure 5.13 shows the clearance gap at the radial contact and Figure 5.14 shows the leakage path model used for the rolling piston [112], which is modelled as a Fanno flow.

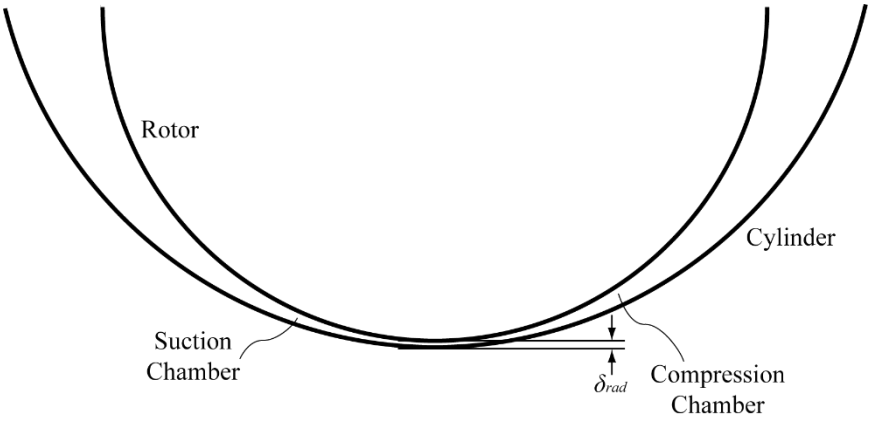

Figure 5.13: Radial Clearance Geometry

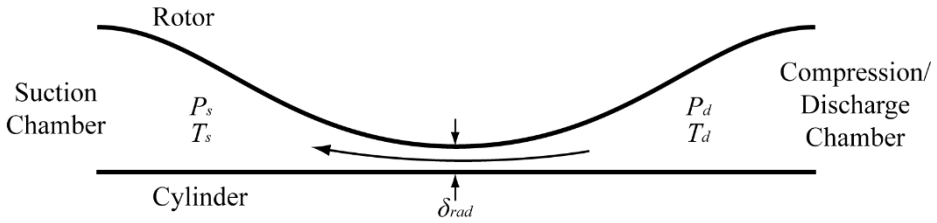

(a): Simplified Geometric Model

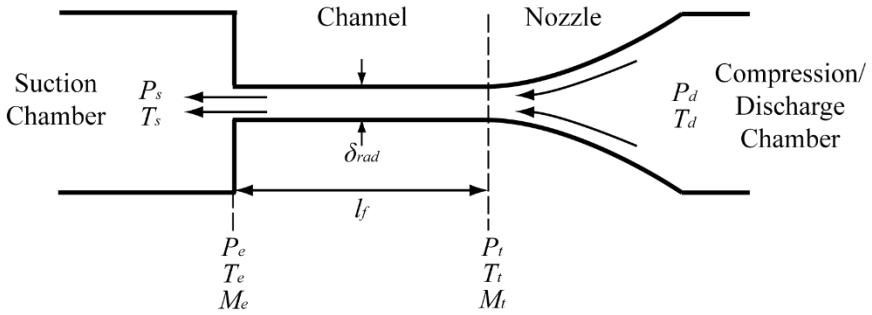

(b): Fanno Flow Model

Figure 5.14: Radial Leakage Flow Model

According to Yanagisawa and Shimizu [112], the flow is first assumed to be choked at the channel exit. When the channel exit is choked, Equations (5.46)–(5.52) apply to the flow describing the equivalent channel length, pressure and temperature ratios, and the leakage flow rate, respectively [112].

$$\lambda \frac{l_f}{2\delta_{rad}} = \frac{1 - M_t^2}{\kappa M_t^2} + \frac{\kappa + 1}{2\kappa} \ln \frac{M_t^2(\kappa + 1)}{2 + M_t^2(\kappa - 1)} \tag{5.46}$$

$$\frac{p_t}{p_e} = \frac{1}{M_t} \sqrt{\frac{\kappa + 1}{2 + M_t^2(\kappa - 1)}} \tag{5.47}$$

$$\frac{p_d}{p_t} = \left(1 + \frac{\kappa - 1}{2} M_t^2\right)^{\frac{\kappa}{\kappa-1}} \tag{5.48}$$

$$\frac{p_d}{p_e} = \frac{p_d}{p_t} \cdot \frac{p_t}{p_e} \tag{5.49}$$

$$T_e = T_d \div \left[1 + \frac{M_e^2(\kappa - 1)}{2}\right] \tag{5.50}$$

$$v_e = M_e \sqrt{\kappa R T_e} \tag{5.51}$$

$$\frac{dm_{leak}}{dt} = \delta_{rad} l_c v_e \left(\frac{p_e}{R T_e}\right) \tag{5.52}$$

where

$$l_f = \frac{2\pi \delta_{rad} r_c}{\varepsilon \sqrt{1 - \left(1 - \frac{\delta}{\varepsilon}\right)^2}} \tag{5.53}$$

$$\lambda = \begin{cases} \dfrac{96}{Re} & (Re \leq 3560) \\ \dfrac{0.3164}{Re^{0.25}} & (Re > 3560) \end{cases} \tag{5.54}$$

$$Re = \frac{2}{\mu l_c} \cdot \frac{dM_{leak}}{dt} \tag{5.55}$$

Following the assumption that the channel exit flow is choked, the calculated pressure ratio in Equation (5.49) is checked against the actual operating pressure ratio between the compression and suction chamber. If the calculated pressure ratio is lower than the actual operating pressure ratio, the leakage channel is indeed choked and the assumption is thus valid.

However, if the calculated pressure ratio is lower than that of the operating pressure ratio, the exit velocity of the fluid is not sonic and to this end, the Mach number at the throat would have to be iterated. A longer friction channel length for the Fanno flow in which the flow would be choked is assumed and illustrated in Figure 5.15.

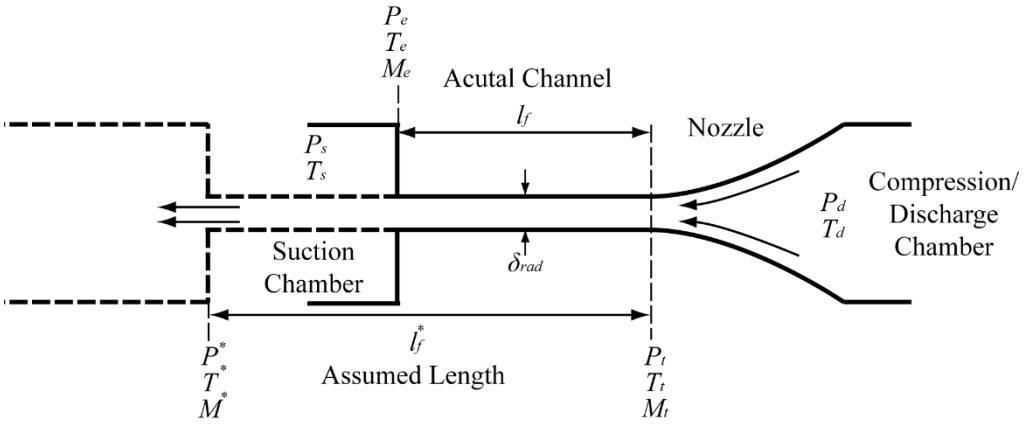

Figure 5.15: Assumed Friction Channel Length

Based on the assumed Mach number at the throat (M_t^*), the new relations describing the flow and equivalent friction channel length are expressed in Equations (5.56)–(5.61). Similarly, the calculated pressure ratio in Equation (5.61) is then compared to that of the actual operating pressure ratio.

$$\lambda \frac{l_f^*}{2\delta_{rad}} = \frac{1 - M_t^{*2}}{\kappa M_t^{*2}} + \frac{\kappa + 1}{2\kappa} \ln \frac{M_t^{*2}(\kappa + 1)}{2 + M_t^{*2}(\kappa - 1)} \tag{5.56}$$

$$\lambda \frac{l_f^* - l_f}{2\delta_{rad}} = \frac{1 - M_e^2}{\kappa M_e^2} + \frac{\kappa + 1}{2\kappa} \ln \frac{M_e^2(\kappa + 1)}{2 + M_e^2(\kappa - 1)} \tag{5.57}$$

$$\frac{p_t}{p^*} = \frac{1}{M_t^*} \sqrt{\frac{\kappa + 1}{2 + M_t^{*2}(\kappa - 1)}} \tag{5.58}$$

$$\frac{p_d}{p_t} = \left(1 + \frac{\kappa - 1}{2} M_t^{*2}\right)^{\frac{\kappa}{\kappa - 1}} \tag{5.59}$$

$$\frac{p_e}{p^*} = \frac{1}{M_e} \sqrt{\frac{\kappa + 1}{2 + M_e^2(\kappa - 1)}} \tag{5.60}$$

$$\frac{p_d}{p_e} = \frac{p_d}{p_t} \cdot \frac{p_t}{p^*} \div \frac{p_e}{p^*} \tag{5.61}$$

The iteration continues each time for assumed Mach numbers at the throat and would stop only when the calculated pressure ratio in Equation (5.61) matches that of the operating pressure ratio after which the leakage flow rate can then be calculated using Equations (5.50)–(5.52).

The iteration process of estimating the equivalent friction channel length to match the prescribed pressure ratio may result in inaccuracy during leakage calculation. The accuracy depends on the convergence criterion for the root-search iteration. The convergence criterion for estimating the equivalent friction channel length is set at ±1% difference between the final calculated pressure ratio and the given pressure ratio.

5.5.2 Vane Tip Leakage

For the vane slot chamber, fluid can enter and exit the control volume when it leaks around the vane tip. Figure 5.16 shows a close up of the leakage path at the vane tip.

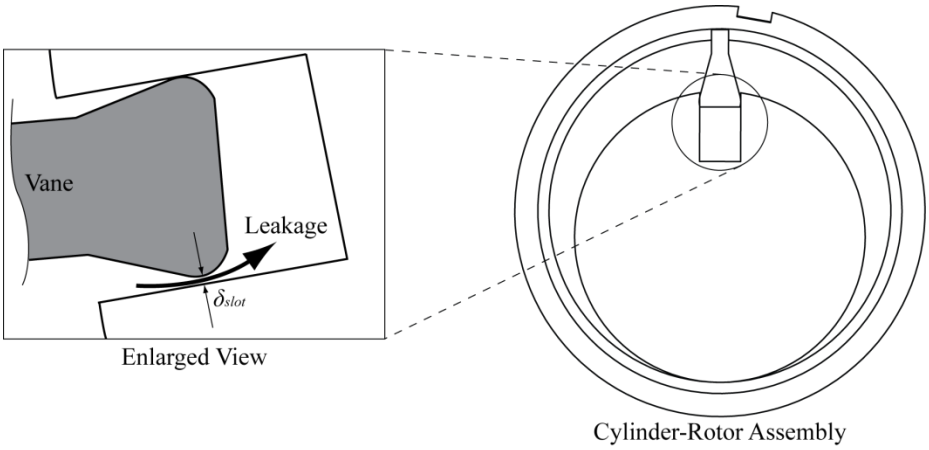

Figure 5.16: Vane Tip Leakage

The shape of the flow channel may be approximated as that of a flow through an orifice and thus, the thick orifice flow model is employed for calculation of the vane tip leakage with the clearance gap as the orifice area. The leakage flow rate for the vane tip is calculated with Equation (5.35) with the orifice area represented by the product of the vane tip clearance δ_{slot} and the chamber length l_c ($A_{orf} = \delta_{slot}\, l_c$).

5.5.3 Vane Endface Leakage

A close up of the vane endface leakage path is depicted in Figure 5.17. It is similar to that of the radial leakage flow model, albeit without the convergent section. Therefore, it can be modelled as a Fanno flow as well.

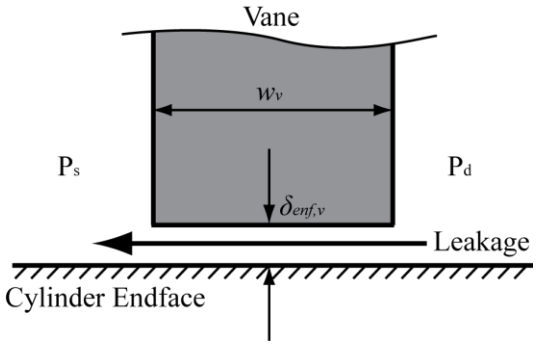

Figure 5.17: Vane Endface Leakage

The method and Equations (5.56) to (5.61) for the radial leakage are thus adapted for application to calculation for the vane endface leakage; the friction channel length for the flow would be none other than the width of the vane and the isentropic relations for convergent section would be neglected. The equivalent Fanno flow path is illustrated in Figure 5.18.

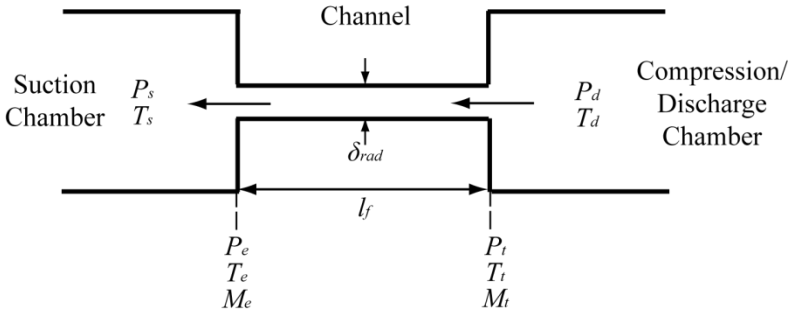

Figure 5.18: Equivalent Fanno Flow Path

The flow is first assumed to be choked at the channel exit and Equations (5.62) to (5.68) would apply. The pressure ratio calculated in Equation (5.63) would have to be lower or equal to the operating pressure ratio in order for the assumption to be valid.

$$\lambda \frac{w_v}{2\delta_{enf,v}} = \frac{1 - M_t^2}{\kappa M_t^2} + \frac{\kappa + 1}{2\kappa} \ln \frac{M_t^2(\kappa + 1)}{2 + M_t^2(\kappa - 1)} \tag{5.62}$$

$$\frac{p_t}{p_e} = \frac{1}{M_t} \sqrt{\frac{\kappa + 1}{2 + M_t^2(\kappa - 1)}} \tag{5.63}$$

$$T_e = T_d \div \left[1 + \frac{M_e^2(\kappa - 1)}{2}\right] \tag{5.64}$$

$$v_e = M_e\sqrt{\kappa R T_e} \tag{5.65}$$

$$\frac{dM_{leak}}{dt} = \delta_{rad} l_v v_e \left(\frac{p_e}{RT_e}\right) \tag{5.66}$$

where

$$\lambda = \begin{cases} \dfrac{96}{Re} & (Re \leq 3560) \\ \dfrac{0.3164}{Re^{0.25}} & (Re > 3560) \end{cases} \tag{5.67}$$

$$Re = \frac{2}{\mu l_c} \cdot \frac{dM_{leak}}{dt} \tag{5.68}$$

However, if the calculated pressure ratio is too high, the Mach number at the channel exit would have to be iterated in a similar fashion to that of the radial clearance leakage in Section 5.5.1. The adapted equations are presented in Equations (5.69) to (5.73).

$$\lambda \frac{l_f^*}{2\delta_{enf,v}} = \frac{1 - M_t^{*2}}{\kappa M_t^{*2}} + \frac{\kappa + 1}{2\kappa} \ln \frac{M_t^{*2}(\kappa + 1)}{2 + M_t^{*2}(\kappa - 1)} \tag{5.69}$$

$$\lambda \frac{l_f^* - w_v}{2\delta_{enf,v}} = \frac{1 - M_e^2}{\kappa M_e^2} + \frac{\kappa + 1}{2\kappa} \ln \frac{M_e^2(\kappa + 1)}{2 + M_e^2(\kappa - 1)} \tag{5.70}$$

$$\frac{p_t}{p^*} = \frac{1}{M_t^*} \sqrt{\frac{\kappa + 1}{2 + M_t^{*2}(\kappa - 1)}} \tag{5.71}$$

$$\frac{p_e}{p^*} = \frac{1}{M_e} \sqrt{\frac{\kappa + 1}{2 + M_e^2(\kappa - 1)}} \tag{5.72}$$

$$\frac{p_t}{p_e} = \frac{p_t}{p^*} \div \frac{p_e}{p^*} \tag{5.73}$$

The iteration continues each time for assumed Mach numbers at the throat and would stop only when the calculated pressure ratio in Equation (5.73) matches that of the operating pressure ratio after which the leakage flow rate can then be calculated using Equations (5.64)–(5.66).

To this end, it is noted that due to the varying width of the vane, the analytical solution for the vane endface leakage would not be as accurate because the majority of the leakage flow would occur at sections of the vane where the width is the shortest with lowest flow resistance. Furthermore, there is also leakage from the compression chamber into the slot chamber as well. Hence, a computational fluid dynamics (CFD) model shall be used to calculate the leakage flow through the actual vane endface gap for comparison. This is to ascertain an equivalent length $l_{v,ef}$ for a uniform cross-section vane to be used in the analytical solution and to determine the ratio of leakage flow that goes into the vane slot chamber.

Figure 5.19 shows the illustration of a rectangular vane with uniform width and the bulbous vane. The next section will proceed onto the CFD model for leakage flow calculation.

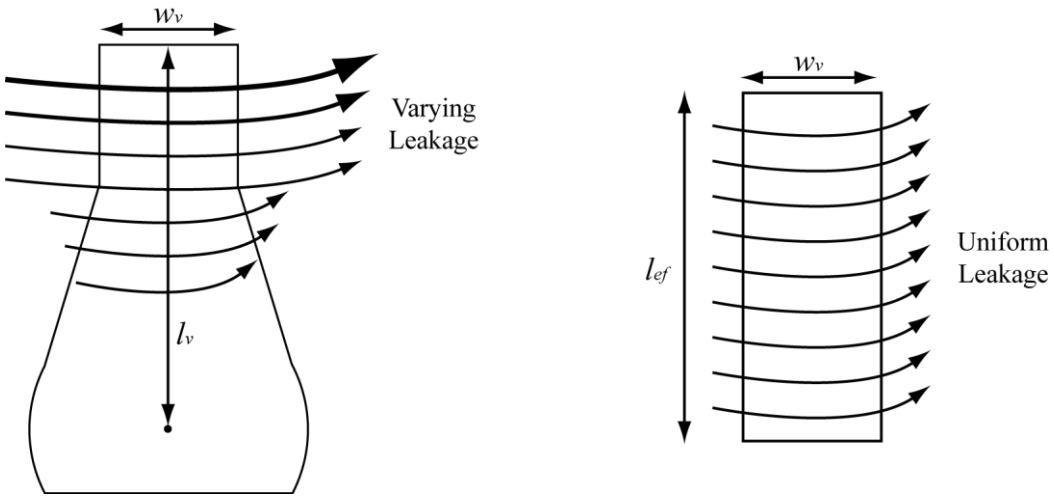

(a): Varying Leakage Due to Bulbous Shape

(b): Equivalent Uniform Leakage Through Rectangular Vane

Figure 5.19: Uniform Rectangular Vane Leakage

5.5.4 CFD Simulation Model and Validation

Yanagisawa and Shimizu [112] provided the validated analytical solution for the leakage through the radial clearance of the rolling piston compressor. As this leakage path is similar to that of the RV, the CFD model used to calculate the RV leakage will first be checked against the analytical model to ascertain its applicability and accuracy for leakage modelling. The assumptions used for the study are similar to that of the analytical model presented by Yanagisawa and Shimizu [112]:

- Pressure, temperature, density remains constant in the respective suction and compression chambers
- There is no heat transfer during the leakage process and the temperatures of the fluid in both chambers are similar
- The walls are stationary
- Steady-state flow

The dimensions of the prototype will be used for the CFD case study except for the clearance gap which is adjusted to 0.1 mm to get an achievable aspect ratio for the mesh. The CFD simulation was done using the ANSYS Workbench 16.0 software with ICEM meshing and Fluent subcomponents. The realizable *k-ε* turbulence flow model was used for the CFD solver and the details on the governing equations can be found with reference to Shih, et al. [113]. These equations are reproduced in Appendix A-2 for ease of reference.

The revised dimensions and operating conditions for the simulation study are presented in Table 5.1. The geometry used in the simulation is found in Figure 5.20.

Table 5.1: CFD Validation Study Parameters

Component	**Value**
Cylinder radius, mm	50.0
Rotor radius, mm	42.5
Cylinder length, mm	23.0
Radial clearance gap, mm	0.1
Operating Conditions	
Working fluid	Air
Suction chamber pressure, bar (abs)	1.0
Compression chamber pressure, bar (abs)	2.0
Temperature, °C	27.0

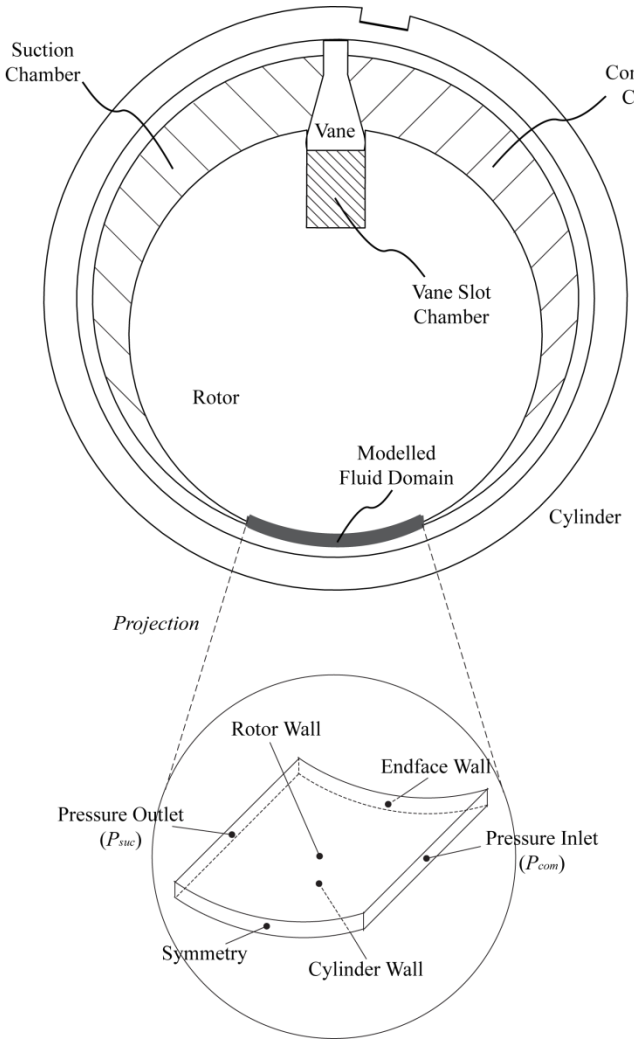

Figure 5.20: Radial Clearance Leakage Fluid Domain and Boundary Conditions

Based on the dimensions and operating conditions in Table 5.1, the analytical solution for the leakage is calculated using the method discussed in Section 5.5.1 and compared to the solution obtained from the CFD simulation. The comparison in Table 5.2 shows that the CFD simulation is accurate with an error of 2.3%. With this result, it can be concluded that the CFD model used is appropriate for modelling the leakage flow within the RV compressor and will be extended for use in the other leakage paths, namely the vane endface and rotor endface leakages.

Table 5.2: CFD Simulation Comparison

Theoretical Leakage Mass Flow, kg s^{-1}	Simulated Leakage Mass Flow, kg s^{-1}	Error, %
5.55×10^{-4}	5.68×10^{-4}	2.3

5.5.5 Vane Endface Leakage CFD Study

To evaluate the leakage mass flow through the vane endface, the vane endface geometry is modelled as shown in Figure 5.21. Similar to that of the radial clearance leakage, the endface clearance gap is set at 0.10 mm. Note that there are actually two leakage modes – the first from the compression chamber to the suction chamber, and the second from the compression chamber to the vane slot chamber.

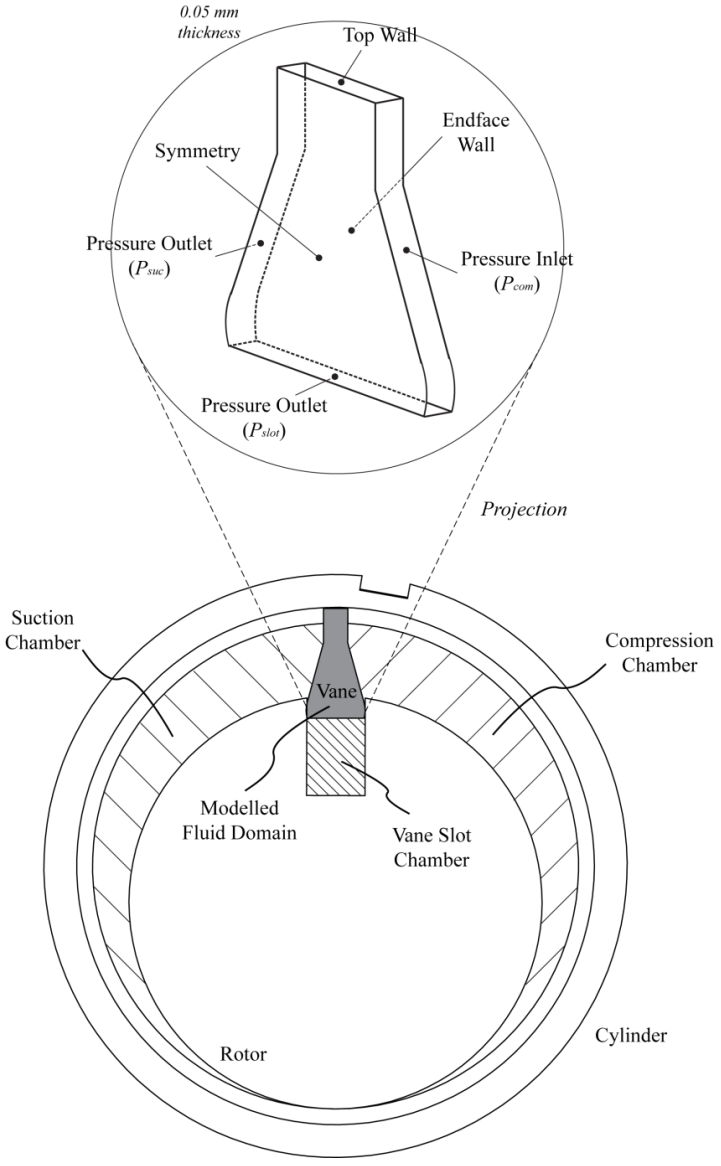

Figure 5.21: Vane Endface Leakage Fluid Domain and Boundary Conditions

The leakage flow is calculated with CFD for a variety of different pressure ratios while keeping the suction chamber pressure constant at 1 bar (abs). The slot chamber pressure is kept

constant and assumed to be the average of the suction and compression chamber pressures for each instance. All other assumptions remain unchanged with the temperature in each chamber kept constant at 27°C. The change in mass flow leakages across the vane endface gap with respect to the pressure ratio is presented in Figure 5.22.

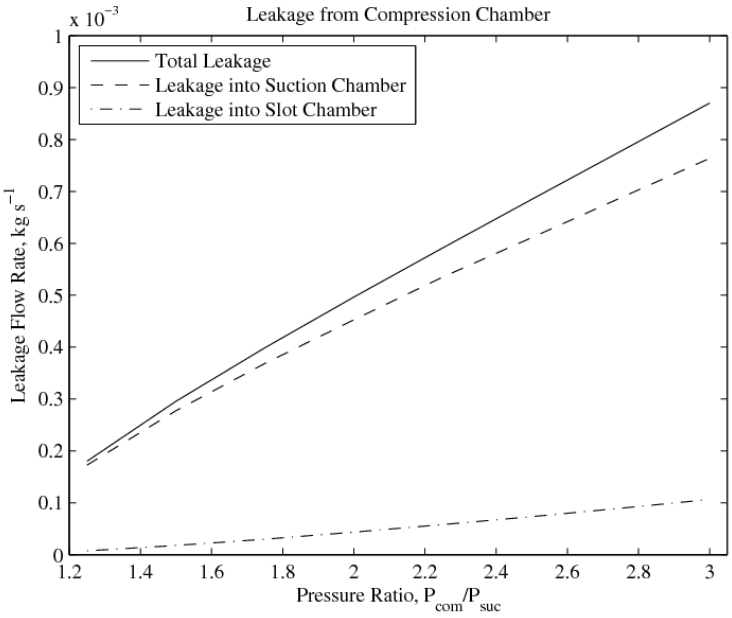

Figure 5.22: Vane Endface Leakage Mass Flow Rate

The total leakage flow rate for each pressure ratio evaluated by CFD simulation (3D leakage flow rate) is divided by the respective Fanno flow model solution (2D leakage flow rate) to produce the equivalent channel width (or vane length) as illustrated in Figure 5.19. These values are shown in Figure 5.23.

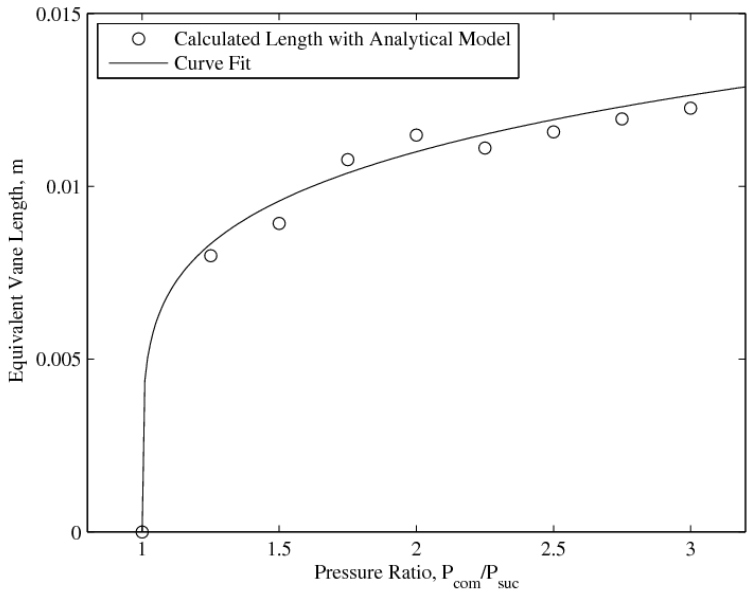

Figure 5.23: Equivalent Vane Length for Total Vane Endface Leakage

The equivalent vane length (leakage flow channel width) was found to vary with the power of the pressure ratio of the compression to suction chamber. To this end, the calculated equivalent lengths can be curve fitted with the relation as expressed in Equation (5.74).

$$l_{ef,vane} = 0.0110\left(\frac{P_{com}}{P_{suc}} - 1\right)^{0.2} \tag{5.74}$$

The proportion of leakage mass flow into the vane slot as compared to the leakage mass flow into the suction chamber is presented in Figure 5.24. It was found that approximately 90% of the leakage from the compression chamber goes into the suction chamber and the remaining 10% into the vane slot chamber. This ratio applies when the vane slot chamber is at the mean of the two pressures in the compression and suction chambers.

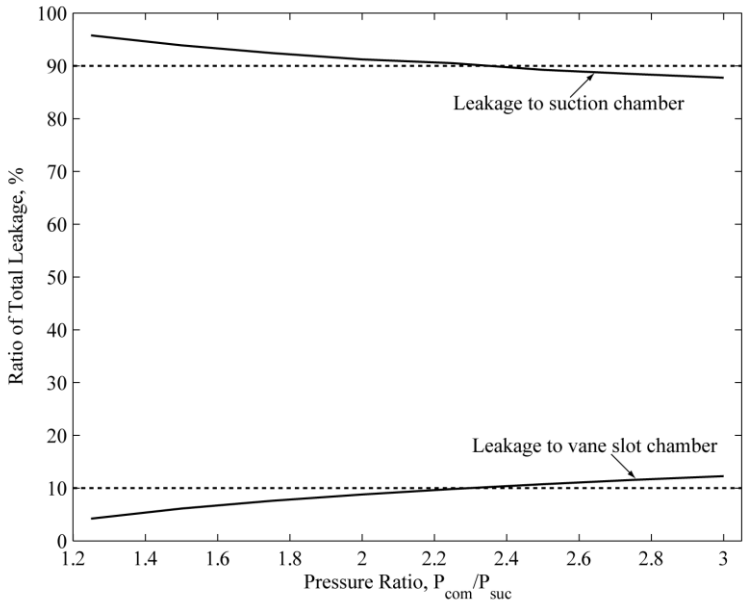

Figure 5.24: Ratio of Vane Endface Leakages

5.5.6 Rotor Endface Leakage CFD Study

Similarly, an analytical solution for the leakage through the rotor endface is not available due to the geometry of the flow path and this is further complicated by the constant rotation of the vane. To this end, a CFD study is also carried out for the rotor endface utilising the same leakage model and assumptions as Section 5.5.4. The operating conditions are the same as those presented in Table 5.1 with the vane slot chamber set at the mean of the suction and compression chamber. The geometry of the rotor endface used for the model is shown in Figure 5.25 with an endface gap of 0.10 mm.

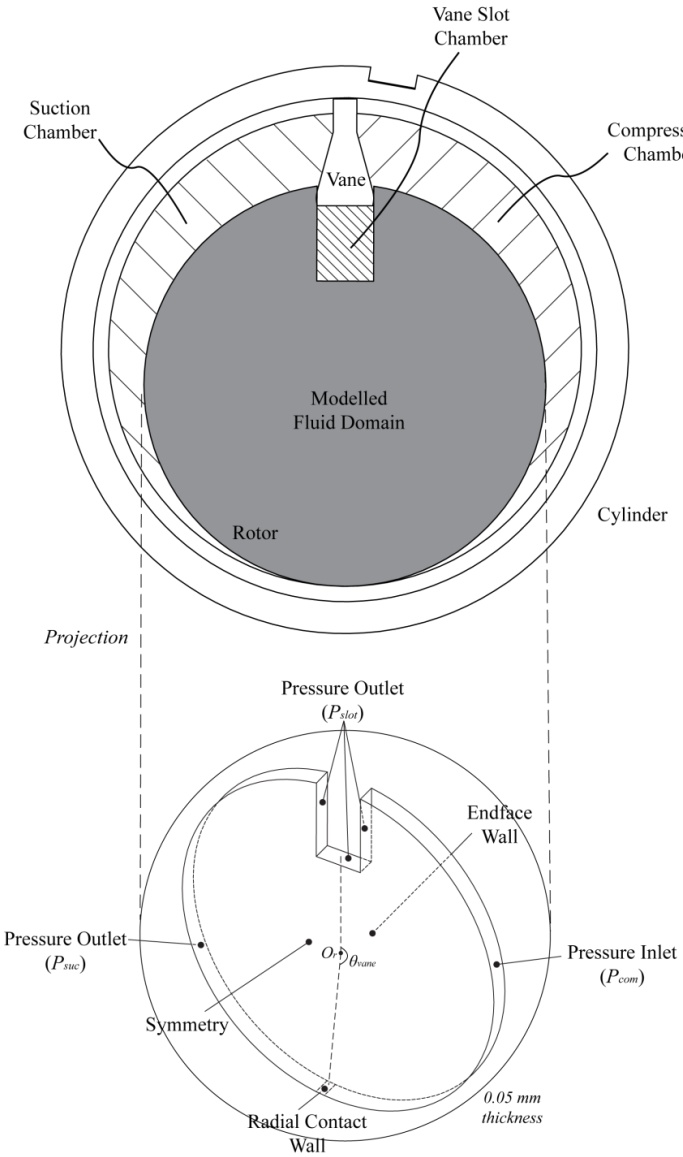

Figure 5.25: Rotor Endface Leakage Fluid Domain and Boundary Conditions

The variation of the rotor endface leakage is more complex compared to that of the vane endface leakage – the leakage flow rate not only varies with pressure ratio, but also with the angle of the vane which separates the compression and suction chambers and affects the leakage flow path geometry. The first part of this study shall deal with the variation of leakage flow rate with respect to the vane rotation.

Due to the constant variation of the geometry due to vane rotation, several instances of the flow are emulated for different vane rotation angles at intervals of 30°. The pressure ratio between the compression and suction chambers is kept constant at 2 for all instances while the

pressure in the vane slot chamber is maintained at the average pressure between the compression and suction chambers.

The change in leakage flow due to vane rotation is shown in Figure 5.26. Generally, maximum leakage occurs at 180° vane angle and decreases during the compression process as the vane angle decreases. Interestingly, the leakage into the vane slot chamber would decrease until there is net flow out of the vane slot chamber and into the suction chamber instead.

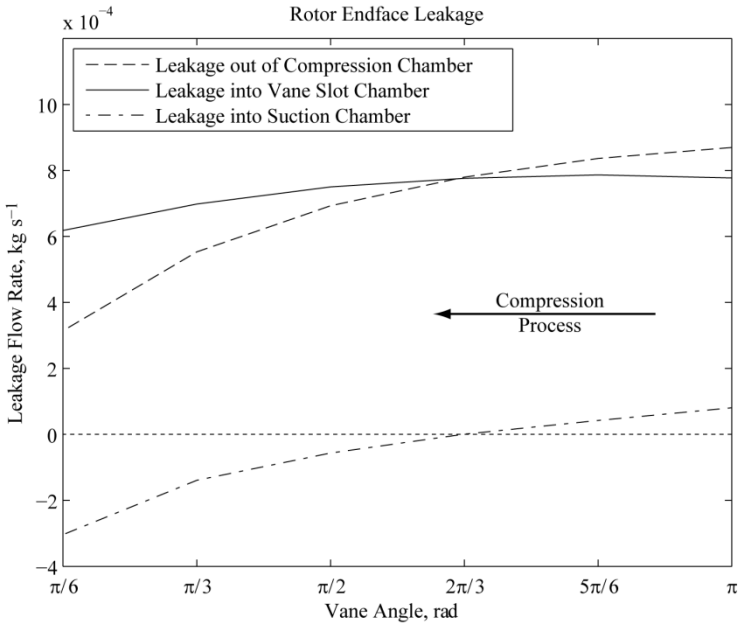

Figure 5.26: Rotor Endface Leakage Mass Flow Rate with Pressure Ratio of Two

The equivalent flow path for theoretical modelling of the rotor endface leakage shall be similar to that of the vane endface leakage presented in Section 5.5.5 – the leakage through the rotor endface shall be evaluated as if it was leaking through a rectangular shaped endface as presented in Figure 5.19(b). The channel length shall be assumed to be similar to that of the vane (5 mm) since it is considered the shortest separation distance between the suction and compression chambers. An equivalent channel width shall then be determined from the CFD data for use in the calculation of the leakage flow rate.

The leakage flow rates at the compression chamber evaluated by CFD simulation are divided by the Fanno flow model solution to obtain the equivalent channel width (or vane length) at different vane angles. The variation of the equivalent vane length with respect to

vane angle for the leakage path can be approximated using a 2nd order polynomial fit with vane angle as the variable shown in Figure 5.27.

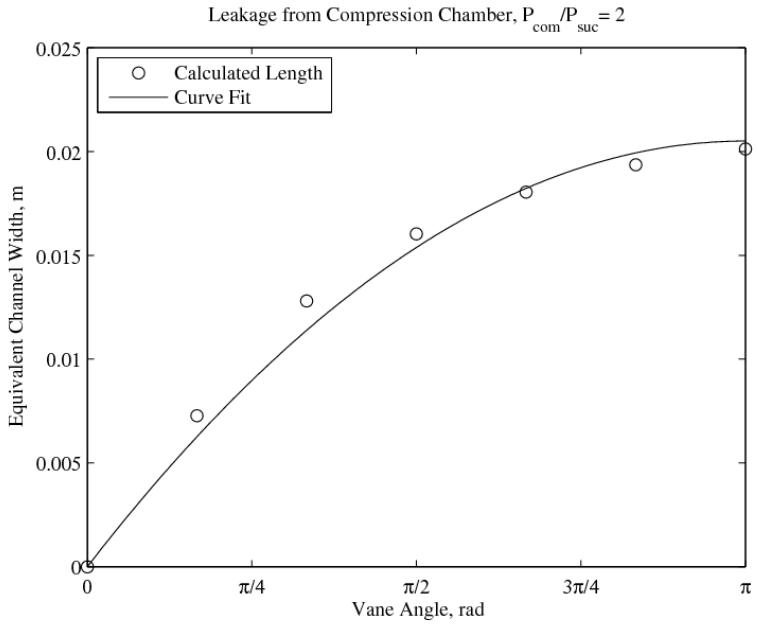

Figure 5.27: Rotor Endface Leakage Curve Fit

Equation (5.75) shows the polynomial function used for the curve fit for the compression chamber leakage. Note that the expression would result in maximum leakage flow rate at a vane angle of 180° consistent with that of CFD results and zero leakage flow at a vane angle of 0°.

$$l_{ef,com} = 0.0205\left[\frac{\theta_r}{\pi}\left(2 - \frac{\theta_r}{\pi}\right)\right] \tag{5.75}$$

The expression for the equivalent channel width with respect to vane angle in Equation (5.75) is only valid for a pressure ratio of 2. Hence, the next step of this study would be to chart the variation of the leakage flow rates with respect to different pressure ratios between the compression and suction chambers.

Since maximum leakage flow rate occurs at a vane angle of 180°, this flow geometry shall be utilised for all the CFD simulation cases while varying the pressure ratios between the compression and suction chambers. Similar to the other CFD cases, the pressure in vane slot chamber is kept at the mean of the compression and suction chamber. The change in leakage

flow rates through the rotor endface with respect to different pressure ratios is plotted in Figure 5.28.

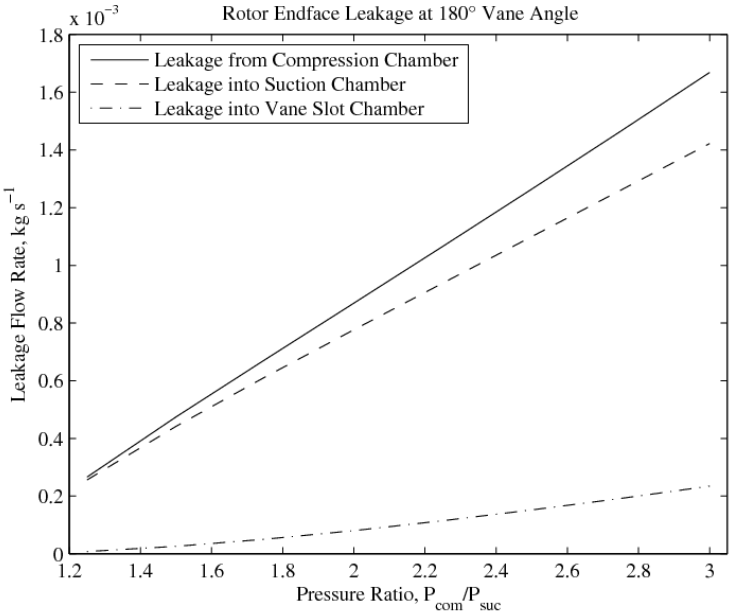

Figure 5.28: Rotor Endface Leakage Mass Flow Rate with Different Pressure Ratios

The variation of the leakage mass flow with respect to different pressure ratios for the rotor endface leakage was found to be very similar to that of the vane endface leakage. In a similar fashion, the total leakage from the compression chamber for each pressure ratio evaluated by CFD is divided by the Fanno flow model solution to produce the equivalent channel length and these points are plotted in Figure 5.29.

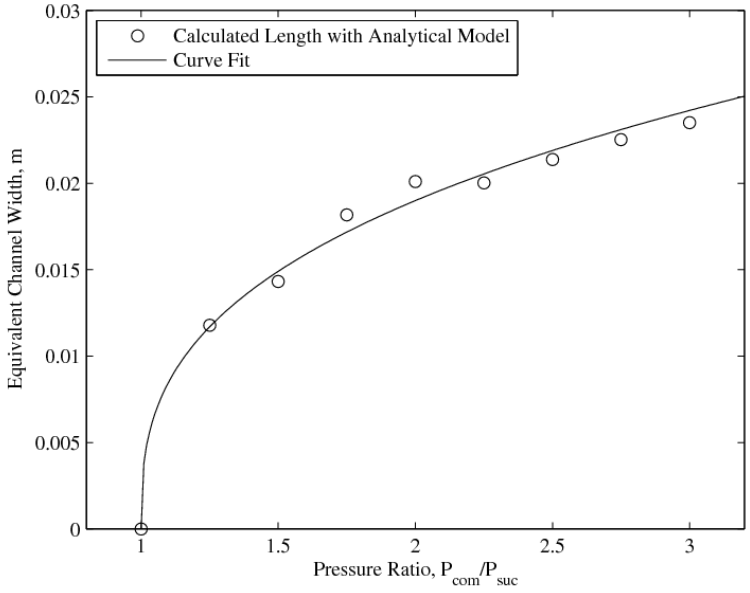

Figure 5.29: Equivalent Channel Width for Rotor Endface Leakage

Similarly, the equivalent channel width (leakage flow channel width) was found to vary with the power of the pressure ratio of the compression to suction chamber. To this end, the calculated equivalent lengths can be curve fitted with the relation as expressed in Equation (5.76).

$$l_{ef,enf} = 0.0190\left(\frac{P_{com}}{P_{suc}} - 1\right)^{0.35} \tag{5.76}$$

Last but not least, with the variation of the equivalent leakage channel width with respect to the different vane angles and pressure ratios known, the findings from both studies can be combined into a single expression as shown in Equation (5.77).

$$l_{ef,enf,com} = 0.0190\left(\frac{P_{com}}{P_{suc}} - 1\right)^{0.35}\left[\frac{\theta_r}{\pi}\left(2 - \frac{\theta_r}{\pi}\right)\right] \tag{5.77}$$

Understandably, the effect of vane angle variation in Equation (5.77) is based on the CFD study for a pressure ratio of 2 and may not be applicable for other pressure ratios. However, it would be computationally intensive to model all the different pressure ratios with different vane angle geometries. Furthermore, strictly speaking, the pressure in the vane slot chamber was kept at a mean value between the compression and suction chamber pressures which is not

truly representative of the characteristics in the working chambers during actual compression operation. Hence, the CFD studies carried out in this section and Section 5.5.5 can only serve to model the trend of leakage variation in the RV compressor. This will be further elaborated in Section 5.5.7.

5.5.7 Equivalent Leakage Flow Channel Width for Practical Operation

As the CFD studies carried out in Sections 5.5.5 and 5.5.6 are only for instances in which the vane slot chamber pressure is of the average value between the compression and suction chamber pressures, the correlations for calculation of the equivalent channel width in Equations (5.74) and (5.77) would not be truly representative of leakage modelling in the actual RV compressor prototype during operation.

The amount of leakage from the compression chamber into the suction and vane slot chamber would depend on the vane slot chamber pressure as well. Figure 5.30 shows the leakage flow rate across the vane endface when the vane slot chamber is set at the same pressure as the suction chamber.

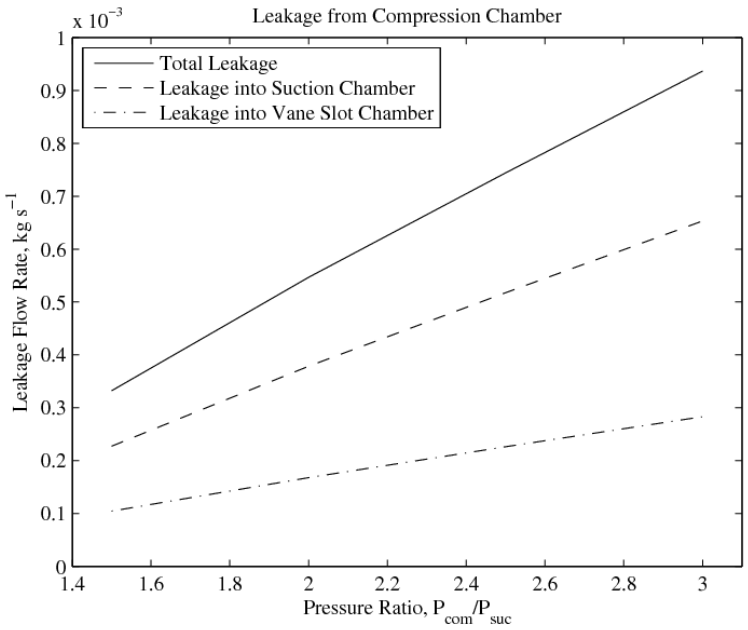

Figure 5.30: Vane Endface Leakage Mass Flow Rate with $P_{slot} = P_{suc}$

The total amount of leakage is now higher than that shown in Figure 5.22 and the ratio of the total leakage that flows into the vane slot chamber has also increased to approximately

30%. Hence, the ratio of the total leakage from the compression chamber into the vane slot chamber is not constant and decreases as the pressure difference gets smaller.

For convenience, it is assumed that the ratio of leakage for the vane slot chamber through the vane endface would be constant at 10% regardless of the pressure difference. This is the same ratio as if the vane slot chamber pressure is at the mean of the pressures between the compression and suction chamber presented in Section 5.5.5.

A curve fit of the equivalent leakage flow channel width for the total leakage across the vane endface would yield a similar expression as that presented in Equation (5.74) albeit with different coefficients.

For the rotor endface leakage, another CFD simulation was carried out. This time, the vane angle was set at 120° and the pressure ratio between the compression and suction chambers was varied. The pressure in the vane slot chamber was still kept at the average of the compression and suction chambers. The change in leakage flow rate with pressure ratio for the rotor endface leakage this time round is plotted in Figure 5.31.

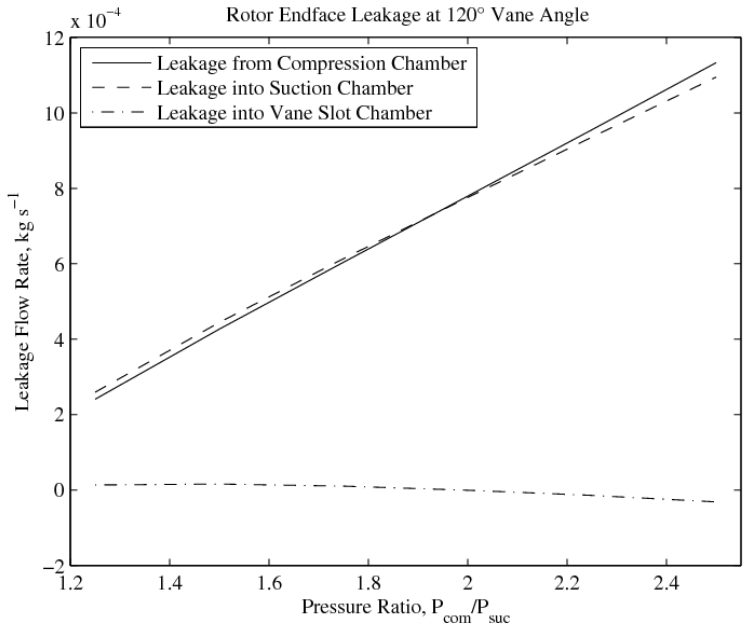

Figure 5.31: Rotor Endface Leakage with Different Pressure Ratios at 120° Vane Angle

For the rotor endface leakage this time round at 120° vane angle with different pressure ratios, the flows to and from the vane slot chamber is approximately zero. A curve fit for

equivalent channel width of the total leakage flow at this instance of 120° vane angle for the different pressure ratios would result in a similar expression as that of Equation (5.76) but with different coefficients.

On the other hand, if the effects of vane angle and pressure ratio were taken into account, the variation of the equivalent leakage flow channel length for the compression chamber through the rotor endface with the pressure ratio would be in a form similar to that shown in Equation (5.77).

For the amount of leakage flow into the vane slot chamber through the rotor endface, it varies according to the different pressure ratios between all three chambers and also the vane angle, which change rapidly during practical operation. Hence, for convenience, it will be assumed that the leakage flow into the vane slot chamber through the rotor endface is also a proportion of the main leakage flow between the compression and suction chamber. Similar to that of the vane endface leakage, the proportion of leakage for the vane slot chamber through the rotor endface would be assumed to be constant at 10%.

In reality, the walls of the leakage channels are moving and the leakage flow rates are not steady-state in nature and therefore vary during practical operation. To this end, the CFD study can only be used to determine the trend of leakage variation for the individual flow paths with different pressure ratios, and also with rotation angle in the case for the rotor endface leakage. The exact leakage flow rates during practical operation would be different from those obtained from the CFD study.

To this end, the variation of the equivalent flow channel width for modelling the vane and rotor endface leakage paths between the compression and suction chambers would be of the forms expressed as shown in Equations (5.78) and (5.79), respectively. In addition, 10% of the leakage flow computed for each path is assumed to flow into the vane slot chamber as long as there is a pressure difference for flow to occur.

$$l_{ef,enf} = C_1 \left(\frac{P_{com}}{P_{suc}} - 1 \right)^{C_2} \quad , \qquad 0 < C_2 < 1 \tag{5.78}$$

$$l_{ef,enf,rot} = C_3 \left(\frac{P_{com}}{P_{suc}} - 1 \right)^{C_4} \left[\frac{\theta_r}{\pi} \left(2 - \frac{\theta_r}{\pi} \right) \right] \quad , \qquad 0 < C_4 < 1 \tag{5.79}$$

Note that the set of coefficients C_1 to C_5 would be determined with data obtained from prototype measurement that will be presented in Chapter 8. A fixed set of values for the coefficients in Equations (5.78) and (5.79) are adapted from the curve fit coefficients in Equations (5.74) and (5.77) such that the same set of values is able to model the internal leakage flow in the RV compressor prototype for different operating conditions.

5.6 Concluding Remarks

The thermodynamics model has been presented in this chapter with special considerations for heat transfer mechanisms and internal leakages. A summary of this chapter is as follows:

- The full thermodynamics model for the working chambers have been formulated by treating each working chamber as a separate control volume.
- The heat transfer correlation by Tan and Ooi [16] is used for modelling the heat transfer between the working fluid and chamber walls. New expressions for the hydraulic diameters and characteristic velocities for the suction and compression chamber have been adapted from the new geometry of the vane and vane slot design.
- The hydraulic diameter and characteristic velocity for the vane slot chamber are similar to that of the reciprocating compressor as the motion of the vane in the vane slot chamber is similar to that of a reciprocating piston.
- The surface areas of the working chamber walls are presented with a separate distinction for the rotor and cylinder walls since they will be of different materials and will not share the same wall temperature.
- The suction and discharge flow models are also presented with care taken to formulate exactly the flow areas for the suction and discharge ports for accurate modelling.
- Due to the absence of lubricants that can help to plug the clearances between the working chambers, internal leakage is expected to be significant for the compressor prototype.
- Orifice flow model is used for modelling the internal leakage through the vane tip.

- Radial clearance leakage is modelled as that of a Fanno flow through a convergent duct.
- Similarly, vane endface clearance leakage is modelled as that of a Fanno flow, but without a convergent duct.
- As the leakage flow geometries at the vane and rotor endfaces are not of a uniform shape, CFD simulation was carried out to quantify these leakage flow rates.
- Based on the CFD data, equivalent flow channel paths with uniform length and width are assumed and used with the Fanno flow model to match the leakage flow rates.
- The equivalent flow channel lengths for both the vane endface and rotor endface are fixed at 5 mm, the narrowest part of the vane that separates the compression and suction chambers. The width will be computed based on the leakage flow rate obtained from the CFD data and Fanno flow model solution.
- The proportion of leakage into the vane slot chamber through the vane endface was found to be not more than 30% of the total leakage flow rate from the compression chamber.
- The proportion of mass that enters the vane slot chamber during internal leakage between the compression and suction chamber is assumed to be 10% as long as there is a pressure difference that enables flow into or out of the vane slot chamber.
- The leakage flow rate through the endface is maximum at a vane angle of 180° and would decrease during the compression process as the vane angle gets smaller.
- Based on the fixed channel length, the width of the leakage flow channel varies with the power of the pressure ratio between the compression and suction chambers in the forms according to Equations (5.78) and (5.79) for the vane endface and rotor endface leakage, respectively.

6 Kinematics and Dynamics Models

After presenting the thermodynamics model for the working fluid processes in the compressor, this chapter will go into the kinematics and dynamics model of the compressor. This chapter will first present the kinematics model of the various components in the RV prototype for use in the dynamics model before proceeding to further discussion with the dynamics model. The model can then be used to characterise the rotational vibration for most generic RV mechanisms which has not been investigated before and will be useful for future design evaluations.

The relations derived from the geometric model in Chapter 3 will be used and the same assumption will apply – the components have perfect geometric dimensions with no tolerances. Lagrangian mechanics is used for the modelling of the RV mechanism, as it is a very flexible and comprehensive approach with considerations for additional components. The fixed vane RV mechanism with the bush component will be used for the modelling as it contains the most components and the derived system of equations can be reduced to model the other design variants by simply removing the bush component terms.

6.1 Kinematics Model

For the RV prototype, the cylinder is connected to the motor and is the main driving component for the compressor. Therefore, the rotor motion is dependent on that of the cylinder. The rotational speed of the rotor and vane sliding speed in the slot can hence be expressed in terms of the cylinder rotation speed as shown in Equations (6.1) and (6.2), respectively.

$$\dot{\theta}_r = \frac{d\theta_r}{dt} = \frac{d\theta_r}{d\theta_c} \cdot \frac{d\theta_c}{dt} \tag{6.1}$$

$$\frac{dr_{vr}}{dt} = \frac{dr_{vr}}{d\theta_c} \cdot \frac{d\theta_c}{dt} \tag{6.2}$$

The acceleration of the rotor and vane can then be expressed as shown in Equations (6.3) and (6.4), respectively.

$$\ddot{\theta}_r = \ddot{\theta}_c \frac{d\theta_r}{d\theta_c} + \dot{\theta}_c^2 \frac{d^2\theta_r}{d\theta_c^2} \tag{6.3}$$

$$\frac{d^2 r_{vr}}{dt^2} = \ddot{\theta}_c \frac{dr_{vr}}{d\theta_c} + \dot{\theta}_c^2 \frac{d^2 r_{vr}}{d\theta_c^2} \tag{6.4}$$

Note that these expressions for the speed and rotation of the rotor and vane are similar in form and can also be extended to that of the bush component if desired. Furthermore, for design variants in which the rotor is the main driving component and the cylinder is the dependent, the same principles apply by simply changing the respective subscripts and adapting the new derivatives from the geometric model. This concludes the kinematics model for the RV mechanism and the dynamics model shall be presented next.

6.2 Lagrangian Mechanics

Due to the multitude of parts for the RV mechanism with bush components, the conventional Newtonian approach might be too complex involving a free-body diagram for each of the individual components. In order to simplify the analysis, Lagrangian mechanics is used instead.

Lagrangian mechanics is a form of analytical mechanics which focuses on the dynamics of the entire system instead of separating the system into individual components [114]. The general form of Lagrange's equations [115] is presented in Equation (6.5).

$$\frac{d}{dt}\left(\frac{\partial L}{\partial \dot{q}_j}\right) - \frac{\partial L}{\partial q_j} = F_j + \sum_k^n \lambda_k(t) \frac{\partial f_k}{\partial q_j} \quad \begin{cases} j = 1,2,\dots,m \\ k = 1,2,\dots,n \end{cases} \tag{6.5}$$

L is defined as the Lagrangian of the system which is the total energy of the system and q represents the generalised coordinates of the system. Note that there are no fixed units for the Lagrange multiplier λ or holonomic constraint f since their units are interdependent. F represents the non-conservative forces acting on the system such as friction or power input.

Assuming that the RV components undergo purely rotational motion with no translational motion within the bearings, the Lagrange equation in Equation (6.5) can be adapted for a rotational system as shown in Equation (6.6) by replacing the non-conservative

force term with that of a torque term. For the RV compressor, these non-conservative torques arise from the work done to the fluid, friction losses and motor work input.

$$\frac{d}{dt}\left(\frac{\partial L}{\partial \dot{q}_j}\right) - \frac{\partial L}{\partial q_j} = T_j + \sum_{k}^{n} \lambda_k(t) \frac{\partial f_k}{\partial q_j} \quad \begin{cases} j = 1,2,\dots,m \\ k = 1,2,\dots,n \end{cases} \tag{6.6}$$

6.3 RV Mechanism Dynamics

6.3.1 Vane Attached to Cylinder

Figure 6.1 illustrates the geometric relations between the cylinder, rotor and bush components for the generic RV mechanism in which the vane is attached to the cylinder. The rotation angles of each of the components and the displacement angle of the bush component due to rotational translation are designated as the generalised coordinates for the RV mechanism. They are represented by θ_c, θ_r, θ_b, ϕ_b for the cylinder, rotor, bush and displacement angle respectively.

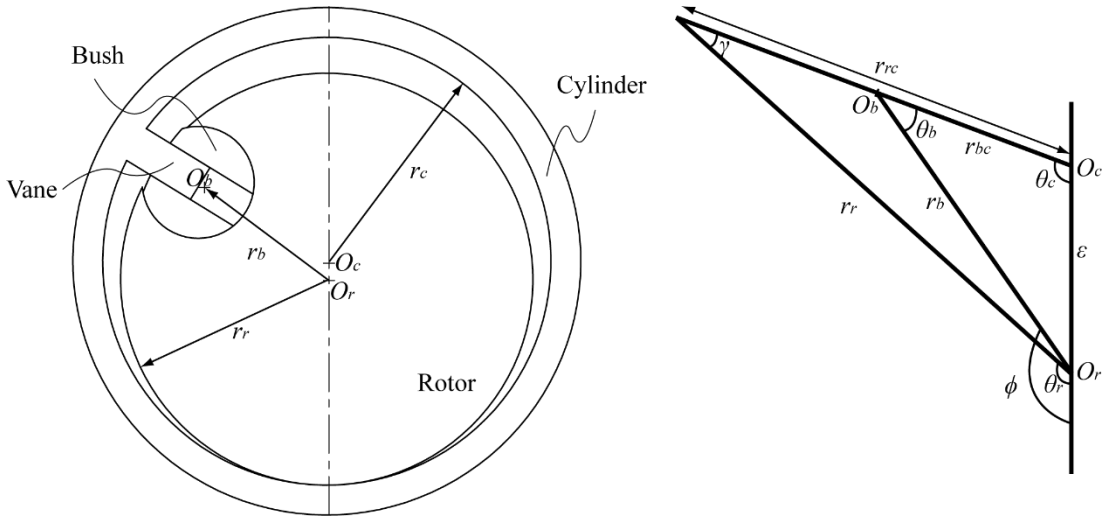

(a): Cross-section **(b): Geometric Relations**

Figure 6.1: Vane Attached to Cylinder Geometric Relations

The Lagrangian of the system is expressed as shown in Equation (6.7) with no potential energy as the bush component undergoes rotational translation in the horizontal plane.

$$L = \frac{1}{2}\left(I_c\dot{\theta}_c^2 + I_r\dot{\theta}_r^2 + I_b\dot{\theta}_b^2 + m_b d_b \dot{\phi}^2\right) \tag{6.7}$$

The non-conservative torques acting on each component are summarised as shown in Equation (6.8). Note that there is a set of separate friction torques for each generalised coordinate rather than for each component. The fluid torque and motor torque acts on the cylinder since the cylinder is the main driving component.

$$\left.\begin{aligned} T_{n,\theta_c} &= T_m + T_g - T_{f,\theta_c} \\ T_{n,\theta_r} &= -T_{f,\theta_r} \\ T_{n,\theta_b} &= -T_{f,\theta_b} \\ T_{n,\phi} &= -T_{f,\phi} \end{aligned}\right\} \tag{6.8}$$

Based on the geometric relations in Figure 6.1, the set of holonomic constraints for the system in Equation (6.9) are obtained.

$$\left.\begin{aligned} \frac{\sin\theta_c}{r_r} = \frac{\sin\theta_r}{r_{rc}}, &\quad \rightarrow f_1 = \frac{\sin\theta_c}{r_r} - \frac{\sin\theta_r}{r_{rc}} = 0 \\ \frac{\sin\theta_c}{r_b} = \frac{\sin\phi}{r_{bc}}, &\quad \rightarrow f_2 = \frac{\sin\theta_c}{r_b} - \frac{\sin\phi}{r_{bc}} = 0 \\ \frac{\sin\theta_c}{r_b} = \frac{\sin\theta_b}{\varepsilon}, &\quad \rightarrow f_3 = \frac{\sin\theta_c}{r_b} - \frac{\sin\theta_b}{\varepsilon} = 0 \end{aligned}\right\} \tag{6.9}$$

The set of Lagrange equations for the vane on cylinder RV mechanism can then be formulated as shown in Equation (6.10) which describe the motion for each of the generalised coordinate.

$$\left.\begin{aligned} I_c\ddot{\theta}_c &= T_m + T_g - T_{f,c} + \lambda_1\frac{\partial f_1}{\partial\theta_c} + \lambda_2\frac{\partial f_2}{\partial\theta_c} + \lambda_3\frac{\partial f_3}{\partial\theta_c} \\ I_r\ddot{\theta}_r &= -T_{f,r} + \lambda_1\frac{\partial f_1}{\partial\theta_r} \\ I_b\ddot{\theta}_b &= -T_{f,\theta_b} + \lambda_3\frac{\partial f_3}{\partial\theta_b} \\ m_b d_b\ddot{\phi} &= -T_{f,\phi} + \lambda_2\frac{\partial f_2}{\partial\phi} \end{aligned}\right\} \tag{6.10}$$

Equations (6.9) and (6.10) form a set of seven simultaneous equations that should be solved for each of the generalised coordinate and Lagrange multiplier. However, by substitution, the Lagrange multipliers can be eliminated and the set of dynamics equations in Equation (6.10) can be reduced to a single equation describing the entire cylinder-rotor assembly for the RV mechanism as shown in Equation (6.11) with the cylinder rotation angle

being the main parameter of interest. The friction torques for each generalised coordinate has been combined into a single term T_f which represents the total friction torque for the assembly.

$$I_c\ddot{\theta}_c = T_m + T_g - \frac{d\theta_r}{d\theta_c}\left(I_r\ddot{\theta}_r\right) - \frac{d\phi}{d\theta_c}\left(m_b d_b \ddot{\phi}\right) - \frac{d\theta_b}{d\theta_c}\left(I_b\ddot{\theta}_b\right) - T_f \tag{6.11}$$

6.3.2 Vane Attached to Rotor

As there are variants of the RV mechanism in which the vane may be attached to the rotor [20], the dynamics of this design variant will be covered in this section for comprehensiveness. Figure 6.2 shows the geometric relations for the components in the RV mechanism in which the vane is attached to the rotor.

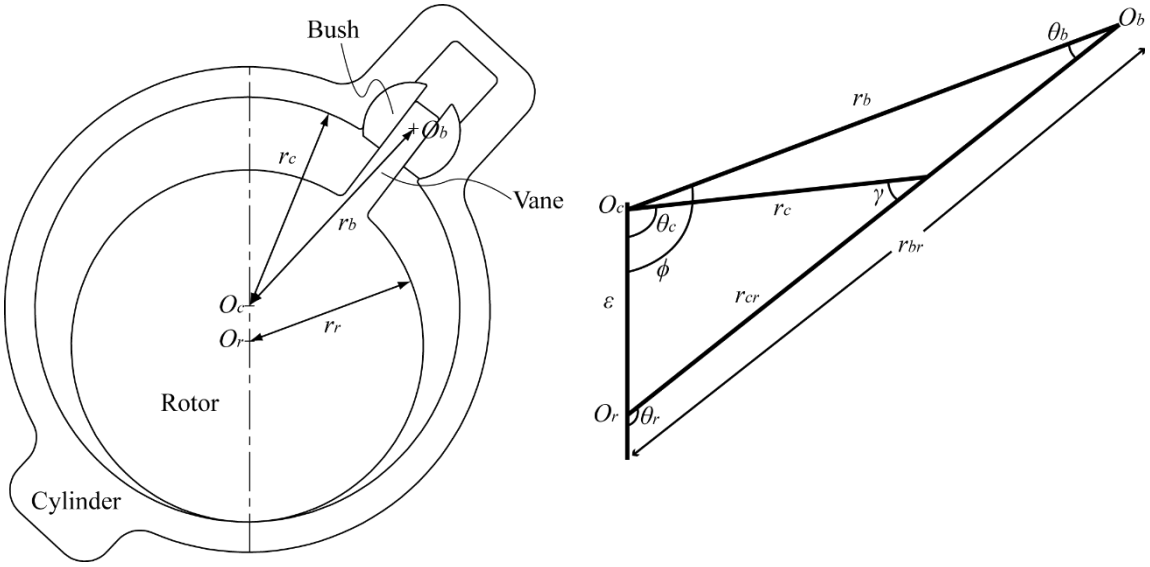

(a): Cross-section **(b): Geometric Relations**

Figure 6.2: Vane Attached to Rotor Geometric Relations

The Lagrangian of the system is the same as that of the vane attached to the cylinder as shown in Equation (6.12). For the non-conservative torques, the gas torque and motor torque now act on the rotor as it is the main driving component. These non-conservative torques are expressed in Equation (6.13).

$$L = \frac{1}{2}\left(I_r\dot{\theta}_r^2 + I_c\dot{\theta}_c^2 + I_b\dot{\theta}_b^2 + m_b r_{br}\dot{\phi}^2\right) \tag{6.12}$$

$$\left.\begin{aligned} T_{n,\theta_r} &= T_m + T_g - T_{f,\theta_r} \\ T_{n,\theta_c} &= -T_{f,\theta_c} \\ T_{n,\theta_b} &= -T_{f,\theta_b} \\ T_{n,\phi} &= -T_{f,\phi} \end{aligned}\right\} \tag{6.13}$$

The set of holonomic constraints for the vane on rotor RV mechanism derived from Figure 6.2 are shown in Equation (6.14).

$$\left.\begin{aligned} \frac{\sin\theta_r}{r_c} = \frac{\sin\theta_c}{r_{cr}}, \quad &\rightarrow f_1 = \frac{\sin\theta_r}{r_c} - \frac{\sin\theta_c}{r_{cr}} = 0 \\ \frac{\sin\theta_r}{r_b} = \frac{\sin\phi}{r_{br}}, \quad &\rightarrow f_2 = \frac{\sin\theta_r}{r_b} - \frac{\sin\phi}{r_{br}} = 0 \\ \frac{\sin\theta_r}{r_b} = \frac{\sin\theta_b}{\varepsilon}, \quad &\rightarrow f_3 = \frac{\sin\theta_r}{r_b} - \frac{\sin\theta_b}{\varepsilon} = 0 \end{aligned}\right\} \tag{6.14}$$

The set of Lagrange equations for the RV mechanism can then be written as shown in Equation (6.15). Apart from the generalised coordinates for the cylinder and rotor, the bush component stays the same.

$$\left.\begin{aligned} I_r\ddot{\theta}_r &= T_m + T_g - T_{f,\theta_r} + \lambda_1\frac{\partial f_1}{\partial\theta_r} + \lambda_2\frac{\partial f_2}{\partial\theta_r} + \lambda_3\frac{\partial f_3}{\partial\theta_r} \\ I_c\ddot{\theta}_c &= -T_{f,\theta_c} + \lambda_1\frac{\partial f_1}{\partial\theta_c} \\ I_b\ddot{\theta}_b &= -T_{f,\theta_b} + \lambda_3\frac{\partial f_3}{\partial\theta_b} \\ m_b r_{br}\ddot{\phi} &= -T_{f,\phi} + \lambda_2\frac{\partial f_2}{\partial\phi} \end{aligned}\right\} \tag{6.15}$$

The dynamics equation for the entire RV assembly can be written as shown in Equation (6.16) with the rotor rotation angle as the main parameter instead.

$$I_r\ddot{\theta}_r = T_m + T_g - \frac{d\theta_c}{d\theta_r}\left(I_c\ddot{\theta}_c\right) - \frac{d\phi}{d\theta_r}\left(m_b d_b\ddot{\phi}\right) - \frac{d\theta_b}{d\theta_r}\left(I_b\ddot{\theta}_b\right) - T_f \tag{6.16}$$

Equations (6.11) and (6.16) describe the two main design variants of the RV mechanism. These equations can be easily adapted for the other design variants by removing the bush terms when necessary and substituting the appropriate geometrical relations and derivatives. The next

Section 6.3.3 will discuss the dynamics equation for the RV compressor prototype and Chapter 9 validates the dynamics equation for that of an RV expander with experimental measurements.

6.3.3 Compressor Shell Housing

The compressor shell housing is only a single component and to this end, Newtonian mechanics would be suited for formulating the dynamics equation for modelling the angle of twist of the housing. Figure 6.3 shows the cross-section of the housing shell and the torques acting on it. Note that these torques are friction counter torques at the bearings and that the discharge fluid exerts a drag force on the housing shell as well.

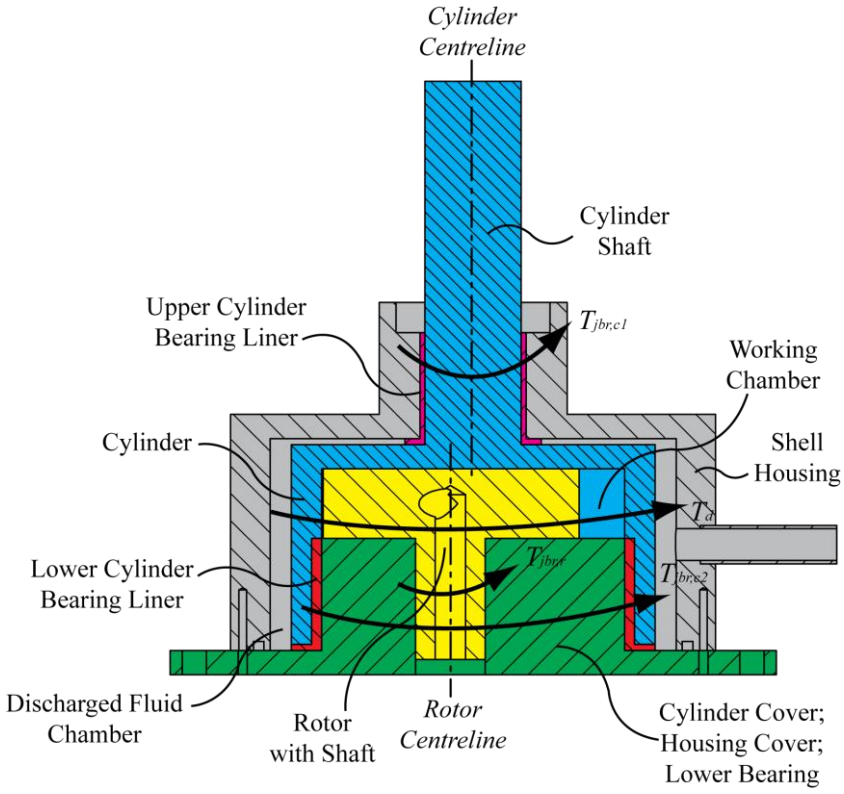

Figure 6.3: Compressor Housing Cross-section and Friction Losses

Apart from the external torques, fixtures on the housing shell hold the compressor in place during operation. Similar to the analysis by Yanagisawa et al. [27] for the rolling piston, these mounts are represented by a damping torque and support torque and assumed to be proportional to the twist rate and angle of twist respectively. The equation of motion for the compressor shell housing is formulated as shown in Equation (6.17).

$$I_h\ddot{\theta}_h = T_{jbr,r} + T_{jbr,c} + T_d - T_{supp} - T_{damp} \tag{6.17}$$

where

$$T_{supp} = C_{supp}\theta_h \tag{6.18}$$

$$T_{damp} = C_{damp}\dot{\theta}_h \tag{6.19}$$

6.3.4 RV Compressor Prototype Dynamics

For the RV compressor prototype discussed in Chapter 3, the vane is attached to the cylinder as shown in Figure 6.4 and thus, Equation (6.11) shall be adapted for use in this section.

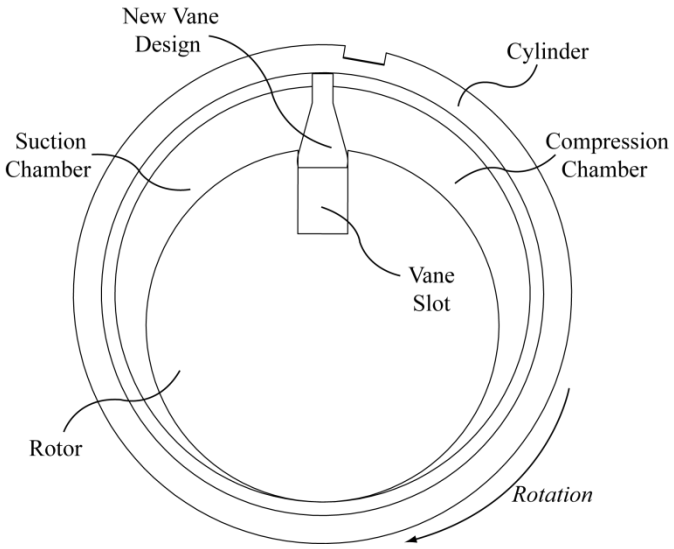

Figure 6.4: RV Prototype Cyliner-Rotor Assembly Cross-Section

Due to the absence of the bush component, the generalised coordinates for the bush θ_b can be omitted from the dynamics equation. The equation of motion describing the cylinder-rotor assembly is presented in Equation (6.20).

$$I_c\ddot{\theta}_c = T_m + T_g - \frac{d\theta_r}{d\theta_c}\left(I_r\ddot{\theta}_r\right) - T_f \tag{6.20}$$

As the cylinder is the main driving component, the rotation angle of the rotor θ_r is expressed in terms of the cylinder rotation angle as shown in Equation (6.21) and after rearrangement, the new equation of motion is depicted in Equation (6.22).

$$\ddot{\theta}_r = \dot{\theta}_c^2 \frac{d^2\theta_r}{d\theta_c^2} + \ddot{\theta}_c \frac{d\theta_r}{d\theta_c} \tag{6.21}$$

$$\left[I_c + I_r \left(\frac{d\theta_r}{d\theta_c} \right)^2 \right] \ddot{\theta}_c = T_m + T_g - I_r \dot{\theta}_c^2 \frac{d\theta_r}{d\theta_c} \frac{d^2\theta_r}{d\theta_c^2} - T_f \tag{6.22}$$

6.3.5 Gas Torque

The gas torque T_g is the torque required to do work on the working fluid to compress it. This is expressed in Equation (6.23).

$$T_g = \frac{\dot{W}_s + \dot{W}_{com}}{\dot{\theta}_c} = P_s \frac{dV_s}{d\theta_c} + P_{com} \frac{dV_{com}}{d\theta_c} \tag{6.23}$$

6.3.6 Motor Torque

A squirrel-cage induction motor would be used to power the compressor. The output torque from the motor T_m is dependent on the frequency of the alternating current (AC) input and the rotation speed of the motor shaft. The synchronous speed of the motor is defined as the speed at which the output torque is zero and this is dependent on the input AC frequency [116]. For such a motor, its synchronous speed is defined as shown in Equation (6.24) where χ is the input frequency and ψ is the number of stator poles in the motor [116].

$$\dot{\theta}_{sync} = \frac{120\chi}{\psi} \cdot \frac{2\pi}{60} = \frac{4\pi\chi}{\psi} \tag{6.24}$$

The speed-torque characteristic curve of an induction motor is shown in Figure 6.5. As the alternating current input frequency to the motor changes, the synchronous speed changes accordingly and the entire curve translates along the x-axis.

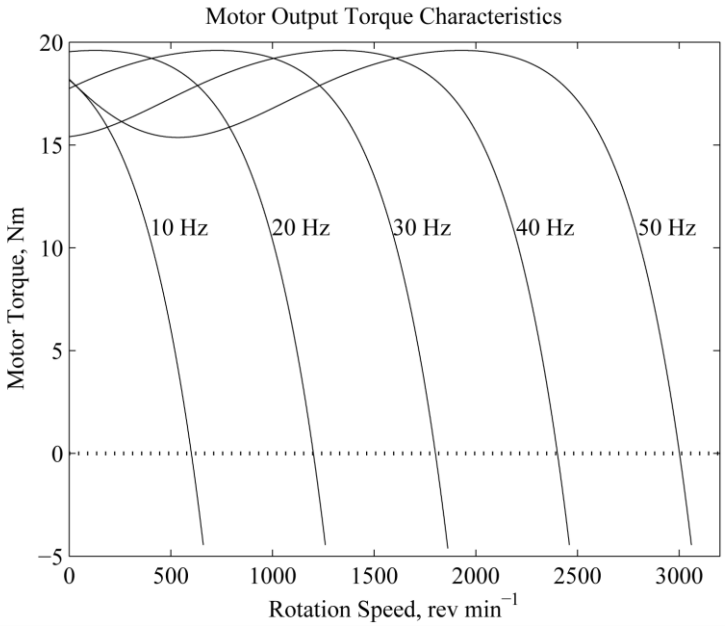

Figure 6.5: Motor Load Curve

To this end, the speed-torque characteristic curve is fitted to a sixth order polynomial function in which the output torque of the motor is expressed as a function of the instantaneous operating speed and synchronous speed as shown in Equation (6.25). This enables the simulation model to emulate the motor torque based on the input frequency and operating speed.

$$T_m = a_0 + a_1(\dot{\theta}_{shaft} - \dot{\theta}_{sync}) + a_2(\dot{\theta}_{shaft} - \dot{\theta}_{sync})^2 + \cdots + a_6(\dot{\theta}_{shaft} - \dot{\theta}_{sync})^6 \quad (6.25)$$

Following the evaluation of the motor torque, Section 6.4 will detail the calculation of the various friction torques present in the oil-free RV compressor. As higher frictional losses are expected in the absence of lubricants, it would be impractical to model the total friction torque as a proportion of the average gas torque which was utilised in the study of the rolling piston compressor by Yanagisawa et al. [27].

6.4 Evaluation of Friction Torques

For the RV mechanism, four sources of friction losses have been identified, namely bearing friction and drag from the discharged fluid in the housing shell as shown in Figure 6.3, together with rotor endface friction and vane sliding friction as illustrated in Figure 6.6

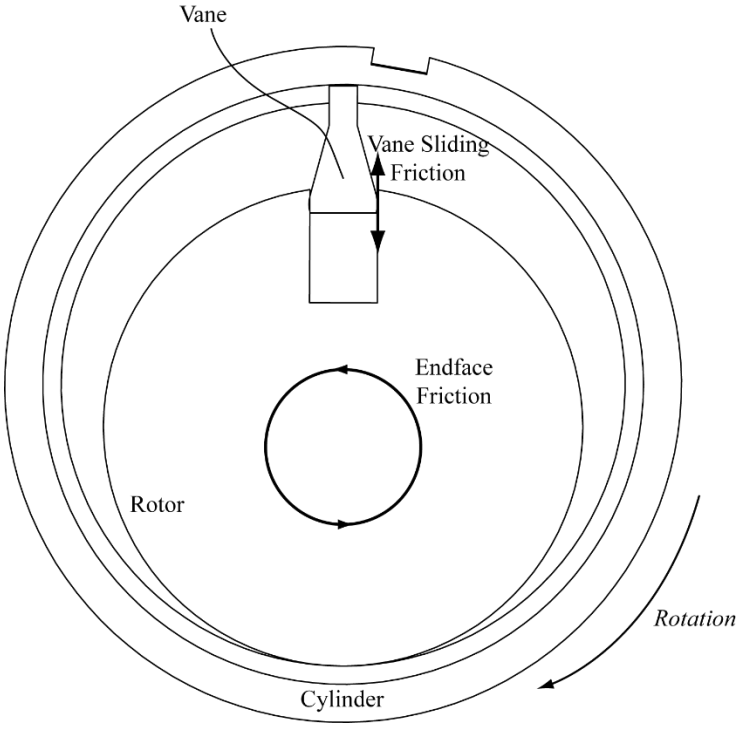

Figure 6.6: Rotor Endface Friction and Vane Sliding Friction

Each of these losses will be looked at in detail as friction losses are expected to be extremely significant for that of an oil-free RV compressor. It is noted that other than the fluid drag, the friction losses arise from dry friction due to the absence of lubricants. The Coulomb friction model given in Equation (6.26) shall be used for calculation of these friction torques. In these cases, μ represents the coefficient of friction and N is the normal reaction force at the rubbing surface.

$$F_f = \mu N \tag{6.26}$$

6.4.1 Endface and Bearing Flange Friction

An orientation-free compressor would not have any fixed orientation; it may be required to operate under different orientations depending on the conditions. Hence, the orientation of the compressor may cause the weight of the components to weigh down on the component endfaces and bearing flanges resulting in friction at these interfaces. This presents an additional source of friction in the compressor. Figure 6.7 shows the layout of the components in the compressor in the upright position and the orientation of the compressor. The cylinder is

supported on both ends by two bearings and the rotor is resting on the endface with the shaft pointing downwards.

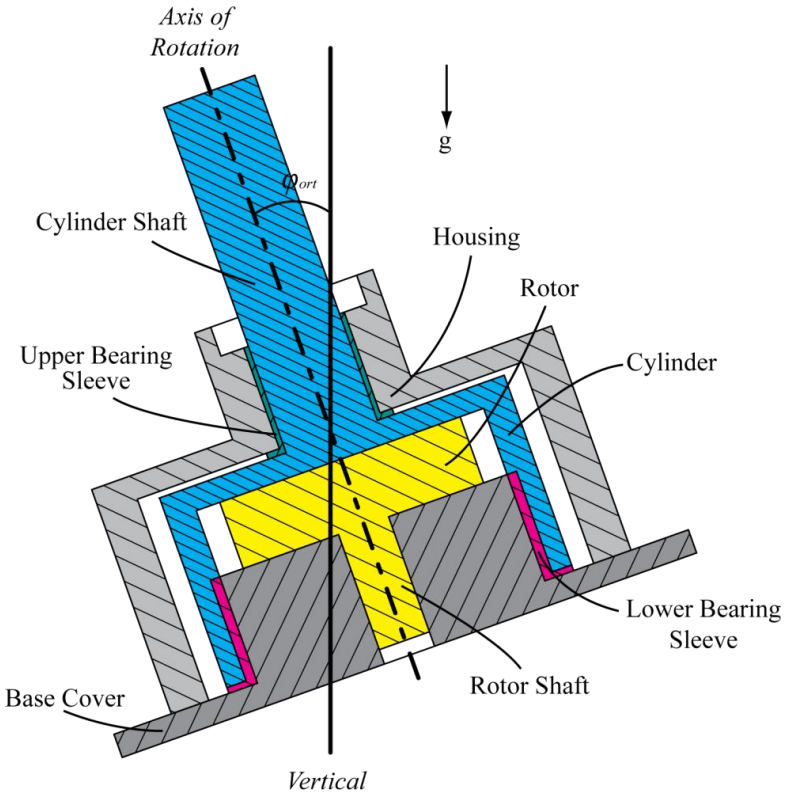

Figure 6.7: Compressor Rotation Orientation

From Figure 6.7, the friction force per unit area acting on each of the bearing flanges due to the weight of the component can be written as shown in Equation (6.27). Note that the friction force due to the weight of the components can only occur on at most one of the flanges depending on the orientation. For the endface, the magnitude friction force per unit area due to the weight of the rotor component and chamber pressure forces can be expressed as shown in Equation (6.28). Note that the forces at the endface might be negative for certain orientations or operating conditions in which the pressure forces at the endfaces are able to support the weight of the rotor; such forces are neglected as the endface force is now acting on the other surface and the alternate expression in Equation (6.29) is used instead.

$$\left.\begin{aligned} f_{bf,1} &= \frac{\mu m_c g \cos\varphi_{ort}}{\pi\left(r_{bf,2}^2 - r_{bf,1}^2\right)} \;, \varphi_{ort} \le \frac{\pi}{2} \\ f_{bf,2} &= -\frac{\mu(m_c + m_r) g \cos\varphi_{ort}}{\pi\left(r_{bf,2}^2 - r_{bf,1}^2\right)} \;, \varphi_{ort} > \frac{\pi}{2} \end{aligned}\right\} \tag{6.27}$$

$$\left|\boldsymbol{f}_{enf}\right| = \frac{\mu}{\pi\left(r_r^2 - r_{shaft,r}^2\right)}\left[m_r g \cos\varphi_{ort} + \pi r_{shaft,r}^2\left(p_{avg} - p_{suc}\right)\right] \tag{6.28}$$

for $$\varphi_{ort} \le \cos^{-1}\left(\frac{\pi r_{shaft,r}^2\left(p_{avg} - p_{suc}\right)}{m_r g}\right),$$

$$\left|\boldsymbol{f}_{enf}\right| = \frac{\mu}{\pi r_r^2}\left[-m_r g \cos\varphi_{ort} - \pi r_{shaft,r}^2\left(p_{avg} - p_{suc}\right)\right] \tag{6.29}$$

where

$$p_{avg} \cong \frac{p_s\theta_r + p_{com}(2\pi - \theta_r)}{2\pi} \tag{6.30}$$

For the bearing flange friction, the torque can be calculated by integrating the unit friction force for the entire flange area. This is achieved as shown in Equation (6.31). Note that the right expression from Equation (6.27) must be used depending on the orientation and affected flange with the appropriate flange dimensions.

$$T_{f,bf} = \int_{r_{bf,1}}^{r_{bf,2}} \int_0^{2\pi} \left(f_{bf} r\right) \cdot r d\theta dr = \frac{2\pi}{3} f_{bf}\left(r_{bf,2}^3 - r_{bf,3}^3\right) \tag{6.31}$$

Due to the plane rotation of the rubbing surface at the endfaces, the method of analysis for the endface friction would be similar to that employed by Subiantoro and Ooi [117]. Instead of fluid shear force from the lubricant acting on the rotor and cylinder, the RV compressor prototype is affected by Coulomb friction instead. Figure 6.8 shows the different endface configurations for the RV mechanism in which the shaded regions show the overlapping endface areas affected by friction.

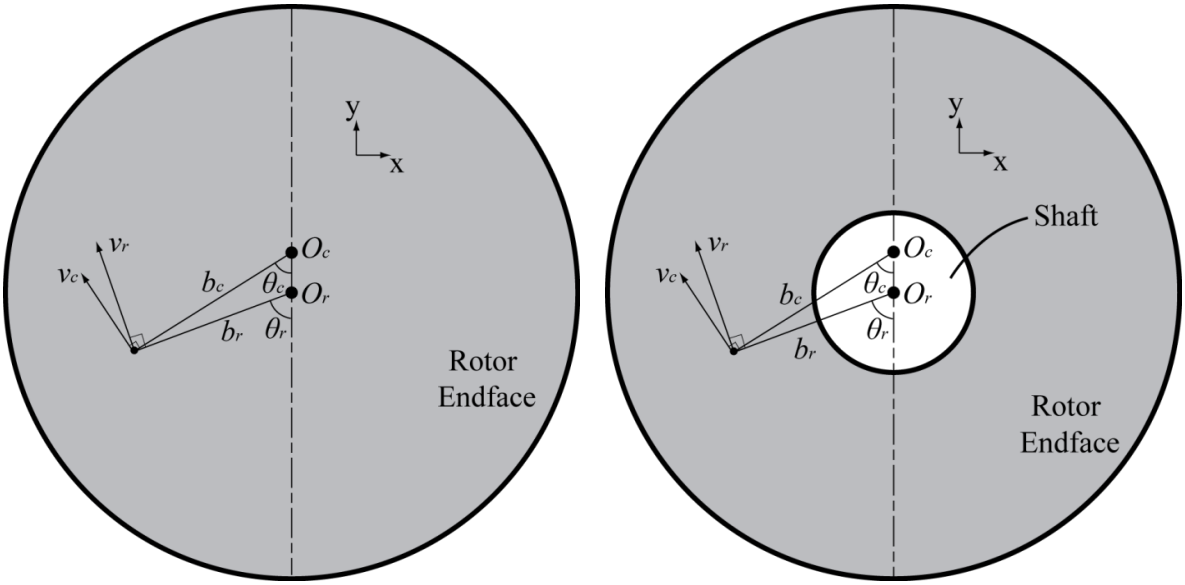

(a): Plain Endface **(b): Endface with Shaft**

Figure 6.8: RV Endface Configurations

For an arbitrary point in the shaded regions for any configuration, the velocity of the cylinder and rotor endfaces are expressed as shown in Equations (6.32) and (6.33) respectively. The relative velocity is then calculated as shown in Equation (6.34).

$$\begin{aligned}\boldsymbol{v}_c &= \boldsymbol{\omega}_c \times \boldsymbol{r}_{d,c} \\ &= \begin{pmatrix} 0 \\ 0 \\ -\omega_c \end{pmatrix} \times \begin{pmatrix} -b_c \sin\theta_c \\ -b_c \cos\theta_c \\ 0 \end{pmatrix} \\ &= -\omega_c b_c \cos\theta_c \, \vec{\boldsymbol{x}} + \omega_c b_c \sin\theta_c \, \vec{\boldsymbol{y}} \end{aligned} \tag{6.32}$$

$$\begin{aligned}\boldsymbol{v}_r &= \boldsymbol{\omega}_r \times \boldsymbol{r}_{d,r} \\ &= -\omega_r b_r \cos\theta_r \, \vec{\boldsymbol{x}} + \omega_r b_r \sin\theta_r \, \vec{\boldsymbol{y}} \end{aligned} \tag{6.33}$$

$$\Delta\boldsymbol{v} = \boldsymbol{v}_c - \boldsymbol{v}_r = [-\omega_c \varepsilon - (\omega_c - \omega_r) b_r \cos\theta_r] \vec{\boldsymbol{x}} + (\omega_c - \omega_r) b_r \sin\theta_r \, \vec{\boldsymbol{y}} \tag{6.34}$$

For these arbitrary points, the direction of the friction force is the opposite as that of the relative velocity vector and thus the friction force is simply the product of the magnitude and the negative unit vector for the relative velocity as shown in Equation (6.35). Note that the friction force at the endface is orientation dependent and must be appropriately selected from either Equations (6.28) or (6.29).

$$\boldsymbol{f}_{enf} = -|\boldsymbol{f}_{enf}|\frac{\Delta \boldsymbol{v}}{|\Delta \boldsymbol{v}|} \tag{6.35}$$

where

$$\begin{aligned} |\Delta \boldsymbol{v}| &= \sqrt{[-\omega_c \varepsilon - (\omega_c - \omega_r) b_r \cos\theta_r]^2 + [(\omega_c - \omega_r) b_r \sin\theta_r]^2} \\ &= \sqrt{\omega_c^2 \varepsilon^2 + (\omega_c - \omega_r)^2 b_r^2 + 2\omega_c \varepsilon (\omega_c - \omega_r) b_r \cos\theta_r} \end{aligned} \tag{6.36}$$

The friction torque produced at the endfaces can then be found by summing up all the points in the shaded regions as shown in Equations (6.37) and (6.38) for the losses with reference to the rotor centre and cylinder centre respectively. Note that analytical solutions from the double integrations for the evaluation of the endface friction torques are not possible due to the complexity of the denominator $|\Delta \boldsymbol{v}|$ and thus, these friction torques would have to be numerically calculated.

$$\boldsymbol{T}_{f,r\,enf} = \int_0^{r_r} \int_0^{2\pi} \left(\boldsymbol{r}_{b,r} \times \boldsymbol{f}_{enf}\right) \cdot b_r \, d\theta_r \, db_r$$

$$= -\int_0^{r_r} \int_0^{2\pi} \begin{pmatrix} -b_r \sin\theta_r \\ -b_r \cos\theta_r \\ 0 \end{pmatrix} \times \begin{pmatrix} -\omega_c \varepsilon - (\omega_c - \omega_r) b_r \cos\theta_r \\ (\omega_c - \omega_r) b_r \sin\theta_r \\ 0 \end{pmatrix} \cdot \frac{|\boldsymbol{f}_{enf}|}{|\Delta \boldsymbol{v}|} \cdot b_r d\theta_r db_r$$

$$= \int_0^{r_r} \int_0^{2\pi} \frac{(\omega_c - \omega_r) b_r^3 + \omega_c \varepsilon b_r^2 \cos\theta_r}{\sqrt{\omega_c^2 \varepsilon^2 + (\omega_c - \omega_r)^2 b_r^2 + 2\omega_c \varepsilon (\omega_c - \omega_r) b_r \cos\theta_r}} \vec{\boldsymbol{z}} \cdot |\boldsymbol{f}_{enf}| d\theta_r db_r \tag{6.37}$$

$$\boldsymbol{T}_{f,c\,enf} = \int_0^{r_r} \int_0^{2\pi} \left(\boldsymbol{r}_{b,c} \times \boldsymbol{f}_{enf}\right) \cdot b_r \, d\theta_r \, dd_r$$

$$= \int_0^{r_r} \int_0^{2\pi} \frac{(\omega_c - \omega_r) b_r^3 + (2\omega_c - \omega_r) \varepsilon b_r^2 \cos\theta_r + \omega_c \varepsilon^2 b_r}{\sqrt{\omega_c^2 \varepsilon^2 + (\omega_c - \omega_r)^2 b_r^2 + 2\omega_c \varepsilon (\omega_c - \omega_r) b_r \cos\theta_r}} \vec{\boldsymbol{z}} \cdot |\boldsymbol{f}_{enf}| d\theta_r db_r \tag{6.38}$$

Equations (6.37) and (6.38) are applicable for plain endface configurations without the shaft and applicable only for when Equation (6.29) is valid. For the other side of the endface with the shaft, extra steps are needed – the integrations in Equations (6.37) and (6.38) are carried out twice; the first for the plain endface friction loss and for the second time, the limits of the integration are changed to that of the shaft diameter as shown in Equations (6.39) and (6.40) for the apparent friction loss at the shaft hole. The respective results are then subtracted

from the original plain endface friction torque calculated by Equations (6.37) and (6.38) to obtain the actual endface friction losses for the rotor and cylinder. Note that the second term in Equation (6.39) represents the friction loss at the endface of the rotor that is in contact with the stationary bearing surface, in which the method of evaluation is similar to that for the bearing flange friction in Equation (6.31).

$$\boldsymbol{T}_{f,r\,shaft} = \int_0^{r_{shaft,c}} \int_0^{2\pi} \left(\boldsymbol{r}_{b,r} \times \boldsymbol{f}_{enf}\right) \cdot b_r \, d\theta_r \, db_r - \frac{2\pi}{3} \left|\boldsymbol{f}_{enf}\right| \left(r_{shaft,c}^3 - r_{shaft,r}^3\right) \quad (6.39)$$

$$\boldsymbol{T}_{f,c\,shaft} = \int_0^{r_{shaft,c}} \int_0^{2\pi} \left(\boldsymbol{r}_{b,c} \times \boldsymbol{f}_{enf}\right) \cdot b_r \, d\theta_r \, db_r \quad (6.40)$$

6.4.2 Vane Sliding Friction

Friction losses occur at the vane slot as the vane slides in and out of the slot, and these losses affect both the rotor and the cylinder. Figure 6.9 shows the free body diagram of the rotor, depicting the normal force to the vane slot and its resultant friction force.

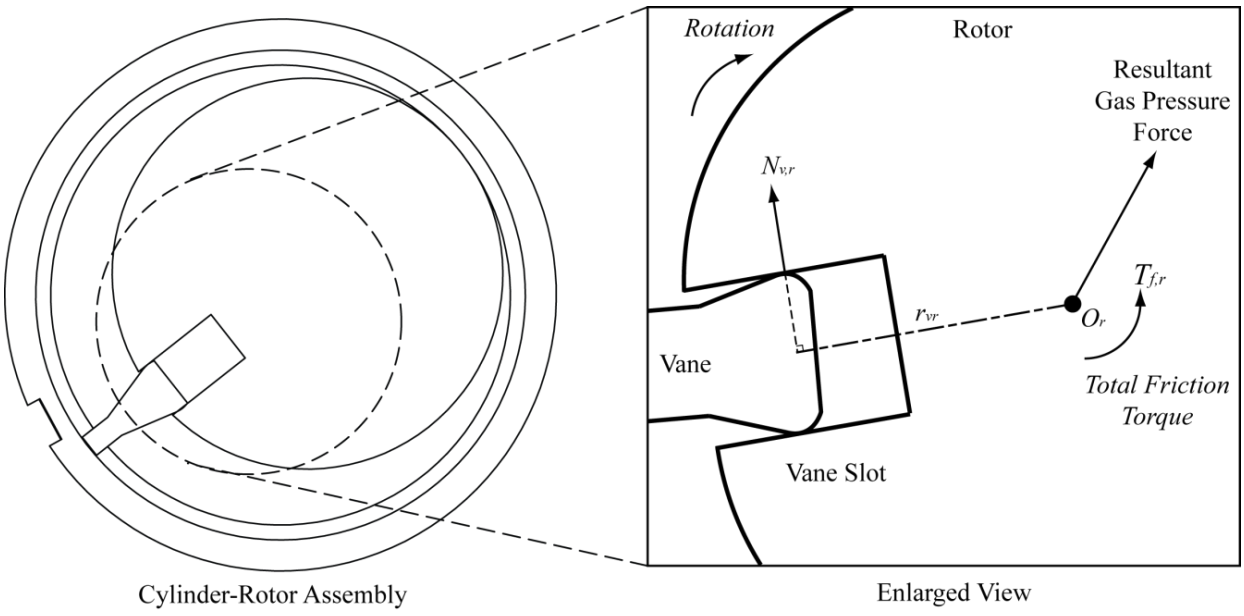

Figure 6.9: Rotor Free Body Diagram

Based on the free body diagram, the equation of motion for the rotor can be written as Equation (6.41) and the normal reaction force at the vane slot is given in Equation (6.42).

$$I_r \ddot{\theta}_r = N_{v,r} r_{vr} - T_{f,r} \quad (6.41)$$

$$N_{v,r} = \frac{1}{r_{vr}}\left(I_r\ddot{\theta}_r + T_{f,r}\right) \tag{6.42}$$

The friction in the vane slot can then be calculated from Equation (6.43) and the corresponding friction torque vane component is then expressed as Equation (6.44). As the direction of friction is opposite to that of the vane sliding direction, the negative unit vector of the vane velocity is included.

$$F_{f,v\,r} = -\mu N_{v,r} \cdot \frac{\frac{dr_{vr}}{dt}}{\left|\frac{dr_{vr}}{dt}\right|} \tag{6.43}$$

$$T_{f,v\,r} = \frac{w_{slot}}{2} \cdot F_{f,v\,r} \tag{6.44}$$

To this end, the friction force on the vane acting on the cylinder is equal and opposite to that of the vane slot. The friction torque at the vane slot acting on the cylinder can then be expressed as shown in Equation (6.45).

$$T_{f,v\,c} = -F_{f,v\,r}\left(\varepsilon \sin\theta_v - \frac{w_{slot}}{2}\right) \tag{6.45}$$

6.4.3 Bearing Friction

The normal forces on the bearings for the cylinder and rotor are affected by both the pressure forces in the chambers and the vane sliding forces. These forces will be evaluated in the plane of rotation and resolved in Cartesian coordinates for ease of calculation. Beginning with the gas pressure forces in the chambers, Figure 6.10 shows the gas pressure forces acting on the cylinder and rotor. The resolved forces due to the suction and compression pressures are then tabulated in Equations (6.46)–(6.53).

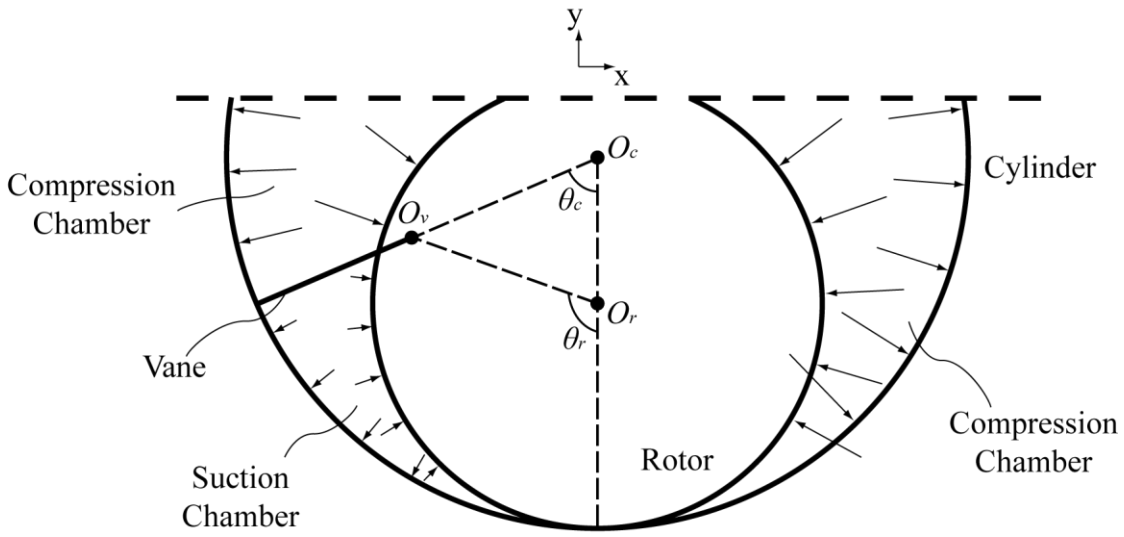

Figure 6.10: Gas Pressure Forces in Working Chambers

Suction:

Cylinder:

$$F_{x,s\,c} = -p_s l_c r_c (1 - \cos\theta_c) \tag{6.46}$$

$$F_{y,s\,c} = -p_s l_c r_c \sin\theta_c \tag{6.47}$$

Rotor:

$$F_{x,s\,r} = p_s l_c r_r (1 - \cos\theta_r) \tag{6.48}$$

$$F_{y,s\,r} = p_s l_c r_r \sin\theta_r \tag{6.49}$$

Compression:

Cylinder:

$$F_{x,com\,c} = p_{com} l_c r_c (1 - \cos\theta_c) \tag{6.50}$$

$$F_{y,com\,c} = p_{com} l_c r_c \sin\theta_c \tag{6.51}$$

Rotor:

$$F_{x,com\,r} = p_{com} l_c r_r (1 - \cos\theta_r) \tag{6.52}$$

$$F_{y,com\,r} = p_{com} l_c r_r \sin\theta_r \tag{6.53}$$

For clarity of presentation, the resolved gas pressure forces are summed as shown in Equations (6.54)–(6.57).

Cylinder:

$$F_{x,g\,c} = (p_{com} - p_s) l_c r_c (1 - \cos\theta_c) \tag{6.54}$$

$$F_{y,g\,c} = (p_{com} - p_s) l_c r_c \sin\theta_c \tag{6.55}$$

Rotor:

$$F_{x,g\,r} = (p_s - p_{com}) l_c r_r (1 - \cos\theta_r) \tag{6.56}$$

$$F_{y,g\,r} = (p_s - p_{com}) l_c r_r \sin\theta_r \tag{6.57}$$

Based on Figure 6.9, the resolved forces at the vane slot due to the vane normal force and sliding friction can be expressed in Equations (6.58) and (6.59).

$$F_{x,v\,r} = -\left(N_{v,r} \cos\theta_r + F_{f,v\,r} \sin\theta_r\right) \tag{6.58}$$

$$F_{y,v\,r} = N_{v,r} \sin\theta_r - F_{f,v\,r} \cos\theta_r \tag{6.59}$$

On the other hand, the resolved forces at the vane tip acting on the cylinder are just equal and opposite to that of the vane slot as shown in Equations (6.60) and (6.61).

$$F_{x,v\,c} = N_{v,r} \cos\theta_r + F_{f,v\,r} \sin\theta_r \tag{6.60}$$

$$F_{y,v\,c} = -N_{v,r} \sin\theta_r + F_{f,v\,r} \cos\theta_r \tag{6.61}$$

The resolved forces can then be summed up and the resultant forces acting on the cylinder and rotor are expressed as shown in Equations (6.62) and (6.63), respectively. Note that these include the weight of the components due to compressor orientation as well and would change according to the orientation angle φ_{ort}. The friction torques as a result of these forces at the bearings can be calculated as shown in Equations (6.64) and (6.65).

$$\left.\begin{aligned} F_c &= \sqrt{\left(F_{x,g\,c} + F_{x,v\,c}\right)^2 + \left(F_{y,g\,c} + F_{y,v\,c}\right)^2 + (m_c g \sin\varphi_{ort})^2}\ , \quad \varphi_{ort} \le \frac{\pi}{2} \\ F_c &= \sqrt{\left(F_{x,g\,c} + F_{x,v\,c}\right)^2 + \left(F_{y,g\,c} + F_{y,v\,c}\right)^2 + [(m_c + m_r) g \sin\varphi_{ort}]^2}\ , \varphi_{ort} \ge \frac{\pi}{2} \end{aligned}\right\} \tag{6.62}$$

$$\left.\begin{aligned} F_r &= \sqrt{\left(F_{x,g\,r} + F_{x,v\,r}\right)^2 + \left(F_{y,g\,r} + F_{y,v\,r}\right)^2 + (m_r g \sin\varphi_{ort})^2}\ , \quad \varphi_{ort} \le \frac{\pi}{2} \\ F_r &= \sqrt{\left(F_{x,g\,r} + F_{x,v\,r}\right)^2 + \left(F_{y,g\,r} + F_{y,v\,r}\right)^2}\ , \varphi_{ort} \ge \frac{\pi}{2} \end{aligned}\right\} \tag{6.63}$$

$$T_{f,jbr\,c} = \frac{1}{2}\mu F_c\left(r_{shaft,lower} + r_{shaft,upper}\right) \tag{6.64}$$

$$T_{f,jbr\,r} = \mu F_r r_{shaft,r} \tag{6.65}$$

6.4.4 Fluid Shear Friction

The design of the RV mechanism results in the cylinder-rotor assembly rotating in the housing shell in which the compressed fluid is discharged to. This creates a drag force on the cylinder assembly caused by the shearing of the gas between the cylinder and the housing, resulting in an excitation force on the housing shell. Due to the high speed rotation of the cylinder in the housing shell, the flow profile of the discharged fluid in the housing shell can be characterised as that of a Taylor-Couette flow [118, 119]. An illustration of this flow is shown in Figure 6.11.

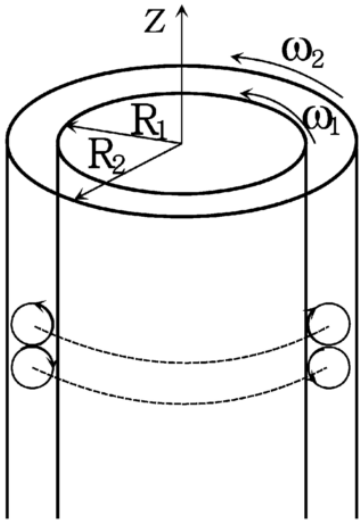

Figure 6.11: Taylor-Couette Flow [118]

Dou, et al. [118, 119] have provided the analytical solution for the calculation of the fluid shear but this solution is not applicable in the case of the RV compressor prototype as the ratio of the cylinder length to the gap between the cylinder-rotor assembly and housing shell is small. In the assumptions used to formulate the analytical solution, the lengths of the cylinders are considered to be infinite compared to the dimension of the concentric gap between them.

Therefore, a more comprehensive two-dimensional computational fluid dynamics (CFD) analysis using the commercially available computational code ANSYS Fluent is used to estimate the fluid shear in the compressor. A two-dimensional axis-symmetric fluid domain for

the discharged fluid is modelled in ANSYS Workbench 14.0 and this is illustrated in Figure 6.12.

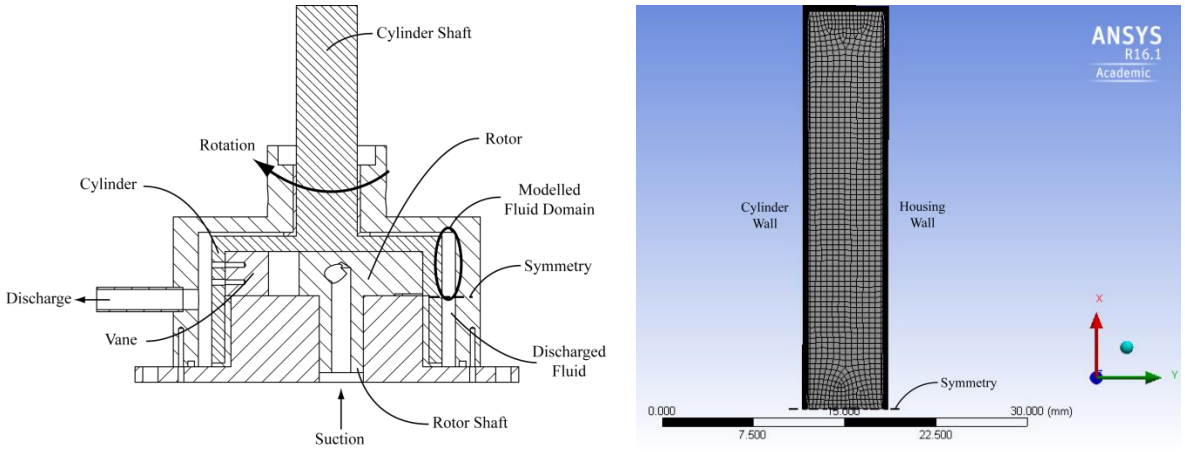

(a): Fluid Domain **(b): Mesh**

Figure 6.12: Modelled Fluid Domain and CFD Mesh

In the simulation, the rotating cylinder assembly is set at a constant rotational speed of 105 rad s^{-1} (1000 rev min^{-1}) with air at room temperature and pressure as the working fluid. The results of the wall shear computed from the simulation for the cylinder assembly and shell housing are illustrated in Figure 6.13.

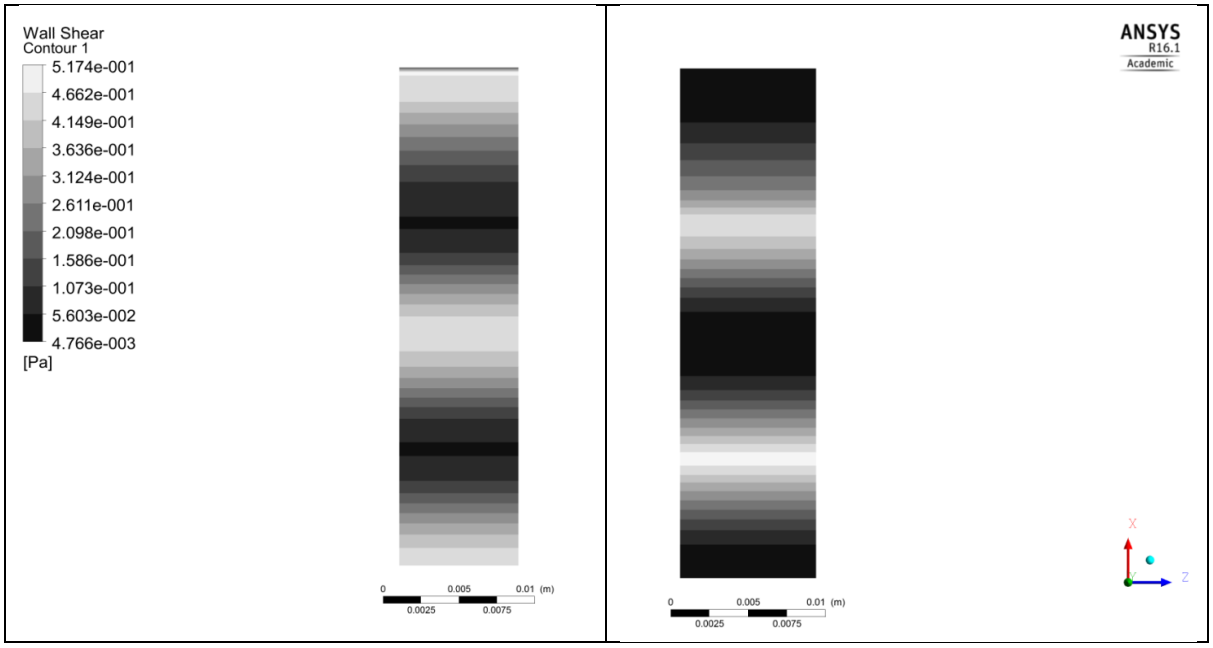

(a): Cylinder Wall Shear **(b): Housing Wall Shear**

Figure 6.13: CFD Wall Shear Results

Distinct bands were noted on both the walls of the cylinder and housing shell albeit in opposing magnitudes. This is evident of eddies present in the discharged fluid of the housing shell. This is observed to be that of the Taylor-Couette flow as demonstrated by Dou, et al. [118]. A better visualisation of the fluid flow in a cross-section diagram is shown in Figure 6.14.

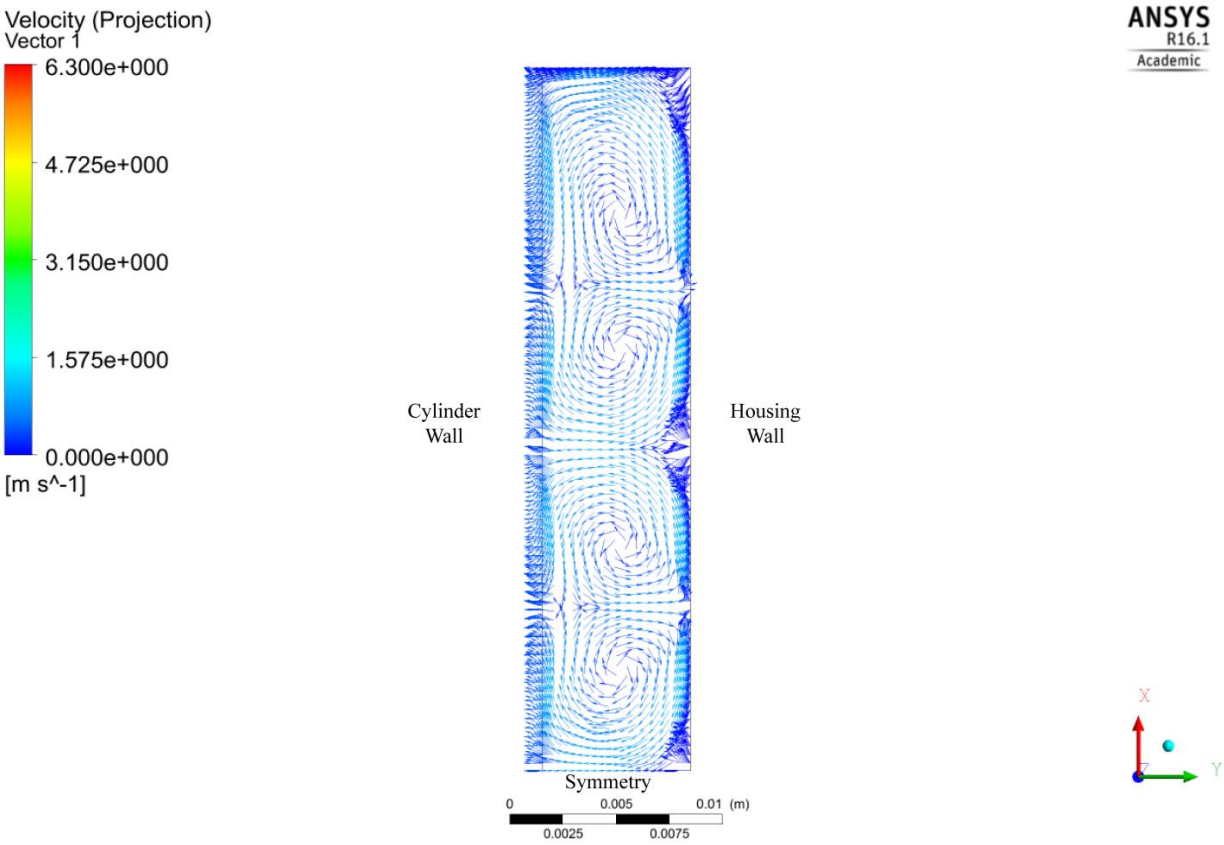

Figure 6.14: Flow Visualisation in Housing Shell

Furthermore, the protruding valve stop on the side of the cylinder also experiences form drag as it rotates in the discharged fluid. An illustration of the valve and valve stop assembly on the cylinder surface is shown in Figure 6.15.

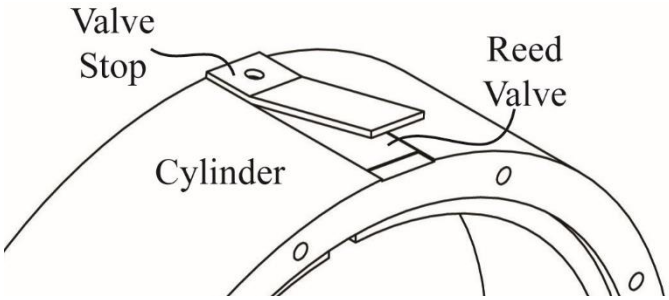

Figure 6.15: Isometric View of Valve and Valve Stop Assembly on Cylinder

With reference to Bertin and Cummings [120], the drag force can be estimated using Equation (6.66) with the expression for the drag coefficient for an incompressible flow over a flat plate in the absence of a pressure gradient shown in Equation (6.67). The length scale used in the equation would be with reference to the width of the valve plate.

$$F_{drag} = \frac{1}{2}\rho \bar{C}_f A_{plate} v^2 \tag{6.66}$$

where

$$\bar{C}_f = \begin{cases} \dfrac{1.328}{\sqrt{Re_l}} & Re_l < 500{,}000 \\ \dfrac{1}{l}\left(\displaystyle\int_0^{crit} \frac{0.664}{\sqrt{Re_x}}dx + \int_{crit}^{l} \frac{0.0583}{Re_x^{0.2}}dx\right) & Re_l \geq 500{,}000 \end{cases} \tag{6.67}$$

$$Re_x = \frac{\rho v x}{\mu} \tag{6.68}$$

$$\text{critical length} = \frac{500{,}000\mu}{\rho v} \tag{6.69}$$

Table 6.1 shows the fluid shear torque for the housing shell and cylinder computed with the wall shear values from the CFD simulation and form drag equation for the valve stop.

Table 6.1: Fluid Shear Torque

Surface	Mean Shear Stress, Pa	Mean Drag Force, N	Mean Torque, N·m	Total Fluid Shear Torque, N·m
Top housing wall	0.139	3.88×10^{-4}	1.30×10^{-5}	Housing Shell: 3.87×10^{-4}
Bottom housing wall	0.139	3.88×10^{-4}	1.30×10^{-5}	
Housing wall	0.183	5.39×10^{-3}	3.61×10^{-4}	
Cylinder wall	0.242	6.02×10^{-3}	3.61×10^{-4}	Cylinder: 3.67×10^{-4}
Valve stop	-	1.08×10^{-4}	6.43×10^{-6}	

6.4.5 Comparison of Friction Torques

Following the evaluation of all friction torques, this section will proceed with a preliminary analysis of these torques. The operating conditions for this study are shown in Table 6.2 with the assumption that there is no internal leakage and heat transfer in the working chambers. This will emulate the ideal operating characteristics of the RV compressor prototype.

Table 6.2: Operating Parameters

Operating Speed, rev min^{-1}	1,000 / 2,000
Working Fluid	Air
Suction Pressure, bar (abs)	1.0
Suction Temperature, °C	27.0
Discharge Pressure, bar (abs)	2.0 / 5.0
Coefficient of Friction	0.4

The torques resulting from the mechanical losses for the case of 1000 rev min^{-1} with suction and discharge pressures at 1 and 2 bar (abs) are plotted in Figure 6.16 as shown. The gas compression torque has been included for comparison as well. The fluid shear torque in the housing shell is not shown as it is four orders of magnitude lower than that of the other torques.

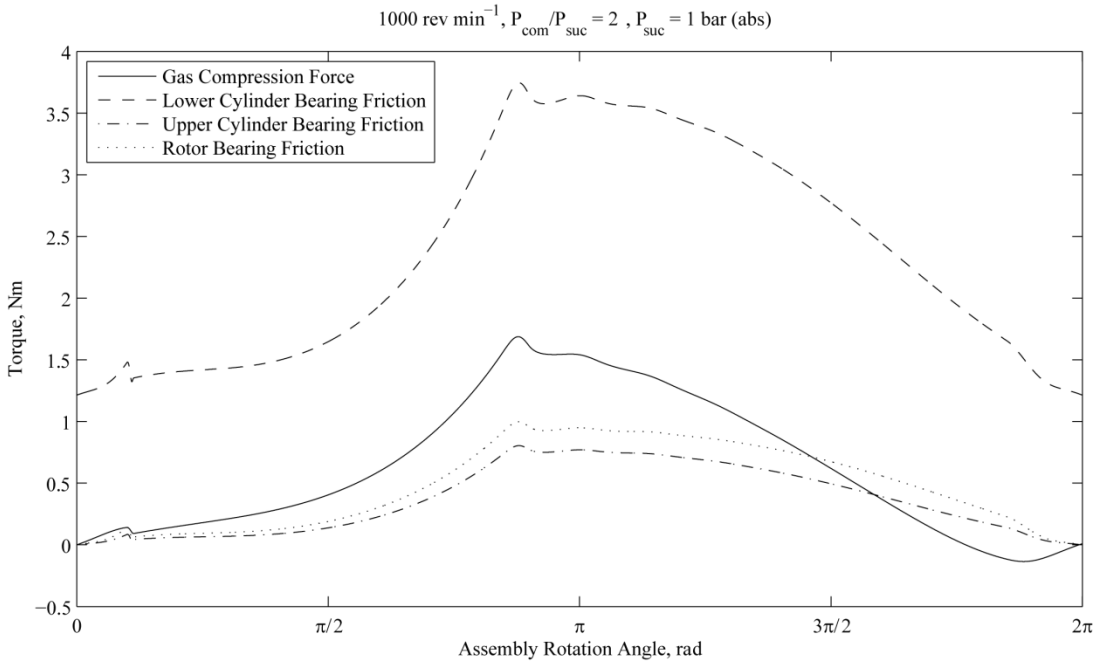

(a): Gas Compression and Bearing Friction Torques

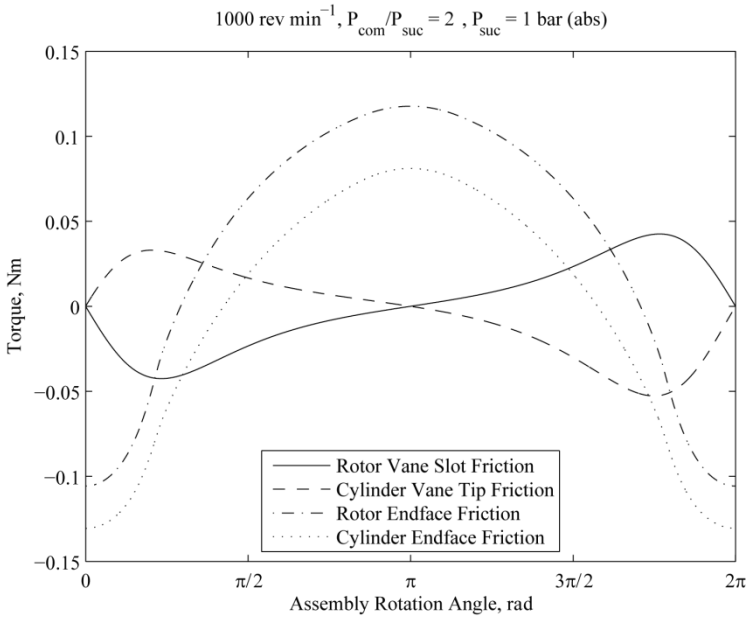

(b): Minor Friction Torques

Figure 6.16: Comparison of Friction Torques at 1000 rev min^{-1} and 1 bar Pressure Difference

The bearing friction torques are significant compared to that of the gas compression torque. Of which, the lower cylinder bearing friction was the highest amongst all the friction torques. This is due to the effect of the assembly weight acting on the lower bearing flanges, thus increasing the friction torque by 1.21 N·m which constitutes 38% of the total friction loss. Furthermore, due to the large bearing radius of 50 mm, the variation of the friction torque at

the lower cylinder bearing is even higher than that of the gas compression torque. The resulting mechanical efficiency for this case is only 16.5%.

On the other hand, if operating at higher pressure ratios, the friction arising from the weight of the assembly becomes less significant. Figure 6.17 shows the comparisons of friction torques at 2000 rev min-1 with suction and discharge pressures of 1 and 5 bar (abs). The mechanical efficiency increases slightly to 19.6% this time round.

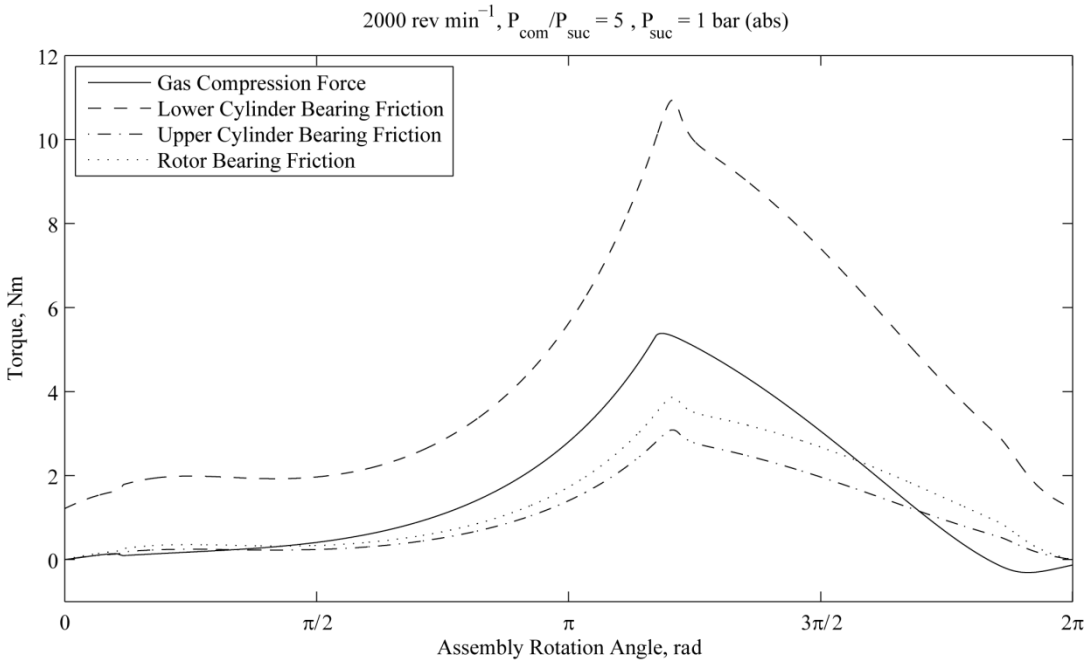

(a): Gas Compression and Bearing Friction Torques

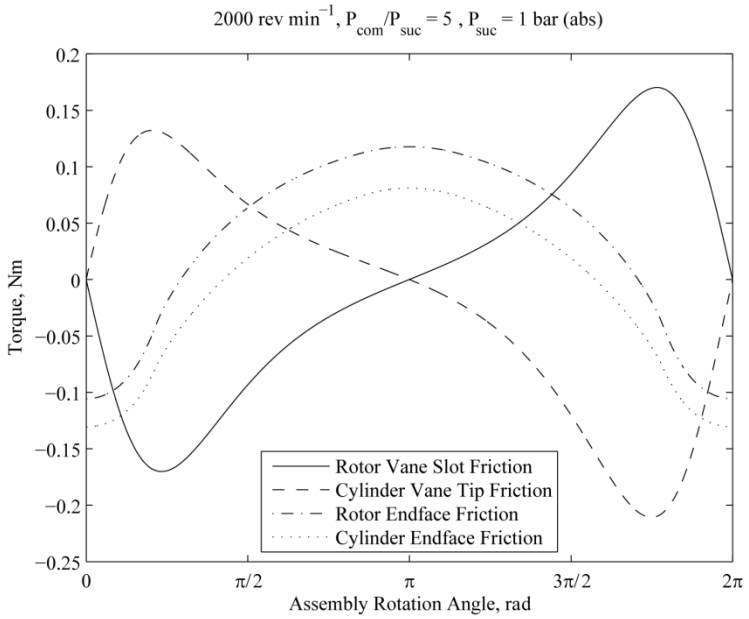

(b): Minor Friction Torques

Figure 6.17: Comparison of Friction Torques at 2000 rev min^{-1} 4 bar Pressure Difference

With a higher pressure difference in this case, friction from the weight of the assembly is now at 18% of the total friction loss. Therefore, at high pressure differences, the effect of the assembly weight becomes less pronounced as it becomes dwarfed by the increase in bearing friction.

It is also observed that the effects of minor friction torques are small compared to the bearing friction torques as seen in both cases of this study. These minor friction torques were about 20 times smaller than that of the bearing friction and gas compression torques. Hence, their effects can be ignored in future studies for convenience. Additionally, the fluid shear torque computed in Section 6.4.4 can be neglected all together since it is of three orders lower than even the minor friction torques.

6.5 Valve Dynamics

Last but not least, the dynamics of the valve shall be discussed in this section with reference to the analysis conducted by Teh et al. [18]. Valve dynamics is a crucial aspect of the discharge process as it affects the flow area for fluid discharge. Due to the unique design of the RV mechanism, the valve is not stationary. Instead, it rotates along with the cylinder and the centripetal force would affect the dynamics of the valve. The free body diagram of a valve element is presented in Figure 6.18 and can be modelled as a cantilever beam.

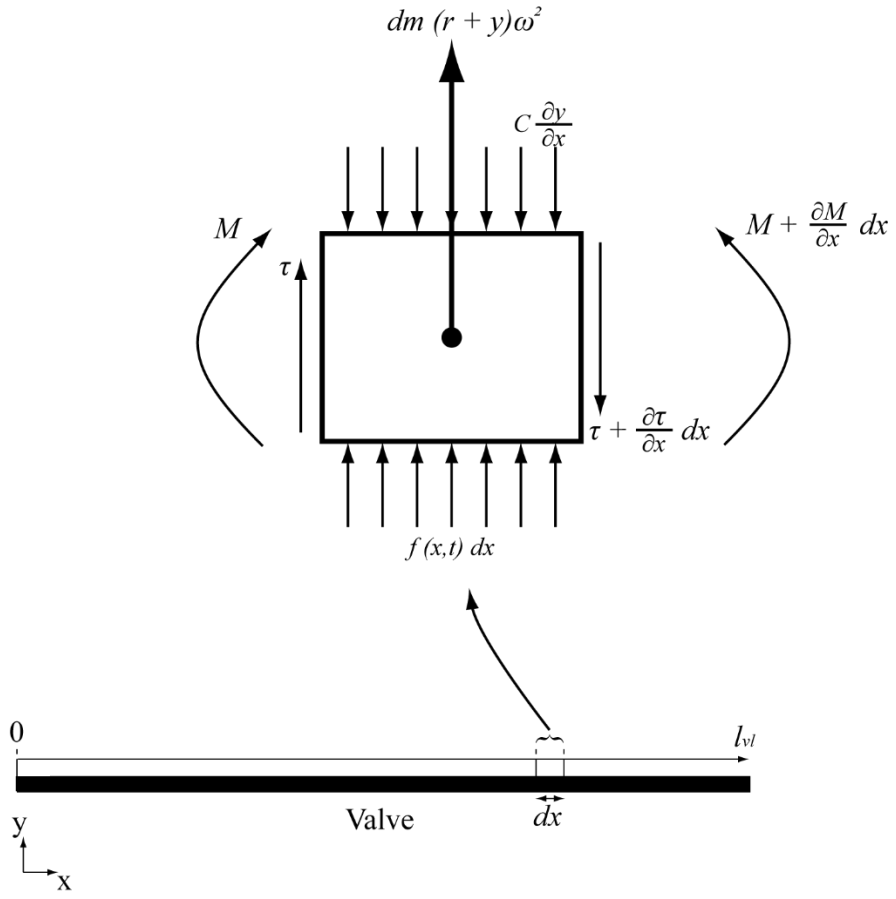

Figure 6.18: Valve Element Free Body Diagram

An analysis of the forces and moments balance on the element of the valve is shown in Equations (6.70) and (6.71) respectively. The expression for the mass per unit length of the valve can be written as shown in Equation (6.72). In addition, the relation between the bending moment and the bending displacement is given in Equation (6.73) [114].

$$\left(\tau + \frac{\partial \tau}{\partial x} dx\right) - \tau + f(x,t)dx + \omega^2(r+y)dm - C\frac{\partial y}{\partial t}dx = \frac{\partial^2 y}{\partial t^2}dm \tag{6.70}$$

$$\tau\frac{dx}{2} + \left(\tau + \frac{\partial \tau}{\partial x}\, dx\right)\frac{dx}{2} + \left(M + \frac{\partial M}{\partial x}dx\right) - M = 0 \tag{6.71}$$

$$dm = \rho A(x)dx \tag{6.72}$$

$$M = EI(x)\frac{\partial^2 y}{\partial x^2} \tag{6.73}$$

Ignoring second order *dx* terms and combining Equations (6.70), (6.71), (6.72) and (6.73) together would yield the dynamics equation for the valve in Equation (6.74).

$$\frac{\partial^2}{\partial x^2}\left[EI(x)\frac{\partial^2 y}{\partial x^2}\right] + \rho A(x)\frac{\partial^2 y}{\partial t^2} + C\frac{\partial y}{\partial t} - \rho A(x)\omega^2 y = \rho A(x)\omega^2 r + f(x,t) \tag{6.74}$$

6.5.1 Free Vibration Mode Shape

In Equation (6.74), the external forces acting on the valve consists of the centripetal force and gas pressure force. The solution would yield the response of the valve to these forces. However, the dynamics of the valve under free vibration would have to be included as well in order to model the behaviour of the valve after excitation. To this end, the free vibration dynamics equation of the valve is written as Equation (6.75) with the external forces on the right hand side of Equation (6.74) removed.

$$\frac{\partial^2}{\partial x^2}\left[EI(x)\frac{\partial^2 y}{\partial x}\right] + \rho A(x)\frac{\partial^2 y}{\partial t^2} + C\frac{\partial y}{\partial t} - \rho A(x)\omega^2 y = 0 \tag{6.75}$$

Equation (6.75) is actually the same as that of a damped vibration of a beam. The solution is in fact variable separable as shown in Equation (6.76) and the dynamics equation is rewritten as Equation (6.77).

$$y(x,t) = U(x)G(t) \tag{6.76}$$

$$\frac{1}{\rho A(x)U}\frac{d^2}{dx^2}\left[EI(x)\frac{d^2U}{dx^2}\right] = \omega^2 - \frac{1}{G}\frac{d^2G}{dt^2} - \frac{C}{\rho A(x)}\frac{1}{G}\frac{dG}{dt} = \chi^2 \tag{6.77}$$

Assuming a uniform cross-section area, Equation (6.77) reduces to a set of homogenous fourth-order (function of *x*) and second-order (function of *t*) differential equations which can then be solved analytically. The solutions are presented as shown in Equations (6.78)–(6.85) with reference to Meirovitch [114]. The boundary conditions of the reed valve are similar to that of the cantilever beam in which it is clamped at one end and free at the other end.

$$U(x) = A_i\left[(\sin\beta x - \sinh\beta x) - \frac{\sin\beta l + \sinh\beta l}{\cos\beta l + \cosh\beta l}(\cos\beta x - \cosh\beta x)\right] \tag{6.78}$$

$$G(t) = e^{-\zeta\Omega t}\left[\frac{G'(0) + \zeta\Omega G(0)}{\Omega\sqrt{1-\zeta^2}}\sin\left(\Omega t\sqrt{1-\zeta^2}\right) + G(0)\cos\left(\Omega t\sqrt{1-\zeta^2}\right)\right] \tag{6.79}$$

where

$$\cos\beta l\cosh\beta l = -1 \tag{6.80}$$

$$\chi_i = (\beta l)_i^2\sqrt{\frac{EI}{\rho A l^4}} \quad , i = 1,2,3,\ldots \tag{6.81}$$

$$\text{for} \quad i = 1, \qquad \beta l = 1.8751$$

$$\Omega_i = \sqrt{\chi_i^2 - \omega^2} \tag{6.82}$$

$$\zeta = \frac{C}{2\rho A\Omega} \tag{6.83}$$

with initial conditions,

$$G(0) = G(t=0) \tag{6.84}$$

$$G'(0) = \left.\frac{dG}{dt}\right|_{t=0} \tag{6.85}$$

The solution of the free vibration for the valve shows that the valve can have up to an infinite number of vibration modes denoted by *i*, each with its own respective vibrational

frequency derived from the solution of (6.80). The first three vibration modes are plotted in Figure 6.19. However, due to the nature of the valve, it can only experience the first vibration mode (i = 1).

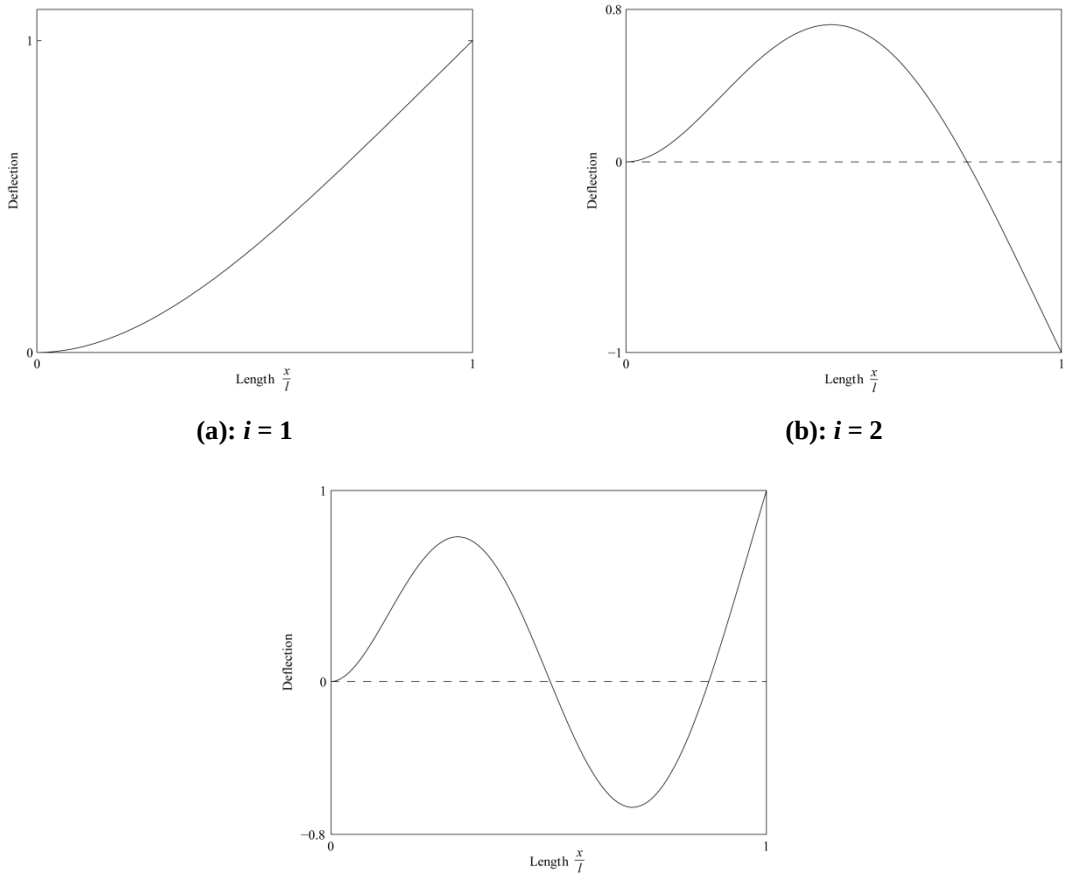

(a): i = 1

(b): i = 2

(c): i = 3

Figure 6.19: Cantilever Beam Mode Shapes

6.5.2 Mode shape for a Valve of Non-uniform Cross-Section

The solution given in Equations (6.78)–(6.85) only applies to that of a valve with constant cross-section area which might not be applicable in designs where the valve has a non-uniform cross-section for its entire length. For comprehensiveness, the solution for a valve with non-uniform cross-section shall be included in this section.

The free vibration mode shape of a cantilever beam with non-uniform cross-section area can be approximated with that of the enhanced Rayleigh-Ritz method in which the mode shape is assumed to be a linear combination of functions [114] which can satisfy the boundary conditions of the problem. For the case of the cantilever valve, its mode shape can be

approximated in the form of a polynomial with reference to Ooi, et al. [121] and this is expressed in Equation (6.86). Note that the mode shape only applies for the fundamental frequency (i = 1).

$$U_1(x) = \left(\frac{x}{l_v}\right)^4 - 4\left(\frac{x}{l_v}\right)^3 + 3 \tag{6.86}$$

The estimate of the frequency for the first mode of vibration can then be estimated by Rayleigh's quotient [114] as shown in Equation (6.87). For a reed valve with constant thickness ι and varying width $w_v(x)$, the Rayleigh's quotient can be rewritten as Equation (6.88).

$$R\big(U_1(x)\big) = \chi_1^2 = \frac{-\int_0^{l_v} U(x)\frac{d^2}{dx^2}\left[EI(x)\frac{d^2U(x)}{dx^2}\right]dx}{\int_0^{l_v}\rho A(x)U^2(x)dx} \tag{6.87}$$

$$R\big(U_1(x)\big) = \chi_1^2 = \frac{-E\iota^2}{12\rho}\cdot\frac{\int_0^{l_v} U(x)\frac{d^2}{dx^2}\left[w_v(x)\frac{d^2U(x)}{dx^2}\right]dx}{\int_0^{l_v} w_v(x)U^2(x)dx} \tag{6.88}$$

With the given valve width, Equation (6.88) is used to calculate the fundamental frequency of the cantilever valve which is in turn required for the solution for the forced vibration response that will be covered in Section 6.5.3.

6.5.3 Forced Vibration

The mode shape for a valve of varying cross-sectional area has been covered and this section will proceed with evaluating the response of the valve to external forces stemming from that of the centripetal acceleration of the rotating assembly and the gas pressure in the working chamber. For the solution of force vibration, it is assumed that it is also variable separable with all the vibration modes combined with the principle of superposition as shown in Equation (6.89). $U_i(x)$ represents all the different mode shapes that the cantilever beam can take, each corresponding to a different natural frequency χ_i.

$$y(x,t) = \sum_{i=1}^{\infty} U_i(x)G_i(t) \tag{6.89}$$

Meirovitch states that the natural vibration modes are orthogonal and provides the orthonormal relations [114] as shown in Equations (6.90) and (6.91) which are used in solving for the valve response.

$$\int_0^l \rho A(x) U_i U_j \, dx = \delta_{ij} \tag{6.90}$$

$$\int_0^l U_i \frac{d^2}{dx^2}\left[EI(x)\frac{d^2U_j}{dx}\right]dx = \int_0^l EI(x)\frac{d^2U_i}{dx^2}\frac{d^2U_j}{dx^2}dx = \chi_i^2\delta_{ij} \tag{6.91}$$

To this end, the normalisation constant A_i in Equation (6.78) can be computed by solving the orthonormal Equation (6.90) as shown in Equation (6.92) which can be integrated numerically.

$$A_i^2 = \frac{1}{\int_0^l \rho A(x)\left[(\sin\beta x - \sinh\beta x) - \frac{\sin\beta l + \sinh\beta l}{\cos\beta l + \cosh\beta l}(\cos\beta x - \cosh\beta x)\right]^2 dx} \tag{6.92}$$

For the time response G_i, Equation (6.89) is substituted into Equation (6.74), multiplied by U_i and integrated over the entire length of the valve as shown in Equation (6.93) which is then reduced to Equation (6.94) with the orthonormal relations.

$$G_i\int_0^l U_i\frac{d^2}{dx^2}\left[EI(x)\frac{d^2U_i}{dx}\right]dx + \frac{d^2G_i}{dt^2}\int_0^l \rho A(x)U_i^2 dx + C\frac{dG_i}{dt}\int_0^l U_i^2 dx - \omega^2 G_i\int_0^l \rho A(x)U_i^2 dx = \int_0^l \rho A(x)\omega^2 r U_i + U_i f(x,t)dx \tag{6.93}$$

$$\frac{d^2G_i}{dt^2} + C\frac{dG_i}{dt}\int_0^l U_i^2 dx + \chi_i^2 G_i - \omega^2 G_i = \int_0^l \rho A(x)\omega^2 r U_i + U_i f(x,t)dx \tag{6.94}$$

For a beam with uniform cross-section, Equation (6.94) can be further reduced to the expression shown in Equation (6.95).

$$\frac{d^2G_i}{dt^2} + \frac{C}{\rho A}\frac{dG_i}{dt}\int_0^l \rho A U_i^2 dx + \Omega^2 G_i = \int_0^l \rho A \omega^2 r U_i + U_i f(x,t) dx$$

$$\rightarrow \frac{d^2G_i}{dt^2} + 2\zeta\Omega\frac{dG_i}{dt} + \Omega^2 G_i = \rho A \omega^2 r \int_0^l U_i dx + \int_0^l U_i f(x,t) dx \qquad (6.95)$$

In the case of the valve, Equation (6.95) can be solved numerically by substituting the force term on the right hand side with the appropriate fluid pressure from the compression chamber. Figure 6.20 shows the illustration of the fluid pressure acting on the valve plate. The force term in Equation (6.95) can then be reduced to the expression shown in Equation (6.96). However, when the valve is deflected, the force term will decrease due to flow of the fluid around the side of the valve. A coefficient $C_{deflect}$ is thus added to the expression to modify the force during valve deflection. For simplicity, it is assumed constant regardless of valve deflection.

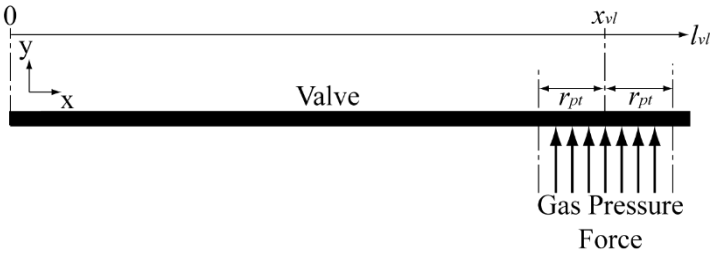

Figure 6.20: Fluid Pressure on Valve

$$\int_0^l U_i f(x,t) dx = C_{deflect} \cdot (p_{com} - p_{dis}) \int_{x_{vl}-r_{pt}}^{x_{vl}+r_{pt}} U_i A_{pt,d} dx \qquad (6.96)$$

where

$$A_{pt,d} = \frac{r_{pt}^2}{2}\left(2\theta_{pt} - \sin 2\theta_{pt}\right) \qquad (6.97)$$

$$\theta_{pt} = \cos^{-1}\left(\frac{x_v - x}{r_{pt}}\right) \qquad (6.98)$$

For the full dynamics of the valve, the solution of Equation (6.95) is to be combined with the mode shape U_i from Equation (6.78) as a product according to Equation (6.89). However, as the valve can only vibrate in its fundamental mode, the analysis is simplified by solving the case for only when $i = 1$.

6.6 Concluding Remarks

This chapter has covered all the aspects of kinematics and dynamics for the RV compressor prototype. This includes the following:

- Kinematics of assembly components with respect to main driving component.
- Dynamics model for generic RV assemblies using Lagrangian mechanics; the model can be employed for most RV design variants.
- Evaluation of individual friction torques for the RV compressor prototype, namely bearing flange endface friction, rotor endface friction, vane sliding friction and fluid shear friction.
- Considerations for orientation have also been taken into account for the computation of the friction torques since the weight of the components acting on the bearings would vary with compressor orientation.
- Valve dynamics for modelling the discharge valve have also been covered, with considerations for valves with non-uniform cross-section as well.

In addition, a preliminary analysis was carried out and the friction torques were individually computed and compared. A summary of the findings from the study is listed as follows:

- Bearing friction torques are significant in the lubricant-free RV compressor system – in fact, the lower cylinder bearing torque is already higher than that of the gas compression torque.
- The weight of the assembly resting on the lower cylinder bearing flanges increase the friction torque by 1.21 N·m.
- The friction loss due to the weight of the assembly contributes to a significant portion of the total friction loss. For a lower pressure difference of 1 bar, this friction loss constitutes about 38% of the total friction losses. At higher pressure differences, the friction loss arising from the weight of the assembly decreases: 18% of the total friction losses at a pressure difference of 4 bar.
- The large friction loss at the lower cylinder bearing is attributed to the large bearing radius which increases the torque loss.

- Vane tip, vane slot, rotor endface and cylinder endface friction are small compared to that of the bearing friction – it is about 20 times smaller than that of the bearing friction torques and hence may be ignored in future studies for convenience.
- Fluid shear torque can also be neglected since it is of four orders of magnitude lower than that of the bearing friction torques.

7 Thermal Model

Following the kinematics and dynamics model, this chapter proceeds to present the thermal model for estimating the steady-state operating temperatures of the RV compressor components. The temperature values are important for the modelling of heat transfer in the working chambers in order to accurately determine compressor performance. Furthermore, as the compressor has no liquid lubricant, dry sliding friction between the moving components would generate excessive heat in the compressor which may compromise the reliability of the compressor. With the model prediction for the component temperatures, precautions may be taken before the compressor fails prematurely due to excessive heat build-up.

The lumped thermal conductance method was employed to model the steady-state heat transfer and component temperatures in a rolling piston compressor [122]. In the heat transfer study, the model was validated with measurements and the majority of the prediction errors were found to be less than ±10% with a maximum error of ±20% for the elements at low temperatures [122]. As the RV compressor shares many similarities with that of the rolling piston, this same method would be used for modelling the heat transfer between the components in the compressor prototype.

7.1 General Model Assumptions and Sub-division of Components

In the lumped thermal conductance method, the components in the compressor are sub-divided into smaller elements with each element having its own bulk temperature and that any heat generation is uniform throughout the element.

Apart from the PEEK components, all other components in the compressor prototype were fabricated from AISI 4140 steel with a thermal conductivity of 42.7 W m^{-1} K^{-1} and specific heat of 473 J kg^{-1} K^{-1} [102]. Under steady-state conditions, spatial temperature variation in the subdivided elements of each steel component can be considered insignificant.

As PEEK has low thermal conductivity of 0.27 – 0.82 W m^{-1} K^{-1}, spatial temperature variation in PEEK components might be significant even during steady-state operation. The sliding thermal contact resistance of PEEK is investigated in Section 7.2.2 and the heat transfer for the PEEK rotor component is discussed in Section 7.3.

There are six components in the compressor which are subdivided into a total of 14 elements with simple geometric shapes. In addition, these elements are concentrically aligned with each other. As the bearing sleeves are thin, each of them is considered as a single element. Figure 7.1 shows the sub-division of the compressor components that will be used for the model. The rotor elements r2, r3 and r4 are concentric as elaborated in Figure 7.1(c).

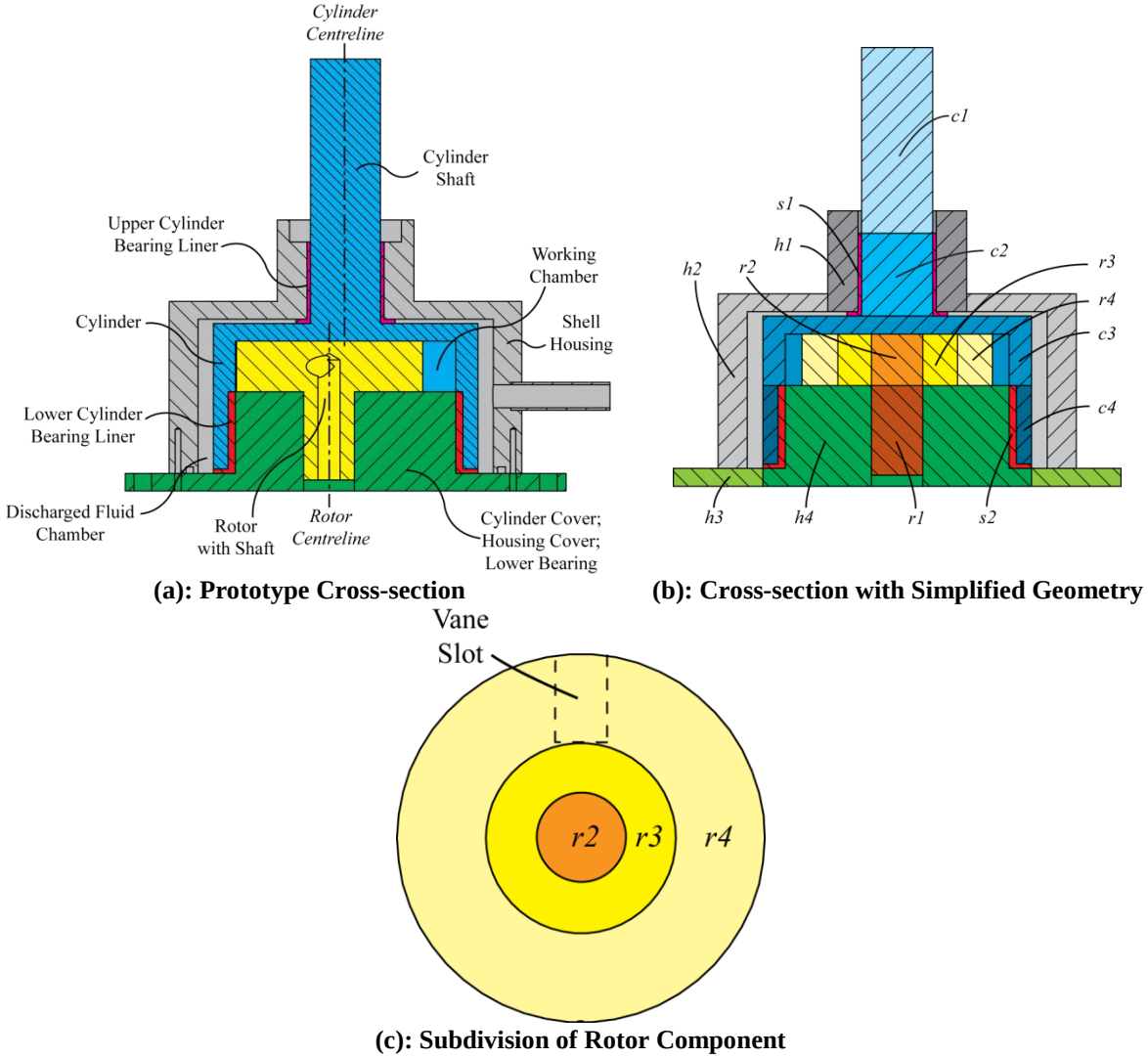

(a): Prototype Cross-section **(b): Cross-section with Simplified Geometry**

(c): Subdivision of Rotor Component

Figure 7.1: Subdivision of RV Components

The following assumptions are made for the thermal model:

- Steady-state condition
- Isothermal elements

- Rotor component is assumed to be concentric with the entire compressor prototype since the eccentricity is small (7.5 mm) compared to the housing diameter (160.0 mm)
- Similarly, the rotor shaft hole in element *h4* is also assumed to be concentric
- One-dimensional heat transfer between adjacent elements in either the radial or axial directions as they are concentrically aligned
- One-dimensional heat transfer between the surroundings and the compressor as the overall prototype is axisymmetric
- The temperatures of the fluid in the housing shell and working chamber are assumed to remain constant during heat transfer
- Thermal contact resistance between steel components are negligible
- Volume changes in element due to thermal expansion/contraction are negligible
- Radiation heat transfer between compressor components is negligible

Existing convection correlations found in the literature will be used for heat transfer at the solid-fluid interfaces [16, 33, 123–126]. Thermal contact and dry sliding friction models from literature [68, 127] will be employed for modelling heat generation and transfer at rubbing interfaces.

7.2 Heat Transfer Model

7.2.1 Heat Transfer Equations

For an element, the First Law of Thermodynamics [105] is applied to the element as shown in Equation (7.1). As the analysis is for the steady-state condition, the time dependent variables on the left-hand side can be ignored and this is shown as Equation (7.2).

$$\frac{d}{dt}\left[m_{cv}\left(u_{cv}+\frac{v_{cv}^2}{2}+gz_{cv}\right)\right]$$

$$=\dot{Q}_{cv}-\dot{W}_{cv}+\sum_i\left(h_i+\frac{v_i^2}{2}+gz_i\right)\dot{m}_i-\sum_o\left(h_o+\frac{v_o^2}{2}+gz_o\right)\dot{m}_o \tag{7.1}$$

$$\dot{Q}_{cv}-\dot{W}_{cv}+\sum_i\left(h_i+\frac{v_i^2}{2}+gz_i\right)\dot{m}_i-\sum_o\left(h_o+\frac{v_o^2}{2}+gz_o\right)\dot{m}_o=0 \tag{7.2}$$

As the elements are made up of a single solid, there is no mass flow in or out of the element. To this end, the enthalpy change due to mass flow can be neglected. Furthermore, it is also assumed that the volume change of the elements due to contraction or expansion is negligible; this signifies that the work is zero ($\dot{W}_{cv}$) which further simplifies the equation to that shown in Equation (7.3).

$$\dot{Q}_{cv} = 0 \tag{7.3}$$

Equation (7.3) shows that the net heat flow for each element is essentially zero at steady-state condition; any heat transfer into the element is balanced by heat transfer out of the material and that any heat generation within the element would be dissipated by heat transfer out of the material as well. To this end, Equation (7.3) can be rewritten as shown in Equation (7.4). A schematic representation of the control volume for a typical element *i* in the thermal model is therefore illustrated in Figure 7.2.

$$\sum_{i} H_i \Delta T_i + \dot{Q}_{gen} = \sum_{o} H_o \Delta T_o \tag{7.4}$$

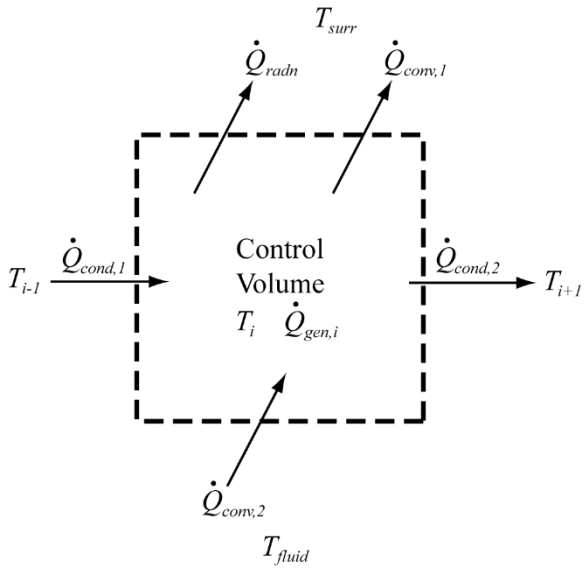

Figure 7.2: Control Volume for Steady-state Heat Transfer

Equation (7.4) is the governing equation that will be used for each element in the compressor for the analysis. The main modes of heat transfer in the compressor are conduction

and convection whereas the main modes of heat transfer between the compressor and its surroundings are convection and radiation.

For conduction heat transfer, it is assumed that there is negligible thermal contact resistance between the stationary components, the thermal properties are constant and uniform throughout the element. For radiation heat transfer, it is assumed that the surfaces are grey and diffuse.

As the elements are axisymmetric and concentrically aligned, the one-dimensional heat transfer equations [123] are written as Equations (7.5) – (7.7) for conduction, convection and radiation respectively.

$$\dot{Q}_{cond} = h_{cond} A_{cond} \Delta T \tag{7.5}$$

$$\dot{Q}_{conv} = h_{conv} A_{conv} \Delta T \tag{7.6}$$

$$\dot{Q}_{radn} = h_{radn} A_{radn} \Delta T \tag{7.7}$$

where

$$h_{cond} = \frac{k}{\Delta x} \text{ or } \frac{k}{r_1 \ln\left(r_2/r_1\right)} \tag{7.8}$$

$$h_{conv} = \frac{k}{l} \mathrm{Nu} \tag{7.9}$$

$$h_{radn} = \varepsilon \sigma F_{ij} (T_w + T_{surr})(T_w^2 + T_{surr}^2) \tag{7.10}$$

7.2.2 Thermal Contact Model for Dry Sliding Interfaces

Due to the lack of lubricants, dry sliding friction at the sliding interfaces is expected to generate great amounts of heat. However, due to the dissimilar rubbing surfaces, the amount of heat that is generated on each surface will be different. This section will delve into quantifying the amount of heat that is generated at each surface for the thermal model.

Equation (7.11) shows the expression for the total heat generated at the interface due to friction. Assuming that frictional heat is generated only at the interface, the heat generation coefficient ξ that governs the ratio of heat being produced on each surface is dependent on the sliding thermal contact resistance R_{sl} as shown in Equation (7.12) [66, 127]. The heat

generation coefficient would split the total frictional heat as generated by surfaces 1 and 2 as shown in Equation (7.13).

$$\dot{Q}_f = F_f v_{sl} = F_f \omega_{shaft} r_{shaft} \tag{7.11}$$

$$\xi = \frac{R_{sl,2}}{R_{sl,1} + R_{sl,2}} \tag{7.12}$$

$$\left.\begin{aligned} \dot{Q}_{f,1} &= \xi \dot{Q}_f \\ \dot{Q}_{f,2} &= (1-\xi)\dot{Q}_f \\ \dot{Q}_f &= \dot{Q}_{f,1} + \dot{Q}_{f,2} \end{aligned}\right\} \tag{7.13}$$

Chantrenne and Raynaud [66] go on to develop a correlation for determining the dimensionless sliding thermal contact resistance for two rough surfaces in dry sliding contact as shown in Equation (7.14). The dimensionless sliding thermal contact resistance can then be converted into the corresponding thermal contact resistance value as shown in Equation (7.15). The correlation is based on the material characteristics, sliding velocity, and profile of the surface asperities.

Chantrenne and Raynaud [66] also investigated the asperity profile of a typical surface from the turning process and this is shown in Figure 7.3. For the model, the surface asperities are assumed to be uniformly periodic with each asperity having the same height and width, separated at a constant distance as illustrated in Figure 7.4.

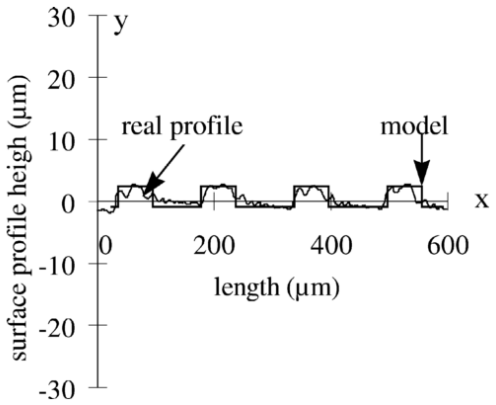

Figure 7.3: Aspertiy Profile of a Turned Surface [66]

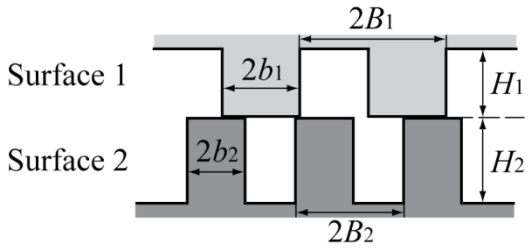

Figure 7.4: Assumed Asperity Profile at Interface

$$R^*_{sl,i} = 0.93\left(\frac{1}{b^*_i} - 1\right)\cdot H^*_i + 0.4\left(\frac{1}{v^*_i}\right)^{0.24}\cdot\left(\frac{1}{b^*_i} - 1\right)^{1.45}, \qquad i = 1,2 \tag{7.14}$$

$$R_{sl,i} = \frac{2B_i R^*_{sl,i}}{k_i} \tag{7.15}$$

where

$$v^*_i = \frac{2v_{sl}B_i\rho_i c_{p_i}}{k_i} \tag{7.16}$$

$$H^*_i = \frac{H_i}{2B_i} \tag{7.17}$$

$$b^*_i = \frac{b_i}{B_i} \tag{7.18}$$

Two different types of PEEK materials are used in the compressor prototype, namely PEEK in its pure form and bearing grade PEEK, which is a composite of PEEK with carbon fibres, PTFE and graphite fillers. A comparison between the sliding thermal contact resistances of the PEEK materials and AISI 4140 steel is computed for a range of velocities is shown in Figure 7.5. There are two rubbing pairs which are those between steel and the two different PEEK materials used.

It is assumed that both the rubbing surfaces have the same roughness of 0.6 µm Ra; with equal values of height, width and separation distance. The asperity dimensions used for this study are arbitrarily determined with reference from the asperity profile in Figure 7.3 and the values are shown in Table 7.1. The material properties are listed in Table 7.2. The material properties of PEEK are obtained from the manufacturer's specifications which can be found in Appendix A-7.

Table 7.1: Asperity Properties

Property	Value, μm
Height, H	0.6
Width, $2b$	0.5
Periodic Separation, $2B$	1.0

Table 7.2: Material Properties

Pure PEEK	Value
Thermal Conductivity, W m^{-1} K^{-1}	0.27
Density, kg m^{-3}	1310
Specific Heat Capacity, J kg^{-1} K^{-1}	1100
Bearing Grade PEEK	
Thermal Conductivity, W m^{-1} K^{-1}	0.82
Density, kg m^{-3}	1440
Specific Heat Capacity, J kg^{-1} K^{-1}	1100
AISI 4140 Steel [102]	
Thermal Conductivity, W m^{-1} K^{-1}	42.7
Density, kg m^{-3}	7700
Specific Heat Capacity, J kg^{-1} K^{-1}	473

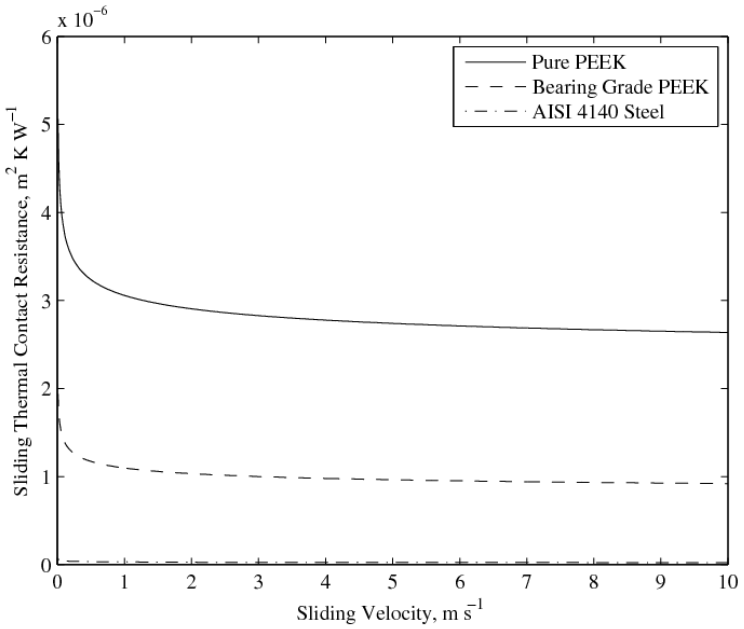

Figure 7.5: Comparison of Thermal Contact Resistance Between PEEK Materials & Steel

It is noted that the difference between the sliding thermal contact resistances of both PEEK materials and AISI 4140 steel decreases with increasing sliding velocity. However, these resistances of both PEEK materials are approximately two orders higher than that of steel.

With respect to the chosen asperity dimensions, an increase in surface roughness would increase the sliding thermal contact resistance for steel. However, with reference to Appendix A-5, only an unrealistic surface roughness profile whereby the periodicity of the asperities is several times its width would give rise to a large increase in sliding thermal contact resistance. Hence, realistic deviations from the assumed asperity dimensions would not cause the sliding thermal contact resistance of steel to have drastic changes.

The heat generation coefficient for the steel surface for the range of sliding velocities for both rubbing pairs can be found in Figure 7.6. The heat generation coefficient for steel can therefore be approximated to 0.99 and 0.975 when rubbing with pure PEEK and bearing grade PEEK, respectively.

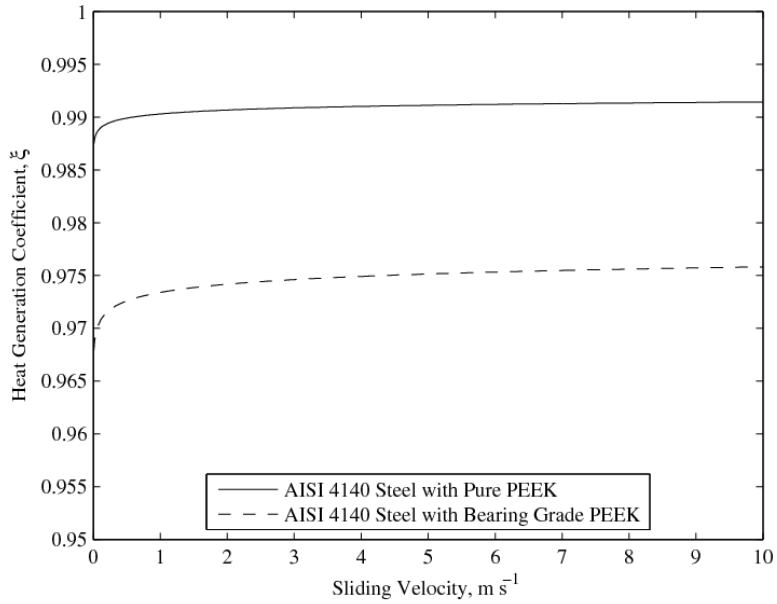

Figure 7.6: Heat Generation Coefficient for AISI 4140 Steel

Therefore, for the friction heat generated between the rotor shaft and bearing, as the shaft is made of bearing grade PEEK, 97.5% of the heat generated shall be absorbed by the steel bearing surface. On the other hand, for rubbing with pure PEEK, the steel surface shall absorb 99% of the heat generated. The remainders of the heat for both cases are absorbed by the PEEK materials.

Hence, PEEK can be assumed to absorb negligible friction heat during dry sliding with steel; all friction heat at the bearings would be absorbed by the steel shaft and/or steel bearing surface. Furthermore, since the PEEK bearing liners can rotate freely with either the shaft or remain stationary with the journal bearing during operation, it shall be assumed that it would remain stationary half of the time while rotating with the shaft for the other half of the time. Thus, there is sliding contact for both the shaft and journal bearing surface. Hence, the friction heat is assumed to be evenly distributed between the shaft and bearing surface.

The PEEK bearing liner is just a thin layer between the steel shaft and steel journal bearing. Since there is negligible heat conduction between the steel shaft/bearing and PEEK bearing liner, the steady-state temperature of the PEEK bearing liner can be assumed to be the average of the steel shaft and bearing temperatures.

To this end, here are the additional assumptions for the PEEK components:

- The absorption of friction heat by the PEEK elements are negligible; all friction heat is absorbed by steel instead
- Friction heat at the bearings is assumed to be split evenly between the steel shaft and bearing surfaces due to free rotation of the PEEK bearing liner.
- The steady-state temperatures of the PEEK bearing liners would be the average of the steel shaft and bearing temperatures.

7.2.3 Other Assumptions and Heat Transfer Correlations

The breakdown of the components presented in Figure 7.1 results in most of the element having standard geometric shapes mostly in the form of cylinders. For element H1 with a slightly more complicated geometry, it is simplified to that of an annular cylinder for the study. The relevant heat transfer correlations for horizontal surfaces, vertical surfaces and cylindrical surfaces of the elements are presented:

i. Free convection heat transfer correlations for housing shell and base cover elements – the Nusselt number correlation for free convection [128] on the upper surface of the housing shell and lower surface of the base cover is given by Equations (7.19) and (7.20), respectively. In addition, as the diameter of the housing shell is large, its outer vertical surface can be treated as that of a vertical plate in which its Nusselt number [129] is given by Equation (7.21).

$$\mathrm{Nu} = \begin{cases} 0.54\mathrm{Ra}_{l_{ch}}^{1/4}, & 10^4 \leq \mathrm{Ra}_{l_{ch}} < 10^7 \\ 0.15\mathrm{Ra}_{l_{ch}}^{1/3}, & 10^7 \leq \mathrm{Ra}_{l_{ch}} < 10^{11} \end{cases} \tag{7.19}$$

$$\mathrm{Nu} = 0.27\mathrm{Ra}_{l_{ch}}^{1/4}, \quad 10^5 \leq \mathrm{Ra}_{l_{ch}} \leq 10^{10} \tag{7.20}$$

$$\mathrm{Nu} = \begin{cases} 0.68 + \dfrac{0.67\mathrm{Ra}_{l_{ch}}^{1/4}}{\left[1 + \left(\dfrac{0.492}{\mathrm{Pr}}\right)^{9/16}\right]^{4/9}}, & 0 < \mathrm{Ra}_{l_{ch}} \leq 10^9 \\ \left[0.825 + \dfrac{0.387\mathrm{Ra}_{l_{ch}}^{1/6}}{\left(1 + \left[\dfrac{0.492}{\mathrm{Pr}}\right]^{9/16}\right)^{8/27}}\right]^2, & \mathrm{Ra}_{l_{ch}} > 10^9 \end{cases} \tag{7.21}$$

where

$$\mathrm{Ra}_{l_{ch}} = \frac{g\rho\beta|T_w - T_\infty|l_{ch}^3}{\mu\alpha} \tag{7.22}$$

$$\mathrm{Pr} = \frac{\mu c_p}{k} \tag{7.23}$$

$$l_{ch} = \frac{\text{Heat transfer area}}{\text{Perimeter}} \tag{7.24}$$

ii. Convective heat transfer coefficient in the working chamber – a number of different heat transfer correlations were tested by Tan and Ooi [16] and it was found that the correlation by Liu and Zhou [33] provided the most accurate prediction of working chamber pressure in the RV compressor. Hence, the same correlation shall be employed here for modelling the convective heat transfer in the working chambers. The correlation presented in Section 5.2 is reproduced here in Equation (7.25). As the current study is for that of steady-state heat transfer, the mean Reynolds number and Prandtl number of the fluid in the working chamber shall be used for this study as shown in Equations (7.26) and (7.27) with the approximation when the angle steps are discretised. In addition, for the calculation of heat transfer, the temperature of the working fluid is assumed to be mean of the suction and discharge temperatures.

$$\mathrm{Nu} = 0.75\overline{\mathrm{Re}}^{0.8}\overline{\mathrm{Pr}}^{0.6} \tag{7.25}$$

where

$$\overline{\mathrm{Re}} = \frac{1}{2\pi}\int_0^{2\pi} \frac{\rho v D}{\mu}\, d\theta \approx \frac{1}{n}\sum_{j=1}^{n} \frac{\rho_j v_j D_j}{\mu_j} \tag{7.26}$$

$$\overline{\mathrm{Pr}} = \frac{1}{2\pi}\int_0^{2\pi} \frac{c_p \mu}{k}\, d\theta \approx \frac{1}{n}\sum_{j=1}^{n} \frac{c_{p_j}\mu_j}{k_j} \tag{7.27}$$

iii. Convective heat transfer coefficient in the housing chamber – the working fluid is discharged into the housing shell from the cylinder and this is another medium of convective heat transfer within the compressor. As investigated in Section 6.4.4, the high speed rotation of the cylinder within the housing shell results in Taylor-Couette flow for the discharged fluid. Therefore, heat transfer correlations for Taylor-Couette flow shall be adopted for modelling the convective heat transfer in the discharge chamber between the cylinder and housing walls as shown in Equation (7.28) [124]. On the other hand, for flow in the annular gap at the endfaces, it is turbulent as demonstrated by the CFD results in Section 6.4.4 and therefore, the turbulent convective heat transfer of a flow over a flat plate can be expressed as shown in Equation (7.29) [123]. The speed of the flow is assumed to be the mean of the cylinder and housing wall speeds and the length would be circumferential length of the gap.

$$\mathrm{Nu} = 0.409\left(\frac{\mathrm{Ta}}{C_{geo}}\right)^{0.241}, \qquad 1700 \le \left(\frac{\mathrm{Ta}}{C_{geo}}\right) \le 10^7 \tag{7.28}$$

$$\mathrm{Nu}_{gap} = 0.037\mathrm{Re}_{gap}^{4/5}\mathrm{Pr}^{1/3} \tag{7.29}$$

where

$$\mathrm{Ta} = \frac{\omega_{crit}^2 \rho^2 r_{avg} \delta_{gap}^3}{\mu^2} \tag{7.30}$$

$$\omega_{crit} = \frac{\pi^4 \mu^2 r_{avg}}{s\delta_{gap}^3 r_i^2} \tag{7.31}$$

$$C_{geo} = \frac{1}{s}\left(\frac{\pi^4}{1697}\right)\left(1 - \frac{\delta_{gap}}{2r_{avg}}\right)^{-2} \tag{7.32}$$

$$s = 0.0572\left(1 - \frac{0.652\delta_{gap}}{r_i}\right) + 0.00056\left(1 - \frac{0.652\delta_{gap}}{r_o}\right)^{-1} \tag{7.33}$$

$$d_{gap} = r_o - r_i \tag{7.34}$$

$$r_{avg} = \frac{r_o + r_i}{2} \tag{7.35}$$

$$\mathrm{Re}_{gap} = \frac{\rho \omega_{avg} r_{avg} l_{gap}}{\mu} \tag{7.36}$$

$$l_{gap} = \pi(r_o + r_i) \tag{7.37}$$

iv. Convective heat transfer on rotating cylinder shaft – for a high speed rotating cylinder in quiescent air, it can be assumed that the convective heat transfer coefficient depends on only the Reynolds number [125, 126]. To this end, the orientation of the rotating cylinder shaft does not affect the convective heat transfer and the correlation by Becker [125] can be used. The average Nusselt number is expressed as shown in Equation (7.38) [125] and is valid for the case of the rotating cylinder shaft at speeds between 250 and 31,300 rev min^{-1} which is well within the operating conditions of the compressor.

$$\mathrm{Nu} = 0.119\mathrm{Re}_r^{2/3} \quad , \qquad 800 \leq \mathrm{Re}_r = \frac{2\rho \omega_{shaft} r_{shaft}^2}{\mu} \leq 10^5 \tag{7.38}$$

v. Radiation heat transfer to surroundings – the emissivity for polished metal surfaces ranges between 0.10 and 0.40 depending on the grade of finishing [123], in which the emissivity increases for duller surfaces. For the polished steel surface of the housing shell, its emissivity shall be estimated to be the average of the given range (0.25). In addition, as the temperature of the compressor is expected to exceed that of the surroundings, there will be net radiation heat transfer to the surroundings and the view factor for the heat transfer in this case would be at unity [123]. Therefore, the heat transfer coefficient for radiation heat transfer can be expressed as shown in Equation (7.39) with the emissivity value of 0.25 and view factor of 1.0.

$$h_{radn} = 0.25\sigma(T_w + T_\infty)(T_w^2 + T_\infty^2) \tag{7.39}$$

7.3 Heat Transfer in the Rotor

The rotor component is made from PEEK material which has very high sliding thermal contact resistance compared to steel. Even though it can be assumed to absorb negligible heat

from friction generated at the rubbing surfaces, the temperature of the PEEK components during steady-state operation will no doubt be higher than ambient in reality.

The working fluid is drawn into the working chambers through the suction line in the rotor. Hence, the friction heat that is absorbed by the rotor has to be dissipated in the suction line or working chambers. In addition, since the heat absorption from friction is almost negligible, heat dissipation into the suction fluid will also be almost negligible and to this end, it can be assumed that the temperature of the suction fluid stays constant. For steady-state analysis, it is assumed that the flow in the suction line is fully developed.

7.3.1 Convective Heat Transfer at Rotor Shaft Tip

One end of the rotor shaft is exposed to ambient and the exposed geometry can be considered as a rotating disc. The Reynolds number for a rotating disc is given in Equation (7.40).

$$\mathrm{Re}_{disc} = \frac{r_{disc}^2 \omega_{disc} \rho}{\mu} \tag{7.40}$$

As the diameter of the shaft is small (Ø23.0 mm), the rotational Reynolds number at 3000 rev min^{-1} is only 2600 as computed from Equation (7.40). Hence, the flow regime at the shaft tip is laminar. An experimental investigation by Cobb and Saunders [130] found that the heat transfer coefficient in the laminar range is best modelled by the correlation given by Wagner [131] as shown in Equation (7.41).

$$\mathrm{Nu} = 0.335\mathrm{Re}_{disc}^{0.5} \ , \qquad \mathrm{Re}_{disc} < 2.4\times10^5 \tag{7.41}$$

7.3.2 Mass Flow Rate in Rotor

The mass flow rate into the suction chamber through the rotor is used to calculate the average flow velocity of the intake fluid in the rotor. This is expressed in Equation (7.42) whereby the flow area of the fluid through the rotor is constant and dictated by the suction port area A_{suc}. The Reynolds number for the axial flow of the fluid inside the rotor can thus be calculated as shown in Equation (7.43) and varies up to a value of 16,000 for a rotation speed of 3000 rev min^{-1} with volumetric efficiency at unity.

$$v_{suc} = \frac{\dot{m}_d}{\rho A_{suc}} \tag{7.42}$$

$$\mathrm{Re}_{suc} = \frac{2\rho v_{suc} r_{pt,suc}}{\mu} = \frac{2\dot{m}_d}{\pi r_{pt,suc}\mu} \tag{7.43}$$

where

$$A_{suc} = \pi r_{pt,suc}^2 \tag{7.44}$$

7.3.3 Convective Heat Transfer in Shaft

The intake of fluid through the rotor first goes through the rotating shaft and is classified as an axial flow through a rotating duct. The rotation of the shaft affects the flow of the fluid; the rotating walls help reduce turbulence in the flow at the vicinity of the wall and thus heat transfer decreases with higher rotation speeds [132–134].

The heat flux is uniform as the shaft is subjected to the same magnitude of friction heating along its entire length. To this end, it is noted that there is linear spatial temperature variation in the rotor shaft along its length due to the constant heat flux but the rotor shaft element shall still be assumed to be of a constant temperature as the linear spatial temperature variation along the shaft is expected to be small.

Seghir-Ouali et al. [134] provide the heat transfer correlations for axial flow inside a rotating cylinder duct with a constant heat flux in Equations (7.45) and (7.46). At low rotation speeds, heat transfer is affected by both the rotation speed of the wall and axial velocity of the flow. However, at high rotation speeds, heat transfer due to the rotation speed of the wall is dominant and the influence of the axial velocity is negligible.

$$\begin{aligned} &\mathrm{Nu} = 0.01963\mathrm{Re}_{suc}^{0.9285} + 8.5101\times10^{-6}\mathrm{Re}_{\omega}^{1.4513}, \\ &\text{for } 0 < \mathrm{Re}_{suc} < 3\times10^{4}, 1600 < \mathrm{Re}_{\omega} \leq 2.77\times10^{5} \end{aligned} \tag{7.45}$$

$$\mathrm{Nu} = 2.85\times10^{-4}\mathrm{Re}_{\omega}^{1.19}, \qquad \mathrm{Re}_{\omega} > 2.77\times10^{5} \tag{7.46}$$

where Re_{ω} is the rotational Reynolds number given as follows:

$$\mathrm{Re}_{\omega} = \frac{2r_{pt}^2\omega_{shaft}\rho}{\mu} \tag{7.47}$$

7.3.4 Convective Heat Transfer in Rotor

From the rotor shaft, the fluid in the suction line continues inside the rotor. Based on the Reynold's number, it is an internal laminar flow with uniform wall temperature. The heat transfer coefficient is thus given in Equation (7.48).

$$\mathrm{Nu} = 3.66\,, \quad \mathrm{Re}_{suc} < 10^4 \tag{7.48}$$

7.4 Linear Algebra Equations for Component Elements

With 12 elements, there will be 12 simultaneous equations that must be solved to obtain the steady state operating temperatures of these elements. The equations can be arranged into a matrix and solved as a linear algebra equation.

As an example, for the cylinder element *c*1 shown in Figure 7.1, it is affected by free convection and heat transfer from element *c*2. Hence, the heat transfer to and from the element can be written as shown in Equation (7.49) which is rearranged into Equation (7.50).

$$H_{c1,c2}(T_{c1} - T_{c2}) + H_{c1,\infty}(T_{c1} - T_{\infty}) = 0 \tag{7.49}$$

$$\big(H_{c1,c2} + H_{c1\infty}\big)T_{c1} + H_{c1,c2}T_{c2} = H_{c1,\infty}T_{\infty} \tag{7.50}$$

where

$$H_{c1,c2} = H_{c2,c1} = \frac{k_{steel}A_{c1,c2}}{l_{c1,c2}} = \frac{2k\pi r_{shaft}^2}{l_{c1} + l_{c2}} \tag{7.51}$$

$$\begin{aligned} H_{c1,\infty} &= \frac{k_{air}A_{c1,\infty}}{l_{c1,\infty}}\big(0.119\mathrm{Re}_r^{2/3}\big) + 0.25A_{c1,\infty}\sigma(T_{c1} + T_{\infty})(T_{c1}^2 + T_{\infty}^2) \\ &= \frac{2k_{air}\pi r_{shaft}l_{c1}}{l_{c1}}\left[0.119\left(\frac{2\rho\omega_{shaft}r_{shaft}^2}{\mu}\right)^{2/3}\right] \\ &\quad + 0.25\sigma(T_{c1} + T_{\infty})(T_{c1}^2 + T_{\infty}^2)\big(2\pi r_{shaft}l_{c1}\big) \end{aligned} \tag{7.52}$$

The process is repeated for each element in the prototype and their corresponding equations are then assembled into a matrix. Due to the insulating PEEK bearing liners separating the cylinder from the housing shell, there is no coupling of temperatures between these two components. Furthermore, the rotor is also considered to be a separate system due to the insulating property of PEEK for heat conduction. Hence, each of the components will have

their own separate matrices as shown in Equations (7.53) – (7.55). $\boldsymbol{T}$ represents the component element temperatures, $\boldsymbol{X}$ represents the heat transfer relations and $\boldsymbol{Y}$ represents the loss to surroundings and heat source terms. Details of the heat transfer relations and full matrices can be found in Appendix A-4.

$$\boldsymbol{X}_c\boldsymbol{T}_c = \boldsymbol{Y}_c \tag{7.53}$$

$$\boldsymbol{X}_r\boldsymbol{T}_r = \boldsymbol{Y}_r \tag{7.54}$$

$$\boldsymbol{X}_h\boldsymbol{T}_h = \boldsymbol{Y}_h \tag{7.55}$$

Equations (7.53) and (7.55) are then solved for their respective $\boldsymbol{T}$ matrices which contains all the elements' temperature values for each component with Matlab's native linear algebra solver [135]. The solution would give the steady-state operating temperatures of the components for the RV compressor prototype.

7.5 Preliminary Analysis

This section will proceed with a preliminary analysis of the thermal model so as to gain some insight on the steady-state operating component temperatures. The operating conditions used for this analysis would be the same as those used in the first analysis presented in Chapter 6. These conditions are reproduced here in Table 7.3. It is assumed that there is no internal leakage occurring between the working chambers.

Table 7.3: Operating Conditions and Ambient Temperature

Operating Speed, rev min^{-1}	1,000 / 2,000
Working Fluid	Air
Suction Pressure, bar (abs)	1.0
Suction Temperature, °C	27.0
Discharge Pressure, bar (abs)	2.0 / 5.0
Coefficient of Friction	0.4
Ambient Temperature, °C	27.0

The steady-state operating temperatures of the elements in the cylinder, rotor and housing shell components at a discharge pressure of 2 bar (abs) are presented in Figure 7.7. The temperature of the upper PEEK bearing liner sleeve *s1* can then be taken as the mean temperature of elements *c2* and *h1* which is 58.5°C. Similarly, the temperature of the lower PEEK bearing liner sleeve *s2* is taken to be the mean temperature of elements *c4* and *h4* which is 72.4°C.

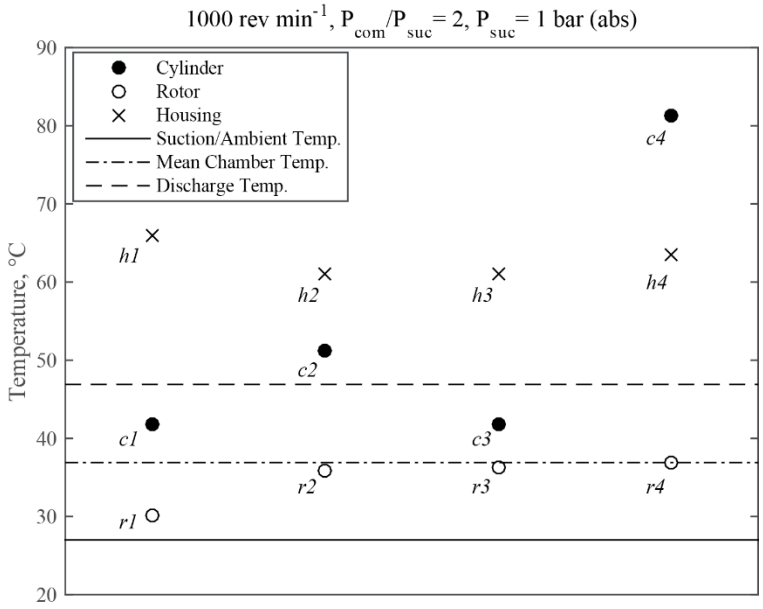

Figure 7.7: Predicted Steady-state Component Temperatures for 1 bar Pressure Difference

For a discharge pressure of 5 bar (abs), the steady-state operating temperatures of the components are presented in. The temperatures of the PEEK bearing sleeves *s1* and *s2* are then determined to be 120.5°C and 149.5°C, respectively.

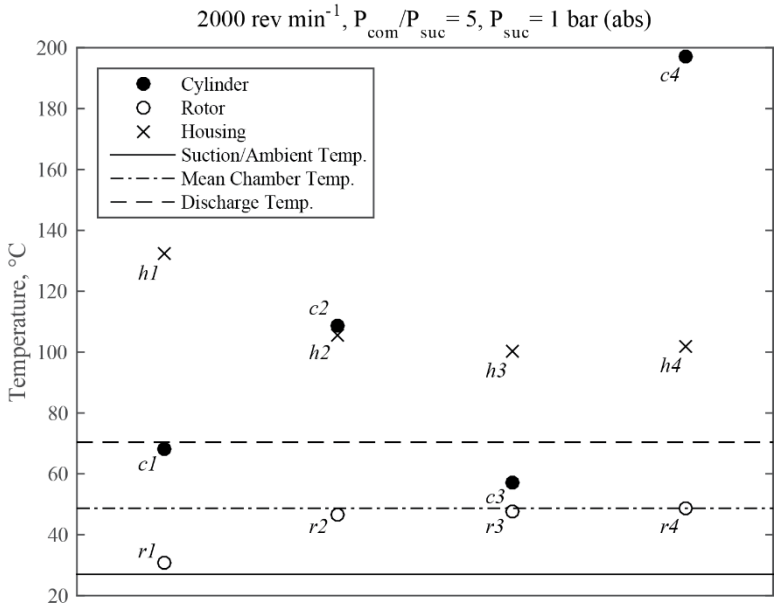

Figure 7.8: Predicted Steady-state Component Temperatures for 4 bar Pressure Difference

From the analysis, it is noted that the steady-state operating temperature of the rotor component (elements *r2, r3, r4*) would always be approximately the same as the average chamber temperature. This is because the rotor has a thermal conductivity of 0.82 W m^{-1} K^{-1} and is thus unable to dissipate heat effectively, so the temperature of the rotor would always be the about same as that of the chamber temperature. On the other hand, there is enhanced convective heat transfer between the rotor shaft and suction air due to the nature of the shaft rotation. This increases heat dissipation at the rotor shaft and results in lower temperatures (element *r1*) when compared to the rotor.

For the cylinder, it is noted that the steady-state operating temperatures have a wide variation between the different elements. The cylinder elements *c1* and *c3* have lower temperatures compared to their adjacent elements *c2* and *c4*. This is because elements *c2* and *c4* constitute the upper and lower cylinder shafts, respectively, and friction heating at these rubbing surfaces would increase the steady-state operating temperatures of these elements. Furthermore, as the lower cylinder shaft has a much larger diameter, friction heating is more severe in its case, thus resulting in very high steady-state operating temperatures. Element *c3* would have the lowest temperature for the cylinder component as there is enhanced in-chamber convective heat transfer whereby the working fluid is cooling the cylinder chamber continuously.

For the housing shell, as it is cooled by free convection from the surrounding air, its temperature variations are not as significant as compared to the cylinder. Element *h1* for the upper cylinder bearing was noted to have a higher temperature than element *h4* for the lower cylinder bearing despite having a lower friction loss owing to its smaller bearing diameter. This is due to the exposure of the lower cylinder bearing to the air in the working chamber whereby the enhanced in-chamber convective heat transfer has enabled element *h4* to dissipate more heat compared to element *h1* in which heat is dissipated via free convection only.

Bearing in mind that the analysis was done under ideal conditions with no internal leakage, the circulation of hot leakage fluid between the suction and compression chambers during actual operation would result in higher steady-state operating temperatures than those presented in Figure 7.7 and Figure 7.8. In addition, practical operation would see the compressor operating under more severe conditions such as higher speeds and larger pressure differences which would result in even higher steady-state operating temperatures.

To this end, the design and use of PEEK bearing liners might not be feasible for practical operation due to severe friction heat in the components. Alternatively, the use of sealed bearings with coefficients of friction in the range of 0.001 – 0.005 [136] is proposed instead which would mitigate the problem of excessive friction heating.

7.6 Concluding Remarks

As friction heating would be significant in that of a lubricant-free compressor, this chapter sets out to model the steady-state operating temperatures of the compressor components. The lumped thermal conductance method was proven to be accurate as validated with measurements in the case of a hermetic rolling piston compressor [122]. As the RV mechanism shares many similarities with the rolling piston, this method is therefore suitable for modelling the heat transfer between the RV compressor components as well. A summary of this chapter is as follows:

- The compressor components are sub-divided into simpler geometry for use with the lumped thermal conductance method.
- The elements are assumed to be isothermal and the temperatures of the working fluid in the chambers are also assumed to be at constant.

- One-dimensional heat transfer is assumed for the model due to the concentric alignment of the components.
- A thermal sliding contact model is used for determining the amount of friction heat absorbed by each surface during sliding contact. Analysis shows that 97.5% and 99% of the friction heat is absorbed by the steel surface for rubbing with bearing grade PEEK and pure PEEK respectively.
- It is assumed that the PEEK components absorb negligible friction heat during sliding contact and thus do not partake in heat transfer in the system since the components are always in sliding contact.
- Conventional heat transfer correlations were presented and used for modelling the heat transfer between the elements.
- Heat transfer equations are then formulated for each component and these equations are combined into a single linear algebra matrix problem to be solved
- Preliminary analysis shows that the steady-state operating temperature of the rotor will be approximately the same as that of the mean chamber temperature. On the other hand, the walls of the suction line in the rotor shaft are rotating, resulting in enhanced heat dissipation and thus, lower temperature values for the rotor shaft.
- The lower cylinder bearing will have the highest steady-state operating temperature due to high friction loss because of having a large bearing diameter. On the other end, the continuous flow of working fluid into and out of the cylinder chamber helps to cool the overall component.
- As ideal, conservative operating conditions were used for the preliminary analysis, even higher operating component temperatures would be expected with internal leakage, faster operating speeds and higher pressure ratios. An alternative would be the use of sealed bearings which has a much lower coefficient of friction in the range of 0.001 – 0.005 [136].

8 Experiment

The prototype designed with the concepts introduced in Chapter 3 was evaluated through experimental investigations. The measurements are then used to validate the accuracy of the theoretical models developed in Chapters 4 to 6 by comparing the values.

8.1 Prototype Physical Dimensions

The AISI-4140 steel components of the compressor prototype were fabricated by the vendor, Swift Precision Engineering Pte Ltd and the PEEK components were machined by the laboratory workshops in Nanyang Technological University. After receiving the components, the dimensions were checked for conformity to the tolerances specified and to determine the exact clearance gaps between the components. The measurements were made with a micrometer screw gauge and digital vernier caliper with accuracies of ±0.001 mm and ±0.01 mm, respectively. Multiple measurements were made for each dimension and the arithmetic mean was computed and recorded. The key dimensions with their specified tolerances and corresponding measurements from the prototype are shown in Table 8.1. The asterisk indicates that the PEEK component has been refabricated/reworked in order to reduce the clearance or correct the erroneous dimension.

Table 8.1: Prototype Dimensions

Component/Dimension	**Specification, mm**	**Measurement, mm**
Rotor (Bearing-grade PEEK)		
Diameter	85.00 ± 0.01	84.98
Length	23.00 – 0.01	22.966
Vane Slot Width	12.00 + 0.01	12.15
Shaft Diameter	23.00 – 0.01	22.997
Shaft Length	40.0 ± 0.1	40.08
Cylinder (Steel)		
Inner Diameter	100.00 ± 0.01	100.01
Chamber Length	23.00 + 0.01	23.03
Upper Shaft Diameter	31.75 – 0.01	31.75

Lower Shaft Diameter	106.50 + 0.01	106.43
Lower Shaft Length	35.00 + 0.01	34.95
Component/Dimension	**Specification, mm**	**Measurement, mm**
Vane (PEEK)*		
Neck Width	5.00 - 0.01	5.01
Tip Diameter	12.00 – 0.01	12.13
Length	23.00 ± 0.01	23.02
Upper Bearing Sleeve (PEEK)		
Inner Diameter*	31.75 + 0.05	31.74
Outer Diameter	35.00 – 0.05	35.00
Flange Thickness*	2.00 – 0.05	1.482
Length	35.00 – 0.05	35.03
Lower Bearing Sleeve (PEEK)		
Inner Diameter	100.00 + 0.05	99.95
Outer Diameter	106.50 – 0.05	106.40
Flange Thickness*	2.00 + 0.05	1.958
Length	35.00 – 0.05	35.02
Housing Shell (Steel)		
Upper Journal Bearing Diameter	35.00 + 0.01	35.00
Rotor Shaft Journal Bearing Diameter	23.00 + 0.01	23.01
Lower Journal Bearing Diameter	100.00 – 0.01	100.05
Lower Journal Bearing Length	37.00 – 0.01	36.86

In addition, the bearing surfaces were measured by a profilometer to determine the surface roughness. The surface roughness measurements were also done multiple times and the average values were recorded. Based on the measured dimensions, the clearance at each of the bearings and surface roughness at each bearing surface are tabulated in Table 8.2. For the bearing clearances, it is the sum of two clearances; the first between the shaft and bearing sleeve, and the second between the bearing sleeve and journal bearing. Note that due to manufacturing defects, some of the bearings have a poor fit, namely that of the upper and lower

cylinder bearings. For the lower cylinder bearing, due to the limited thickness and large diameter of the bearing sleeve, the bearing sleeve was found to be warped – the bearing liner was not entirely circular, resulting in an interference fit in certain areas despite the clearance indicated from measurements. This was identified as the main cause of seizure in the compressor that will be elaborated in Section 8.4.

Table 8.2: Bearing Clearance and Surface Roughness

Bearing	Clearance, μm	Surface Roughness, μm Ra
Upper Cylinder	– 10	2.67
Lower Cylinder	15	1.20
Rotor	13	1.60

Lastly, the endface and radial clearances for calculation of leakage are tabulated in Table 8.3. Note that the default radial clearance is small compared to that of the endface clearances; accounting for the average total clearance at both endfaces (155 μm), the gap was found to be approximately ten times that of the radial clearance (15 μm). To this end, the dominant leakage paths can be considered to be that of the endface leakages.

Table 8.3: Leakage Path Clearance

Leakage Path	Clearance, μm
Radial	15
Slot (Vane Tip)	20
Vane Endface (one end)	64
Rotor Endface (one end)	91

In all, the prototype was found to be less than satisfactory in terms of the accuracy of the fabrication. However, due to the limited resources allocated for this project, only certain components were able to be reworked and the rest were left as it was.

8.2 Experimental Setup

The experimental setup is designed to measure the performance of the compressor, namely the discharge pressure and input torque. For simplicity, the compressor is employed in an open loop air cycle. Atmospheric air is drawn into the prototype directly and the compressed

air is discharged into a Swagelok 304L-HDF4-300-PD receiver tank in which the discharge pressure is measured by a Kulite XT-375 pressure transducer with a measurement capability up to 35 bar (gauge). A needle valve controls the outflow of the compressed air from the receiver tank and the discharge flow rate is then measured by a Gilmont GF-1400 glass float rotameter with a range of 1000 – 36,000 ml min^{-1}. The combination of the receiver tank and needle valve reduces the pulsation of the compressor discharge which allows steady measurement readings from the rotameter. The compressor is powered by an ABB 2.2kW two-pole induction motor with a frequency controller to regulate the output rotation speed. A Futek TRS605 torque transducer with a ±50 N·m measurement range is connected between the motor and compressor shafts to measure the torque input to the prototype. Type T (bare-wire, AWG 24) thermocouples were connected to the receiver tank and at the discharge from the rotameter to measure the discharge temperature and also the flow temperature at the rotameter for density corrections in the mass flow calculation. In addition, four other thermocouples were connected to the compressor shell housing at various locations to determine the component temperatures, namely the upper cylinder bearing, lower bearing, compressor base mount and compressor shell housing. The ambient air conditions for the compressor inlet were measured by a weather station in the lab as shown in Figure 8.1. The maximum measurement uncertainties associated with these devices are tabulated in Table 8.4. A schematic of the experiment setup is shown in Figure 8.2 and the actual setup is shown in Figure 8.3.

Table 8.4: Measurement Uncertainties

Pressure transducer	±0.1 bar
Rotameter	±360 ml min^{-1}
Torque transducer	±0.1 N·m
Type-T Thermocouple	±1.0 K [137, 138]

Figure 8.1: Weather Station

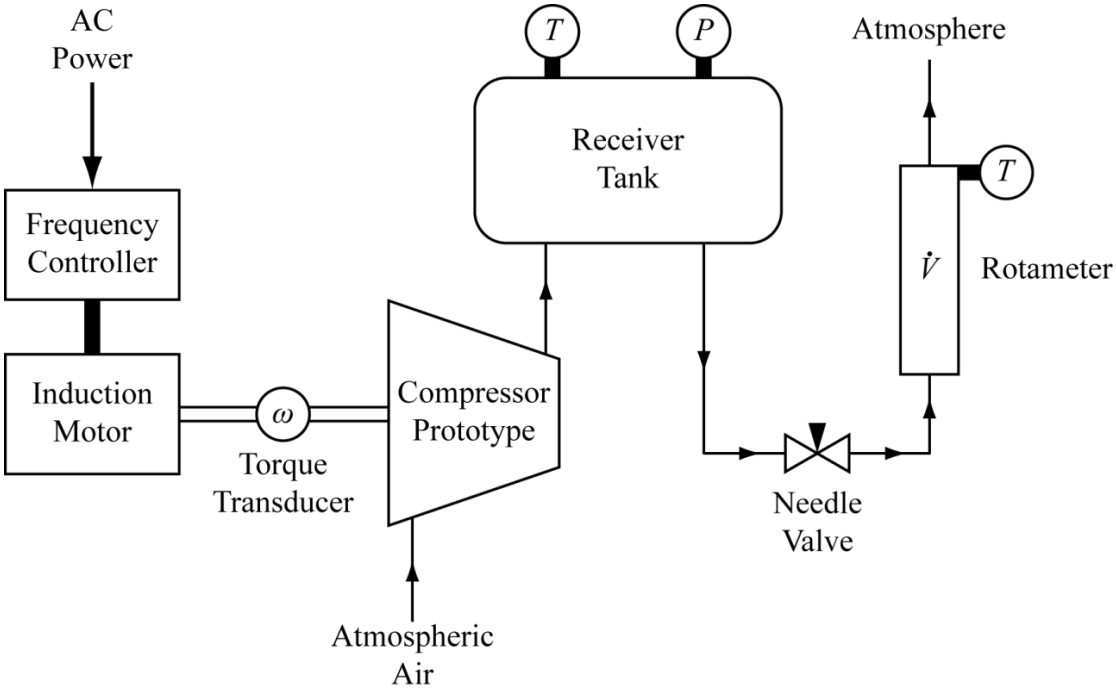

Figure 8.2: Experiment Setup Schematic

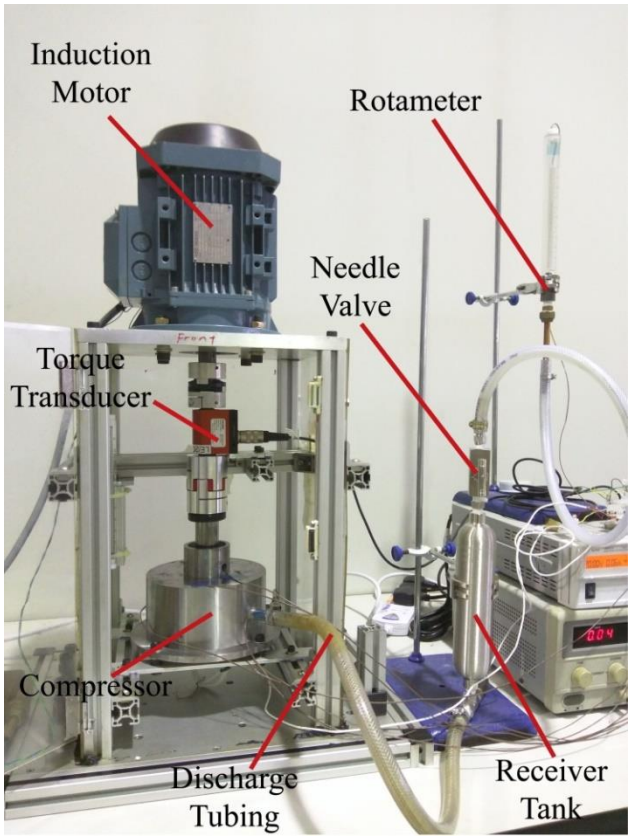

Figure 8.3: Actual Experiment Layout

The measurement devices are hooked up to the Yokogawa MX 100 data acquisition unit and readings are taken at the maximum rate of 100 Hz. The calibration details and data of the devices can be found in Appendix A-8.

Ideally, a data logger with a high sampling rate would be more suitable for determining the instantaneous torque to the compressor but it was unavailable due to the lack of resources allocated for the project. Equation (8.1) shows the expected number of data points per revolution (n_{data}) based on the sampling rate of the data logger (χ_{data}) and rotation speed (ω)

$$n_{data} = \frac{2\pi\chi_{data}}{\omega} \tag{8.1}$$

In spite of the sampling rate limitation, the motor torque readings from the data logger can still be used to determine the average operating speed with the relations presented in Section 6.3.6. Therefore, the data logger is still useful in determining the average operating speed of the compressor. Together with the discharge pressure and temperature readings, the

performance characteristics of the prototype can be ascertained albeit without useful instantaneous torque readings.

8.3 Experimental Procedure

It was observed that the prototype was very prone to seizure and would stop after about less than a minute of operation at operating speeds above 800 rev min^{-1}. Hence, the experiment to evaluate the compressor had involved varying the mass flow rate instead of varying the discharge pressure. Details on this problem would be discussed in Section 8.4. The experimental procedures for measurement of prototype performance were hence tailored for short operating time windows as follows:

1. The pipes and fittings were firstly ensured to be securely connected to prevent possible leakage.
2. The motor frequency controller was adjusted to the desired operating motor synchronous speed. The relation between the synchronous speed and input frequency can be found in Equation (6.24).
3. The motor was turned on and the needle valve was then adjusted to attain the desired flowmeter reading.
4. Once the desired flowmeter reading was obtained, the motor was then switched off to vent the pressurised air in the receiver tank.
5. Measurements were then taken – upon switching on the motor, 20 s of measurements were then recorded for the stipulated flow rate before switching off the motor.
6. A time period of about 15 min was allocated between each measurement run to allow the compressor components to cool down so as to avoid seizure.
7. Steps 3–5 were repeated for obtaining measurements based on different flow rates for a constant operating speed.
8. When the motor operating speed was changed, the experimental procedure was restarted from step 2.

8.4 General Observations

As expected, the prototype performance had two main problems. Due to the absence of lubricants, its performance was severely affected by frequent seizures during operation and internal leakage. The prototype was prone to seizure and would stop after only one to two minutes of operation. In addition, severe leakage was observed in the prototype, as only small increments in pressure were detected in the receiver tank during operation.

Due to the short operating timespan of the compressor, there was insufficient time for the effects of frictional heating at the bearing surfaces to propagate into the working chambers. Hence, it will be assumed that the chamber walls remained at room temperature in the theoretical model during validation of the model.

8.4.1 Seizure

It is absolutely necessary that the rubbing surfaces of such a lubricant-free compressor be clean and free from any contaminants such as oil or dirt. Oil was used to prevent rusting of the prototype. For the lubricant-free RV prototype, the accidental presence of residual lubricant can cause the compressor to seize up as well. Residual oil was present during the initial test run of the compressor causing seizure at the journal bearings – due to the high friction heat at the rubbing surface with no lubricant network to circulate the oil, the trapped oil decomposed into hard carbon particles which then caused the compressor to seize up. Figure 8.4 shows the decomposed carbon particles on the rotor shaft, rotor shaft journal bearing surface, lower cylinder shaft, lower cylinder shaft and cylinder bearing sleeves of the RV prototype – the discolouration on the surfaces are the remnants of the burnt/decomposed oil residue.

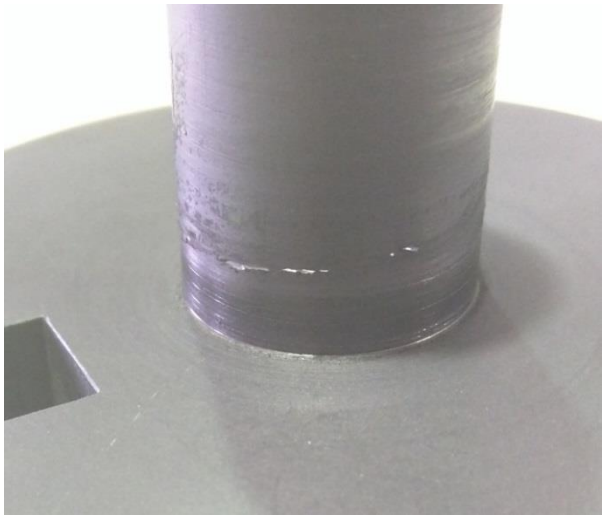

(a): Rotor Shaft

(b): Rotor Journal Bearing

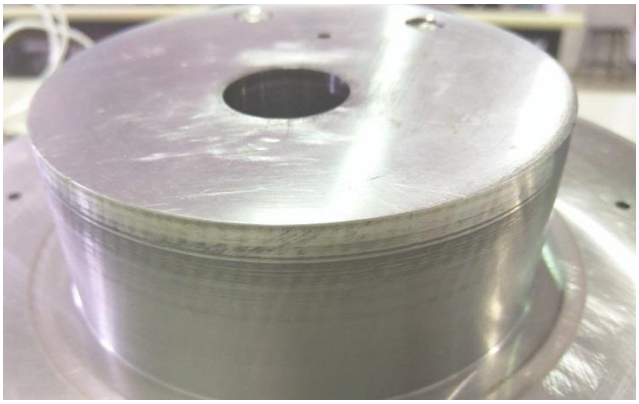

(c): Lower Cylinder Shaft

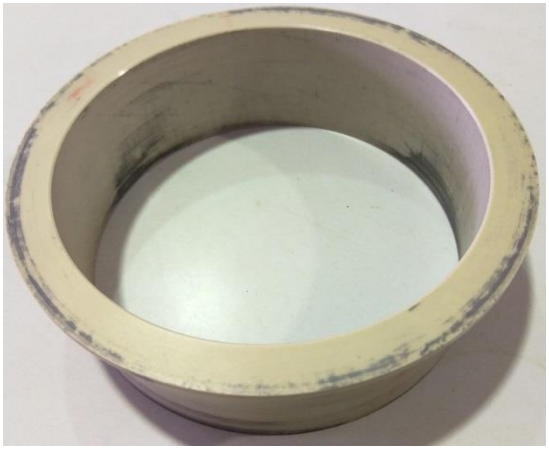

(d): Lower Cylinder Journal Bearing Sleeve

(e): Upper Journal Bearing Sleeve

Figure 8.4: Decomposed Oil Particles on Bearing Surfaces

After cleaning up and ensuring that the bearing surfaces were free from contaminants, the compressor was tested again in order to evaluate its performance. However, it was still

prone to seizure which can be attributed to the buildup of friction heat at the lower cylinder bearing. Figure 8.5 shows the variation of the compressor component temperatures while operating at an average speed of 800 rev min^{-1}. Compressor operation was started with all the components at room temperature. Notice the rapid buildup of temperature at the lower bearing consisting of both the lower cylinder shaft and the rotor shaft. Interestingly, the buildup of friction heat at the upper cylinder bearing is negligible compared to the rest of the components.

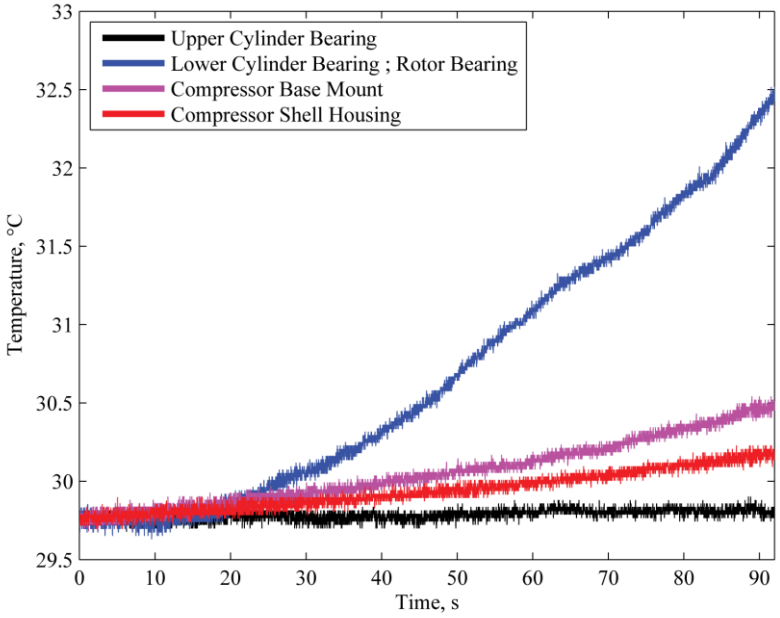

Figure 8.5: Compressor Component Temperature Variation

Due to the orientation of the compressor, the entire weight of the cylinder and rotor is resting on the lower bearing, thus greatly increasing the contact force and the subsequent friction force at that bearing. This increases the friction heat buildup at the bearing which causes the shaft to expand and since the bearing liner has been warped, it jams easily. The significant increase in the temperature of the base mount that is connected to the lower bearing is further proof of the friction heat produced at the lower bearing. Therefore, the compressor can only be operated for short periods before seizure at high operating speeds above 800 rev min^{-1}. Figure 8.6 shows the motor torque and discharge pressure measured for the average operating speed of 981 rev min^{-1}. Seizure occurred in this example as insufficient time was given for the bearings to cool and the measurements were taken while the bearings were at elevated temperatures.

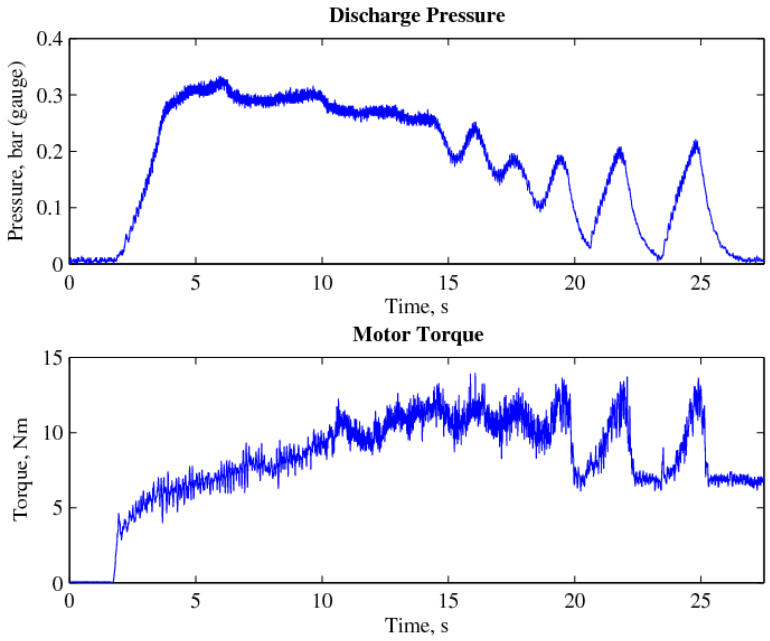

Figure 8.6: Discharge Pressure and Motor Torque Measurement until Prototype Seizure

Note that the compressor was able to reach peak discharge pressure quickly within about three seconds of starting up while on the other hand, the motor torque steadily increases until intermittent seizure at about the 20 second mark before stopping completely at 25 s.

Henceforth, the torque measurements from the prototype would not be useful for validating the dynamics model due to the effects of having a warped bottom bearing liner. The contact points and magnitude of the force at the bearings would vary with compressor operation and bearing temperature. This irregularity is difficult to model deterministically. Hence, an alternative RV mechanism shall be used to validate the dynamics model instead – the validation of the dynamics model shall be carried out in Chapter 9 using measurement data from the experimental investigation of an RV air expander [139].

8.4.2 Leakage

The cause of severe leakage in the prototype is due to the large leakage path clearances measured in Table 8.3 compared to that of the designed clearances of 10 μm. Severe internal leakage was observed; air in the compression chamber would leak through the large endface and vane clearances into the suction chamber, resulting in poor volumetric efficiencies. Notice the lacklustre discharge pressure of the compressor prototype of 0.3 bar (gauge) at best as

shown in Figure 8.6. Attempts to achieve higher pressure ratios by increasing the operating speeds were hampered by the fact that the compressor prototype was prone to seizure at high rotational speeds.

8.5 Results

Due to frequent seizure in the prototype, steady state measurement of the experiment was difficult and measurement was carried out during for about the first 20 s of starting up the compressor according to the experimental procedures in Section 8.3.

In the first few revolutions of compressor operation, the high mass flow output causes the pressure in the receiver tank to rise rapidly since the mass flow rate out of the tank is regulated by the needle valve. Consequently, the discharge pressure increases and this increases the amount of internal leakage in the compressor as well. Internal leakage would increase until the mass flow from the compressor matches the mass flow rate stipulated by the needle valve resulting in steady discharge pressure.

Due to the nature of the small receiver tank, steady-state pressure can be built up quickly for measurement purposes but steady-state component temperature measurement is not possible as the compressor would have seized up before that. With a short operating period and given sufficient time for the bearings to cool, "pseudo-steady-state" measurements can be observed. Figure 8.7 shows the typical measurement readout of a run at 800 rev min^{-1}. In this example, data between the 10 – 15 s period would be used for evaluating the prototype performance.

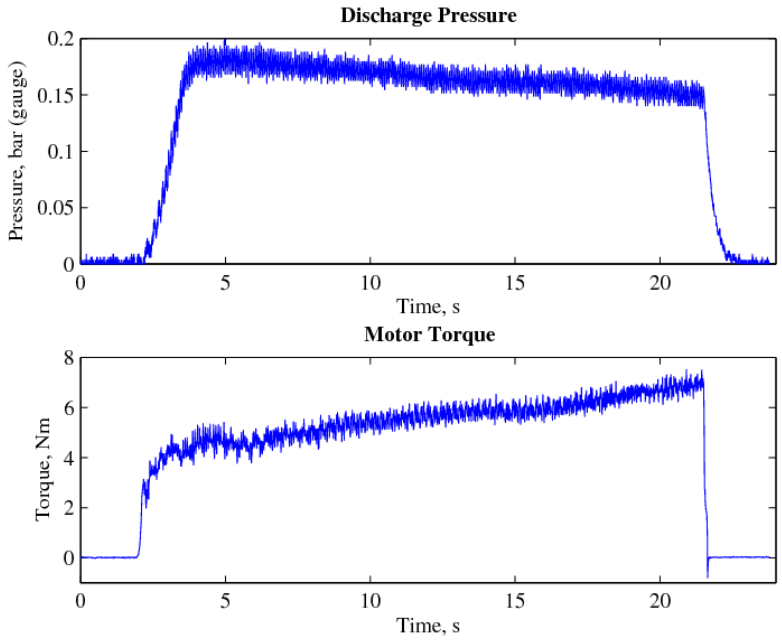

Figure 8.7: Typical Measurement Readout for Short Operating Periods

Generally, the discharge pressure is at its highest upon starting up the compressor but as the compressor operates, the increase in friction heat would lead to a further increase in friction at the bearings, thus increasing the input motor torque while slowing down the compressor operating speed and as a consequence, the discharge pressure decreases since the mass flow rate from the compressor decreases as well.

To this end, useful measurement data can still be obtained although the compressor is only operated for short periods without giving time for the heat produced at the bearing surfaces to propagate to the working chamber. In this fashion, the variation of discharge pressure and compressor operating speeds with respect to stipulated mass flow rates according to the experimental procedure in Section 8.3 are plotted as shown in Figure 8.8.

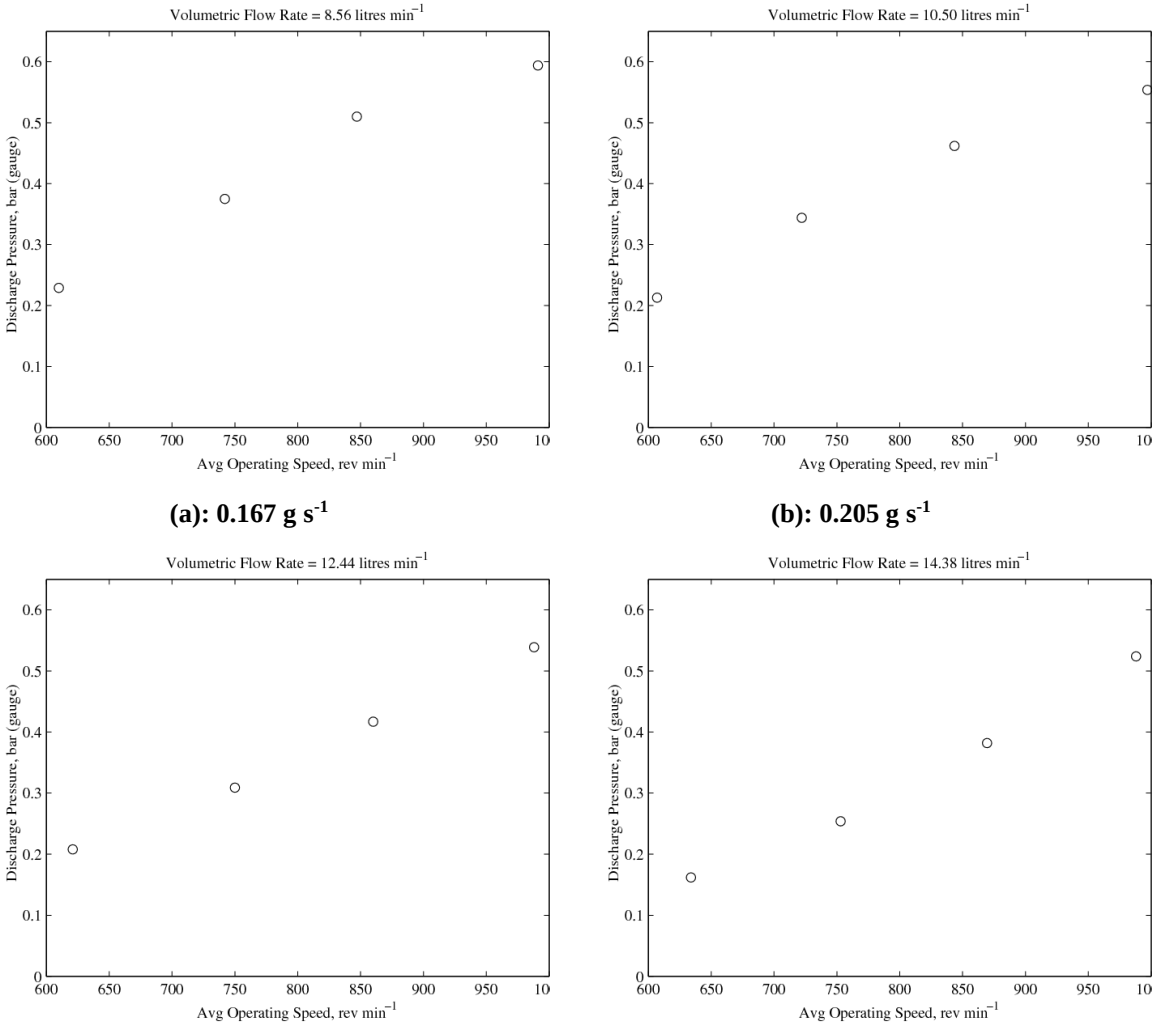

(a): 0.167 g s^{-1} **(b): 0.205 g s^{-1}**

(c): 0.243 g s^{-1} **(d): 0.281 g s^{-1}**

Figure 8.8: Measured Discharge Pressure based on Stipulated Mass Flow Rates

It is observed that higher discharge pressures can be achieved at higher operating speeds albeit at lower flow rates. As discharge pressure decreases at constant operating speeds, the flow rate would increase. This results in better volumetric efficiencies at high mass flow rates and low discharge pressures.

8.6 Validation of Thermodynamics and Leakage Model

In order to validate the theoretical thermodynamics and leakage model presented in Chapters 4 – 5, the measured data from the experiment in Section 8.5 are compared to that of the predicted data and presented in this section.

As the theoretical model requires discharge pressure as one of the inputs, the predicted discharge mass flow rate shall be compared against that of the measured values. As explained in Section 5.3, the orifice flow coefficients were chosen from a range of 0.58 – 0.65 as provided by Munson et al. [111] such that the same set of values would fit all operating conditions. With reference to Section 5.5.7, the set of leakage coefficients were adapted from the values of the curve fit coefficients obtained in the leakage CFD study such that the theoretical predictions with the same set of selected values would agree with those of the measured values regardless of operating conditions. The coefficients used for the modelling are presented in Table 8.5 and the values are applicable for all operating conditions.

Table 8.5: Thermodynamics and Leakage Channel Width Coefficients

Orifice Flow Coefficient	**Value**
Suction/discharge ports	0.60
Internal leakage	0.65
Equivalent Leakage Channel Width Coefficients	
C_1	0.0125
C_2	0.400
C_3	0.0300
C_4	0.650

For the comparison of mass flow rates, the data are grouped according to average operating speeds and displayed in Figure 8.9.

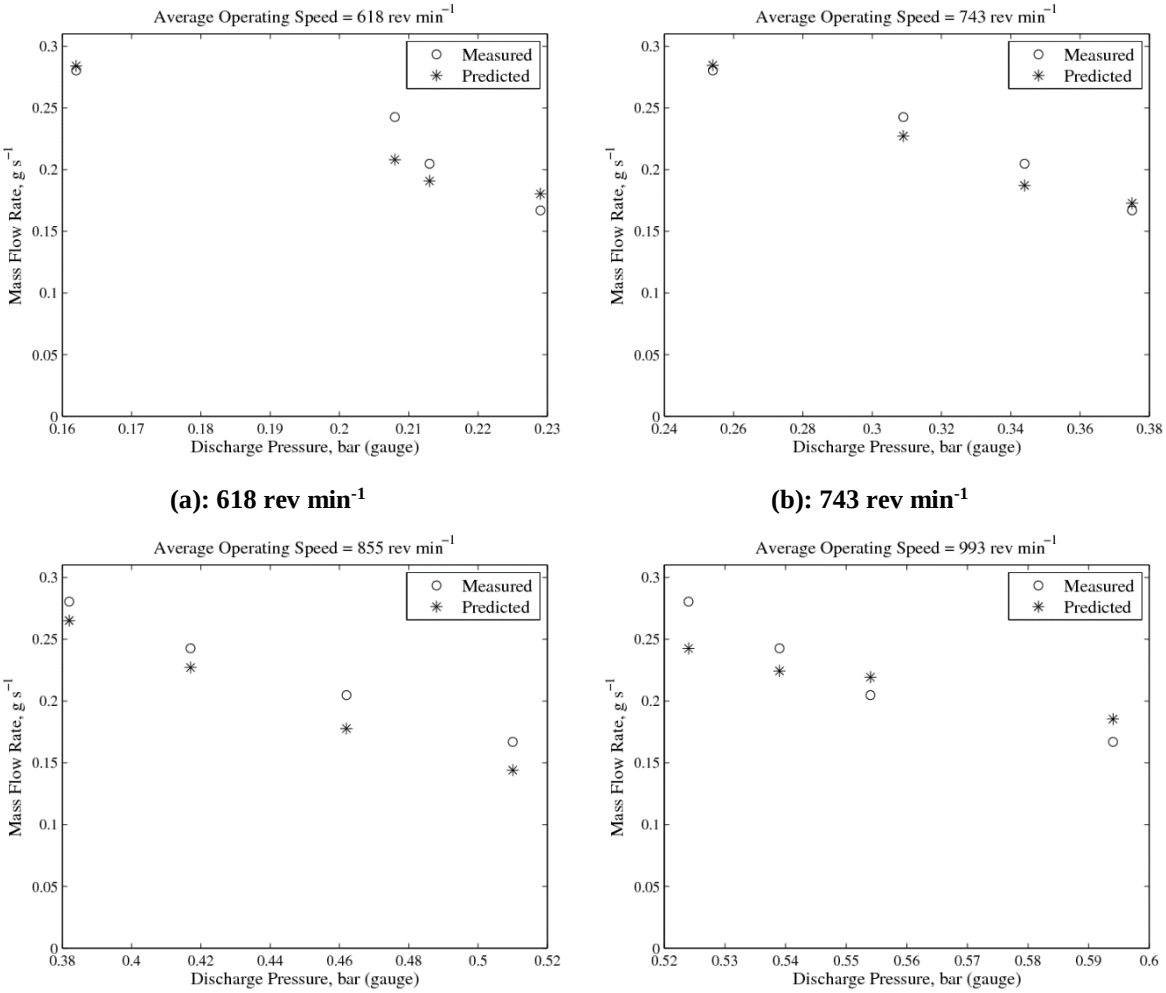

(a): 618 rev min^{-1} **(b): 743 rev min^{-1}**

(c): 855 rev min^{-1} **(d): 993 rev min^{-1}**

Figure 8.9: Comparison of Predicted Mass Flow rates against Measured Data

The predicted mass flow rates are found to be in good agreement with the measured data with an error of ±15%. Note that the average operating speeds according to the title of the graphs are approximate and the exact average operating speed can be found in Appendix A-6 along with the prediction errors.

8.7 Prototype Compressor Volumetric Efficiency

The volumetric efficiency of a compressor is defined by the ratio of the actual output mass flow rate to the theoretical mass flow rate with no internal leakage. Based on the measured average operating speed and mass flow rate from the RV prototype compressor, the volumetric efficiency of the compressor can be calculated as shown in Equation (8.2).

$$\eta = \frac{\rho_o \dot{V}_{measured}}{\rho_{suc} V_{cham} \omega_{measured}} \tag{8.2}$$

The volumetric efficiencies of the prototype for the different operating conditions are computed and plotted in Figure 8.10. The uncertainty analysis for the error bars can be found in Appendix A-6.

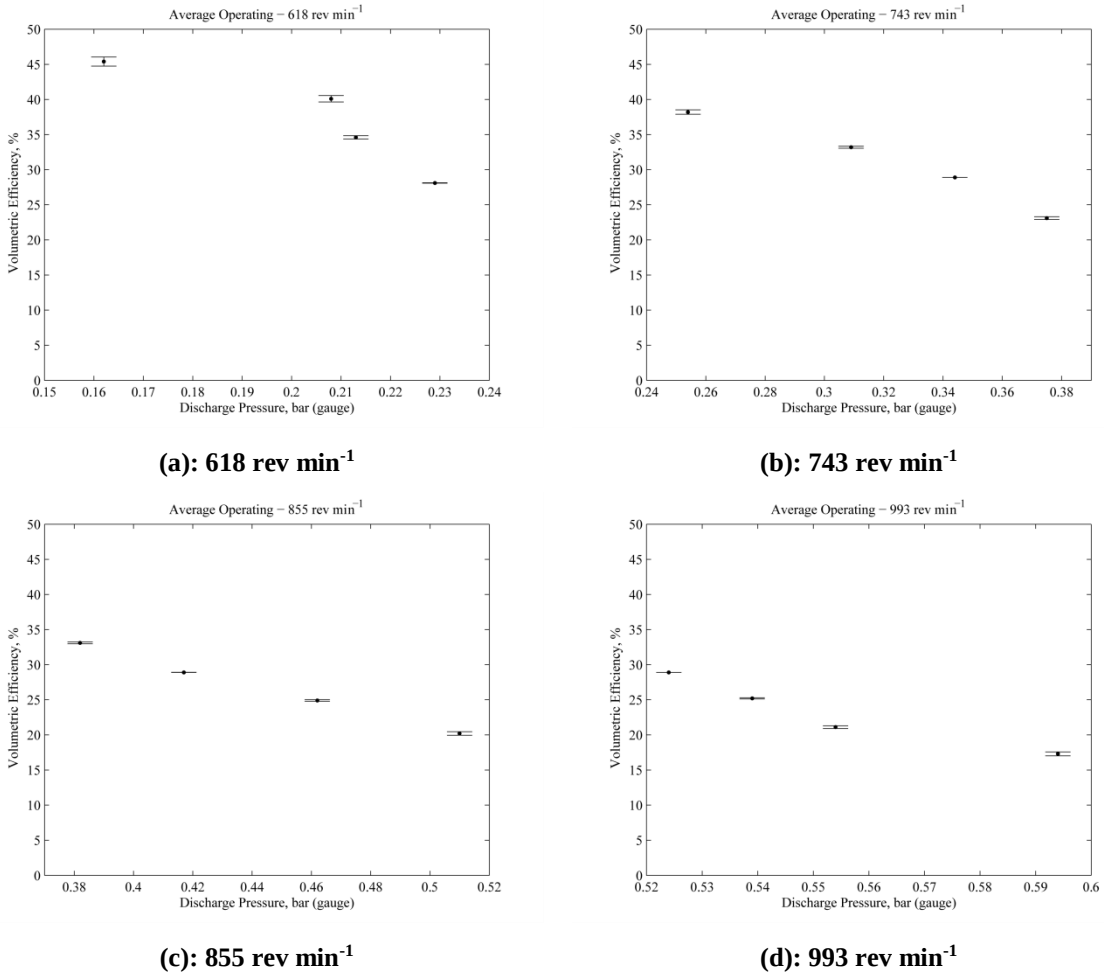

(a): 618 rev min^{-1} **(b): 743 rev min^{-1}**

(c): 855 rev min^{-1} **(d): 993 rev min^{-1}**

Figure 8.10: Compressor Volumetric Efficiencies Computed from Measurements

The volumetric efficiency of the prototype compressor ranges between 17% and 45% from measurements. The poor efficiency is due to the large clearance gaps at the vane and rotor endfaces as seen in Table 8.3 through which internal leakage occurs. Poor tolerance control during the fabrication process has resulted in these large clearance gaps.

On the other hand, if the specified values for the clearance gaps presented in Table 8.1 were attained during fabrication, the volumetric efficiency of the prototype can be greatly

improved. Figure 8.11 shows the predicted volumetric efficiencies for the prototype if the clearance gaps at the vane and rotor endface were at the specified value of 10 μm on each sides of the endfaces (20 μm in total). The average operating speeds and discharge pressure were kept the same as those measured from the experiment while the volumetric efficiency is calculated with the expected clearance gap values.

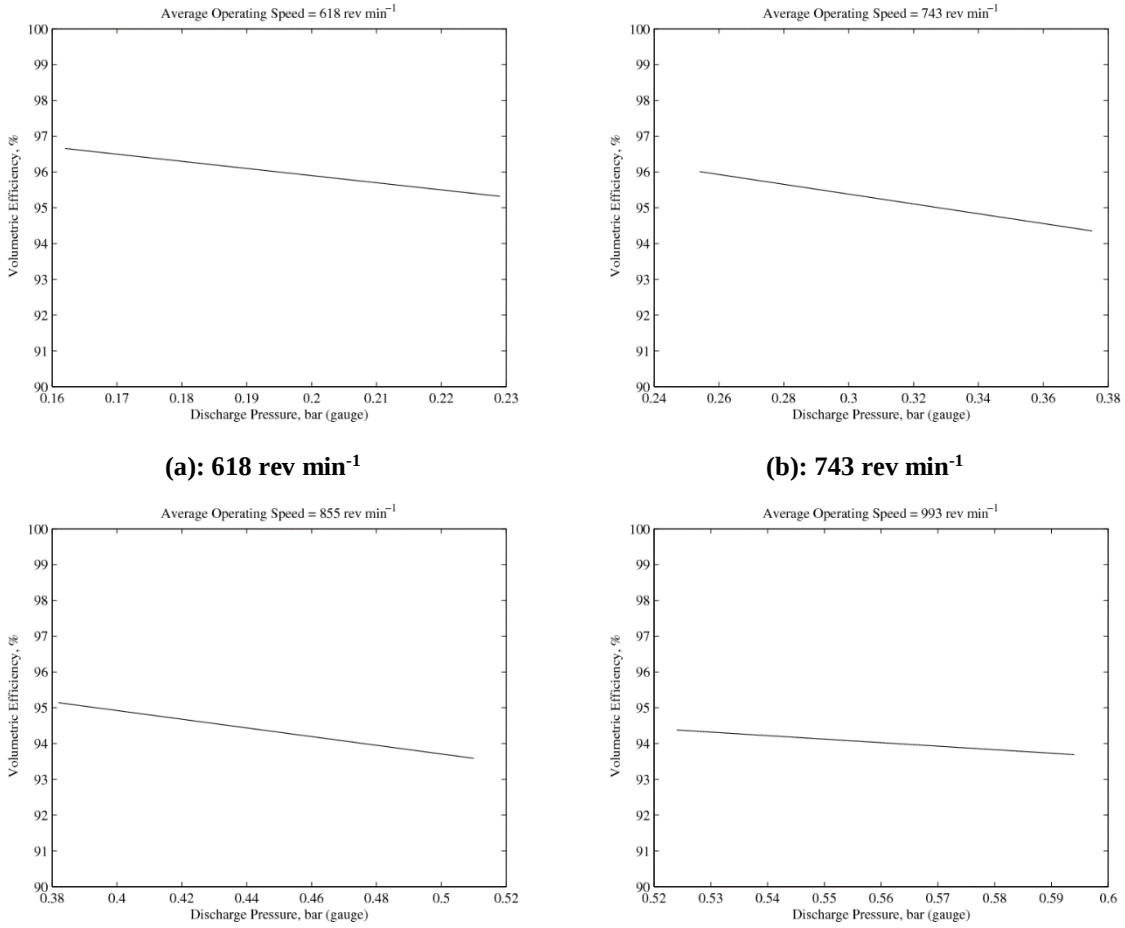

(a): 618 rev min^{-1} **(b): 743 rev min^{-1}**

(c): 855 rev min^{-1} **(d): 993 rev min^{-1}**

Figure 8.11: Predicted Volumetric Efficiencies with Smaller Leakage Clearance Gaps

From Figure 8.11, a compressor with better manufacturing tolerances and hence smaller clearance gaps would have an operating volumetric efficiency between 93.6% and 96.7%, which is an increase of 110% – 390% in mass flow rate. Hence, with better tolerance control, the lubricant-free RV compressor would no doubt still be feasible in terms of volumetric efficiency.

8.8 Concluding Remarks

Due to friction heating at the lower bearing, the shaft expands and would cause the bearing liner to wedge the bearing clearance gap, causing the compressor to seize. Furthermore, this problem is aggravated at higher operating speeds in which the friction heat buildup would be at higher rates leading to seizure in less than a minute of operation. Hence, measurement of steady-state operating values proved to be difficult and can only be carried out when the bearing is around room temperature instead of elevated temperatures and even so, the compressor can be operated for only a short period.

In addition, the vane and rotor endface clearance gaps in the prototype were measured to be 64 μm and 91 μm respectively, which is six to nine times higher than specified. As a result, the prototype was only able to achieve low discharge pressures of 0.16 – 0.59 bar (gauge) and furthermore at low volumetric efficiencies between 17% – 45%.

The modelling for the compressor performance has been adapted for such circumstances by assuming that the component temperatures are at room temperature for the modelling of heat transfer in the working chamber. Based on the measured average operating speed and discharge pressure, the theoretical model was able to predict the mass flow rate to within ±15% of the measured flow rate.

With better tolerance control during fabrication, the volumetric efficiency of the compressor can be improved. If the endface clearance gaps were at 10 μm instead, the mass flow rate would potentially increase by 110% – 390% as compared to the current prototype, thus resulting in volumetric efficiencies between 93.6% and 96.7% for the same operating speeds and discharge pressures measured from the experiment.

Suggestions for improvement in future development of the lubricant-free RV compressor based on experiment results and observations are as follows:

- For mechanical machine design, tolerance control is very important and even more so for lubricant-free mechanisms. Any discrepancy can cause parts to wedge together, resulting in seizure.
- Tolerance control is important for mitigating internal leakage losses.

- Care must be taken during assembly to ensure rubbing surfaces such as the bearings have to be clean of any contaminants such as oil and dust.
- Avoid the use of bearings with large radii as there will be severe friction heating due to the high friction losses.

9 Validation of Dynamics Model – RV Air Expander

Following the presentation of the dynamics model for a generic RV mechanism, this chapter shall proceed to validate the model with measurements from the experiment on an RV air expander. This will allow evaluation of the robustness of the proposed dynamics model. The model shall be used to predict the output torque from the RV air expander and comparison shall be made with that from experiment measurements. Section 9.1 shall cover a preamble on the background and current technology for that of pneumatic engines, otherwise known as air expanders.

9.1 Air Expander Preamble

Compressed air energy systems (CAES) have been proposed as an alternative energy resource to that of conventional fossil fuels. In CAES, compressed air is used to power air expanders from which energy is extracted. It requires no electrical power input and has been proposed as an alternative power source for hybrid vehicles [140–142] in which it is employed in conjunction with an internal combustion engine, replacing the electric motor in conventional hybrid vehicles. Such hybrid power systems for road vehicles can improve thermal efficiency by utilising waste heat from the engine and extending the operating range of such vehicles when compared to electrical hybrids [142]. In addition, there are also initiatives into developing road vehicles that are solely air-powered [143–145] and a study has been carried out to compare the type of storage for such vehicles [146]. Other than its potential uses as alternative clean energy for automotive vehicles, it is suitable for robotic automation [147] due to its inexpensive and favourable power to weight ratio characteristics.

Pneumatic power systems have also been proposed to be incorporated into novel applications [148] which can further boost efficiency. With increasing potential in the applications for such power systems, accurate modelling of such systems have been developed [143, 149, 150], along with its respective precision controls [151–153].

Many different air expanders have been developed, consisting of both conventional piston designs [144, 154] and rotary designs [145, 147, 155]. The RV mechanism was initially designed for compressor but has been adapted for air expansion operation and a study on the

overall performance of the RV expander variant for low to medium pressure conditions has been carried out [156].

Prior work was concerned with the overall performance of the RV mechanism, such as the mechanical and volumetric efficiencies, and average power output [139]. As the output torque of an air expander varies during each aspect of operation and is further affected by vibration, it would be advantageous to characterise and analyse the output of the RV air expander during steady-state operation for efficient design and better control for integration into CAES or hybrid power source systems. This method of analysis for the vibration can be derived from the dynamics model presented in Chapter 6 and the measurements from the experiment would be used to validate the dynamics model.

9.2 Revolving Vane Air Expander

Following the preamble on air expanders, this section will proceed to detail the mechanism of the RV air expander and explain the adaptation of the dynamics model for use in modelling the air expander.

9.2.1 Air Expander Mechanism

The RV mechanism for use in an air expander remains largely unchanged, except that the suction chamber now draws in pressurised air and expands it while the discharge chamber would discharge the expanded air; a reverse of the typical compression cycle. A cross-section of the RV expander cylinder-rotor assembly can be found in Figure 9.1 and more detailed explanations on the working principle of the expander can be found in the article by Subiantoro et al. [139].

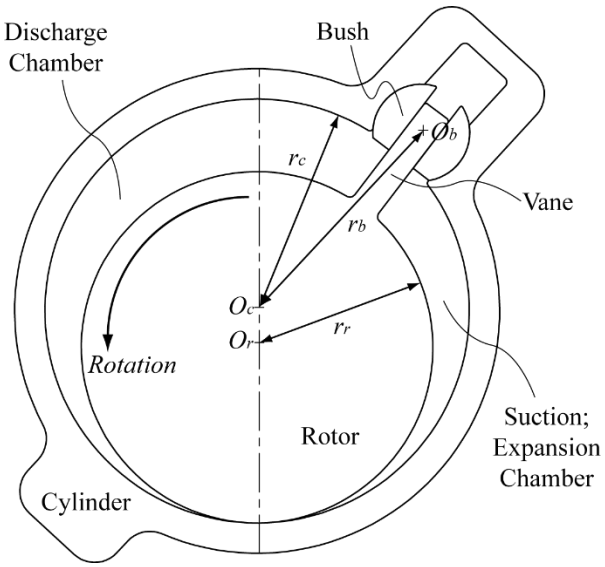

Figure 9.1: Revolving Vane Expander Schematic

9.2.2 Adapted Dynamics Model

The dynamics model for the RV mechanism variant in which the vane attached to the rotor was covered in Section 6.3.2. As the RV mechanism for the expander is similar, the model can be easily and readily adapted. For the expander, the motor torque term (T_m) in Equation (6.16) has been changed to that of the output torque term (T_{load}) as shown in Equation (9.1).

$$I_r\ddot{\theta}_r = T_g - T_{load} - \frac{d\theta_c}{d\theta_r}\left(I_c\ddot{\theta}_c\right) - \frac{d\phi}{d\theta_r}\left(m_b d_b \ddot{\phi}\right) - \frac{d\theta_b}{d\theta_r}\left(I_b\ddot{\theta}_b\right) - T_f \qquad (9.1)$$

Furthermore, the expander has a conventional lubrication system. To this end, the friction torque can be simply estimated as a ratio of the gas torque similar to that of the rolling piston [27]. In addition, as the friction loss increases with operating speed, this can be modelled by the addition of a loss term that is proportional to that of the operating speed and this acts as a damping term. The friction torque term can thus be expressed as shown in Equation (9.2).

$$T_f = C_1 T_g + C_2\dot{\theta}_r \qquad (9.2)$$

The values of the coefficients C_1 and C_2 have been arbitrarily chosen such that the estimated friction torque is able to provide a good prediction for the output torque across different operating conditions of the experiment. These values are displayed in Table 9.1.

Table 9.1: Friction Loss Coefficients

Coefficient	Value
C_1	0.3
C_2	0.005

9.3 Air Expander Experiment

9.3.1 Experiment Setup

The measurement data were extracted from the experiment conducted by Subiantoro et al. [139] and the experiment schematic is reproduced in Figure 9.2. Air was used as the working fluid and supplied by a compressor. It was an open loop system in which the expanded air was discharged to the ambient. A Torquemaster TM107 transducer was used to measure the output torque and the average rotational velocity was measured by a magnetic pickup sensor.

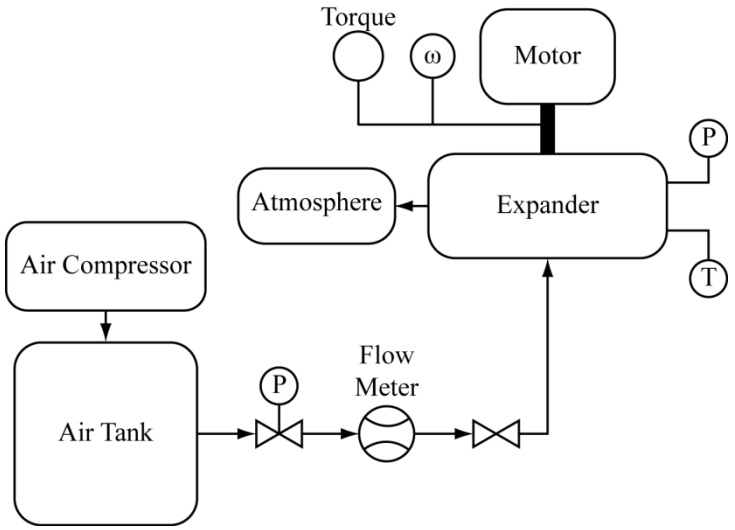

Figure 9.2: Air Expander Experimennt Schematic [139]

An ABB 2.2kW two-pole induction motor with a frequency controller was connected to the air expander to serve as the load for the expander. As explained in Section 6.3.6, the motor torque is dependent on the instantaneous speed and input frequency. The curve fit for evaluating the motor torque output is used for validating the model. Based on the dynamics model, predicted instantaneous operating speed shall be used to determine the corresponding output torque. The equation for determining the motor output torque is reproduced here as Equation (9.3) for ease of reference.

$$T_m = a_0 + a_1(\dot{\theta}_{shaft} - \dot{\theta}_{sync}) + a_2(\dot{\theta}_{shaft} - \dot{\theta}_{sync})^2 + \cdots + a_6(\dot{\theta}_{shaft} - \dot{\theta}_{sync})^6 \quad (9.3)$$

Measurements were carried out while the prototype was operated under different conditions. The air compressor was used to supply inlet pressures of 2 bar (gauge) and 3 bar (gauge), and the prototype was operated at average rotational speeds between 120 rev min^{-1} and 360 rev min^{-1} at intervals of 120 rev min^{-1} for both inlet pressures.

The dimensions of the RV prototype are given in Table 9.2. Note that there is no bush component in the prototype.

Table 9.2: RV Air Expander Dimensions

Component	Dimension
Rotor radius, mm	29.0
Cylinder radius, mm	35.0
Cylinder thickness, mm	5.0
Chamber length, mm	25.0
Vane length, mm	16.0
Vane width, mm	4.0
Working volume, cm^3	12.0

9.3.2 Results

As the prototype lacked a bush component, the equation of motion for the cylinder-rotor assembly in Equation (6.16) can be further simplified to that as shown in Equation (9.4) with substitutions for the friction and load torque terms.

$$I_r\ddot{\theta}_r = (1 - C_1)T_g + T_m - \frac{d\theta_c}{d\theta_r}(I_c\ddot{\theta}_c) - C_2\dot{\theta}_r \quad (9.4)$$

The comparisons between the predicted torque and measured torque for the six different operating conditions are shown in Figure 9.3.

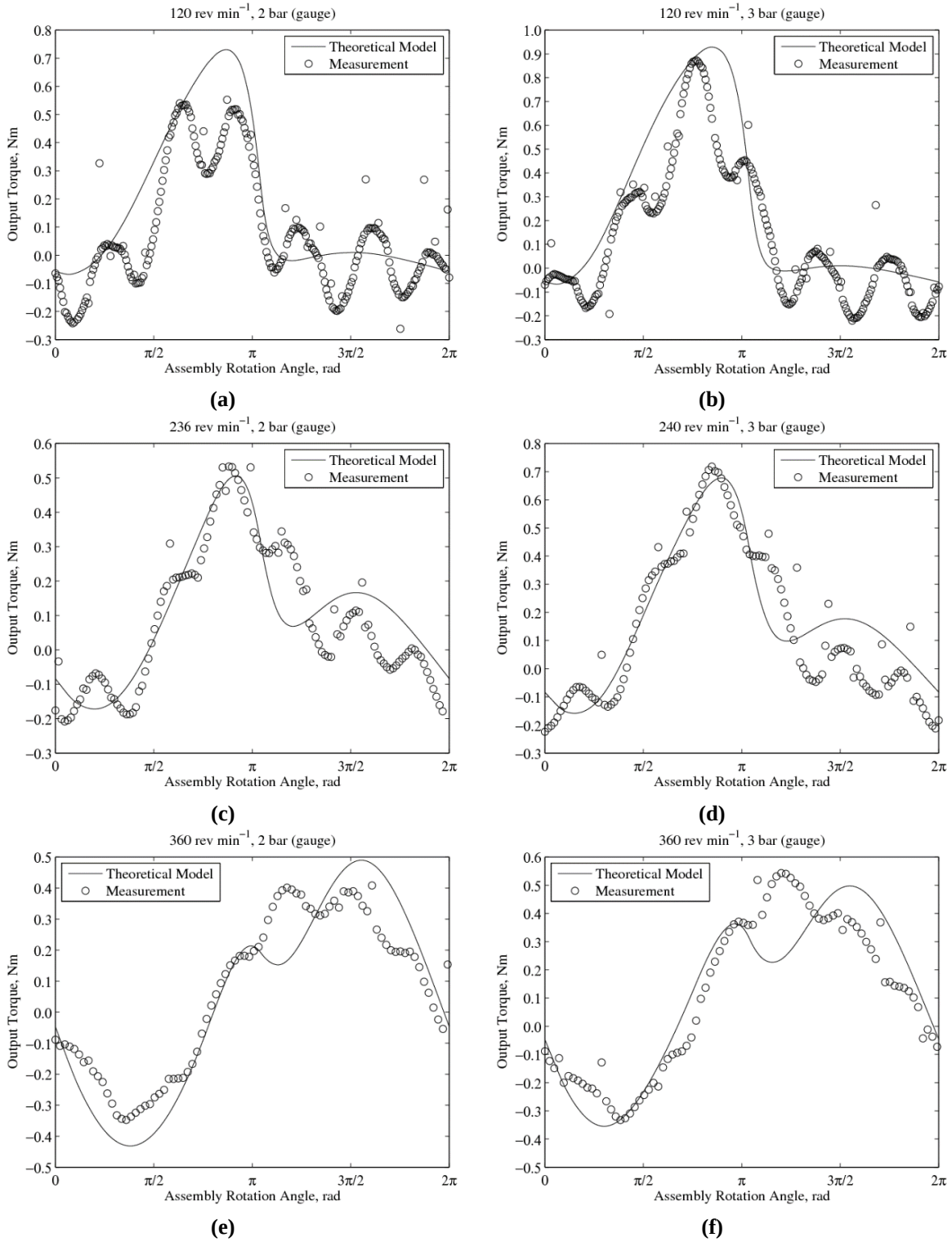

Figure 9.3: Comparison between Theoretical Model and Measurements

Large discrepancies for the peak torque were noted in Figure 9.3(a) and Figure 9.3(e) when the pressure ratio of the suction pressure to discharge pressure was 2. At a higher inlet pressure of 3 bar (gauge), the errors in peak torques were found to be within the range of ±10%.

The main source of these discrepancies is due to the bimodal nature of the assembly vibration as displayed in the measured data.

9.3.3 Secondary Vibration Mode

The presence of a secondary waveform in the measurements indicates that the vibration of the RV prototype is bimodal; arising from the presence of a clearance gap between the vane and the vane slot due to manufacturing tolerances. This phenomenon is termed as 'vane knocking' [157]. The eccentricity between the rotor and cylinder centres of rotation causes their rotation speeds to vary during operation as shown in Figure 9.4.

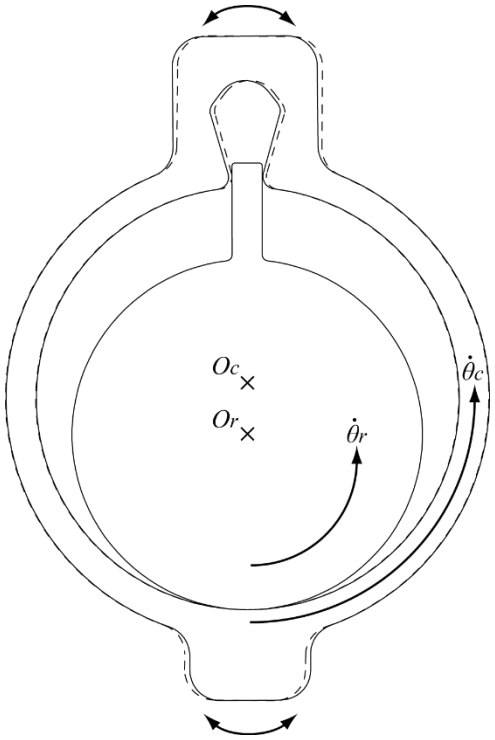

Figure 9.4: Secondary Vibration Mode in RV Air Expander

Due to the presence of the clearance gap and differences in rotation speeds, there will be instances when the vane will lose contact momentarily with the vane slot wall on the cylinder resulting in the oscillation of the vane slot wall about the vane.

In the RV air expander, the driven cylinder component has a larger moment of inertia compared to the rotor, the resulting impacts would distort the output torque of the pneumatic engine as observed in the measurements. In Figure 9.3(a), Figure 9.3(e) and Figure 9.3(f), the impacts coincide with the peak torque which caused the large discrepancies between the

measured and predicted value. In Figure 9.3(f), these impacts have caused the peak torque to be higher than predicted and with a phase shift as well.

It is also noted that the secondary vibration tends to be less significant at higher rotation speeds and this is due to the reduction in oscillation times at high operating speeds; the time period in which the vane loses contact with the slot wall gets shorter at higher speeds and consequently, the change in angular momentum of the cylinder is less pronounced upon impact. Hence, the model was noted to be more accurate at higher operating speeds.

This provides an insight into the performance of that of the RV compressor prototype as well since the proposed vane design is also lacking a bush component and therefore, there will be a clearance gap between the vane and vane slot as well.

9.4 Concluding Remarks

Overall, the results show that the predicted output torque values are in good agreement with that of the measured values. It is also noted to have a consistent accuracy of ±10% for peak torque calculations at a higher operating pressure ratio of 3.

Hence, the proposed dynamics model for the RV mechanism presented in Chapter 6 is indeed suitable for modelling the vibration and dynamics of RV machines. For the RV expander, the dynamics model is able to predict the characteristic of the output torque albeit with discrepancies for the value and phase angle of the peak torque. These discrepancies are mainly attributed to the vane knocking effect arising from manufacturing tolerences which were ignored as a necessary assumption in developing the model.

A summary of this chapter is as follows:

- The dynamics model for generic RV mechanism was adapted for that of an RV air expander.
- Measurement data from the experimental investigation of an RV air expander prototype would be used to validate the accuracy of the dynamics model by comparing the predicted output torque characteristic of the model against the measured data.

- Comparison shows that the predicted output torque characteristics are in good agreement with that of the measured data albeit with some discrepancies.
- The discrepancies can be attributed to the ‘vane knocking’ effect which causes the vibration of the RV air expander to be bimodal in nature.
- The rotor and cylinder rotate at different speeds due to eccentricity and the presence of a clearance gap between the vane and vane slot wall cause oscillations of the cylinder about the rotor, termed as ‘vane knocking’.
- The resulting impacts between the vane and vane slot wall affect the output torque especially since the cylinder possesses higher rotational inertia.
- These impacts can affect the magnitude of the peak output torque if the instances of impacts coincide with maximum torque output.
- However, this phenomenon is less significant at high operating speeds since the oscillation time is reduced.
- This also gives an insight into the vibration characteristic of the RV compressor since the new vane design would result in the same ‘vane knocking’ effect as there will exist a clearance gap between the vane tip and vane slot wall.
- The vibration of the RV compressor prototype would be bimodal as well, but the effects would be less pronounced at high operating speeds.

10 Conclusion and Recommendations for Future Work

In this thesis project, developmental work has been carried out on a lubricant-free revolving vane (RV) compressor. In this chapter, a summary of the developmental work carried out for the compressor and the respective key findings and observations will be presented. Last but not least, a list of recommendations for future work is also included.

10.1 Developmental Work

Developmental work has been carried out in this project on the lubricant-free RV compressor. This includes conceptual designs for improvements in RV mechanism and a comprehensive mathematical model for the compressor. These are summarised as follows:

10.1.1 Design

- A new triangular-tipped vane and straight vane slot design were proposed to reduce the number of components in the assembly by two. The new design negates the requirement of the two split bush components.

- Rubbing components in the compressor for the vane, rotor and bearings were proposed to be made from self-lubricating materials to reduce friction losses and material wear. Bearing liners made from such materials were employed at the journal bearings to prevent metal-to-metal contact at these bearings

- A separate, purpose-built experiment has been carried out to select a suitable self-lubricating material for use in the rubbing components of the prototype. Between polytetrafluoroethylene (PTFE) and polyether-etherketone (PEEK), the latter was chosen for its wear-resistant properties and low coefficient of frictions at higher loads and increased rubbing speeds.

10.1.2 Mathematical Modelling

- New geometric relations and working chamber volume variations were formulated for the new vane and vane slot design.

- A comprehensive thermodynamics model for the RV compressor prototype was developed which includes heat transfer in the working chamber and the modelling of each internal leakage flow path.

- New expressions for the hydraulic diameters and characteristic velocities for the suction, compression and vane slot chambers are presented for use with existing heat transfer relations [16].

- Computational fluid dynamics (CFD) was used to model internal leakage flow paths with non-uniform cross-section flow channels. For comparison of the CFD data with the Fanno flow model, an equivalent leakage flow channel of uniform cross-section is assumed.

- For the internal leakage flow model, correlations for the variations of channel widths with the pressure ratios were derived from the CFD data together with the Fanno flow solutions. The channel lengths were assumed to be constant.

- Lagrangian mechanics was used for dynamics modelling of the RV mechanism and the resulting equation of motion can be modified for use with other RV design variants. This allowed for the study of the rotational vibration characteristics of the RV mechanism.

- Individual friction losses for each part of the compressor prototype were formulated and presented.

- CFD simulation was carried out to quantify the fluid shear torque of the discharged fluid in the housing shell acting on the cylinder-rotor assembly.

- The lumped thermal conductance method was used to model heat transfer among the components in the compressor prototype during steady-state operation and predict their temperatures.

10.2 Key Findings and Observations

Key findings from analysis and observations obtained during the measurement and evaluation of the lubricant-free RV compressor prototype are presented as follows:

- The addition of a fillet to the new vane design reduced the amount of dead volume in the vane slot chamber by approximately 20% for the current prototype dimensions.

- The maximum vane slot chamber volume would constitute 8.3% of the total working volume for the compressor prototype.

- For the modelling of the internal leakage flow, the equivalent leakage flow channel widths for the internal endface leakages were discovered to vary with the pressure ratios raised to a power between zero and unity.

- Friction losses at the rotor endface, cylinder endface, vane slot and vane tip were approximately 20 times smaller than that of bearing losses for the current prototype.

- The fluid shear torque of the discharged fluid in the shell housing was found to be four orders smaller than that of the bearing friction torques.

- The proportion of friction loss at the bearings arising from the weight of the compressor components to the total friction loss decreases with increasing pressure differential between suction and discharge: 38% at 1000 rev min^{-1} with a pressure difference of 1 bar and on the other hand, 18% at 2000 rev min^{-1} with a pressure difference of 4 bar.

- An analysis for dry sliding contact between AISI 4140 steel and PEEK materials was conducted. It showed that 99% of the friction heat produced is absorbed by the steel surface and the remaining 1% is absorbed by the pure PEEK material for rubbing between steel and pure PEEK. For rubbing between AISI 4140 steel and bearing grade PEEK, 97.5% of the heat produced is absorbed by steel and the remaining 2.5% by the bearing grade PEEK material.

- The steady-state operating temperature of the rotor will be approximately the same as that of the mean chamber temperature whereas the cylinder and housing shell component temperatures will be at much higher temperatures due to friction heating depending on the operating condition.

- In a preliminary analysis that assumes an ideal case whereby there is no internal leakage between the working chambers, a conservative operating condition of 2000 rev min^{-1} with a pressure difference of 4 bar between suction and discharge, the average steady-state operating temperatures of the housing shell, cylinder and rotor are found to be 110.1°C, 107.2°C and 43.4°C, respectively. Friction heating at the bearings and enhanced heat dissipation in the working chamber results in a large temperature variation for the cylinder component – the temperature at the lower cylinder bearing was found to be 197.2°C while the temperature of the cylinder walls in the working chamber was found to be 51.7°C.

- As ideal, conservative operating conditions were used for the preliminary analysis of component steady-state operating temperatures, the compressor would no doubt experience even higher temperatures than those calculated in the analysis during practical operation. For practical operation, the compressor may operate at higher speeds up to 3000 rev min^{-1} and higher compression ratios when working with refrigerants. Furthermore, internal leakage between the working chambers would circulate hot fluid between the chambers which will increase the average chamber temperature.

- It was unintentionally found that the accidental presence of residual oil in the lubricant-free prototype would cause seizure due to the formation of hard carbon particles at the bearings when the oil decomposed under high friction heat.

- The prototype was affected by severe internal leakage due to the presence of large endface gaps arising from poor machining accuracies: 0.13 mm for the vane endface and 0.18 mm for the rotor endface. This resulted in poor volumetric efficiencies of 17% – 45% for compression ratios between 1.2 – 1.6 when running between 610 – 1000 rev min^{-1}.

- Additionally, the prototype was also prone to seizures due to overheating at the journal bearings. Overheating at the bearings compounded the problem of the warped PEEK bearing liners wedging the bearings, leading to premature seizure after approximately 90s of operation.

- Due to the problem of severe internal leakage and frequent seizure, the prototype has unfortunately, failed to match the operating requirements of conventional positive displacement compressors.

- Theoretically predicted output mass flow rates from the thermodynamics and leakage model were found to be in good agreement with the measured values, with ±15% prediction errors.

- Theoretical prediction shows that the mass flow rate from the compressor prototype would increase by 110% – 390% if the endface clearance gaps were at the design values of 10 μm instead. This shows that with the proper manufacturing tolerances, a lubricant-free RV compressor would be feasible in terms of volumetric efficiency.

- Output torque measurements from the experimental investigation of an RV air expander conducted by Subiantoro et al. [139] were used to validate the dynamics model. The predicted variations in fluctuations in output torque due to rotational vibration were found to be in good agreement with measurements as shown in Figure 8.3.

- The rotational vibration of the RV mechanism is bimodal in nature, arising from the presence of a clearance gap between the vane and vane slot wall. However, this effect becomes less pronounced as running speed increases.

10.3 Recommendations for Future Work

As presented in Chapter 8 which discusses the findings of the experimental investigation of the lubricant-free RV prototype, its performance was poor and far from being operational since it was prone to seizures and had significant internal leakage. Hence, there are still many areas of improvement for the development of the lubricant-free compressor. The list of recommendations for continuing the work presented in this thesis is as follows:

1. Re-fabrication of RV compressor prototype with better tolerance control such that the finished components remains true to the intended design tolerances of ±10 μm and the bearing liners must be free from distortion. This will ensure proper operation without interruptions and attain higher compression pressures with lesser internal leakage. The

prototype should also be redesigned with bearings with smaller diameters to reduce friction loss. Additionally, it is also recommended that sealed bearings should be used to further reduce friction losses as proposed in Chapter 7. This will address the issue of severe overheating due to friction.

2. The intermittent operating behaviour of the current compressor prototype made obtaining steady-state operating temperature values from the components difficult. With an improved prototype with better machining accuracy and component tolerances, it is believed that steady-state temperature measurements can then be successfully obtained to validate and improve the current thermal model presented in Chapter 7

3. The performance of the lubricant-free compressor after prolonged effects of material wear can also be investigated. Wear at the rubbing surfaces would increase the clearance gaps which can lead to translational vibration at the bearings and at the same time, increases the amount of internal leakage. This proposed study can help to determine the operating lifespan of the lubricant-free RV compressor and predict the changes in compressor performance with varying amounts of wear.

4. Acoustic effects of fluid pulsation at the discharge port can be studied for the case of the RV compressor. The propagation of acoustic effects can cause vibration in the connecting pipes which will affect the integrity of the pipe walls. As the discharge valve is always rotating with the cylinder-rotor assembly, this might cause interesting flow-induced acoustic effects. This proposed study can include fluid structure interaction (FSI) modelling between the valve reed and working fluid.

5. Design improvements via geometric optimisation of the compressor should be carried out as well. Parametric studies on the compressor performance should first be carried out to identify design variables which have significant effects on the performance of the compressor. These design parameters would then be used as free variables in the optimisation study. Algorithms such as the genetic algorithm or numerical multi-variable direct search techniques such as “Complex” can be employed.

6. Additional design improvements can be further made for the lubricant-free RV compressor in the aspect of material selection. A lubricant-free compressor would be susceptible to overheating during operation due to friction. Thus, materials with lower

coefficients of friction and/or those able to withstand high temperatures would be required. This includes the testing and use of other self-lubricating materials as presented in the Literature Review in Chapter 2. It is not limited to only one type of material as was used for the current prototype but rather different components can be made from different materials to achieve the best sliding properties. Such work would include optimisation of the different materials for the different components.

7. Last but not least, in the case of refrigeration, injecting the condensed refrigerants into the working chambers for scroll [158, 159] and spool [160] compressors during operation had shown to improve compressor performance as this helped to cool the working chamber. This method may be applied to the RV compressor when used for refrigeration to mitigate the heat build-up from dry sliding friction. Other than injection into the working chamber, the liquid refrigerant may also be injected into the housing shell to cool the bearings.

10.4 Final Remarks

The revolving vane mechanism has shown great promise and potential for development into a lubricant-free compressor. The scope of developmental work for such a compressor is indeed very vast due to the many practical challenges and problems that it faces as mentioned in this project, namely overheating, high friction losses and increased internal leakage. However, the author is hopeful that the insights gained and groundwork covered in this thesis should help in future developmental work and bring the lubricant-free compressor to fruition and with it, perhaps other operating variants such as an expander or even a hybrid compressor-expander unit. With this final remark, this thesis has reached the end.

References

1. Kus, B., & Nekså, P. (2013). Oil free turbo-compressors for CO2 refrigeration applications. *International Journal of Refrigeration*, *36*(5), 1576–1583.

2. Qi, M., Ma, C., & Yang, C. (2008). Numerical Optimization on a Centrifugal Turbocharger Compressor. *SAE International Journal of Fuels and Lubricants*.

3. Min, G., & Rowe, D. M. (2000). Improved model for calculating the coefficient of performance of a Peltier module. *Energy Conversion & Management*, *41*, 163–171.

4. Dai, Y. J., Wang, R. Z., & Ni, L. (2003). Experimental investigation and analysis on a thermoelectric refrigerator driven by solar cells. *Solar Energy Materials and Solar Cells*, *77*(4), 377–391.

5. He, W., Zhou, J., Hou, J., Chen, C., & Ji, J. (2013). Theoretical and experimental investigation on a thermoelectric cooling and heating system driven by solar. *Applied Energy*, *107*, 89–97.

6. Transparency Market Research. (2016). *Thermoelectric Modules Market - Global Industry Analysis, Size, Share, Growth, Trends and Forecast 2015 - 2023*. Albany, NY. Retrieved from http://www.transparencymarketresearch.com/thermoelectric-modules-market.html

7. Hiller, C. C., & Glicksman, L. R. (1976). Detailed Modeling and Computer Simulation of Reciprocating Refrigeration Compressors. In *International Compressor Engineering Conference* (pp. 12–17).

8. Kaiser, H., & Kruse, H. (1984). An Investigation on Reciprocating and Rotary Refrigeration Compressors. In *International Compressor Engineering Conference*.

9. Shiga, T., Ishijima, K., Sakainc, M., & Chu, I. (1978). Analysis of The Rolling-Piston Type Rotary Compressor. In *International Compressor Engineering Conference*.

10. Yanagisawa, T., Shimizu, T., Chu, I., & Ishijima, K. (1982). Motion Analysis of Rolling Piston in Rotary Compressor. In *International Compressor Engineering Conference* (pp. 185–192).

11. Tothero, D., & Keeney, D. (1978). A Rotary Vane Compressor for Automotive Air Conditioning Applications. In *International Compressor Engineering Conference*.

12. Klein, R. (1978). Screw Compressors for Heat Pump Application. In *International Compressor Engineering Conference*.

13. Halay, J. (1984). Small Screw Compressor Application to Transit Air Conditioning Systems. In *International Compressor Engineering Conference*.

14. Tojo, K., Ikegawa, M., Shiibayashi, M., Arai, N., Arai, A., & Uchikawa, N. (1984). A Scroll Compressor for Air Conditioners. In *International Compressor Engineering Conference*.

15. Teh, Y. L., & Ooi, K. T. (2009). Experimental study of the Revolving Vane (RV) compressor. *Applied Thermal Engineering*, *29*(14–15), 3235–3245.

16. Tan, K. M., & Ooi, K. T. (2011). Heat transfer in compression chamber of a revolving vane (RV) compressor. *Applied Thermal Engineering*, *31*(8–9), 1519–1526.

17. Teh, Y. L., & Ooi, K. T. (2009). Theoretical study of a novel refrigeration compressor – Part I: Design of the revolving vane (RV) compressor and its frictional losses. *International Journal of Refrigeration*, *32*(5), 1092–1102.

18. Teh, Y. L., Ooi, K. T., & Djamari, D. W. (2009). Theoretical study of a novel refrigeration compressor – Part II: Performance of a rotating discharge valve in the revolving vane (RV) compressor. *International Journal of Refrigeration*, *32*(5), 1103–1111.

19. Teh, Y. L., & Ooi, K. T. (2009). Theoretical study of a novel refrigeration compressor-Part III: Leakage loss of the revolving vane (RV) compressor and a comparison with that of the rolling piston type. *International Journal of Refrigeration*, *32*(5), 945–952.

20. Tan, K. M., & Ooi, K. T. (2011). A novel revolving vane compressor with a fixed-vane. *International Journal of Refrigeration*, *34*(8), 1980–1988.

21. Tan, K. M., & Ooi, K. T. (2011). Journal bearings design for a novel revolving vane compressor. *International Journal of Refrigeration*, *34*(1), 94–104.

22. Gasche, J. L., Andreotti, T., & Maia, C. R. M. (2012). A model to predict R134a refrigerant leakage through the radial clearance of rolling piston compressors. *International Journal of Refrigeration*, *35*(8), 2223–2232.

23. Yanagisawa, T., & Shimizu, T. (1986). Foaming of refrigerating oil in a rolling piston type rotary compressor. *International Journal of Refrigeration*, *9*(1), 17–20.

24. Padhy, S. K., & Dwivedi, S. N. (1994). Heat transfer analysis of a rolling-piston rotary compressor. *International Journal of Refrigeration*, *17*(6), 400–410.

25. Kim, H. J. (2005). Lubrication oil pumping by utilizing vane motion in a horizontal rotary compressor. *International Journal of Refrigeration*, *28*(4), 498–505.

26. Sheiretov, T., Van Glabbeek, W., & Cusano, C. (1995). Simulative friction and wear study of retrofitted swash plate and rolling piston compressors. *International Journal of Refrigeration*, *18*(5), 330–335.

27. Yanagisawa, T., Mori, M., Shimizu, T., & Ogi, Y. (1984). Vibration of a rolling piston type rotary compressor. *International Journal of Refrigeration*, *7*(4), 237–244.

28. Ooi, K. T., Wong, T. N., & Kwek, E. C. (1994). Effects of Vane Spring Stiffness on Compressor Performance. In *International Compressor Engineering Conference* (pp. 549–553).

29. Liu, Y., & Kosco, J. (1998). Vane Dynamics Analysis of a Tilted Vane Rotary Compressor. In *International Compressor Engineering Conference* (pp. 403–408).

30. Sung, H. C. (1998). Tribological characteristics of various surface coatings for rotary compressor vane. *Wear*, *221*(2), 77–85.

31. Adair, R. P., Qvale, E. B., & Pearson, J. T. (1972). Instantaneous Heat Transfer to the Cylinder Wall in Reciprocating Compressors. In *International Compressor Engineering Conference*.

32. Benson, R. S., Annand, W. J. D., & Baruah, P. C. (1975). A simulation model including intake and exhaust systems for a single cylinder four-stroke cycle spark ignition engine. *International Journal of Mechanical Sciences*, *17*(2), 97–124.

33. Liu, R., & Zhou, Z. (1984). Heat Transfer Between Gas and Cylinder Wall of Refrigerating Reciprocating Compressor. In *International Compressor Engineering Conference* (pp. 110–115).

34. Zhao, Y., Li, L., Shen, J., Zhang, W., & Shu, P. (2003). Research on oil-free air scroll compressor with high speed in 30 kW fuel cell. *Applied Thermal Engineering*, *23*(5), 593–603.

35. Ni, S. S., & Cai, D. K. (2002). Oil-Free "Floating Scroll" Compressor. In *International Compressor Engineering Conference*.

36. Li, Z., Li, L., Zhao, Y., Bu, G., & Shu, P. (2009). Theoretical and experimental study of dry scroll vacuum pump. *Vacuum*, *84*(3), 415–421.

37. Grzyll, L. R., & Cole, G. S. (2000). A Prototype Oil-Less Compressor for the International Space Station Refrigerated Centrifuge. In *International Compressor Engineering Conference*.

38. Imaichi, K., Fukushima, M., Muramatsu, S., & Ishii, N. (1982). Vibration Analysis of Rotary Compressors. In *International Compressor Engineering Conference* (p. Paper 407).

39. Levecque, N., Mahfoud, J., Violette, D., Ferraris, G., & Dufour, R. (2011). Vibration reduction of a single cylinder reciprocating compressor based on multi-stage balancing. *Mechanism and Machine Theory*, *46*(1), 1–9.

40. Kurka, P. R. G., Izuka, J. H., & Paulino, K. L. G. (2012). Dynamic loads of reciprocating compressors with flexible bearings. *Mechanism and Machine Theory*, *52*(0), 130–143.

41. Chen, Y. N. (1967). Calculation of gas vibrations due to simultaneous excitations in reciprocating compressor piping systems with allowance for frictional effect and temperature change in the flow. *Journal of Sound and Vibration*, *5*(2), 215–256.

42. Yu, B., Yu, X., & Feng, Q. (2010). Simple Modeling and Modal Analysis of Reciprocating Compressor Crankshaft System. In *International Compressor Engineering Conference*.

43. Gavric, L. (1998). Vibro-Acoustic Modeling of Hermetic Reciprocating Compressors. In *International Compressor Engineering Conference* (pp. 319–324).

44. Erol, H., & Gurdogan, A. (2000). The Noise and Vibration Characteristics of a Reciprocating Compressor: Effects of Size and Profile of Discharge Port. In *International Compressor Engineering Conference* (pp. 677–684).

45. Kjeldsen, K., & Madsen, P. (1978). Reduction of Compressor Vibrations by Optimizing the Locations of the Counterweight and the Internal Springs. In *International Compressor Engineering Conference* (p. Paper 246).

46. Yoshimura, T., Koyama, T., Morita, I., Kobayashi, M., & Uetsuji, T. (1992). A Study of the Vibration Reduction of Rolling , Piston Type Rotary Compressor. In *International Compressor Engineering Conference* (p. Paper 920).

47. Padmanabhan, C. (1996). Modeling of Compressor Vibration for Improved Dynamic Design. In *International Compressor Engineering Conference* (pp. 693–696).

48. Bukac, H. (2004). Self-Excited Vibration in a Radially and Axially Compliant Scroll Compressor. In *International Compressor Engineering Conference* (p. Paper 1664).

49. Chao, Y. J., Qi, X., & Tang, W. (2003). Heat Transfer in Friction Stir Welding—Experimental and Numerical Studies. *Journal of Manufacturing Science and Engineering*, *125*(1), 138.

50. Grimm, A., Schulze, S., Silva, A., Göbel, G., Standfuss, J., Brenner, B., … Füssel, U. (2015). Friction Stir welding of Light Metals for Industrial Applications. *Materials Today: Proceedings*, *2*, S169–S178.

51. Reilly, A., Shercliff, H., Chen, Y., & Prangnell, P. (2015). Modelling and visualisation of material flow in friction stir spot welding. *Journal of Materials Processing Technology*, *225*, 473–484.

52. Fereiduni, E., Movahedi, M., & Kokabi, A. H. (2015). Aluminum/steel joints made by an alternative friction stir spot welding process. *Journal of Materials Processing Technology*, *224*, 1–10.

53. Tabor, D. (1981). Friction—The Present State of Our Understanding. *Journal of Lubrication Technology*, *103*(2), 169–179.

54. Uetz, H., & Föhl, J. (1978). Wear as an energy transformation process. *Wear*, *49*(2), 253–264. 1

55. Kennedy, F. E. (1984). Thermal and thermomechanical effects in dry sliding. *Wear*, *100*(1–3), 453–476.

56. Abdel-Aal, H. A. (1997). A remark on the flash temperature theory. *International Communications in Heat and Mass Transfer*, *24*(2), 241–250.

57. Kennedy, F. E. (2000). Frictional Heating and Contact Temperatures. In B. Bhushan (Ed.), *Modern Tribology Handbook*. CRC Press.

58. Abdel-Aal, H. a. (2003). Efficiency of thermal energy dissipation in dry rubbing. *Wear*, *255*(1–6), 348–364.

59. Ling, F. F., & Pu, S. L. (1964). Probable interface temperatures of solids in sliding contact. *Wear*, *7*(1), 23–34.

60. Dimarogonas, A. D., & Michalopoulos, D. (1981). A compilation of heat distribution parameters at sliding contacts. *Tribology International*, *14*(4), 225–229.

61. Abdel-Aal, H., & Smith, S. (1998). On friction-induced temperatures of rubbing metallic pairs with temperature-dependent thermal properties. *Wear*, *48*, 41–59.

62. Floquet, A., Play, D., & Godet, M. (1977). Surface Temperatures in Distributed Contacts. Application to Bearing Design. *Journal of Lubrication Technology*, *99*(2), 277–283.

63. Majcherczak, D., Dufrenoy, P., & Berthier, Y. (2007). Tribological, thermal and mechanical coupling aspects of the dry sliding contact. *Tribology International*, *40*(5), 834–843.

64. Salti, B., & Laraqi, N. (1997). Two-Dimensional Numerical Model for Calculation of the Thermal Contact Resistance Between Two Sliding Solids. *Heat and Technology*, *15*(1), 17–22.

65. Salti, B., & Laraqi, N. (1999). 3-D numerical modeling of heat transfer between two sliding bodies: temperature and thermal contact resistance. *International Journal of Heat and Mass Transfer*, *42*(13), 2363–2374.

66. Chantrenne, P., & Raynaud, M. (2001). Study of a macroscopic sliding contact thermal model from microscopic models. *International Journal of Thermal Sciences*, *40*(7), 603–621.

67. Laraqi, N., Baïri, a., & Ségui, L. (2004). Temperature and thermal resistance in frictional devices. *Applied Thermal Engineering*, *24*(17–18), 2567–2581.

68. Chantrenne, P., & Raynaud, M. (1997). A microscopic thermal model for dry sliding contact. *Int. J. Heat Mass Tran.*, *40*(5), 1083–1094.

69. Hamraoui, M., & Zouaoui, Z. (2009). Modelling of heat transfer between two rollers in dry friction. *International Journal of Thermal Sciences*, *48*(6), 1243–1246.

70. Aderghal, N., Loulou, T., Bouchoucha, A., & Rogeon, P. (2011). Analytical and numerical calculation of surface temperature and thermal constriction resistance in transient dynamic strip contact. *Applied Thermal Engineering*, *31*(8–9), 1527–1535.

71. Tian, X., & Kennedy, F. E. (1993). Temperature rise at the sliding contact interface for a coated semi-infinite body. *Journal of Tribology*, *115*(January), 1–9.

72. Gamulya, G. D., Ostrovskaya, Y. L., Ostapenko, I. L., Presnyakova, G. N., & Strel'nitskij, V. E. (1994). Friction behaviour and wear resistance of diamond-like carbon films under cryogenic temperatures. *Diamond and Related Materials*, *3*(11–12), 1381–1384.

73. Habig, K.-H. (1995). Fundamentals of the tribological behaviour of diamond, diamond-like carbon and cubic boron nitride coatings. *Surface and Coatings Technology*, *76–77*, 540–547.

74. Lee, K.-R., Eun, K. Y., Kim, K.-M., & Choi, K.-C. (1995). Application of diamond-like carbon films for anti-abrasion and low friction properties of VCR head drums. *Surface and Coatings Technology*, *76–77*, 786–790.

75. Liu, Y., Erdemir, A., & Meletis, E. I. (1996). A study of the wear mechanism of diamond-like carbon films. *Surface and Coatings Technology*, *82*(1–2), 48–56.

76. Miyoshi, K. (1996). Friction and wear properties of as-deposited and carbon ion-implanted diamond films. *Materials Science and Engineering: A*, *209*(1–2), 38–53.

77. Banerji, A., Bhowmick, S., & Alpas, A. T. (2014). High temperature tribological behavior of W containing diamond-like carbon (DLC) coating against titanium alloys. *Surface and Coatings Technology*, *241*, 93–104.

78. Liang, C.-H., Wang, W.-L., Huang, C.-F., Tsai, H.-Y., & Yang, C.-C. (2014). The influence of microstructural variations on mechanical and tribological properties of low-friction TiC/diamond-like carbon nanocomposite films. *Ceramics International*, *40*(8), 13329–13337.

79. Winer, W. O. (1967). Molybdenum disulfide as a lubricant: A review of the fundamental knowledge. *Wear*, *10*(6), 422–452.

80. Holinski, R., & Gänsheimer, J. (1972). A study of the lubricating mechanism of molybdenum disulfide. *Wear*, *19*(3), 329–342.

81. Wang, H., Xu, B., Liu, J., & Zhuang, D. (2007). Molybdenum disulfide coating deposited by hybrid treatment and its friction-reduction performance. *Surface and Coatings Technology*, *201*(15), 6719–6722.

82. Ye, Y., Chen, J., & Zhou, H. (2009). An investigation of friction and wear performances of bonded molybdenum disulfide solid film lubricants in fretting conditions. *Wear*, *266*(7–8), 859–864.

83. Dunckle, C. G., Aggleton, M., Glassman, J., & Taborek, P. (2011). Friction of molybdenum disulfide–titanium films under cryogenic vacuum conditions. *Tribology International*, *44*(12), 1819–1826.

84. Miyajima, T., Tanaka, Y., Iwai, Y., Kagohara, Y., Haneda, S., Takayanagi, S., & Katsuki, H. (2013). Friction and wear properties of lead-free aluminum alloy bearing material with molybdenum disulfide layer by a reciprocating test. *Tribology International*, *59*, 17–22.

85. Brainard, W. A., & Buckley, D. H. (1973). Adhesion and friction of PTFE in contact with metals as studied by Auger spectroscopy, field ion and scanning electron microscopy. *Wear*, *26*(1), 75–93.

86. Briscoe, B. J., Steward, M. D., & Groszek, A. J. (1977). The effect of carbon aspect ratio on the friction and wear of PTFE. *Wear*, *42*(1), 99–107.

87. Biswas, S. K., & Vijayan, K. (1992). Friction and wear of PTFE — a review. *Wear*, *158*(1–2), 193–211.

88. Su, F., Zhang, Z., & Liu, W. (2008). Friction and wear behavior of hybrid glass/PTFE fabric composite reinforced with surface modified nanometer ZnO. *Wear*, *265*(3–4), 311–318.

89. Ye, J., Khare, H. S., & Burris, D. L. (2013). Transfer film evolution and its role in promoting ultra-low wear of a PTFE nanocomposite. *Wear*, *297*(1–2), 1095–1102.

90. Conte, M., Pinedo, B., & Igartua, A. (2013). Role of crystallinity on wear behavior of PTFE composites. *Wear*, *307*(1–2), 81–86.

91. Aderikha, V. N., Krasnov, A. P., Shapovalov, V. A., & Golub, A. S. (2014). Peculiarities of tribological behavior of low-filled composites based on polytetrafluoroethylene (PTFE) and molybdenum disulfide. *Wear*, *320*, 135–142.

92. Tzanakis, I., Conte, M., Hadfield, M., & Stolarski, T. A. (2013). Experimental and analytical thermal study of PTFE composite sliding against high carbon steel as a function of the surface roughness, sliding velocity and applied load. *Wear*, *303*(1–2), 154–168.

93. Voss, H., & Friedrich, K. (1987). On the wear behaviour of short-fibre-reinforced peek composites. *Wear*, *116*(1), 1–18.

94. Zhang, G., Liao, H., Li, H., Mateus, C., Bordes, J.-M., & Coddet, C. (2006). On dry sliding friction and wear behaviour of PEEK and PEEK/SiC-composite coatings. *Wear*, *260*(6), 594–600.

95. Zhang, G., & Schlarb, A. K. (2009). Morphologies of the wear debris of polyetheretherketone produced under dry sliding conditions: Correlation with wear mechanisms. *Wear*, *266*(7–8), 745–752.

96. Zhang, G., Rasheva, Z., & Schlarb, A. K. (2010). Friction and wear variations of short carbon fiber (SCF)/PTFE/graphite (10 vol.%) filled PEEK: Effects of fiber orientation and nominal contact pressure. *Wear*, *268*(7–8), 893–899.

97. Greco, A. C., Erck, R., Ajayi, O., & Fenske, G. (2011). Effect of reinforcement morphology on high-speed sliding friction and wear of PEEK polymers. *Wear*, *271*(9–10), 2222–2229.

98. Koike, H., Kida, K., Santos, E. C., Rozwadowska, J., Kashima, Y., & Kanemasu, K. (2012). Self-lubrication of PEEK polymer bearings in rolling contact fatigue under radial loads. *Tribology International*, *49*(0), 30–38.

99. Zhang, G., Chang, L., & Schlarb, A. K. (2009). The roles of nano-SiO2 particles on the tribological behavior of short carbon fiber reinforced PEEK. *Composites Science and Technology*, *69*(7–8), 1029–1035.

100. Adahan, C. (2008). Single-Vane Rotary Pump or Motor. Jerusalem, IL.

101. Hibbeler, R. C. (2011). *Mechanics of Materials* (8th Ed.). Prentice Hall.

102. EFunda. (n.d.). eFunda: Properties of Alloy Steel AISI 4140. Retrieved from http://www.efunda.com/Materials/alloys/alloy_steels/show_alloy.cfm?ID=AISI_4140&prop=all&Page_Title=AISI 4140

103. Wang, Q. (1997). Seizure failure of journal-bearing conformal contacts. *Wear*, *210*(1–2), 8–16.

104. Unal, H., Mimaroglu, A., Kadıoglu, U., & Ekiz, H. (2004). *Sliding friction and wear behaviour of polytetrafluoroethylene and its composites under dry conditions*. *Materials & Design* (Vol. 25).

105. Cengel, Y. A., & Boles, M. A. (2006). *Thermodynamics: An Engineering Approach* (5th ed.). McGraw Hill.

106. Lemmon, E. W., & Huber, M. L. (2010). NIST Reference Fluid Thermodynamic and Transport Properties Database (REFPROP): Version 9.1. Gaithersburg: National Institute of Standards and Technology.

107. Disconzi, F. P., Deschamps, C. J., & Pereira, E. L. L. (2012). Development of an In-Cylinder Heat Transfer Correlation for Reciprocating Compressors. In *International Compressor Engineering Conference*.

108. Fagotti, F., Todescat, M. L., Ferreira, R. T. S., & Prata, A. T. (1994). Heat Transfer Modeling in a Reciprocating Compressor. In *International Compressor Engineering Conference*.

109. Fagotti, F., & Prata, A. T. (1998). A New Correlation for Instantaneous Heat Transfer Between Gas and Cylinder in Reciprocating Compressors. In *International Compressor Engineering Conference*.

110. Potter, M., Wiggert, D., & Ramadan, B. (2011). *Mechanics of Fluids* (4th ed.). Cengage Learning.

111. Munson, B. R., Young, D. F., Okiishi, T. H., & Huebsch, W. W. (2009). *Fundamentals of Fluid Mechanics* (6th ed.). Jefferson City: John Wiley & Sons, Inc.

112. Yanagisawa, T., & Shimizu, T. (1985). Leakage losses with a rolling piston type rotary compressor. I. Radical clearance on the rolling piston. *International Journal of Refrigeration*, *8*(2), 75–84.

113. Shih, T.-H., Liou, W. W., Shabbir, A., Yang, Z., & Zhu, J. (1994). A New K-epsilon Eddy Viscosity Model for High Reynolds Number Turbulent Flows: Model Development and Validation. *NASA Technical Report*. Retrieved from http://ntrs.nasa.gov/search.jsp?R=19950005029

114. Meirovitch, L. (2001). *Fundamentals of Vibrations* (Intl Ed.). McGraw-Hill.

115. Thornton, S. T., & Marion, J. B. (2004). *Classical Dynamics of Particles and Systems* (5th ed.). Belmont, CA: Brooks/Cole.

116. Keljik, J. (2009). *Electricity 4: AC/DC Motors, Controls, and Maintenance* (9th ed.). Cengage Learning.

117. Subiantoro, A., & Ooi, K. T. (2011). Analytical study of the endface friction of the revolving vane mechanism. *International Journal of Refrigeration*, *34*(5), 1276–1285.

118. Dou, H.-S., Khoo, B. C., & Yeo, K. S. (2008). Instability of Taylor–Couette flow between concentric rotating cylinders. *International Journal of Thermal Sciences*, *47*(11), 1422–1435.

119. Dou, H.-S., Khoo, B. C., & Yeo, K. S. (2007). Energy loss distribution in the plane Couette flow and the Taylor–Couette flow between concentric rotating cylinders. *International Journal of Thermal Sciences*, *46*(3), 262–275.

120. Bertin, J. J., & Cummings, R. M. (2009). *Aerodynamics for Engineers* (5th ed.). Prentice Hall.

121. Ooi, K. T., Chai, G. B., & Kwek, E. C. (1992). A Simple Valve Model to Study the Performance of a Small Compressor. In *International Compressor Engineering Conference*.

122. Ooi, K. T. (2003). Heat transfer study of a hermetic refrigeration compressor. *Applied Thermal Engineering*, *23*(15), 1931–1945.

123. Incropera, F. P., Bergman, T. L., DeWitt, D. P., Lavine, A., Seetharamu, K. N., & R, S. T. (2011). *Fundamentals of Heat and Mass Transfer* (6th ed.). Wiley.

124. Gardiner, S. R. ., & Sabersky, R. . (1978). Heat transfer in an annular gap. *International Journal of Heat and Mass Transfer*, *21*(12), 1459–1466.

125. Becker, K. M. (1963). Measurements of convective heat transfer from a horizontal cylinder rotating in a tank of water. *International Journal of Heat and Mass Transfer*, *6*(12), 1053–1062.

126. Özerdem, B. (2000). Measurement of convective heat transfer coefficient for a horizontal cylinder rotating in quiescent air. *International Communications in Heat and Mass Transfer*, *27*(3), 389–395.

127. Bardon, J. P. (1994). Bases physiques des conditions de contact thermique imparfait entre milieux en glissement relatif. *Revue générale de thermique*, *33*(386).

128. McAdams, W. H. (1954). *Heat Transmission* (3rd Ed.). New York: McGraw-Hill.

129. Churchill, S. W., & Chu, H. H. S. (1975). Correlating equations for laminar and turbulent free convection from a vertical plate. *International Journal of Heat and Mass Transfer*, *18*(11), 1323–1329.

130. Cobb, E. C., & Saunders, O. A. (1956). Heat Transfer from a Rotating Disk. *Proceedings of the Royal Society of London. Series A, Mathematical and Physical Sciences*, *236*(1206), 343–351.

131. Wagner, C. (1948). Heat Transfer from a Rotating Disk to Ambient Air. *Journal of Applied Physics*, *19*(9).

132. Reich, G., Weigand, B., & Beer, H. (1989). Fluid flow and heat transfer in an axially rotating pipe -I. Effect of rotation on turbulent pipe flow. *International journal for Heat and Mass transfer*, *32*(9), 551–562.

133. Reich, G., Weigand, B., & Beer, H. (1989). Fluid flow and heat transfer in an axially rotating pipe -II. Effect of rotation on laminar pipe flow. *International journal for Heat and Mass transfer*, *32*(9), 563–574.

134. Seghir-Ouali, S., Saury, D., Harmand, S., Phillipart, O., & Laloy, D. (2006). Convective heat transfer inside a rotating cylinder with an axial air flow. *International Journal of Thermal Sciences*, *45*(12), 1166–1178.

135. Mathworks. (2015). Matrix inverse - MATLAB inv. *R2015a Documentation*. Retrieved from http://www.mathworks.com/help/matlab/ref/inv.html

136. SKF. (2015). Estimating the frictional moment - Table 1. Retrieved from http://www.skf.com/sg/products/bearings-units-housings/ball-bearings/principles/friction/estimating-frictional-moment/index.html

137. Omega Engineering. (n.d.). Thermocouples: Using Thermocouples in Temperature Measurement. Retrieved from http://www.omega.com/prodinfo/thermocouples.html

138. Reotemp Instrument Corporation. (n.d.). Type T Thermocouple. Retrieved from http://www.thermocoupleinfo.com/type-t-thermocouple.htm

139. Subiantoro, A., Yap, K. S., & Ooi, K. T. (2013). Experimental investigations of the revolving vane (RV-I) expander. *Applied Thermal Engineering*, *50*(1), 393–400.

140. Huang, K. D., & Tzeng, S.-C. (2005). Development of a hybrid pneumatic-power vehicle. *Applied Energy*, *80*(1), 47–59.

141. Huang, K. D., Tzeng, S.-C., Ma, W.-P., & Chang, W.-C. (2005). Hybrid pneumatic-power system which recycles exhaust gas of an internal-combustion engine. *Applied Energy*, *82*(2), 117–132.

142. Huang, K. D., Tzeng, S.-C., & Chang, W.-C. (2005). Energy-saving hybrid vehicle using a pneumatic-power system. *Applied Energy*, *81*(1), 1–18.

143. Hung, Y.-H., Tung, Y.-M., & Li, H.-W. (2014). A real-time model of an automotive air propulsion system. *Applied Energy*, *129*, 287–298.

144. Wang, Y.-W., You, J.-J., Sung, C.-K., & Huang, C.-Y. (2014). The Applications of Piston Type Compressed Air Engines on Motor Vehicles. *Procedia Engineering*, *79*, 61–65.

145. Shen, Y.-T., & Hwang, Y.-R. (2009). Design and implementation of an air-powered motorcycles. *Applied Energy*, *86*(7–8), 1105–1110.

146. Chen, H., Ding, Y., Li, Y., Zhang, X., & Tan, C. (2011). Air fuelled zero emission road transportation: A comparative study. *Applied Energy*, *88*(1), 337–342.

147. Zhang, Y., & Nishi, A. (2003). Low-pressure air motor for wall-climbing robot actuation. *Mechatronics*, *13*(4), 377–392.

148. Liu, J.-L., & Wang, J.-H. (2015). Thermodynamic analysis of a novel tri-generation system based on compressed air energy storage and pneumatic motor. *Energy*, *91*, 420–429.

149. Wang, J., Pu, J., Moore, P. R., & Zhang, Z. (1998). Modelling study and servo-control of air motor systems. *International Journal of Control*, *71*(3), 459–476.

150. Kokaew, V., Moshrefi-Torbati, M., & Sharkh, S. M. (2013). Maximum Efficiency or Power Tracking of Stand-alone Small Scale Compressed Air Energy Storage System. *Energy Procedia*, *42*, 387–396.

151. Tokhi, M. O., Al-Miskiry, M., & Brisland, M. (2001). Real-time control of air motors using a pneumatic H-bridge. *Control Engineering Practice*, *9*(4), 449–457.

152. Lu, C.-H., Hwang, Y.-R., & Shen, Y.-T. (2011). Backstepping sliding mode tracking control of a vane-type air motor X-Y table motion system. *ISA transactions*, *50*(2), 278–86.

153. Lu, C.-H., & Hwang, Y.-R. (2012). Hybrid sliding mode position control for a piston air motor ball screw table. *ISA transactions*, *51*(3), 373–85.

154. Liu, C.-M., You, J.-J., Sung, C.-K., & Huang, C.-Y. (2015). Modified intake and exhaust system for piston-type compressed air engines. *Energy*, *90*, 516–524.

155. Naranjo, J., Kussul, E., & Ascanio, G. (2010). A new pneumatic vanes motor. *Mechatronics*, *20*(3), 424–427.

156. Subiantoro, A., & Ooi, K. T. (2014). Comparison and performance analysis of the novel revolving vane expander design variants in low and medium pressure applications. *Energy*, *78*, 747–757.

157. Subiantoro, A. (2012). *Development of a Revolving Vane Expander*. Nanyang Technological University.

158. Wang, B., Shi, W., & Li, X. (2009). Numerical analysis on the effects of refrigerant injection on the scroll compressor. *Applied Thermal Engineering*, *29*(1), 37–46.

159. Wang, B., Shi, W., Han, L., & Li, X. (2009). Optimization of refrigeration system with gas-injected scroll compressor. *International Journal of Refrigeration*, *32*(7), 1544–1554.

160. Mathison, M. M., Braun, J. E., & Groll, E. A. (2013). Modeling of a novel spool compressor with multiple vapor refrigerant injection ports. *International Journal of Refrigeration*, *36*(7), 1982–1997.

161. Mathworks. (2014). Numerically evaulate double integral - MATLAB integral2. *R2014b Documentation*. Retrieved from http://www.mathworks.com/help/matlab/ref/integral2.html

Appendices

A-1 Compressor Simulation Model

All aspects of the RV compressor model have been covered in Chapters 4 to 7. This appendix section will go into detail, the simulation procedure for the RV compressor using the models.

Simulation Blocks

The mathematical models are coded with MATLAB, with the incorporation of REFPROP [106] for the calculation of the thermophysical properties of the working fluid. The mathematical models are divided into five distinct blocks as follows:

1. Geometric
2. Initialization
3. Dynamics
4. Thermal
5. Full thermodynamics

The geometric block calculates the geometric properties of the RV compressor based on the compressor dimensions such as the volume variations along with the port opening areas. The initialization block calculates the initial thermodynamics properties of the fluid in the suction and compression chambers with the assumption that the processes are adiabatic and without any internal leakage. The dynamics block evaluates the frictional forces, vibration characteristics and clearances in the compressor with the given thermodynamics data. The thermal block calculates the steady state operating temperature of the components. The full thermodynamics block calculates the thermodynamics properties of the working fluid in both the suction and compression chambers with internal leakage and heat transfer taken into consideration.

Simulation Algorithm

With the compressor dimensions, the geometric block evaluates the geometric properties of the RV compressor covered in Chapter 4, Section 5.4 (flow orifice areas), which are independent of the operating conditions. Following this, the operating conditions and calculated geometric properties are then utilized in the initialization block to obtain the

estimates of the thermodynamics properties of the working fluid in the chambers. The thermodynamics model from Chapter 5 is adapted for use in the initialization block albeit without the leakage and heat transfer equations. The initial thermodynamics properties are then used in the dynamics block to calculate the rotational vibration, bearing forces, friction forces and radial clearance in the compressor as presented in Chapter 6. This is then followed by the thermal block that utilizes the frictional losses from the dynamics block to solve for the component temperatures of the compressor with the model discussed in Chapter 7.

To this end, the full initialization of the RV compressor has been completed from which iterations will be carried out with the combination of the full thermodynamics, dynamics and thermal blocks. The full thermodynamics block first recalculates the thermodynamic properties of the working fluid in the chambers with the leakage and heat transfer equations. In this block, iterations are repeated until the mass and pressure values in each chamber coincide with each other during the start and end of each cycle – the suction pressure and mass values at the end of the suction cycle should coincide with the starting compression pressure and mass values and vice versa. The resultant thermodynamic properties are then passed into the respective dynamics and thermal blocks to reevaluate the rotational vibration and component temperatures. In the dynamics block, iterations are carried out until the rotation speed at the end of the cycle coincides with the initial speed at the start of the cycle. After the thermal block, it marks the end of a full iteration for the RV compressor. This entire process is then repeated until the final values of the mass flow rates, rotation speeds and component temperatures coincide with each other between two full iterations.

Within the blocks where necessary, differential equations with initial value problems such as those in Chapter 5 and 6 are solved with the 4^{th}-order Runge Kutta method. The time dependent differential equations are transformed to that of angle-step dependent differential equations and a step size of 0.02° is used.

The bisection interval search method with a convergence criterion of 1.0% difference between the iterated roots was employed for solving the roots of equations numerically or to iterate the equivalent flow channel lengths for determining internal leakage.

Numerical integration is achieved with the trapezoidal method. In cases where numerical double integration is required, an in-built MATLAB function [161] is used instead. Matrix

inversion for solution of simultaneous equations is achieved with Gaussian elimination using MATLAB's native matrix operators [135].

The algorithm of the MATLAB code is presented in a flow chart shown in Figure A1-1. The convergence criterion used in the final check of the algorithm before ending the programme is set at 1.0%.

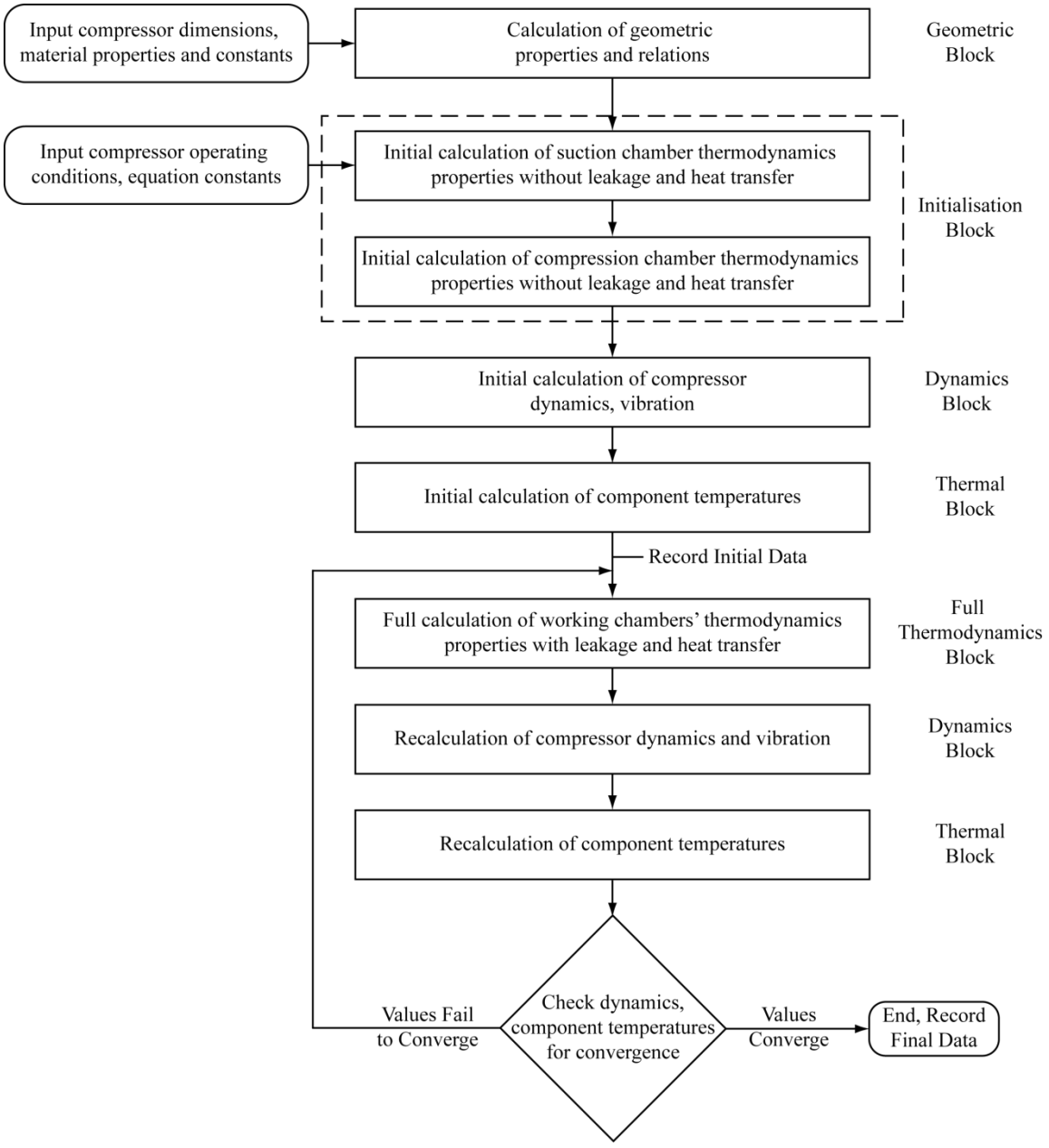

Figure A1-1: MATLAB Simulation Algorithm

A-2 Realizable *k-ε* Turbulence Flow Model

The realizable *k-ε* turbulence flow model [113] was used for modelling the CFD simulation in ANSYS Fluent for the different leakage paths in the RV compressor prototype. This model was developed as more robust alternative to the standard *k-ε* turbulence flow model. The model consists of three equations: a turbulent kinetic energy (k) equation, the turbulent kinetic energy dissipation rate (ε) equation and the turbulent viscosity (υ_t) equation, reproduced in this appendix section for ease of reference. The equations are written in tensor notation, with u corresponding to the velocity and subscripts i, j, k referring to coordinate directions.

$$k_{,t} + u_j k_{,j} = \left(\upsilon_t k_{,j}\right)_{,j} - u_{i,j}\left[\upsilon_t\left(u_{i,j} + u_{j,i}\right) - \frac{2}{3}k\delta_{ij}\right] - \varepsilon \tag{A1}$$

$$\varepsilon_{,t} + u_j \varepsilon_{,j} = \left(\frac{\upsilon_t}{1.2}k_{,j}\right)_{,j} + Cs\varepsilon - 1.9\frac{\varepsilon^2}{k + \sqrt{\frac{\mu\varepsilon}{\rho}}} \tag{A2}$$

$$\upsilon_t = C_\mu \frac{k^2}{\varepsilon} \tag{A3}$$

where

$$C = \max(0.43, \frac{\eta}{\eta + 5}) \tag{A4}$$

$$\eta = \frac{sk}{\varepsilon} \tag{A5}$$

$$s = \sqrt{2 s_{ij} s_{ij}} \tag{A6}$$

$$s_{ij} = \frac{1}{2}\left(u_{i,j} + u_{j,i}\right) \tag{A7}$$

$$C_\mu = \frac{1}{4.04 + \sqrt{6}\left(U\frac{k}{\varepsilon}\right)\cos\phi} \tag{A8}$$

$$\phi = \frac{1}{3}\cos^{-1}\sqrt{6}W \tag{A9}$$

$$W = \frac{\sqrt{8} s_{ij} s_{jk} s_{ik}}{s^3} \tag{A10}$$

$$U = \sqrt{s_{ij} s_{ij} + \widetilde{\Omega}_{ij}\widetilde{\Omega}_{ij}} \tag{A11}$$

$$\widetilde{\Omega}_{ij} = \Omega_{ij} - 2\varepsilon_{ijk}\omega_k \tag{A12}$$

$$\Omega_{ij} = \overline{\Omega}_{ij} - \varepsilon_{ijk} \tag{A13}$$

where $\bar{\Omega}_{ij}$ is the average rotation rate in the rotating reference frame corresponding to the angular velocity ω_k.

A-3 Dynamics Equations and Calculations

The time derivatives of the rotation angles for the compressor components can be converted into a form in terms of only the time derivatives of the rotation angle of the main driving component. For the case presented below, the time derivatives of the rotor angle are converted into that of the cylinder angle which is the main driving component for the case of the compressor prototype. Note that the final forms in Equations (A14) and (A15) are applicable to other components by simply the subscripts.

$$\begin{aligned}\dot{\theta}_r &= \frac{d\theta_r}{dt} = \frac{d\theta_r}{d\theta_c}\cdot\frac{d\theta_c}{dt} \\ &= \dot{\theta}_c\frac{d\theta_r}{d\theta_c}\end{aligned} \tag{A14}$$

$$\begin{aligned}\ddot{\theta}_r &= \frac{d}{dt}\left(\frac{d\theta_r}{d\theta_c}\cdot\frac{d\theta_c}{dt}\right) = \frac{d}{d\theta_c}\left(\frac{d\theta_r}{d\theta_c}\cdot\frac{d\theta_c}{dt}\right)\frac{d\theta_c}{dt} \\ &= \frac{d^2\theta_R}{d\theta_c^2}\cdot\frac{d\theta_c}{dt}\cdot\frac{d\theta_c}{dt} + \frac{d\theta_r}{d\theta_c}\cdot\frac{d}{d\theta_c}\left(\frac{d\theta_c}{dt}\right)\frac{d\theta_c}{dt} \\ &= \frac{d^2\theta_r}{d\theta_c^2}\left(\frac{d\theta_c}{dt}\right)^2 + \frac{d\theta_r}{d\theta_c}\cdot\frac{d}{dt}\left(\frac{d\theta_c}{dt}\right) \\ &= \dot{\theta}_c^2\frac{d^2\theta_r}{d\theta_c^2} + \ddot{\theta}_c\frac{d\theta_r}{d\theta_c}\end{aligned} \tag{A15}$$

Detailed values from the calculations of the fluid shear torque on the cylinder and the form drag on the valve stop during operation are presented below.

Cylinder wall fluid shear torque calculations:

Area:

Cylinder length: 66 x 10^{-3} m

Cylinder outer radius: 60 x 10^{-3} m

Calculated cylinder wall area = 1.24 x 10^{-2} m^2

Housing wall height: 70 x 10^{-3} m

Housing wall inner radius: 67 x 10^{-3} m

Calculated housing wall area = 1.47 x 10^{-2} m^2

Calculated for the top or bottom housing endfaces = $\pi(672 - 602) \times 10^{-6} = 2.79 \times 10^{-3}$ m^2

Drag forces:

Calculated drag force on cylinder wall = 6.02×10^{-3} N

Calculated drag force on housing wall = 5.39×10^{-3} N

Calculated drag force on housing endface wall = 3.88×10^{-4} N

Form drag calculation for valve stop:

Valve stop width: 10×10^{-3} m

Valve stop length: 22.53×10^{-3} m

Calculated valve stop area = 2.25×10^{-4} m^2

Radial displacement of valve stop from cylinder centre: 59.5 x 10-3 m

Calculated radial speed at 1000 rev min^{-1} = 6.25 m s^{-1}

Fluid properties of air at room temperature, pressure:

Density = 1.16 kg m-3

Viscosity = 1.858 x 10-5 Pa s

Calculated Reynolds No. for valve stop = 3902 < 500,000

Calculated drag coefficient = 0.0212

Calculated drag force = 1.08×10^{-4} N

Calculated torque = 6.43×10^{-6} N·m

A-4 Heat Transfer Equations

The heat transfer equations for each of the elements in the compressor prototype are presented in Equations (A16) to (A27) and the expressions for the heat transfer coefficients in Equations (A28) to

(A53).

$$H_{c1,c2}(T_{c1}-T_{c2})+H_{c1,\infty}(T_{c1}-T_{\infty})=0$$
$$\rightarrow \left(H_{c1,c2}+H_{c1\infty}\right)T_{c1}-H_{c1,c2}T_{c2}=H_{c1,\infty}T_{\infty} \quad \text{(A16)}$$

$$H_{c2,c1}(T_{c2}-T_{c1})+H_{c2,c3}(T_{c2}-T_{c3})=0.99\left(\frac{1}{2}\dot{Q}_{f,s1}\right)$$
$$\rightarrow -H_{c2,c1}T_{c1}+\left(H_{c2,c1}+H_{c2,c3}\right)T_{c2}-H_{c2,c3}T_{c3}=0.99\left(\frac{1}{2}\dot{Q}_{f,s1}\right) \quad \text{(A17)}$$

$$H_{c3,c2}(T_{c3}-T_{c2})+H_{c3,c4}(T_{c3}-T_{c4})+H_{c3,fluid}\left(T_{c3}-T_{fluid}\right)+H_{c3,dis}(T_{c3}-T_{dis})=0$$
$$\rightarrow -H_{c3,c2}T_{c2}+\left(H_{c3,c2}+H_{c3,c4}+H_{c3,fluid}+H_{c3,dis}\right)T_{c3}-H_{c3,c4}T_{c4}=H_{c3,fluid}T_{fluid}+H_{c3,dis}T_{dis} \quad \text{(A18)}$$

$$H_{c4,c3}(T_{c4}-T_{c3})+H_{c4,dis}(T_{c4}-T_{dis})=0.99\left(\frac{1}{2}\dot{Q}_{f,s2}+\dot{Q}_{f,v}\right)$$
$$\rightarrow -H_{c4,c3}T_{c3}+\left(H_{c4,c3}+H_{c4,dis}\right)T_{c4}=0.99\left(\frac{1}{2}\dot{Q}_{f,s2}+\dot{Q}_{f,v}\right)+H_{c4,dis}T_{dis} \quad \text{(A19)}$$

$$H_{r1,r2}(T_{r1}-T_{r2})+H_{r1,\infty}(T_{r1}-T_{\infty})+H_{r1,suc}(T_{r1}-T_{suc})=0.025\dot{Q}_{f,r}$$
$$\rightarrow \left(H_{r1,r2}+H_{r1,\infty}+H_{r1,suc}\right)T_{r1}-H_{r1,r2}T_{r2}=0.025\dot{Q}_{f,r}+H_{r1,\infty}T_{\infty}+H_{r1,suc}T_{suc} \quad \text{(A20)}$$

$$H_{r2,r1}(T_{r2}-T_{r1})+H_{r2,r3}(T_{r2}-T_{r3})+H_{r2,suc}(T_{r2}-T_{suc})=0$$
$$\rightarrow -H_{r2,r1}T_{r1}+\left(H_{r2,r1}+H_{r2,r3}+H_{r2,suc}\right)T_{r2}-H_{r2,r3}T_{r3}=H_{r2,suc}T_{suc} \quad \text{(A21)}$$

$$H_{r3,r2}(T_{r3}-T_{r2})+H_{r3,r4}(T_{r3}-T_{r4})+H_{r3,suc}(T_{r3}-T_{suc})=0$$
$$\rightarrow -H_{r3,r2}T_{r2}+\left(H_{r3,r2}+H_{r3,r4}+H_{r3,suc}\right)T_{r3}-H_{r3,r4}T_{r4}=H_{r3,suc}T_{suc} \quad \text{(A22)}$$

$$H_{r4,r3}(T_{r4}-T_{r3})+H_{r4,suc}(T_{r4}-T_{suc})+H_{r4,fluid}\left(T_{r4}-T_{fluid}\right)=0$$
$$\rightarrow -H_{r4,r3}T_{r3}+\left(H_{r4,r3}+H_{r4,suc}+H_{r4,fluid}\right)T_{r4}=H_{r4,suc}T_{suc}+H_{r4,fluid}T_{fluid} \quad \text{(A23)}$$

$$H_{h1,h2}(T_{h1}-T_{h2})+H_{h1,\infty}(T_{h1}-T_{\infty})=0.99\left(\frac{1}{2}\dot{Q}_{f,s1}\right)$$
$$\rightarrow \left(H_{h1,h2}+H_{h1,\infty}\right)T_{h1}-H_{h1,h2}T_{h2}=0.99\left(\frac{1}{2}\dot{Q}_{f,s1}\right)+H_{h1,\infty}T_{\infty} \quad \text{(A24)}$$

$$H_{h2,h1}(T_{h2}-T_{h1})+H_{h2,h3}(T_{h2}-T_{h3})+H_{h2,\infty}(T_{h2}-T_{\infty})+H_{h2,dis}(T_{h2}-T_{dis})=0$$
$$\rightarrow -H_{h2,h1}T_{h1}+\left(H_{h2,h1}+H_{h2,h3}+H_{h2,\infty}+H_{h2,dis}\right)T_{h2}-H_{h2,h3}T_{h3}=H_{h2,\infty}T_{\infty}+H_{h2,dis}T_{dis} \quad \text{(A25)}$$

$$H_{h3,h2}(T_{h3}-T_{h2})+H_{h3,h4}(T_{h3}-T_{h4})+H_{h3,\infty}(T_{h3}-T_{\infty})+H_{h3,dis}(T_{h3}-T_{dis})=0$$
$$\rightarrow -H_{h3,h2}T_{h2}+\left(H_{h3,h2}+H_{h3,h4}+H_{h3,\infty}+H_{h3,dis}\right)T_{h3}-H_{h3,h4}T_{h4}=H_{h3,\infty}T_{\infty}+H_{h3,dis}T_{dis} \quad \text{(A26)}$$

$$H_{h4,h3}(T_{h4}-T_{h3})+H_{h4,\infty}(T_{h4}-T_{\infty})+H_{h4,fluid}\left(T_{h4}-T_{fluid}\right)=0.99\left(\frac{1}{2}\dot{Q}_{f,s2}\right)+0.975\dot{Q}_{f,r}$$

$$\rightarrow -H_{h4,h3}T_{h3} + \left(H_{h4,h3} + H_{h4,\infty} + H_{h4.fluid}\right)T_{h4} = 0.99\left(\frac{1}{2}\dot{Q}_{f,s2}\right) + 0.975\dot{Q}_{f,r} + H_{h4,\infty}T_{\infty} + H_{h4,fluid}T_{fluid} \tag{A27}$$

where

$$H_{c2,c1} = H_{c1,c2} = \frac{k_{steel}A_{c1,c2}}{l_{c1,c2}} = \frac{2k_{steel}\pi r_{shaft}^2}{l_{c1} + l_{c2}} \tag{A28}$$

$$H_{c1,\infty} = \frac{k_{air}A_{c1,\infty}}{D_{c1,\infty}}\left(0.119\mathrm{Re}_r^{2/3}\right) + 0.25A_{c1,\infty}\sigma(T_{c1} + T_{\infty})(T_{c1}^2 + T_{\infty}^2) = 0.119k_{air}l_{c1}\mathrm{Re}_r^{2/3} + 0.5\pi r_{shaft}l_{c1}\sigma(T_{c1} + T_{\infty})(T_{c1}^2 + T_{\infty}^2) \tag{A29}$$

$$H_{c2,c3} = H_{c3,c2} = \frac{k_{steel}A_{c2,c3}}{l_{c2,c3}} = \frac{2k_{steel}\pi r_{shaft}^2}{l_{c2} + l_{c3}} \tag{A30}$$

$$H_{c3,c4} = H_{c4,c3} = \frac{k_{steel}A_{c3,c4}}{l_{c3,c4}} = \frac{2k_{steel}\pi\left(r_{c4_o}^2 - r_{c4_i}^2\right)}{l_{c3} + l_{c4}} \tag{A31}$$

$$H_{c3,fluid} = \frac{\bar{\bar{k}}_{fluid}A_{c3,fluid}}{\bar{D}_{c3,fluid}}(0.75\overline{\mathrm{Re}}^{0.8}\overline{\mathrm{Pr}}^{0.6}) = \frac{0.75\bar{k}_{fluid}\overline{\mathrm{Re}}^{0.8}\overline{\mathrm{Pr}}^{0.6}\left(A_{c,com} + A_{c,suc} + A_{ef,suc} + A_{ef,com}\right)}{\bar{D}_{c3,fluid}} \tag{A32}$$

$$H_{c3,dis} = \frac{k_{fluid}A_{c3,dis}}{D_{c3}}\left[0.409\left(\frac{\mathrm{Ta}}{C_{geo}}\right)_{c3}^{0.241}\right] = 0.409k_{fluid}l_{c3}\left(\frac{\mathrm{Ta}}{C_{geo}}\right)_{c3}^{0.241} \tag{A33}$$

$$H_{c4,dis} = \frac{k_{fluid}A_{c4,dis}}{D_{c4}}\left[0.409\left(\frac{\mathrm{Ta}}{C_{geo}}\right)_{c4}^{0.241}\right] = 0.409k_{fluid}l_{c4}\left(\frac{\mathrm{Ta}}{C_{geo}}\right)_{c4}^{0.241} \tag{A34}$$

$$H_{r1,r2} = H_{r2,r1} = \frac{k_{PEEK}A_{r1,r2}}{l_{r1,r2}} = \frac{2k_{PEEK}\pi r_{shaft}^2}{l_{r1} + l_{r2}} \tag{A35}$$

$$H_{r1,\infty} = \frac{k_{air}A_{r1,\infty}}{D_{c1,\infty}}\left(0.335\mathrm{Re}_{disc}^{0.5}\right) = k_{air}\pi\left(r_{shaft} + r_{pt,suc}\right)\left(0.335\mathrm{Re}_{disc}^{0.5}\right) \tag{A36}$$

$$H_{r1,suc} = \frac{k_{air}A_{r1,suc}}{D_{r1,suc}}(0.01963\mathrm{Re}_{suc}^{0.9285} + 8.5101\times10^{-6}\mathrm{Re}_{\omega}^{1.4513}) = k_{air}l_{r1}(0.01963\mathrm{Re}_{suc}^{0.9285} + 8.5101\times10^{-6}\mathrm{Re}_{\omega}^{1.4513}) \tag{A37}$$

$$H_{r2,r3} = H_{r3,r2} = \frac{k_{PEEK}A_{r2,r3}}{\frac{1}{2}\left(r_{r2} + r_{pt,suc}\right)\ln\left[\frac{0.5(r_{r3} + r_{r2})}{0.5\left(r_{r2} + r_{pt,suc}\right)}\right]} = \frac{4k_{PEEK}\pi r_{r2}l_{r2}}{\left(r_{r2} + r_{pt,suc}\right)\ln\left(\frac{r_{r3} + r_{r2}}{r_{r2} + r_{pt,suc}}\right)} \tag{A38}$$

$$H_{r2,suc} = \frac{3.66k_{air}A_{r2,suc}}{D_{r2,suc}} = 3.66k_{air}r_{r2} \tag{A39}$$

$$H_{r3,r4} = H_{r4,r3} = \frac{k_{PEEK}A_{r3,r4}}{\frac{1}{2}(r_{r3} + r_{r2})\ln\left[\frac{0.5(r_{r4} + r_{r3})}{0.5(r_{r3} + r_{r2})}\right]} = \frac{4k_{PEEK}\pi r_{r3}l_{r3}}{(r_{r3} + r_{r2})\ln\left(\frac{r_{r4} + r_{r3}}{r_{r3} + r_{r2}}\right)} \tag{A40}$$

$$H_{r3,suc} = \frac{3.66k_{air}A_{r3,suc}}{D_{r3,suc}} = 3.66k_{air}(r_{r3} - r_{r2}) \tag{A41}$$

$$H_{r4,fluid} = \frac{\bar{k}_{fluid}A_{r4,fluid}}{\bar{D}_{r4,fluid}}(0.75\overline{\mathrm{Re}}^{0.8}\overline{\mathrm{Pr}}^{0.6}) = \frac{0.75\bar{k}_{fluid}\overline{\mathrm{Re}}^{0.8}\overline{\mathrm{Pr}}^{0.6}\left(A_{r,com} + A_{r,suc} + A_{r,slot}\right)}{\bar{D}_{r4,fluid}} \tag{A42}$$

$$H_{r4,suc} = \frac{3.66 k_{air} A_{r4,suc}}{D_{r4,suc}} = 3.66 k_{air}(r_{r4} - r_{r3}) \tag{A43}$$

$$H_{h1,h2} = H_{h2,h1} = \frac{k_{steel} A_{h1,h2}}{0.5\left(r_{h1_o} + r_{h1_i}\right) \ln\left[\frac{0.5\left(r_{h2_o} + r_{h1_o}\right)}{0.5\left(r_{h1_o} + r_{h1_i}\right)}\right]} = \frac{4 k_{steel} \pi r_{h1_o} t_{h2}}{\left(r_{h1_o} + r_{h1_i}\right) \ln\left(\frac{r_{h2_o} + r_{h1_o}}{r_{h1_o} + r_{h1_i}}\right)} \tag{A44}$$

$$H_{h1,\infty} = k_{air}\left[\frac{A_{h1,\infty,top}}{l_{h1,top}}\left(0.54\mathrm{Ra}^{\frac{1}{4}}_{l_{h1,top}}\right) + \frac{A_{h1,\infty,wall}}{l_{h1,wall}}\left(0.68 + \frac{0.67\mathrm{Ra}^{\frac{1}{4}}_{l_{h1,wall}}}{\left[1 + \left(\frac{0.492}{\mathrm{Pr}}\right)^{\frac{9}{16}}\right]^{\frac{4}{9}}}\right)\right]$$

$$+0.25 A_{h1,\infty}\,\sigma(T_{h1} + T_\infty)\left(T_{h1}^2 + T_\infty^2\right)$$

$$= k_{air}\left[\frac{\left(r_{h1_o} - r_{h1_i}\right)}{2}\left(0.54\mathrm{Ra}^{\frac{1}{4}}_{l_{h1,top}}\right) + 2\pi r_{h1_o}\left(0.68 + \frac{0.67\mathrm{Ra}^{\frac{1}{4}}_{l_{h1,wall}}}{\left[1 + \left(\frac{0.492}{\mathrm{Pr}}\right)^{\frac{9}{16}}\right]^{\frac{4}{9}}}\right)\right] \tag{A45}$$

$$+0.25\pi\sigma(T_{h1} + T_\infty)\left(T_{h1}^2 + T_\infty^2\right)\left[r_{h1_o}^2 - r_{h1_i}^2 + 2 r_{h1_o}(l_{h1} - t_{h2})\right]$$

$$H_{h2,h3} = H_{h3,h2} = \frac{k_{steel} A_{h2,h3}}{l_{h2,h3}} = \frac{2 k_{steel} \pi\left(r_{h2_o}^2 - r_{h2_i}^2\right)}{l_{h2} + t_{h3}} \tag{A46}$$

$$H_{h2,\infty} = k_{air}\left\{\frac{A_{h2,\infty,top}}{l_{h2,top}}\left(0.54\mathrm{Ra}^{1/4}_{l_{h2,top}}\right) + \frac{A_{h2,\infty,wall}}{l_{h2,wall}}\left(0.68 + \frac{0.67\mathrm{Ra}^{1/4}_{l_{h2,wall}}}{\left[1 + \left(\frac{0.492}{\mathrm{Pr}}\right)^{9/16}\right]^{4/9}}\right)\right\}$$

$$+ 0.25 A_{h2,\infty}\sigma(T_{h2} + T_\infty)(T_{h2}^2 + T_\infty^2)$$

$$= k_{air}\left\{\frac{\left(r_{h2_o} - r_{h1_o}\right)}{2}\left(0.54\mathrm{Ra}^{1/4}_{l_{h2,top}}\right) + 2\pi r_{h2_o}\left(0.68 + \frac{0.67\mathrm{Ra}^{1/4}_{l_{h2,wall}}}{\left[1 + \left(\frac{0.492}{\mathrm{Pr}}\right)^{9/16}\right]^{4/9}}\right)\right\} \tag{A47}$$

$$+ 0.25\pi\sigma(T_{h2} + T_\infty)\left(T_{h2}^2 + T_\infty^2\right)\left(r_{h2_o}^2 - r_{h1_o}^2 + 2 r_{h2_o} l_{h2}\right)$$

$$H_{h2,dis} = k_{fluid}\left\{\frac{A_{h2,dis}}{D_{h2}}\left[0.409\left(\frac{\mathrm{Ta}}{C_{geo}}\right)^{0.241}_{h2}\right] + \frac{A_{h2,gap}}{l_{gap}}\left(0.037\mathrm{Re}_{gap}^{4/5}\mathrm{Pr}^{1/3}\right)\right\}$$

$$= k_{fluid}\left\{0.409 l_{h2_i}\left(\frac{\mathrm{Ta}}{C_{geo}}\right)^{0.241}_{h2} + \frac{\left(r_{h2_i} - r_{c3_o}\right)}{2}\left(0.037\mathrm{Re}_{gap}^{4/5}\mathrm{Pr}^{1/3}\right)\right\} \tag{A48}$$

$$H_{h3,h4} = H_{h4,h3} = \frac{k_{PEEK} A_{h3,h4}}{\frac{1}{2}\left(r_{h4_o} + r_{h4_i}\right) \ln\left[\frac{0.5\left(r_{h3_o} + r_{h3_i}\right)}{0.5\left(r_{h4_o} + r_{h4_i}\right)}\right]} = \frac{4 k_{steel} \pi r_{h3_i} t_{h3}}{\left(r_{h4_o} + r_{h4_i}\right) \ln\left(\frac{r_{h3_o} + r_{h3_i}}{r_{h4_o} + r_{h4_i}}\right)} \tag{A49}$$

$$H_{h3,\infty} = k_{air}\left\{\frac{A_{h3,\infty,top}}{l_{h3,top}}\left(0.54\mathrm{Ra}_{l_{h3,top}}^{1/4}\right) + \frac{A_{h3,\infty,bot}}{l_{h3,bot}}\left(0.27\mathrm{Ra}_{l_{h3,bot}}^{1/4}\right)\right.$$
$$\left. + \frac{A_{h3,\infty,side}}{l_{h3,side}}\left(0.68 + \frac{0.67\mathrm{Ra}_{l_{h3,side}}^{1/4}}{\left[1+\left(\frac{0.492}{\mathrm{Pr}}\right)^{9/16}\right]^{4/9}}\right)\right\} + 0.25A_{h3,\infty}\sigma(T_{h3}+T_\infty)(T_{h3}^2+T_\infty^2)$$
$$= k_{air}\left\{\frac{(r_{h3_o}-r_{h2_o})}{2}\left(0.54\mathrm{Ra}_{l_{h3,top}}^{\frac{1}{4}}\right) + \frac{(r_{h3_o}-r_{h4_o})}{2}\left(0.27\mathrm{Ra}_{l_{h3,bot}}^{\frac{1}{4}}\right)\right.$$
$$\left. + 2\pi r_{h3_o}\left(0.68 + \frac{0.67\mathrm{Ra}_{l_{h3,side}}^{1/4}}{\left[1+\left(\frac{0.492}{\mathrm{Pr}}\right)^{9/16}\right]^{4/9}}\right)\right\} \quad \text{(A50)}$$
$$+ 0.25\pi\sigma(T_{h3}+T_\infty)(T_{h3}^2+T_\infty^2)\left[(r_{h3_o}^2-r_{h2_o}^2)+(r_{h3_o}^2-r_{h4_o}^2)+2r_{h3_o}t_{h3}\right]$$

$$H_{h3,dis} = \frac{k_{fluid}A_{h3,gap}}{l_{gap}}\left(0.037\mathrm{Re}_{gap}^{4/5}\mathrm{Pr}^{1/3}\right) = \frac{k_{fluid}(r_{h2_i}-r_{c4_o})}{2}\left(0.037\mathrm{Re}_{gap}^{4/5}\mathrm{Pr}^{1/3}\right) \quad \text{(A51)}$$

$$H_{h4,fluid} = \frac{\bar{k}_{fluid}A_{h4,fluid}}{\bar{D}_{h4,fluid}}\left(0.75\overline{\mathrm{Re}}^{0.8}\overline{\mathrm{Pr}}^{0.6}\right) = \frac{0.75\bar{k}_{fluid}\overline{\mathrm{Re}}^{0.8}\overline{\mathrm{Pr}}^{0.6}\left(A_{ef,suc}+A_{ef,com}\right)}{\bar{D}_{h4,fluid}} \quad \text{(A52)}$$

$$H_{h4,\infty} = \frac{k_{air}A_{h4,\infty}}{l_{h4}}\left(0.27\mathrm{Ra}_{l_{h4}}^{1/4}\right) + 0.25A_{h4,\infty}\sigma(T_{h4}+T_\infty)(T_{h4}^2+T_\infty^2)$$
$$= \frac{k_{air}(r_{h4_o}-r_{h4_i})}{2}\left(0.27\mathrm{Ra}_{l_{h4}}^{1/4}\right) + 0.25\pi\sigma(T_{h4}+T_\infty)(T_{h4}^2+T_\infty^2)\left(r_{h4_o}^2-r_{h4_i}^2\right) \quad \text{(A53)}$$

With the equations for each element established, they can be rearranged to form two separate matrices which are then solved to obtain the steady state operating temperatures of the components. Equations (A54) – (A56) present the matrix for the cylinder, rotor and housing shell elements, respectively. Note that initial estimates for the element temperatures must be provided for the radiation heat transfer coefficient on the right hand side of the Equations (A54) and (A56). The solution component temperatures are then substituted back into the equations for subsequent iterations until the solution temperatures converges.

$$\begin{pmatrix} H_{c1,c2}+H_{c1\infty} & -H_{c1,c2} & 0 & 0 \\ -H_{c2,c1} & H_{c2,c1}+H_{c2,c3} & -H_{c2,c3} & 0 \\ 0 & -H_{c3,c2} & H_{c3,c2}+H_{c3,c4}+H_{c3,fluid}+H_{c3,dis} & -H_{c3,c4} \\ 0 & 0 & -H_{c4,c3} & H_{c4,c3}+H_{c4,dis} \end{pmatrix} \begin{pmatrix} T_{c1} \\ T_{c2} \\ T_{c3} \\ T_{c4} \end{pmatrix}$$

$$= \begin{pmatrix} H_{c1,\infty}T_{\infty} \\ \frac{1}{2}\left(0.99\dot{Q}_{f,s1}\right) \\ H_{c3,fluid}T_{fluid}+H_{c3,dis}T_{dis} \\ \frac{1}{2}\left(0.99\dot{Q}_{f,s2}\right)+H_{c4,dis}T_{dis} \end{pmatrix} \quad \text{(A54)}$$

$$\begin{pmatrix} H_{r1,r2}+H_{r1\infty}+H_{r1,suc} & -H_{r1,r2} & 0 & 0 \\ -H_{r2,r1} & H_{r2,r1}+H_{r2,r3}+H_{r2,suc} & -H_{r2,r3} & 0 \\ 0 & -H_{r3,r2} & H_{r3,r2}+H_{r3,r4}+H_{r3,suc} & -H_{r3,r4} \\ 0 & 0 & -H_{r4,r3} & H_{r4,r3}+H_{r4,suc}+H_{r4,fluid} \end{pmatrix}$$

$$\times \begin{pmatrix} T_{r1} \\ T_{r2} \\ T_{r3} \\ T_{r4} \end{pmatrix} = \begin{pmatrix} 0.025\dot{Q}_{f,r}+H_{r1,\infty}T_{\infty}+H_{r1,suc}T_{suc} \\ H_{r2,suc}T_{suc} \\ H_{r3,suc}T_{suc} \\ H_{r4,fluid}T_{fluid}+H_{r4,suc}T_{suc} \end{pmatrix} \quad \text{(A55)}$$

$$\begin{pmatrix} H_{h1,h2}+H_{h1,\infty} & -H_{h1,h2} & 0 & 0 \\ -H_{h2,h1} & H_{h2,h1}+H_{h2,h3}+H_{h2,\infty}+H_{h2,dis} & -H_{h2,h3} & 0 \\ 0 & -H_{h3,h2} & H_{h3,h2}+H_{h3,h4}+H_{h3,\infty}+H_{h3,dis} & -H_{h3,h4} \\ 0 & 0 & -H_{h4,h3} & H_{h4,h3}+H_{h4,\infty} \end{pmatrix} \begin{pmatrix} T_{h1} \\ T_{h2} \\ T_{h3} \\ T_{h4} \end{pmatrix}$$

$$= \begin{pmatrix} \frac{1}{2}\left(0.99\dot{Q}_{f,s1}\right)+H_{h1,\infty}T_{\infty} \\ H_{h2,\infty}T_{\infty}+H_{h2,dis}T_{dis} \\ H_{h3,\infty}T_{\infty}+H_{h3,dis}T_{dis} \\ \frac{1}{2}\left(0.99\dot{Q}_{f,s2}\right)+0.975\dot{Q}_{f,r}+H_{h4,\infty}T_{\infty} \end{pmatrix} \quad \text{(A56)}$$

A-5 Effect of Surface Roughness on Sliding Thermal Contact Resistance

It is known that surface roughness affects the sliding thermal contact resistance. Taller asperity heights, smaller asperity widths and larger periodicity of asperities contribute to an increase in surface roughness which in turn increases the sliding thermal contact resistance. This appendix section will present the effect of surface roughness on the sliding thermal contact resistance of AISI 4140 steel using the model developed by Chantrenne and Raynaud [66].

For the study, the sliding velocity is kept constant while varying the surface roughness. A sliding velocity of 5.0 m s^{-1} is chosen as it corresponds to the sliding speed of the cylinder shaft (Ø31.75 mm) in the bearing at an operating speed of 3000 rev min^{-1}.

Effect of Periodicity

The asperity width is kept constant at 0.5 μm while varying the asperity periodicity and asperity height. The variation of sliding thermal contact resistance with respect to asperity periodicity and asperity height is shown in Figure A5-1. For a constant asperity width, it is noted that the sliding thermal contact resistance experiences a polynomial growth when periodicity increases. Effect of asperity height is small compared to the effect of periodicity.

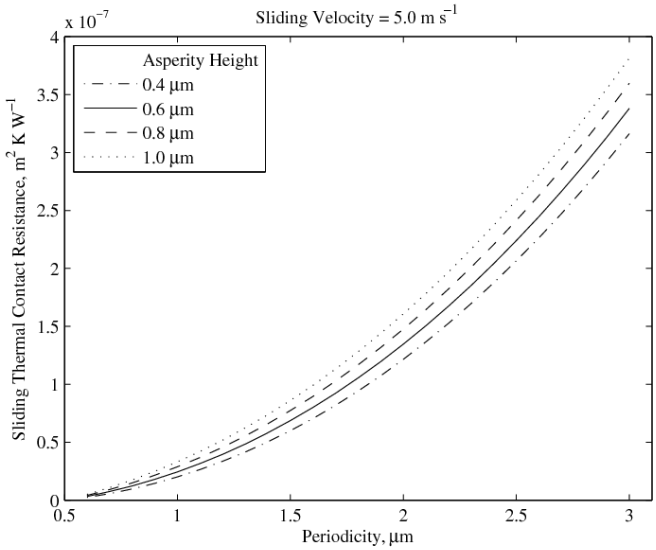

Figure A5-1: Effect of Periodicity

Effect of Asperity Width

The asperity periodicity is kept constant at 1.0 μm while varying the asperity width and height. The variation of sliding thermal contact resistance with respect to asperity width and height is shown in Figure A5-2. For a constant asperity periodicity, it is noted that smaller asperity widths would result in an exponential increase for the sliding thermal contact resistance. Similarly, the effect of asperity height is small compared to the effect of asperity width.

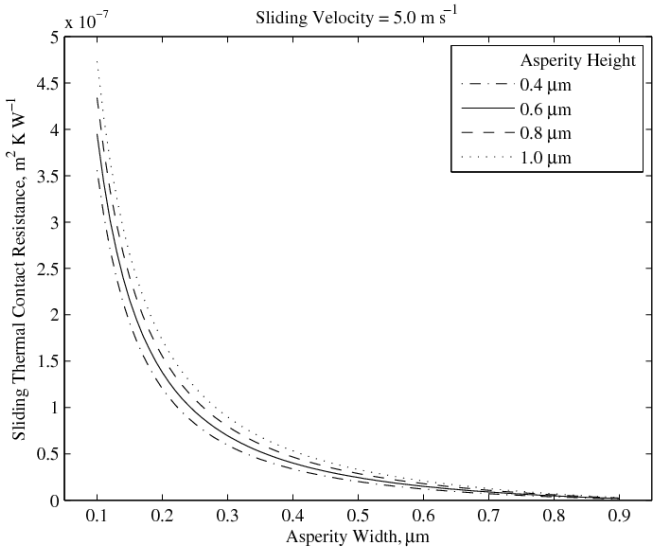

Figure A5-2: Effect of Asperity Width

Effect of Asperity Height

As seen in Figures A5-1 and A5-2, the effect of asperity height on sliding thermal contact resistance is small compared to the effects of asperity periodicity and width. To determine the exact influence of asperity height on sliding thermal contact resistance, the asperity periodicity and width is kept constant at 1.2 μm and 0.4 μm, respectively while varying the asperity height. The variation of sliding thermal contact resistance with respect to asperity height is shown in Figure A5-3. It is noted that the relationship between sliding thermal contact resistance and asperity height is approximately linear.

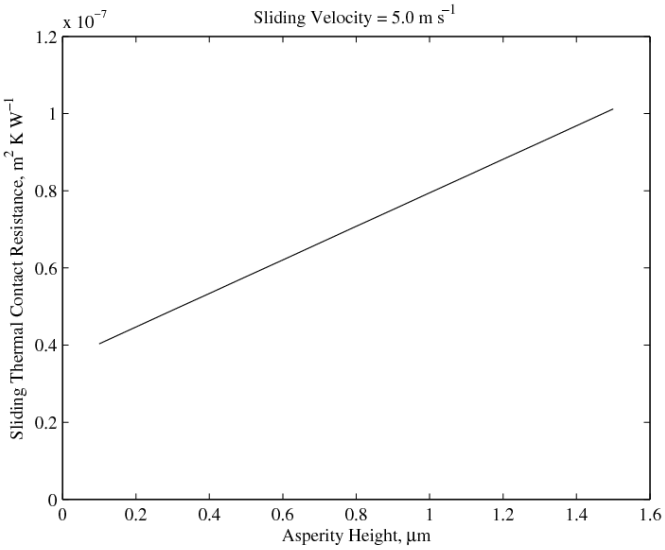

Figure A5-3: Effect of Asperity Height

Overall Effect of Surface Roughness

The effects of asperity width and periodicity influence the sliding thermal contact resistance to a great extent. In the model by Chantrenne and Raynaud [66], a parameter b_i^* is used to represent the ratio of the asperity width to the asperity periodicity.

In Chapter 7, it is noted that the sliding thermal contact resistance of AISI 4140 steel is of two orders smaller than those of the PEEK materials, based on arbitrary chosen asperity width and periodicity values for an asperity height of 0.6 µm (0.6 Ra). Evident in Figures A5-1 and A5-2, a small b_i^* value would increase the sliding thermal contact resistance of AISI 4140 steel greatly so much so that it becomes significant when compared to those of the PEEK materials.

However, bear in mind that a small b_i^* value would also mean that physically, the periodicity would be several times of the asperity width and such asperities would be relatively far apart from each other. Such a surface profile for steel is therefore unrealistic especially for those fabricated by conventional machining processes such as turning and polishing. Hence, the arbitrary chosen asperity dimensions would still be a valid estimate for the steel surface and any realistic deviations from the chosen values will not greatly affect the calculated sliding thermal resistance of AISI 4140 steel.

A-6 Measurement Data, Theoretical Prediction and Uncertainty Analysis

The values of the measured mean operating speeds, discharge pressures, mass flow rates, and volumetric efficiencies are presented in Table A6-1 and compared to the predicted mass flow rates from the theoretical model. The last column provides the prediction errors for each of the operating condition.

Table A6-1: Measurement Values and Predicted Values

Mean operating speed, rev min^{-1}	Discharge Pressure, bar (gauge)	Measured Mass flow rate, g s^{-1}	Volumetric Efficiency, %	Predicted mass flow rate, g s^{-1}	Prediction Error, %
610	0.229	0.167	28.1	0.180	8.03
607	0.213	0.205	34.6	0.191	-6.82
621	0.208	0.243	40.1	0.208	-14.22
634	0.162	0.280	45.4	0.284	1.30
742	0.375	0.167	23.1	0.173	3.53
728	0.344	0.205	28.9	0.187	-8.57
750	0.309	0.243	33.2	0.227	-6.32
753	0.254	0.280	38.2	0.285	1.50
847	0.510	0.167	20.2	0.144	-13.73
843.5	0.462	0.205	24.9	0.178	-13.23
860	0.417	0.243	28.9	0.227	-6.39
869.5	0.382	0.280	33.1	0.265	-5.50
991	0.594	0.167	17.3	0.185	11.06
997	0.554	0.205	21.1	0.219	7.09
988	0.539	0.243	25.2	0.224	-7.52
996.5	0.524	0.280	28.9	0.243	-13.51

Table A6-2 shows the comparison between the measured mass flow rates and predicted mass flow rates in the prototype if the endface gaps in the compressor were at the intended value of 10 μm. The last column shows the improvements in flowrates.

Table A6-2: Predicted Mass Flow Rates with Smaller Endface Clearances

Mean operating speed, rev min^{-1}	Discharge Pressure, bar (gauge)	Measured mass flow rate, g s^{-1}	Predicted flow rate, g s^{-1}	Volumetric efficiency, %	Increase in flow rate, %
610	0.229	0.167	0.567	95.3	214
607	0.213	0.205	0.566	95.6	196
621	0.208	0.243	0.580	95.8	179
634	0.162	0.281	0.598	96.7	110
742	0.375	0.167	0.683	94.4	295
728	0.344	0.205	0.672	94.6	259
750	0.309	0.243	0.697	95.3	207
753	0.254	0.281	0.705	96.0	148
847	0.510	0.167	0.773	93.6	437
843.5	0.462	0.205	0.774	94.1	336
860	0.417	0.243	0.794	94.7	250
869.5	0.382	0.281	0.807	95.1	204
991	0.594	0.167	0.905	93.7	388
997	0.554	0.205	0.915	94.1	317
988	0.539	0.243	0.907	94.2	304
996.5	0.524	0.281	0.917	94.4	278

Uncertainty Analysis

With reference to the expression for volumetric efficiency presented in Equation (8.2), this section will calculate the uncertainty associated with the volumetric efficiency based on the measurement uncertainties for the volumetric flow rate and average rotation speed. The measurement uncertainties for the volumetric flow rate and average rotation speed are shown in Table A6-3. Note that the uncertainty for the average rotation speed is based on the read off error of the motor torque curve in Appendix A-8.

Table A6-3: Measurement Uncertainties

Measurement	Uncertainty
Rotameter	±360 ml/min
Motor Speed	±25 rev min^{-1}

The first order approximated total differential for the volumetric efficiency is presented in Equation (A42) and the calculated volumetric efficiency uncertainties for the each of the operating conditions are shown in Table A6-4.

$$\Delta\eta \approx \frac{\partial\eta}{\partial\dot{V}}\Delta\dot{V} + \frac{\partial\eta}{\partial\omega}\Delta\omega$$
$$= \frac{\rho_o}{\rho_{suc}V_{cham}\omega}\Delta\dot{V} - \frac{\rho_o\dot{V}}{\rho_{suc}V_{cham}\omega^2}\Delta\omega \quad \text{(A57)}$$

Table A6-4: Calculated Volumetric Efficiency Uncertainties

Mean operating speed, rev min^{-1}	Discharge Pressure, bar (gauge)	Measured volumetric flow rate, ml min^{-1}	Volumetric Efficiency, %	Volumetric Efficiency Uncertainty (Δη), %
610	0.229	8560	28.1	0.0301
607	0.213	10500	34.6	-0.239
621	0.208	12440	40.1	-0.454
634	0.162	14380	45.4	-0.653
742	0.375	8560	23.1	0.193
728	0.344	10500	28.9	-0.00158
750	0.309	12440	33.2	-0.146
753	0.254	14380	38.2	-0.312
847	0.510	8560	20.2	0.253
843.5	0.462	10500	24.9	0.116
860	0.417	12440	28.9	-0.00379
869.5	0.382	14380	33.1	-0.123
991	0.594	8560	17.3	0.291
997	0.554	10500	21.1	0.194
988	0.539	12440	25.2	0.0915
996.5	0.524	14380	28.9	-0.00153

A-7 Material Specifications for PEEK

Natural PEEK (pure PEEK) was used to fabricate the bearing liners and vane whereas bearing grade PEEK (composite PEEK with carbon fibres, PTFE and graphite) was used to fabricate the rotor and rotor shaft. The specifications for these PEEK materials used to fabricate the rubbing components of the compressor prototype are shown as follows:

Natural PEEK:

Ensinger

TECAPEEK natural - Stock Shapes

Chemical Designation
PEEK (Polyetheretherketone)

Colour
beige opaque

Density
1.31 g/cm^3

Main features
- good heat deflection temperature
- good machinability
- inherent flame retardant
- resistance against high energy radiation
- good slide and wear properties
- very good chemical resistance
- high creep resistance
- hydrolysis and superheated steam resistant

Target Industries
- chemical technology
- mechanical engineering
- electrical engineering
- aircraft and aerospace technology
- automotive industry
- food engineering
- semiconductor technology
- vacuum technology
- textile industry

Mechanical properties	*parameter*	*value*	*unit*	*norm*		*comment*
Modulus of elasticity (tensile test)	1mm/min	4200	MPa	DIN EN ISO 527-2	1)	(1) For tensile test: specimen type 1b (2) For flexural test: support span 64mm, norm specimen. (3) Specimen 10x10x10mm (4) Specimen 10x10x50mm, modulus range between 0.5 and 1% compression. (5) For Charpy test: support span 64mm, norm specimen. n.b. = not broken (6) Specimen in 4mm thickness
Tensile strength	50mm/min	116	MPa	DIN EN ISO 527-2		
Tensile strength at yield	50mm/min	116	MPa	DIN EN ISO 527-2		
Elongation at yield	50mm/min	5	%	DIN EN ISO 527-2		
Elongation at break	50mm/min	15	%	DIN EN ISO 527-2		
Flexural strength	2mm/min, 10 N	175	MPa	DIN EN ISO 178	2)	
Modulus of elasticity (flexural test)	2mm/min, 10 N	4200	MPa	DIN EN ISO 178		
Compression strength	1% / 2% 5mm/min, 10 N	23 / 43	MPa	EN ISO 604	3)	
Compression modulus	5mm/min, 10 N	3400	MPa	EN ISO 604	4)	
Impact strength (Charpy)	max. 7,5J	n.b.	kJ/m^2	DIN EN ISO 179-1eU	5)	
Notched impact strength (Charpy)	max. 7,5J	4	kJ/m^2	DIN EN ISO 179-1eA		
Ball indentation hardness		253	MPa	ISO 2039-1	6)	

Thermal properties	*parameter*	*value*	*unit*	*norm*		*comment*
Glass transition temperature		150	°C	DIN 53765	1)	(1) Found in public sources. (2) Found in public sources. Individual testing regarding application conditions is mandatory.
Melting temperature		341	°C	DIN 53765		
Heat distortion temperature	HDT, Method A	162	°C	ISO-R 75 Method A		
Service temperature	short term	300	°C		2)	
Service temperature	long term	260	°C			
Thermal expansion (CLTE)	23-60°C, long.	5	10^{-5} K^{-1}	DIN EN ISO 11359-1;2		
Thermal expansion (CLTE)	23-100°C, long.	5	10^{-5} K^{-1}	DIN EN ISO 11359-1;2		
Thermal expansion (CLTE)	100-150°C, long.	7	10^{-5} K^{-1}	DIN EN ISO 11359-1;2		
Specific heat		1.1	J/(g*K)	ISO 22007-4:2008		
Thermal conductivity		0.27	W/(K*m)	ISO 22007-4:2008		

Electrical properties	*parameter*	*value*	*unit*	*norm*		*comment*
Specific surface resistance	Silver electrode, 23°C, 12% r.h.	10^{15}	Ω	DIN IEC 60093	1)	(1) Specimen in 20mm thickness (2) Specimen in 1mm thickness
Specific volume resistance	Silver electrode, 23°C, 12% r.h.	10^{15}	Ω*cm	DIN IEC 60093		
Dielectric strength	23°C, 50% r.h.	73	kV/mm	ISO 60243-1	2)	
Resistance to tracking (CTI)	Platin electrode, 23°C, 50% r.h., solvent A	125	V	DIN EN 60112		

Other properties	*parameter*	*value*	*unit*	*norm*		*comment*
Water absorption	24h / 96h (23°C)	0.02 / 0.03	%	DIN EN ISO 62	1)	(1) Ø ca. 50mm, h=13mm (2) + good resistance (3) - poor resistance (4) on request
Resistance to hot water/ bases		+		-	2)	
Resistance to weathering		-		-	3)	
Flammability (UL94)	listed (value at 1.5mm)	V0		DIN IEC 60695-11-10;	4)	

→ TECAPEEK products are based on Victrex® PEEK polymer.

Ensinger GmbH
Rudolf-Diesel Str. 8
71154 Nufringen - Deutschland

Tel +49 7032 819 0
Fax +49 7032 819 100
www.ensinger-online.com

Date: 2014/07/21

Version: AC

Bearing-grade PEEK:

Ensinger

TECAPEEK PVX black - Stock Shapes

Chemical Designation
PEEK (Polyetheretherketone)

Colour
black opaque

Density
1.44 g/cm^3

Fillers
carbon fibres, PTFE, graphite

Main features
- good heat deflection temperature
- high creep resistance
- good slide and wear properties
- hydrolysis and superheated steam resistant
- good wear properties
- inherent flame retardant
- very good chemical resistance

Target Industries
- mechanical engineering
- chemical technology
- conveyor technology
- automotive industry
- textile industry
- precision engineering
- aircraft and aerospace technology

Mechanical properties	*parameter*	*value*	*unit*	*norm*		*comment*
Modulus of elasticity (tensile test)	1mm/min	5500	MPa	DIN EN ISO 527-2	1)	(1) For tensile test: specimen type 1b (2) For flexural test: support span 64mm, norm specimen. (3) Specimen 10x10x10mm (4) Specimen 10x10x50mm, modulus range between 0.5 and 1% compression. (5) For Charpy test: support span 64mm, norm specimen. (6) Specimen in 4mm thickness
Tensile strength	50mm/min	84	MPa	DIN EN ISO 527-2		
Tensile strength at yield	50mm/min	84	MPa	DIN EN ISO 527-2		
Elongation at yield	50mm/min	3	%	DIN EN ISO 527-2		
Elongation at break	50mm/min	3	%	DIN EN ISO 527-2		
Flexural strength	2mm/min, 10 N	142	MPa	DIN EN ISO 178	2)	
Modulus of elasticity (flexural test)	2mm/min, 10 N	6000	MPa	DIN EN ISO 178		
Compression strength	1% / 2% 5mm/min, 10 N	23 / 44	MPa	EN ISO 604	3)	
Compression modulus	5mm/min, 10 N	4000	MPa	EN ISO 604	4)	
Impact strength (Charpy)	max. 7,5J	28	kJ/m^2	DIN EN ISO 179-1eU	5)	
Ball indentation hardness		250	MPa	ISO 2039-1	6)	

Thermal properties	*parameter*	*value*	*unit*	*norm*		*comment*
Glass transition temperature		146	°C	DIN 53765	1)	(1) Found in public sources. (2) Found in public sources. Individual testing regarding application conditions is mandatory.
Melting temperature		341	°C	DIN 53765		
Service temperature	short term	300	°C		2)	
Service temperature	long term	260	°C			
Thermal expansion (CLTE)	23-60°C, long.	3	10^{-5} K^{-1}	DIN EN ISO 11359-1;2		
Thermal expansion (CLTE)	23-100°C, long.	3	10^{-5} K^{-1}	DIN EN ISO 11359-1;2		
Thermal expansion (CLTE)	100-150°C, long.	4	10^{-5} K^{-1}	DIN EN ISO 11359-1;2		
Specific heat		1.1	J/(g*K)	ISO 22007-4:2008		
Thermal conductivity		0.82	W/(K*m)	ISO 22007-4:2008		

Electrical properties	*parameter*	*value*	*unit*	*norm*		*comment*
Specific surface resistance	Conductive rubber, 23°C, 12% r.h.	10^4 - 10^{11}	Ω	DIN EN 61340-2-3	1)	(1) Specimen in 20mm thickness (2) Due to the black colourant and moisture uptake of the material the electrical insulation properties cannot be 100% guaranteed, despite single measurements suggesting otherwise.
Specific volume resistance	Conductive rubber, 23°C, 12% r.h.	10^7 - 10^{12}	Ω*cm	DIN EN 61340-2-3	2)	

Other properties	*parameter*	*value*	*unit*	*norm*		*comment*
Water absorption	24h / 96h (23°C)	0.02 / 0.03	%	DIN EN ISO 62	1)	(1) Ø ca. 50mm, h=13mm (2) + good resistance (3) - poor resistance (4) Corresponding means no listing at UL (yellow card). The information might be taken from resin, stock shape or estimation. Individual testing regarding application conditions is mandatory.
Resistance to hot water/ bases		+		-	2)	
Resistance to weathering		-		-	3)	
Flammability (UL94)	corresponding to	V0		DIN IEC 60695-11-10;	4)	

→ TECAPEEK products are based on Victrex® PEEK polymer.

Ensinger GmbH
Rudolf-Diesel Str. 8
71154 Nufringen - Deutschland

Tel +49 7032 819 0
Fax +49 7032 819 100
www.ensinger-online.com

Date: 2011/11/29

Version: AA

A-8 Specifications for Measurement Instruments & Induction Motor

The specifications for the instruments used for measurements in the experiments that are directly carried out for the research project are listed in this section of the appendix. The Torquemaster TM107 was used to measure the friction torques of self-lubricating materials in dry rubbing with metal shafts in Chapter 3.

Torquemaster TM107:

7.2 Torque Measuring System

The following specifications are valid for all ratings of transducers in the series TM 104 - TM 113. They are quoted for the transducer and its associated UAE 757 / UAE 763 signal conditioning module.

Accuracy class (1)	: 0.1
Rated output (RO) of TM ... unit	: ±5 V DC (depending on direction of the applied torque)
Temperature influence on the signal	
- Specification range 1	: +10 °C to +60 °C
On zero	: < ±0.1 % of RO / 10K
On sensitivity (2)	: < ±0.1 % of RO / 10K
- Specification range 2	: -25 °C to +80 °C
On zero	: < ±0.2 % of RO / 10K
On sensitivity (2)	: < ±0.2 % of RO / 10K
Speed influence on the signal (including wobble)	
- TM 104 to TM 108	: < 0.005 % of RO / 1000 rpm
- TM 109 to TM 113	: < 0.01 % of RO / 1000 rpm
Power supply	
- AC component (20 kHz, sine wave)	: 40 mA RMS
- DC component (pre-amplifier powering)	: 24 V DC
Combined error (linearity + hysteresis)	: ≤ 0.1 % of RO
Repeatability	: < 0.1 % of RO
Long-term stability of zero signal	: < ±0.05 % of RO / year
Long-term stability of rated output	: < ±0.05 % of RO / year

Notes

(1) Greatest individual error where temperature influence is based on ΔT of 10 K.

(2) This value defines the influence on the whole analog measuring chain (TM ... transducer and UAE... module). Note that for this test the UAE... module was kept at ambient temperature and the temperature of the TM transducer was varied.

In Chapter 8, the Gilmont GF1500 correlated rotameter was used to measure the volumetric flow rate from the receiver tank during the testing of the compressor prototype and the Kulite XTL375 pressure transducer was used to measure the discharge pressure. The input torque to the prototype was measured by the Futek TR605 torque transducer

Gilmont flowmeter:

GILMONT INSTRUMENTS, INC.

Correlated Flow Table

Fluid Air
Density 0.00120000 grams/ml
Viscosity 0.01812000 ep

Tube Size 5 & 250
Float Type Glass/Stainless-Steel
Serial No. 55044
Date Jun 19, 2007

Measured & flowing at 1.00 atm and 70 °F
R at 0 = 1.31; R at 50 = 13.58; R at 100 = 26.41

FLOW L/MIN GLASS	SCALE	FLOW L/MIN S.S.	FLOW L/MIN GLASS	SCALE	FLOW L/MIN S.S.	FLOW L/MIN GLASS	SCALE	FLOW L/MIN S.S.	FLOW L/MIN GLASS	SCALE	FLOW L/MIN S.S.
1.999	1	4.587	20.74	26	39.00	41.94	51	76.54	65.62	76	118.6
2.589	2	5.803	21.55	27	40.43	42.84	52	78.13	66.62	77	120.3
3.202	3	7.043	22.36	28	41.87	43.74	53	79.73	67.62	78	122.1
3.870	4	8.390	23.17	29	43.30	44.65	54	81.34	68.62	79	123.9
4.574	5	9.700	23.99	30	44.75	45.56	55	82.96	69.62	80	125.7
5.259	6	10.97	24.80	31	46.20	46.48	56	84.58	70.63	81	127.5
5.907	7	12.21	25.62	32	47.65	47.40	57	86.21	71.64	82	129.3
6.642	8	13.61	26.45	33	49.11	48.32	58	87.85	72.65	83	131.1
7.385	9	15.02	27.28	34	50.58	49.25	59	89.50	73.67	84	132.9
8.133	10	16.43	28.11	35	52.05	50.18	60	91.15	74.69	85	134.7
8.886	11	17.84	28.94	36	53.53	51.12	61	92.81	75.71	86	136.5
9.647	12	19.24	29.78	37	55.01	52.06	62	94.48	76.73	87	138.4
10.43	13	20.65	30.62	38	56.50	53.01	63	96.15	77.76	88	140.2
11.21	14	22.05	31.47	39	58.00	53.95	64	97.84	78.79	89	142.0
12.00	15	23.47	32.32	40	59.51	54.91	65	99.53	79.82	90	143.9
12.79	16	24.87	33.18	41	61.02	55.86	66	101.2	80.85	91	145.7
13.58	17	26.28	34.03	42	62.54	56.82	67	102.9	81.89	92	147.6
14.37	18	27.68	34.90	43	64.07	57.79	68	104.6	82.93	93	149.4
15.16	19	29.09	35.76	44	65.60	58.75	69	106.4	83.97	94	151.3
15.95	20	30.50	36.63	45	67.14	59.72	70	108.1	85.01	95	153.1
16.75	21	31.91	37.51	46	68.69	60.70	71	109.8	86.05	96	155.0
17.54	22	33.32	38.38	47	70.24	61.68	72	111.5	87.10	97	156.9
18.34	23	34.74	39.27	48	71.81	62.66	73	113.3	88.14	98	158.7
19.14	24	36.16	40.15	49	73.38	63.64	74	115.0	89.19	99	160.6
19.94	25	37.58	41.04	50	74.96	64.63	75	116.8	90.24	100	162.5

Kulite XTL-375 (M) pressure transducer:

MINIATURE RUGGEDIZED IS® PRESSURE TRANSDUCER

XTL-375 (M) SERIES

- Excellent Stability
- All Welded Construction
- Robust Construction
- High Natural Frequencies
- 3/8-24 UNJF or M10 X 1 Thread
- Patented Leadless Technology VIS®

The XTL-375 is a miniature threaded pressure transducer. The hexagonal head and o-ring seal make it easy to mount and simple to apply.

The XTL-375 utilizes Kulite's Patented Leadless Technology. A solid state piezoresistive sensing element is protected by a metal screen. This sensing sub assembly is welded to a stainless steel body.

This advanced construction results in a highly stable, reliable and rugged instrument with all the advantages of microcircuitry: significant miniaturization, excellent repeatability, low power consumption, etc. The miniaturization process also yields a marked increase in the natural frequencies of the transducers, making them suitable for use even in shock pressure measurements.

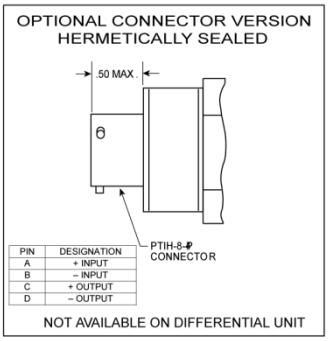

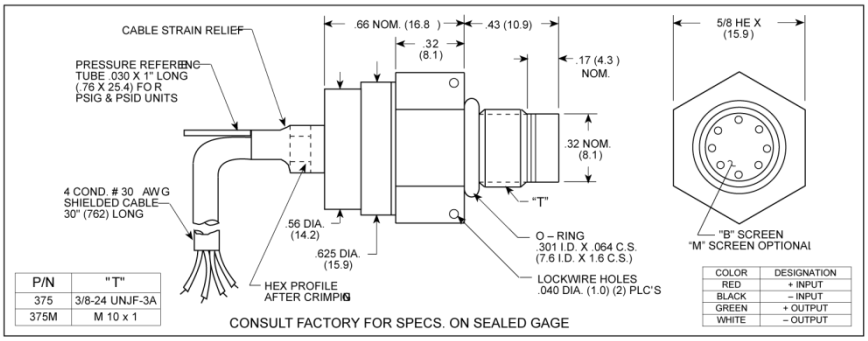

INPUT	Pressure Range	0.35 5	0.7 10	1.7 25	3.5 50	7 100	17 250	35 500	70 1000	140 BAR 2000 PSI
	Operational Mode	Absolute, Gage, Sealed Gage, Differential					Absolute, Sealed Gage			
	Over Pressure	2 Times Rated Pressure to a Maximum of 3000 PSI (210 BAR)								
	Burst Pressure	3 Times Rated Pressure to a Maximum of 3000 PSI (210 BAR)								
	Pressure Media	All Nonconductive, Noncorrosive Liquids or Gases (Most Conductive Liquids and Gases - Please Consult Factory)								
	Rated Electrical Excitation	10 VDC/AC								
	Maximum Electrical Excitation	12 VDC/AC								
	Input Impedance	1000 Ohms (Min.)								
OUTPUT	Output Impedance	1000 Ohms (Nom.)								
	Full Scale Output (FSO)	100 mV (Nom.)								
	Residual Unbalance	± 5 mV (Typ.)								
	Combined Non-Linearity, Hysteresis and Repeatability	± 0.1% FSO BFSL (Typ.), ± 0.5% FSO (Max.)								
	Resolution	Infinitesimal								
	Natural Frequency of Sensor Without Screen (KHz) (Typ.)	150	175	240	300	380	550	700	1000	1400
	Acceleration Sensitivity % FS/g Perpendicular	$1.5x10^{-3}$	$1.0x10^{-3}$	$5.0x10^{-4}$	$3.0x10^{-4}$	$1.5x10^{-4}$	$1.0x10^{-4}$	$6.0x10^{-5}$	$4.5x10^{-5}$	$2.0x10^{-5}$
	Insulation Resistance	100 Megohm Min. @ 50 VDC								
ENVIRONMENTAL	Operating Temperature Range	-65°F to +350°F (-55°C to +175°C)								
	Compensated Temperature Range	+80°F to +180°F (+25°C to +80°C) Any 100°F Range Within The Operating Range on Request								
	Thermal Zero Shift	± 1% FS/100°F (Typ.)								
	Thermal Sensitivity Shift	± 1% /100°F (Typ.)								
	Linear Vibration	10-2,000 Hz Sine, 100g. (Max.)								
	Mechanical Shock	20g half Sine Wave 11 msec. Duration								
PHYSICAL	Electrical Connection	4 Conductor 30 AWG Shielded Cable 30" Long								
	Weight	17 Grams (Max.) Excluding Cable								
	Pressure Sensing Principle	Fully Active Four Arm Wheatstone Bridge Dielectrically Isolated Silicon on Silicon Patented Leadless Technology								
	Mounting Torque	80 Inch-Pounds (Max.) 6Nm								

Note: Custom pressure ranges, accuracies and mechanical configurations available. Dimensions are in inches. Dimensions in parenthesis are in millimeters. All dimensions nominal. (I)
Continuous development and refinement of our products may result in specification changes without notice.
Kulite miniature pressure transducers are intended for use in test and research and development programs and are not necessarily designed to be used in production applications. For products designed to be used in production programs, please consult the factory.

KULITE SEMICONDUCTOR PRODUCTS, INC. • One Willow Tree Road • Leonia, New Jersey 07605 • Tel: 201 461-0900 • Fax: 201 461-0990 • http://www.kulite.com

Futek TRS 605 torque transducer

FUTEK MODEL TRS605

NON CONTACT SHAFT TO SHAFT ROTARY TORQUE SENSOR W/ ENCODER

Drawing Number: FI1029-H

INCH [mm] | R.O.= Rated Output

CE COMPLIANT

CONNECTOR CODE (CABLE PACKAGE WIRING CODE)

Torque Connections

Power	GROUND	SIGNAL OUTPUT	GROUND
PIN 'F' (RED)	PIN 'E (BLACK)	PIN 'C' (GREEN)	PIN 'D' (WHITE)

Angle Connections

Power	GROUND	Signal (Angle 1)	Signal (Angle 2)
PIN 'H' (ORANGE)	PIN 'E (BLACK)	PIN 'B' (BLUE)	PIN 'G' (BROWN)

Shunt Cal Connections

Power	GROUND
PIN 'K' (PURPLE)	PIN 'A' (YELLOW)

Shield Connection

Shield (Floating)
PIN 'M'

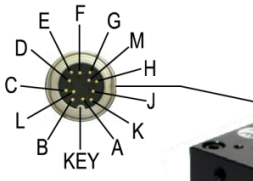

BINDER RECEPTACLE
09-0331-90-12
(MATING CONNECTOR
99-2030-09-12
NOT INCLUDED)

-OUTPUT (CCW) +OUTPUT (CW)

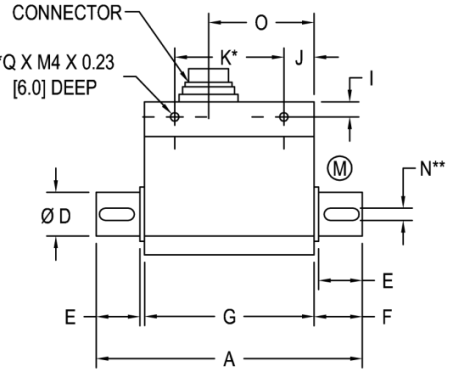

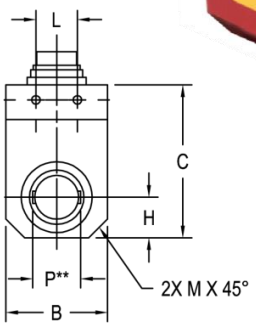

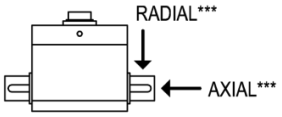

Ⓜ=MEASURING SIDE

* ANTI-ROTATION HOLES, NOT TO BE USED TO SUPPORT LOAD.

** FEATHER KEYWAYS APPLY TO 20 AND 50 N m PER DIN 6885. KEYWAYS COME PRE-INSTALLED.

*** MAXIMUM LOAD ALLOWED, NOT FOR MEASUREMENT.

STOCK #	CAPACITY in-lb	CAPACITY N m	Ø D	A	B	C	E	F	G	H	I	J	K*	L	M	N**	O	P**	Q	*** MAX. AXIAL FORCE lb [N]	*** MAX. RADIAL FORCE lb [N]	WEIGHT lb [kg]
FSH02052	9	1	0.394 [10] g6	3.62 [92]	1.10 [28]	2.04 [52]	0.63 [16]	0.67 [17]	2.28 [58]	0.55 [14]	0.19 [5]	0.43 [11]	-	0.31 [8]	0.31 [8]	N/A	1.46 [37]	N/A	6	4.5 [20]	1 [5]	0.7 [0.30]
FSH02053	18	2																		11 [50]	1 [5]	
FSH02054	44	5																			2 [10]	
FSH02055	89	10																		34 [150]	4.5 [20]	
FSH02056	177	20	0.630 [16] g6	4.09 [104]	1.49 [38]	2.28 [58]	0.78 [20]	0.90 [23]	2.32 [59]	0.75 [19]	0.19 [5]	0.47 [12]	1.38 [35]	0.55 [14]	0.40 [10]	0.197 [5]	1.50 [38]	0.787 [20]	8		7 [30]	1.3 [0.60]
FSH02057	443	50																		45 [200]	11 [50]	

TORQUE SPECIFICATIONS:

RATED OUTPUT	±5VDC
SAFE OVERLOAD	150% of R.O.
ZERO BALANCE	±1% of R.O.
EXCITATION (VDC)	11-26 VDC, 1 Watt
NONLINEARITY	±0.2% of R.O.
HYSTERESIS	±0.1% of R.O.
NONREPEATABILITY	±0.2% R.O.
TEMP. SHIFT ZERO	±0.01% of R.O. / °F [±0.02% of R.O. /°C]
TEMP. SHIFT SPAN	±0.01% of Load / °F [±0.02% of Load /°C]
OPERATING TEMP.	-13 to 176°F [-25 to +80°C]
COMPENSATED TEMP.	41 to 122°F [+5 to +50°C]
ROTATIONAL SPEED	7000 RPM MAX
CONNECTOR:	12 pin Binder Series #581 (09-0331-90-12)

ACCESSORIES AND RELATED INSTRUMENTS AVAILABLE

CALIBRATION (STD)	Certificate of Conformance
CALIBRATION (AVAILABLE)	5pt CW and CCW
CALIBRATION TEST EXCITATION	12 VDC
SHUNT CALIBRATION	With sensor fully connected apply 11-26 VDC to Pins A & K to generate 5VDC nom output.

ENCODER SPECIFICATIONS:

OUTPUT	IMPULSE (TTL)
PULSES / REV	2 x 360
EXCITATION	5 VDC
ANGLE 1- LEADING PULSE	
ANGLE 2- TRAILING PULSE (90°)	

FUTEK ADVANCED SENSOR TECHNOLOGY, INC.

10 THOMAS
IRVINE, CA 92618 USA
1-800-23-FUTEK (38835)

INTERNET:
http://www.futek.com

Type T Thermocouple

Revised Thermocouple Reference Tables

TYPE T

Reference Tables
N.I.S.T. Monograph 175
Revised to ITS-90

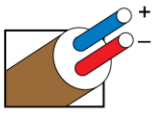

Thermocouple Grade

Copper vs. Copper-Nickel

Extension Grade

MAXIMUM TEMPERATURE RANGE
Thermocouple Grade
– 328 to 662°F
– 200 to 350°C
Extension Grade
– 76 to 212°F
– 60 to 100°C
LIMITS OF ERROR
(whichever is greater)
Standard: 1.0°C or 0.75% Above 0°C
1.0°C or 1.5% Below 0°C
Special: 0.5°C or 0.4%
COMMENTS, BARE WIRE ENVIRONMENT:
Mild Oxidizing, Reducing Vacuum or Inert; Good Where Moisture Is Present; Low Temperature and Cryogenic Applications
TEMPERATURE IN DEGREES °C
REFERENCE JUNCTION AT 0°C

Thermoelectric Voltage in Millivolts

°C	-10	-9	-8	-7	-6	-5	-4	-3	-2	-1	0	°C
-260	-6.258	-6.256	-6.255	-6.253	-6.251	-6.248	-6.245	-6.242	-6.239	-6.236	-6.232	-260
-250	-6.232	-6.228	-6.223	-6.219	-6.214	-6.209	-6.204	-6.198	-6.193	-6.187	-6.180	-250
-240	-6.180	-6.174	-6.167	-6.160	-6.153	-6.146	-6.138	-6.130	-6.122	-6.114	-6.105	-240
-230	-6.105	-6.096	-6.087	-6.078	-6.068	-6.059	-6.049	-6.038	-6.028	-6.017	-6.007	-230
-220	-6.007	-5.996	-5.985	-5.973	-5.962	-5.950	-5.938	-5.926	-5.914	-5.901	-5.888	-220
-210	-5.888	-5.876	-5.863	-5.850	-5.836	-5.823	-5.809	-5.795	-5.782	-5.767	-5.753	-210
-200	-5.753	-5.739	-5.724	-5.710	-5.695	-5.680	-5.665	-5.650	-5.634	-5.619	-5.603	-200
-190	-5.603	-5.587	-5.571	-5.555	-5.539	-5.523	-5.506	-5.489	-5.473	-5.456	-5.439	-190
-180	-5.439	-5.421	-5.404	-5.387	-5.369	-5.351	-5.334	-5.316	-5.297	-5.279	-5.261	-180
-170	-5.261	-5.242	-5.224	-5.205	-5.186	-5.167	-5.148	-5.128	-5.109	-5.089	-5.070	-170
-160	-5.070	-5.050	-5.030	-5.010	-4.989	-4.969	-4.949	-4.928	-4.907	-4.886	-4.865	-160
-150	-4.865	-4.844	-4.823	-4.802	-4.780	-4.759	-4.737	-4.715	-4.693	-4.671	-4.648	-150
-140	-4.648	-4.626	-4.604	-4.581	-4.558	-4.535	-4.512	-4.489	-4.466	-4.443	-4.419	-140
-130	-4.419	-4.395	-4.372	-4.348	-4.324	-4.300	-4.275	-4.251	-4.226	-4.202	-4.177	-130
-120	-4.177	-4.152	-4.127	-4.102	-4.077	-4.052	-4.026	-4.000	-3.975	-3.949	-3.923	-120
-110	-3.923	-3.897	-3.871	-3.844	-3.818	-3.791	-3.765	-3.738	-3.711	-3.684	-3.657	-110
-100	-3.657	-3.629	-3.602	-3.574	-3.547	-3.519	-3.491	-3.463	-3.435	-3.407	-3.379	-100
-90	-3.379	-3.350	-3.322	-3.293	-3.264	-3.235	-3.206	-3.177	-3.148	-3.118	-3.089	-90
-80	-3.089	-3.059	-3.030	-3.000	-2.970	-2.940	-2.910	-2.879	-2.849	-2.818	-2.788	-80
-70	-2.788	-2.757	-2.726	-2.695	-2.664	-2.633	-2.602	-2.571	-2.539	-2.507	-2.476	-70
-60	-2.476	-2.444	-2.412	-2.380	-2.348	-2.316	-2.283	-2.251	-2.218	-2.186	-2.153	-60
-50	-2.153	-2.120	-2.087	-2.054	-2.021	-1.987	-1.954	-1.920	-1.887	-1.853	-1.819	-50
-40	-1.819	-1.785	-1.751	-1.717	-1.683	-1.648	-1.614	-1.579	-1.545	-1.510	-1.475	-40
-30	-1.475	-1.440	-1.405	-1.370	-1.335	-1.299	-1.264	-1.228	-1.192	-1.157	-1.121	-30
-20	-1.121	-1.085	-1.049	-1.013	-0.976	-0.940	-0.904	-0.867	-0.830	-0.794	-0.757	-20
-10	-0.757	-0.720	-0.683	-0.646	-0.608	-0.571	-0.534	-0.496	-0.459	-0.421	-0.383	-10
0	-0.383	-0.345	-0.307	-0.269	-0.231	-0.193	-0.154	-0.116	-0.077	-0.039	0.000	0
0	0.000	0.039	0.078	0.117	0.156	0.195	0.234	0.273	0.312	0.352	0.391	0
10	0.391	0.431	0.470	0.510	0.549	0.589	0.629	0.669	0.709	0.749	0.790	10
20	0.790	0.830	0.870	0.911	0.951	0.992	1.033	1.074	1.114	1.155	1.196	20
30	1.196	1.238	1.279	1.320	1.362	1.403	1.445	1.486	1.528	1.570	1.612	30
40	1.612	1.654	1.696	1.738	1.780	1.823	1.865	1.908	1.950	1.993	2.036	40
°C	0	1	2	3	4	5	6	7	8	9	10	°C

°C	0	1	2	3	4	5	6	7	8	9	10	°C
50	2.036	2.079	2.122	2.165	2.208	2.251	2.294	2.338	2.381	2.425	2.468	50
60	2.468	2.512	2.556	2.600	2.643	2.687	2.732	2.776	2.820	2.864	2.909	60
70	2.909	2.953	2.998	3.043	3.087	3.132	3.177	3.222	3.267	3.312	3.358	70
80	3.358	3.403	3.448	3.494	3.539	3.585	3.631	3.677	3.722	3.768	3.814	80
90	3.814	3.860	3.907	3.953	3.999	4.046	4.092	4.138	4.185	4.232	4.279	90
100	4.279	4.325	4.372	4.419	4.466	4.513	4.561	4.608	4.655	4.702	4.750	100
110	4.750	4.798	4.845	4.893	4.941	4.988	5.036	5.084	5.132	5.180	5.228	110
120	5.228	5.277	5.325	5.373	5.422	5.470	5.519	5.567	5.616	5.665	5.714	120
130	5.714	5.763	5.812	5.861	5.910	5.959	6.008	6.057	6.107	6.156	6.206	130
140	6.206	6.255	6.305	6.355	6.404	6.454	6.504	6.554	6.604	6.654	6.704	140
150	6.704	6.754	6.805	6.855	6.905	6.956	7.006	7.057	7.107	7.158	7.209	150
160	7.209	7.260	7.310	7.361	7.412	7.463	7.515	7.566	7.617	7.668	7.720	160
170	7.720	7.771	7.823	7.874	7.926	7.977	8.029	8.081	8.133	8.185	8.237	170
180	8.237	8.289	8.341	8.393	8.445	8.497	8.550	8.602	8.654	8.707	8.759	180
190	8.759	8.812	8.865	8.917	8.970	9.023	9.076	9.129	9.182	9.235	9.288	190
200	9.288	9.341	9.395	9.448	9.501	9.555	9.608	9.662	9.715	9.769	9.822	200
210	9.822	9.876	9.930	9.984	10.038	10.092	10.146	10.200	10.254	10.308	10.362	210
220	10.362	10.417	10.471	10.525	10.580	10.634	10.689	10.743	10.798	10.853	10.907	220
230	10.907	10.962	11.017	11.072	11.127	11.182	11.237	11.292	11.347	11.403	11.458	230
240	11.458	11.513	11.569	11.624	11.680	11.735	11.791	11.846	11.902	11.958	12.013	240
250	12.013	12.069	12.125	12.181	12.237	12.293	12.349	12.405	12.461	12.518	12.574	250
260	12.574	12.630	12.687	12.743	12.799	12.856	12.912	12.969	13.026	13.082	13.139	260
270	13.139	13.196	13.253	13.310	13.366	13.423	13.480	13.537	13.595	13.652	13.709	270
280	13.709	13.766	13.823	13.881	13.938	13.995	14.053	14.110	14.168	14.226	14.283	280
290	14.283	14.341	14.399	14.456	14.514	14.572	14.630	14.688	14.746	14.804	14.862	290
300	14.862	14.920	14.978	15.036	15.095	15.153	15.211	15.270	15.328	15.386	15.445	300
310	15.445	15.503	15.562	15.621	15.679	15.738	15.797	15.856	15.914	15.973	16.032	310
320	16.032	16.091	16.150	16.209	16.268	16.327	16.387	16.446	16.505	16.564	16.624	320
330	16.624	16.683	16.742	16.802	16.861	16.921	16.980	17.040	17.100	17.159	17.219	330
340	17.219	17.279	17.339	17.399	17.458	17.518	17.578	17.638	17.698	17.759	17.819	340
350	17.819	17.879	17.939	17.999	18.060	18.120	18.180	18.241	18.301	18.362	18.422	350
360	18.422	18.483	18.543	18.604	18.665	18.725	18.786	18.847	18.908	18.969	19.030	360
370	19.030	19.091	19.152	19.213	19.274	19.335	19.396	19.457	19.518	19.579	19.641	370
380	19.641	19.702	19.763	19.825	19.886	19.947	20.009	20.070	20.132	20.193	20.255	380
390	20.255	20.317	20.378	20.440	20.502	20.563	20.625	20.687	20.748	20.810	20.872	390
°C	0	1	2	3	4	5	6	7	8	9	10	°C

ABB Induction Motor – Torque Curve

ABB Motors and Generators	Starting Curves		
	Project	Location	
Department/Author	Customer name	Customer ref.	Item name 1.00001
Our ref.	Rev/Changed by Date of issue A 10/24/2013	Saving ident untitled.xls	Pages 3(3)

Type of product	TEFC, 3-phase, squirrel cage induction motor				
Type/Frame	M2AA 90 L 2				
Product code	3GAA 091 002-BSE		Frequency (Hz)	50	
Rated output P_N	2.2 kW		Rated current I_N	4.6	A
Type of duty	S1(IEC) 100%				

J_{motor} (kgm2)	0.0024	Voltage (V) 100%	*400*	Voltage (V)	*400V(100%)*
J_{load} (kgm2)		T_{start}/T_N	*2.5*	T_{start}/T_N	*2.5*
Speed (r/min)	2890	Starting time (s)		Run-up time (s)	
T_N (Nm)	7.3	Speed (r/min)		Speed (r/min)	
T_{load} (Nm)		I_s/I_n	*7*	I_s/I_n	*7*
Nbr. of consecutive starts		T_{max}/T_n	*2.7*	T_{max}/T_n	*2.7*

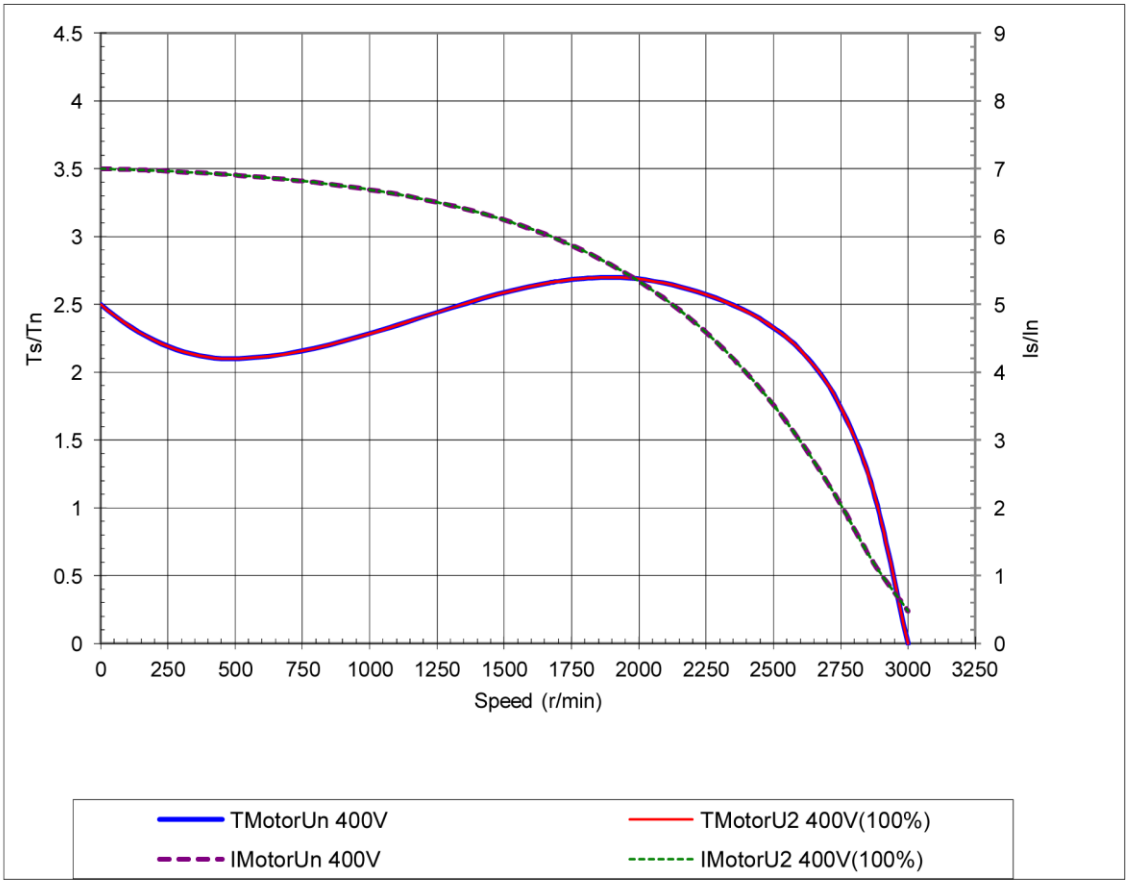

Load characteristics (IEC 60034-2-1:2007)
Data based on situation 4/10/2012
All data subject to tolerances in accordance with IEC